Transport of Solutes and Colloids in Multi-Scale Porous Media Under Single and Multi-Phase Flow

Microscopic Experiments and Pore-Scale Modeling

Enno Tijmen de Vries

Environmental Hydrogeology Group

The reading committee:

prof. dr. M. Flury

dr. S.A. Bradford

prof. dr. H.-J. Vogel

prof. dr. R. Sethi

prof. dr. V. Cnudde

The examination committee:

prof. dr. ir. M.Th. van Genuchten

prof. dr. M. Flury

dr. S.A. Bradford

prof. dr. H.-J. Vogel

prof. dr. R. Sethi

ISBN: 978-90-6266-613-3

NUR: 934, Hydrology

Author contact: ETdevries@protonmail.com

Printed in the Netherlands by Ipskamp

Transport of Solutes and Colloids in Multi-Scale Porous Media Under Single and Multi-Phase Flow

Microscopic Experiments and Pore-Scale Modeling

Transport van opgeloste stoffen en colloïden onder enkel en meerfasestroming in poreuze media met meerdere schalen

microscopische experimenten en poriënschaal modellering
(met een samenvatting in het Nederlands)

PROEFSCHRIFT

ter verkrijging van de graad van doctor aan de Universiteit Utrecht
op gezag van de
rector magnificus, prof.dr. H.R.B.M. Kummeling,
ingevolge het besluit van het college voor promoties
in het openbaar te verdedigen op

vrijdag 17 december 2021 des middags te 2.15 uur

door

Enno Tijmen de Vries

geboren op 2 juni 1992

te Wijk bij Duurstede

Promotor:

prof. dr. R.J. Schotting

Co-promotor and supervisor:

dr. A. Raoof

This thesis was accomplished with partial fininacial support from the Netherlands Organisation of Scientific Research (NWO). This work is part of the Veni Talent Scheme awarded to A. Raoof with project number 016.151.047.

Acknowledgments

While I always was undecided on which study to follow, I stumbled upon the Earth Sciences bachelor due to a cancellation on a study market and I decided to join one of my classmates to attend the Earth Sciences presentation. This grabbed my attention and I decided to enroll. My bachelor was mostly still a search to find where my interest lies in the earth sciences. During the bachelor I got acquainted with Ruud Schotting, who does an amazing job in teaching Math in the first year, and in the third year Water in Geoprocesses. During this course you get introduced to the world of porous media flow and transport. I enjoyed this course a lot and decided to enroll for the Hydrogeology master. Here my interest in porous media was further enlightened by Ruud, Majid Hassanizadeh, Rien van Genuchten, Veerle Cnudde, and Amir Raoof. What especially fascinated me were the pore scale processes, so I decided to perform my MSc thesis with Amir Raoof. He introduced me to flow and transport in complex porous media and offered me to start a PhD project in solute and colloid transport after my MSc thesis. Thank you, Amir, for the trust, guidance, and support that you have given me over the years!

I am very grateful for Ioannis Zarikos for all his help in the lab, as well outside the lab. We made many trips to TU Delft, Kavli cleanroom, where Ioannis taught me how to manufacture the molds for the PDMS micromodels. I thank you for teaching me all the tricks and for all the tips that you gave to me in all the hours we spend in the lab. I express my gratitude to Qianjing Tang for his help performing the experiments in the lab and the many discussions we have had. I would like to thank Sanli Faez for the help he offered building the microscope set-up and for the discussions we had about the experiments. And thanks to Anne de Waal, Giovanni Dammers and Mahin Baghery for the general support in the lab. I appreciate the contribution to my work of the following students: Bernadette Raaijmakers, and Vincent Hoogenboom for their work in the lab, and Joris Dekker for his work on image analysis.

I would like to express my sincere gratitude to Rien van Genuchten and Betty May for their support and the many presents from Brazil! Many thanks to William Godoy, Thiago Carvalho, and Paulo Couto for their invitation to visit their lab at Universidade Federal do Rio de Janeiro. I have had enlightening discussions on the pore-scale networks of complex rocks with dual-scale porosity, as well of having the opportunity to further develop my 2D pore scale grain generator. Unfortunately, during experimental work things do not always turn out as planned, so I was not able to perform the planned PTV experiments.

Thanks to our group secretary Annuska Exel for her support during my PhD, she was always available for help, as well for conversation during coffee breaks. Besides, I am grateful to my two office mates Vahid Nikpeyman and Lifei Yan with whom I had a lot of coffee breaks discussing ongoing work. Furthermore, I would like to thank the members of the Environmental hydrogeology group who I have met over the years; Chao-Zhong Qin, Thomas Sweijen, Jan van Lopik, Niels Hartog, Willem-Bart Bartels, Suzanne Faber, Hamed Aslannejad, Matthijs de Winter, Alraune Zech, Luwen Zhang, Mojtaba Mahmoodlu, Johan van Leeuwen, Gillian Schout, Amir Hossein Tavangarrad, Xiaoguang Yin, Mandana Samari Kermani, and Tuong Hoang.

I gratefully acknowledge my friends who supported me and always helped to have some healthy distractions during my PhD project. I would like to mention in particular: Reijer, Lars, Lennard, Stef, Ludo, Pavan, Marvin, Ed, Hans, Irwin, Kenley, and Sjoerd.

My cat Kiki, who helped me a lot while working at home during the pandemic. I would have never known how good she is in coding and writing by sitting on the keyboard!

Above all, my work would have been impossible without the support of my family. I am very thankful to my parents, Wietse en Marieke, for their advice, encouragements, and continuing support. My siblings, Tidde and Kimberley, Alies, and Jorn, who are always there for me. My nephews and nieces, Naud, Thomas, Sara, and Lisa who are always there with a healthy dose of energy!

Enno de Vries
Autumn of 2021

Contents

Chapter 1

Introduction

Solute and colloid transport in dual-porosity media. Pollution of soil and groundwater resources by a broad range of industrial and agricultural contaminants is an ever-increasing problem worldwide. While applications of fertilizers and pesticides have a significant impact on food production, they also put increased pressure on soils and the subsurface environment (Hantush et al., 2000; Ferro et al., 2013; Zhou et al., 2013; Czachor et al., 2015). Several industries now are also increasingly producing engineered colloidal and nano- particles (Wang et al., 2016). As a result, medicine residues, and personal care or other products are more and more found in drinking water production wells (Kolpin et al., 2002; Ma et al., 2018; Hill et al., 2019). Changes in the soil environment often also causes remobilization of in-situ colloids (Kretzschmar et al., 1999).

Dissolved components and colloids can leach through the vadose zone to find their way to groundwater resources (Figure 1.1). Contaminants can move rapidly through soils due to the existence of macropores, leading to preferential flow paths (Flury et al., 1994; Hendrickx and Flury, 2001; Šimůnek et al., 2003; Allaire et al., 2009; Wang et al., 2013). Macropores may be in the soil due to cracks, fissures, fractures, aggregation of fine soil particles, dead root channels and/or movement of earthworms (Van Genuchten 1985). The fast movement of fertilizers leads to lower efficiency and hence may motivate their increased use, thus contributing to surface and subsurface pollution problems. In addition, macropores in relation to colloid transport leads to the size exclusion effect, which can lead to a lower residence time of contaminants in the subsurface (Kretzschmar et al., 1999; Sirivithayapakorn and Keller, 2003; Bradford and Torkzaban, 2008; Miller et al., 2010).

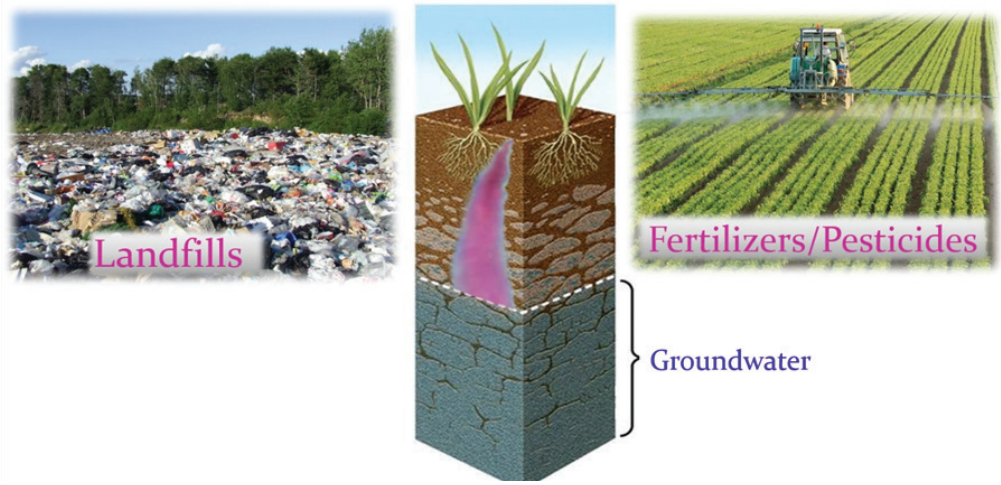

Figure 1.1. Illustration of contaminants and chemicals leaching into the subsurface.

The multi-scale structure of an aggregated soil is shown in Figure 1.2. Aggregated soils are characterized by macropores (inter-aggregate pores) and the soil matrix (intra-aggregate pores), which results in a bi-modal pore size distribution (Van Genuchten and Wierenga, 1976; Gerke and Van Genuchten, 1993; Zhou et al., 2014; Martinez et al., 2015; Vries et al., 2017; Bai et al., 2018). The inter-aggregate pores provide dominant pathways for flow and transport where advection is the main transport mechanism. By contrast, advection in the smaller intra-aggregate pores may be negligible, causing diffusion to become the dominant transport mechanism. The pore space within aggregates greatly affects the transport of chemicals and in many aspects plays an essential role of soil health, including storage of water, microbial activity, soil aeration, prevention of erosion, and protection of organic matter (Brusseau, 1993; Gerke and Van Genuchten, 1993; Arias et al., 2005; O'Donnell et al., 2007). Aggregates vary in size, from around 250 μm to mm size (Tisdall and Oades, 1982; Ferro et al., 2012, 2013; Czachor et al., 2015), and also often vary in shape (Van Genuchten, 1985). Microaggregates are mainly formed by sand, silt, and clay-sized particles (<20 μm) which are bonded together using persistent binding agents such as organic matter and oxides (Tisdall and Oades, 1982). Using temporary and transient binding agents such as fungal hyphae (Degens et al., 1996), micro-aggregates can further bound together to form macro-aggregates.

Over the years different non-equilibrium continuum models have been developed to model preferential flow caused by the bi-modal pore size distribution, including dual-porosity, dual- permeability, multi-porosity, and multi-permeability models (Gerke and Van Genuchten, 1993; Šimůnek et al., 2003). These models assume mobile water flow in the inter -aggregate pores and immobile water in the intra-aggregate pores. Interactions

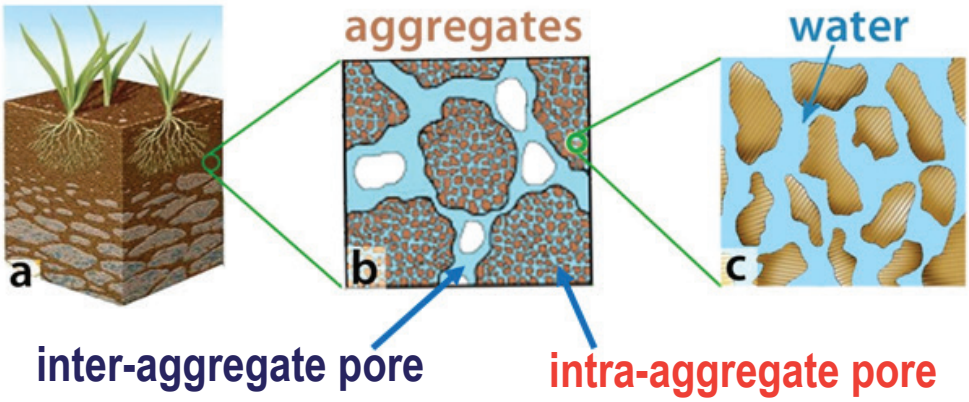

Figure 1.2. Multi-scale structure of an aggregated soil resulting in a hierarchical pore structure. a) Schematic of a soil column, b) soil sample composed of porous aggregates, and c) pore space within an aggregate.

between the two domains are often described using a first-order exchange term, leading to a mobile-immobile (MIM) type dual-porosity model (Coats and Smith, 1964; Van Genuchten and Wierenga, 1976). The mass transfer term integrates several porous media characteristics, such as pore geometry and connectivity, diffusion properties, colloid characteristics (e.g., shape and size), as well as fluid flow properties (Hillel, 2003). Low Peclet numbers can lead to complete mixing between the macropores and the soil matrix, while high Peclet numbers can lead to low diffusion times, in which case exchange becomes small. While this assumption can be made when pore water flow velocities within the soil matrix are negligible, in general this may not be the case due to the complex structure of aggregates (Mangalassery et al., 2013; Zhou et al., 2013; Martinez et al., 2015).

Pore-scale modeling. Pore scale simulations based on methods such as the volume of fluids and lattice Boltzmann approaches can provide details of flow and transport in pore structures obtained from x-ray tomography. However, resolving complex and three-dimensional pore structures requires substantial computational costs. Imaging porous media with bimodal pore structures is also a difficult task due to multiple length scales involved (Ferro et al., 2013). While the macropores can be imaged at micrometer resolution, the smaller intra-aggregate pores may have sub-micron sizes which needs other imaging methods like focused ion beam scanning electron microscope (FIB-SEM) or synchrotron based tomography (Peth et al., 2008; Zhou et al., 2013). A more computationally efficient modeling approach is pore network modeling where pore space is divided into pore elements made up of pore bodies representing larger voids, and pore throats representing narrow openings (Raoof et al., 2013).

Figure 1.3 shows an example of constructing a pore network based on a slice of sand imaged using x-ray tomography. The approach allows one to capture the complex morphology of the porous media, including the number of pores, pore sizes, shape,

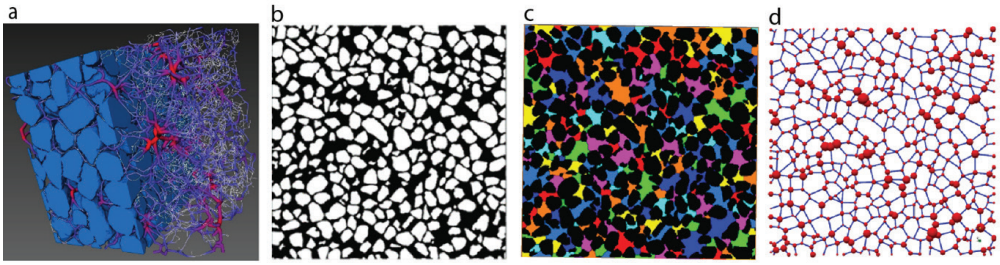

Figure 1.3. 3D to 2D representation of a porous medium and the pore network constructions. a) 3D representation, b) 2D slice, c) segmented pores, and d) pore network; red markers are the pore bodies and blue links are the pore throats.

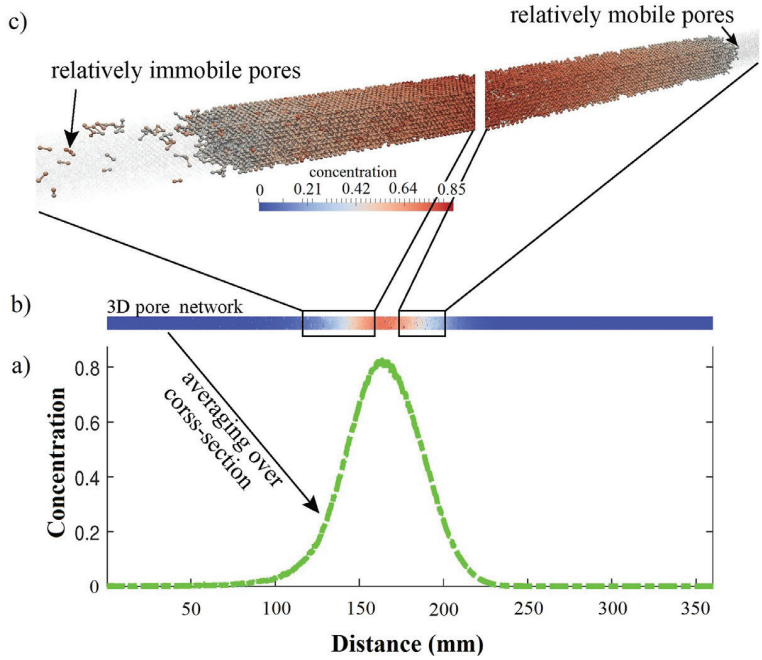

Figure 1.4. Profile of the average (1D) concentration along the three-dimensional sample (a) obtained by cross-sectional averaging the three-dimensional pore scale concentrations (b). Plot c provides pore scale concentration distributions behind and ahead of the BTC for concentrations between the peak concentration value and half the peak value (Source: Mahmoodlu et al., 2020).

and the coordination number (number of throats connected to a given pore body). By incorporating these structures into a pore network model, the local pore-scale behavior can be predicted in an efficient manner. Flow and transport can then be simulated by applying mass balance equations to the individual pore segments. Average properties can be determined by averaging over a large bundle of pores. Pore network modeling has been successfully employed for reactive transport (Raoof et al., 2013), two-phase flow (Bultreys et al., 2015; Yin et al., 2018), flow and permeability estimation (Godoy et al., 2019), solute transport (Qin and Hassanizadeh, 2015; Mahmoodlu et al., 2020), and colloid transport (Zhang et al., 2015). The computational efficiency of pore network modeling enables simulating a very large number of pores in three dimensions. For example, Mahmoodlu et al. (2020) used pore network modeling to simulate experimental observations for flow of water and the transport of a tracer solute in a very large, 36-cm long sand column (Figure 1.4). Incorporating dual-scale problems into a pore network is challenging. Methods

have been developed to add microporosity to the microporosity domain using pore and grain filling approaches (Mehmani and Prodanovic, 2014; Prodanovic et al., 2014), and handling microporosity as continuous media by assigning average flow parameters to these domains (Bultreys et al., 2015).

Micromodel experiments. The interaction between mobile and immobile regions is governed at the pore scale. Useful tools to directly observe details of the pore-scale processes under a wider range of spatial and temporal scales, are microfluidic devices. These devices have a dominant 2D structure with a specific depth to allow fluids to pass, and therefore are called also 2.5D or quasi 2D samples. Generally, micromodels are made from silica glass, quartz, or a clear silicone elastomer like polydimethylsiloxane (PDMS), or a polymer such as polymethyl methacrylate (PMMA). These materials share a common characteristic of being optically transparent. An example of a PDMS micromodel with a flowing fluorescein solution is shown in Figure 1.5.

Geometries used for the micromodels include regularly-placed pillars in a repeating order (Auset and Keller, 2006; Blois et al., 2015; Liu et al., 2019), replicating small irregular structures (Corapcioglu et al., 1997; Willingham et al., 2008), irregularly-placed and sized pillars (Zarikos et al., 2018), pore network capillaries (Karadimitriou et al., 2013), Voronoi tessellation based (Wu et al., 2012) and many others.

Microfluidic devices have been used in various research areas to explore pore-scale phenomena, single-and two-phase flow (Zarikos et al., 2018), transport of solutes (Corapcioglu et al., 1997; Karadimitriou et al., 2016; Jiménez-Martinez et al., 2017) and colloids (Zhang et al., 2013, 2014, 2015; Liu et al., 2019), reactive transport (de Anna et

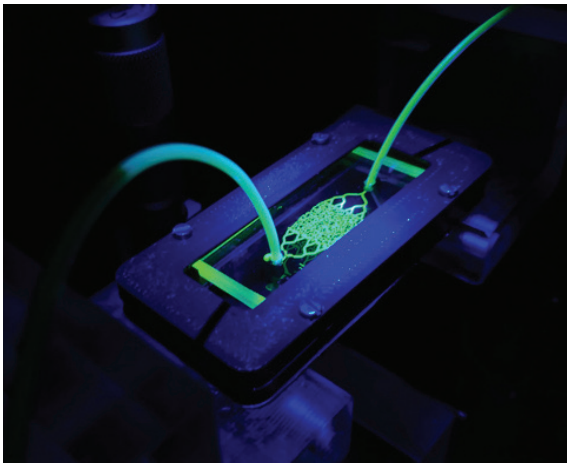

Figure 1.5. Example of a PDMS micromodel during transport of a fluorescein solution through the pore network.

al., 2013), enhanced oil recovery (Jiménez-Martinez et al., 2016) as well as organ on a chip (Helm et al., 2016).

Research objectives.

- Microscopic experiments using micromodels to observe transport of solutes and colloids over a large number of pores and at multiple scales to better understand the effect of pore space heterogeneity.
- Multiple cycles of imbibition and drainage in microfluidics will be performed to explore the effect of moving interfaces and fluid distribution on colloid transport in heterogeneous media.

Outline thesis.

In Chapter 1 a general introduction on solute and colloid transport, dual-porosity systems,pore-scale modeling, and microfluidic experiments is presented.

Chapter 2 describes the development of an optic set-up for tracking colloids during their transport through a micromodel. In this chapter a new method of constructing the breakthrough curve is introduced and detailed information of colloidal trajectories through porous media is provided.

In Chapter 3 we explored dual-porosity media using a Fluorescence Recovery and Photobleaching (FRAP) set-up in micromodel experiments. The micromodel developed in Chapter 2 was used as a base model in which each solid grain of the base model is replaced by a large number of smaller grains by different fractions (i.e., number of grains replaced) to explore the effect of dual porosity on solute displacement by flowing water. We explored the impact of aggregate fraction on solute front development by determining the front length, average concentration gradient, and the front region area. Moreover, we studied the effect of flow velocity on the distribution of the solute in the micromodel.

In Chapter 4 we used pore network modeling to explore the solute transport inside large-size porous media. A pore-network model of 100 mm × 20 mm × 20 mm was obtained using the pore network generator introduced by Raoof et al. (2013). This pore network served as the macro space in which we randomly included 1000 aggregates (each containing a large number of pores) . By changing pore sizes, we explored the effect of aggregate porosity by changing the pore body sizes, while the throat sizes were fixed. Next, we explored the effect of aggregate permeability by changing the sizes of the pore throats, while keeping the pore body sizes fixed.

In Chapter 5 we focused on colloid transport in dual-porosity micromodels. We further used the dual-porosity micromodels from Chapter 3 together with the original micromodel introduced in Chapter 2 to determine the effects of aggregates on colloid transport. We investigated in detail attachment and remobilization of colloids. Moreover, we looked at the effects of flow velocity on transport of colloids in dual-porosity media.

In Chapter 6 we explored two-phase flow in a dual-porosity medium in terms of its drainage and imbibition cycles. For this study, we replaced 50 % of the solid grains with microporous grains. We first performed a water-saturated experiment by introducing colloids to the media. Next, we drained the system using an immiscible Fluorinert solution. While full images of the whole system were obtained, we focused on tracking attachment of colloids within two aggregates in the system to explore colloid transport. Afterwards, we imbibed the system with water, and subsequently drained the system again. As the last step, the system was imbibed another time. We followed remobilization of the attached colloids, as well the fluid distributions inside the porous media to explore the effects of the aggregates on fluid and transport.

Lastly, in Chapter 7 the summary and conclusions of this study are presented.

Chapter 2

Fluid Flow and Colloid Transport Experiment in Single-Porosity Sample

Tracking of Colloid Transport Behavior across a Saturated Micromodel

Abstract

Release of colloids and their subsequent transport into the subsurface environments takes place during a wide range of applications such as industrial, energy storage, and agricultural activities. Therefore, processes contributing to transport, attachment, and re-mobilization of colloids in porous media are attracting attention. A fraction of the released colloids may cross the soil vadose zone to reach the saturated groundwater. In this study, we explored colloid transport in a micromodel with high repulsion energy barrier where colloid retention is assumed to be low. Three major shortcomings were improved: pore space domain size, imaging resolution, and speed of imaging. The flow path of 1357 colloids with a size of 4 μm were tracked and these enabled precise determination of individual colloid transport mechanism as well as the integrated behavior of the system.

Our direct observations have shown that even under unfavorable attachment conditions (defined based on the DLVO theory) colloids deposition occurred which was mainly due to the local flow velocity fluctuations and grain surface heterogeneity. Using the information from collective trajectories, we have quantified the contribution of differently behaved colloids in the observed breakthrough curve which show an integrated, macroscopic, behavior of the system and is often the only available information when performing column or field scale experiments to explore colloid transport in porous media. Furthermore, we have shown that attachment and remobilization of colloids increased the dispersion coefficient, and consequently the dispersivity value of the media.

2.1. Introduction

The increased use of natural and engineered colloids and nanoparticles in agriculture, industry, and consumer products lead to more exposure of soils to these particles (Kretzschmar et al., 1999; Troester et al., 2016; Wang et al., 2016). Moreover, in the recent years the subsurface environment is being extensively used for energy storage applications which promote creation and remobilization of colloids. Particle transport in the subsurface is therefore attracting much attention since particles are now being detected in larger amounts in the environment, including in drinking water supplies, which can pose health threats (Kretzschmar and Schafer, 2005; Rodrigues et al., 2016; Zhou et al., 2017). The vadose zone of soil generally acts as a natural barrier against groundwater pollution. Therefore, the groundwater is less prone to pollution than the surface water due to natural attenuation processes taking place in this section of the earth. However, once contaminated, pollution in groundwater can remain for very long periods of time, with groundwater remediation often being very complicated (Troester et al., 2016). Although a large fraction of pollutants may be filtered out by the vadose zone, more intense land usage causes more pollution of groundwater (i.e., the saturated zone) where contaminants can be transported and spread relatively fast. The subsurface is often very heterogeneous chemically and physically(Argent et al., 2015; Bradford et al., 2015), with the transport of colloids being affected by several coupled processes (Mitropoulou et al., 2013; Sang et al., 2013). Therefore, predicting the final state and transport of colloids in the subsurface is very complicated and requires a fundamental understanding of the main governing processes.

For surfaces with opposite charges, particle deposition is favorable because van der Waals and electric double layer type interactions are both attractive, which allows colloid transport to be well-predicted using colloid filtration theory, CFT (Yao et al., 1971; Baumann and Werth, 2004; Massoudieh and Ginn, 2010). Using CFT, the removal of particles from the bulk fluid can be calculated with a single collector efficiency. However, when the two surfaces are similarly charged (which is often encountered in the earth subsurface), electric double layer interactions are repulsive while van der Waals interactions attractive. An energy barrier against deposition can develop under these electrostatically unfavorable conditions. In that case, an extra parameter, defined as the attachment efficiency, is employed to account for the repulsive forces (Tufenkji and Elimelech, 2004; Miele et al., 2019). To determine the various parameters, colloid transport experiments are often caried out at the column length scale (Syngouna and Chrysikopoulos, 2015), from which colloid breakthrough curves are obtained at the column exit. Empirical absorption coefficients can be estimated by fitting the breakthrough data

using macroscopic formulations (Molnar, Johnson, et al., 2015). The Derjaguin-Landau-Verwey-Overbeek (DLVO) theory may be used to determine the net-interaction energy between a collector surface and a colloid, or between colloids by combining van der Waals attraction forces and the electrostatic repulsion forces (Ryan and Elimelech, 1996; Peng et al., 2010). The theory assumes smooth surfaces with uniform chemical properties, although the approach does not consider local roughness (Argent et al., 2015) and local surface charge fluctuations that may happen due to chemical nonuniformities (Bradford et al., 2015). Spatial variability in the pore water velocity is also known to affect colloid transport of colloids, which is not included in the DLVO theory.

A wide range of adsorption processes act on colloids (e.g., straining, bridging, electrostatic interaction, and aggregation), with their occurrence and frequency depending on the dynamics of flow and the surface properties (Bradford and Torkzaban, 2015). These processes interact with the spatially variable pore velocities to ultimately affect the attachment and remobilization of colloids. Observing such interactions requires relatively large samples where pore sizes and pore connectivity are considered to capture both velocity variations and the occurrence of different adsorption processes. However, large domain sizes together with the required imaging resolution to observe individual colloids provide major challenges for direct observations of colloid transport in porous media and therefore upscaling of colloid transport in porous media. These challenges produce much uncertainty in linking the observed colloid breakthrough curves obtained to the basic processes (Wang et al., 2012; Bradford and Torkzaban, 2015; Molnar, Gerhard, et al., 2015). To overcome these difficulties, pore-scale experiments should be performed where colloid transport, adsorption, and mobilization can be observed directly and simultaneously within a sufficient number of pores to accurately represent the target porous medium. So far, for porous media in the size ranges of sand (i.e., grain sizes of around 100 μm), direct observations have been carried out using microscopy methods such as confocal scanning microscopy (Lazouskaya et al., 2011, 2013; Zhang et al., 2013). These methods provide micrometer-scale observations, however for relatively small domain sizes. The imaged domain sizes then often cover one pore or even smaller (e.g., part of a pore located close to the collector surface). Local roughness and flow field variations between different pores in that case are left out when using single flow channels (Lazouskaya et al., 2011; Sun et al., 2018), capillary tubes, or in case of using limited number of pores or regular/periodic pore structure (Auset and Keller, 2006; Wang et al., 2011; Liu et al., 2019). Periodicity in porous media is known to lead to a dependency on the direction of the flow with respect to the periodicity of the medium (Nguyen et al., 2017; Reichhardt and Reichhardt, 2021).

In this study, we investigated colloid transport under unfavorable conditions using realistic pore structure composed of a large number of pores. Meanwhile, the whole pore structure together with all individual colloids are imaged simultaneously and over time. We developed for this purpose an optical set-up allowing to image the micromodel with a resolution of 2.9 μm, using a micromodel with a length and width of 10 millimeters with an irregular pore structure, and a frame rate of 10 frames per second to track colloid trajectories. The transport paths of the colloids, involving a total of over 1300 separate trajectories within the domain, were further categorized into three groups of colloids: i-mobile colloids, ii-immobilized colloids, and ii-remobilized particles. Transport properties of each category, and then analyzed in detail. The main goal is to capture the full trajectory of colloids flowing through the pore network and observe their dynamic behavior in the presence of a high repulsion energy barrier where retention is presumed to be low.

2.2. Experimental approach

Pore space topology. In this study, we used real pore structures obtained by 3D imaging a sand sample using x-ray tomography. The 3D image was used to extract a 2D slice to develop a mask needed to fabricate a polydimethylsiloxane (PDMS) micromodel. The pore structures were fabricated using soft lithography techniques. The pore domain had a physical size of 10 mm × 10 mm, and the full micromodel (including the inlet and the outlet structures) had a size of 25 mm ×10 mm with a depth of 20 μm and a porosity of 0.40. The

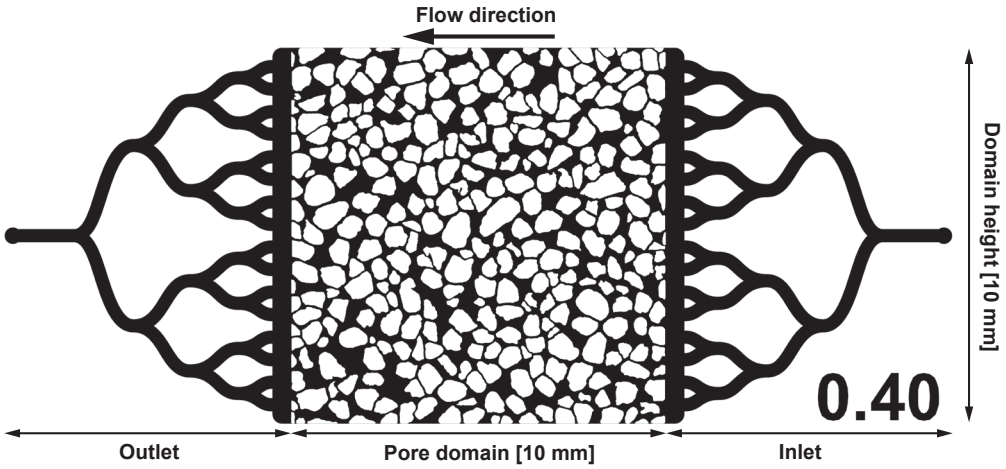

Figure 2.1. Micromodel structure including the inlet and outlet structures designed to provide an accurate and even distribution of fluid flow and colloids entering the domain during the experiment.

Table 2.1. Information about the solid phase and pore space of the micromodel.

	Property	Value
Solid phase	Number of grains	317
	Grain diameter [mm]	0.473 (0.144)*
	Grains shape factor [−]	0.811
Pore space	Number of pore bodies	460
	Number of pore throats	708
	Pore body diameter [mm]	0.324 (0.092)*
	Pore throat diameter [mm]	0.145 (0.063)*
	Pore shape factor [−]	0.435 (0.133)*

*values in parenthesis indicate standard deviations

micromodel allows for direct observation of colloid transport, although due to the quasi-2D structure grain-grain contacts are present although they do not accurately represent the contact points of a 3D porous media. Figure 2.1 shows the complete micromodel structure, with Table 2.1 providing details of the solid phase and the pore space. Detailed information is provided in Appendix A.

The microscopy setup and the experimental procedure. We developed a home-build microscope setup to perform particle tracking. The setup consisted of two 595 nm LED's (Thorlabs M595) with band-pass filters of 580 ± 10 nm (Thorlabs FB580-10) to excite the colloids (Figure 2.2). We used 4-μm colloids (FluoSpheres™ Sulfate Microspheres (580/605), ThermoFischer) which emitted red light at a peak wavelength of 605 nm. The emitted light was isolated and captured using a long-pass filter of 600 nm (Thorlabs FEL0600) placed in front of the camera (Basler acA5472-17um). Fluid flow was established using a syringe pump (Harvard Apparatus Pump 11 Pico Plus Elite) connected by a tube to the micromodel main inlet channel. The main outlet channel was connected to a fluid reservoir. Figure 2.2 provides the configuration of the setup.

The pore space is initially fully saturated with ethanol. Afterward, we injected 100 pore volumes (PV) of colloid-free water into the pore space to provide fully saturated water flow and steady state condition. The experiment was continued by injecting 5 PV of the solution containing colloids followed by 10 PV of a colloid-free solution at an average pore-water velocity of 12.0 m day^{-1}. A low input concentration was used to stay in the single-colloid

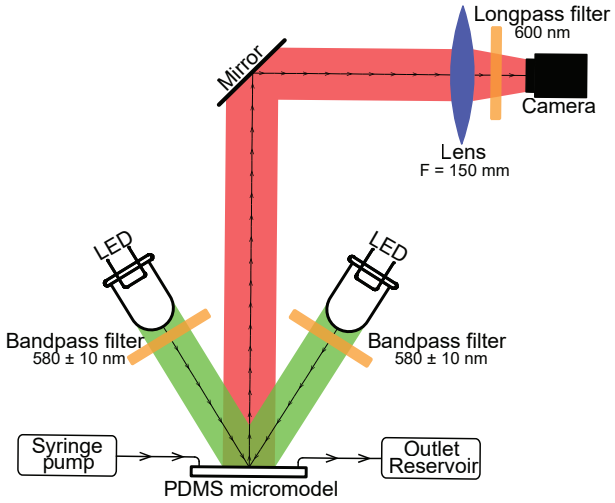

Figure 2.2. Schematic of the microscopy set-up: two green LED's (Thorlabs M595) with bandpass filters of 580 ± 10 nm were used to excite the colloids. The emitted red light by colloids, with a peak wavelength of 605 nm, was isolated using a long-pass filter of 600 nm. Images are captured with a Basler acA5472-17um using a frame rate of 10 frames per second.

limit which is usually the case in the earth subsurface environment such as transport of pathogenic bacteria and viruses where they are present under low concentrations to increase their survival chances for long time periods of several months (Pekdeger and Matthess, 1983; Schijven and Hassanizadeh, 2000). Under such low concentrations, clogging and plugging of pores does not happen due to bridging and straining processes, unlike other studies that focus on clogging of porous media under relevant conditions (Auset and Keller, 2006; Reichhardt and Reichhardt, 2017; Péter et al., 2018; Parvan et al., 2021). Accurate imaging required minimum disturbance and vibration of the setup during the injection experiments. To achieve this, the complete sequence of solutions (i.e., the sequence of clean solutions and solutions having colloids) were injected prior to the start of experiments into the inlet tube. This approach allowed different target solutions to enter the micromodel without changing the tubing of the system or using any flow switch which can affect the accuracy of injection and imaging. Throughout the experiment images were recorded at a resolution of 2.9 μm with an imaging rate of 10 frames per second.

The imaging processes. An image of a fully rhodamine saturated micromodel was taken to serve as the reference image (mask) for the pore space during analyses. Comparisons of images taken during the experiments against the reference image provides images of only the pore space, including the colloids. We used image analysis to detect colloids within each individual image and tracking individual colloids between successive frames

(i.e., one-to-one paring of colloids in each frame n to colloids in a successive frame n+1) to obtain complete colloid trajectories. Laplacian of Gaussian particle detection (LoG detector) was used to detect particles (Lindeberg, 1998), and the Linear Assignment Problem (LAP) particle-linking algorithm (Jaqaman et al., 2008), applied in the TrackMate package developed by Tinevez et al. (2017), for our experiments as it is optimized for non-dense particle systems. The obtained trajectories were further analyzed in MATLAB and details of the imaging process and analysis as well as the trajectory information are provided in Appendix A. As noted earlier, the acquired trajectories were divided into three categories representing: i-mobile colloids, ii-remobilized colloids, and iii) permanently attached colloids (i.e., immobilized colloids). All trajectories describe the full path from the point of entry until the colloids either deposited or passed through the entire domain.

Using the obtained comprehensive information from experiments several transport properties were calculated including the tortuosity of particle trajectories, residence time of particles, frequency of attachment and remobilization events for each particle, as well as the penetration depth and the 1st and 2nd moments of the attached mass. Detailed information on the transport properties is provided in Appendix A.

Zeta potential. The zeta potential measurements were carried out with a Zetasizer Nano ZS analyser (Malvern Instruments, Worcestershire, UK). The colloid solution was prepared with a specific concentration in deionized water to measure the electrophoretic mobility of the dispersed colloids in solution. Before the measurements, the suspension was sonicated in an ultrasonic bath. Measurements were taken at 20 degrees Celsius at neutral pH. The zeta potential was derived from the electrophoretic mobility assuming applicability of Henry's equation and Smoluchowski approximation (Sze et al., 2003) to calculate the DLVO forces. The equations to calculate the DLVO forces are given in Appendix A.

Breakthrough curve (BTC). Traditionally, concentration breakthrough curves (i.e., BTCs) are measured at the outlet of the system by collecting the outflow solution. When using micromodel experiments, this is done by measuring fluorescence intensity at the outlet location of the domain (Zhang et al., 2015). The breakthrough curve shows an integrated, average, behavior of the system and does not uniquely reveal the contribution of the internal local behaviors. Nevertheless, BTC's are of importance for upscaling using macroscopic continuum-scale modelling (Baumann and Werth, 2004). In our experiments, we simultaneously capture the internal pore-scale behavior of colloids as well as the average behavior which is obtained using the BTCs measured at the sample outlet.

2.3. Experimental results and analysis

Colloid transport experiments under unfavorable conditions resulted in a total of 1357 trajectories of the colloids, of which 1309 were transported through the entire domain without any deposition, 19 attached and then remobilized, and 29 colloids permanently attached to a collector surface. Figure 2.3 shows the collection of trajectories that passed through the domain. While a large number of colloids percolated through the sample, we have observed several pores which never received any colloids. These pores are mainly dead-end pores and/or pores oriented perpendicular to the overall flow direction (-i.e.,

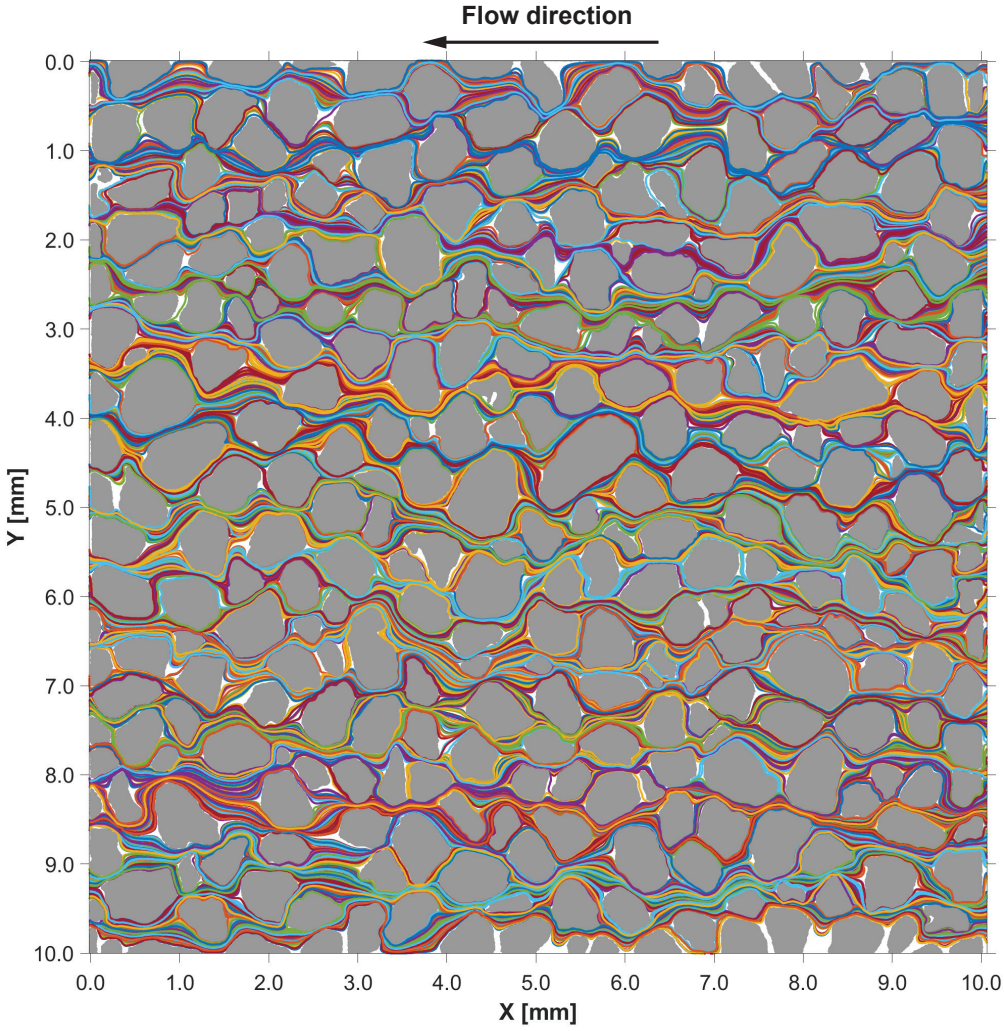

Figure 2.3. Trajectories of all the colloids that were transported through the micromodel pore structures. Flow is from the right towards the left.

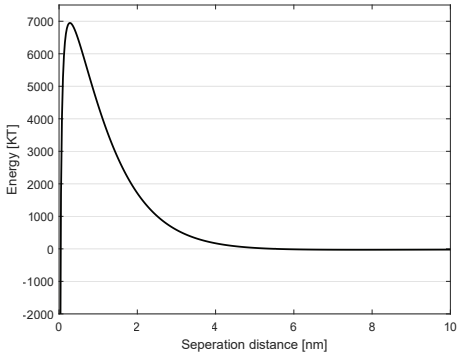

Figure 2.4. DLVO energy profile between the collector surface (i.e., the micromodel PDMS solid grains) and colloid.

normal to the generated pressure gradients, leading to low flow velocities). In what follows, we first discuss the DLVO profile, next we focus on the integrated behavior of colloids in the system, followed by characterizing trajectories of the attached colloids, and the breakthrough curves.

DLVO profile. The measured zeta potential of the colloids in deionized water was −47 mV. The zeta potential for the PDMS was taken as −80 mV (Sze et al., 2003; Kirby and Hasselbrink, 2004; Almutairi et al., 2012) and the ionic strength close to zero. Figure 2.4 shows that the DLVO profile between the colloids and the collector surface has a high primary minimum barrier, but no secondary minimum due to the low ionic strength. This indicates unfavorable conditions under which colloid attachment is not probable when only DLVO forces were taken into consideration. However, several other processes could contribute to attachment including local grain roughness, surface charge heterogeneities, and local flow conditions (Bradford and Torkzaban, 2015; Bradford et al., 2015), which could lead to lower effective energy barrier and cause colloid attachment.

Tortuosity, normal distance to grain surface, and trajectory average velocity. Figure 2.5 together with Table 2.2 (average values) show the behavior of colloid trajectories divided into three categories of mobile, remobilized and attached colloids. The probability distributions for the parameters are given in Appendix A. Results show that colloids that moved closer to the grain surfaces, had longer trajectories which increased their tortuosity (Figure 2.5a), and caused lower observed transport velocities (Figure 2.5b). Although data points are scattered in Figure 2.5c, they show a general linear trend between the normal distance from the grains and the velocity of colloid trajectories. The outliers may be impacted by the measurement procedure (which is discussed in Appendix A). For colloids that were permanently attached inside the pore network, average values were calculated

up to the moment of attachment. The attached colloids generally show transport at close distances to the solid grains, however they show a wide range of tortuosity values. When colloids were attached close to the inlet, the tortuosity of their trajectories remains close to 1.0 because of their short travel time and distance. The attached colloids which deposited at larger distances within the pore space showed higher tortuosity values mainly because they followed the curved grain surfaces during their transport. Therefore, the average tortuosity of colloids that became permanently attached inside the domain can be even lower compared to other colloids. Remobilized colloids showed an average tortuosity value of 1.225 which is larger than the average tortuosity of mobile colloids (1.205). This is mainly because remobilized colloids follow more twisted paths during their relatively large residence times across the pore network. We can conclude that colloids subject to attachment have a higher tortuosity as they generally travel for longer times in the vicinity of solid surfaces and create longer paths compared to the colloids that were mobile and transported rather through the central regions of the pore spaces.

Overall, the trajectory of remobilized and permanently attached colloids pass close to the grain surfaces, which causes the average velocity to be lower than the mobile colloids. Local variations in the flow velocity distribution and DLVO forces will determine the ultimate attachment of colloids.

Remobilization. In this section, we will describe colloid remobilization events. Of the trajectories that became permanently attached, none showed attachment and remobilization events before deposition, whereas 19 colloids showed attachment and

Table 2.2. Average values of the tortuosity, distance from the grain surface, velocity of the trajectory, and the transport time in the domain for the three types of colloids categorized based on their behavior. Transport time for the attached particles refer to the elapsed time up to the moment of colloid attachment. The probability distributions are given in the Supplementary Materials.

Trajectory type	Tortuosity [-]	Distance to solid [m]	Velocity [ms^{-1}]	Transport time [s]
Mobile	1.205 (0.038)	5.692 $(1.060)\times10^{-5}$	1.362 $(0.369)\times10^{-4}$	92.4 (27.6)
Remobilized	1.225 (0.046)	5.057 $(1.565)\times10^{-5}$	1.230 $(0.353)\times10^{-4}$	144.4 (41.74)
Attached	1.200 (0.081)	4.445 $(1.199)\times10^{-5}$	1.233 $(0.433)\times10^{-4}$	59.2 (39.7)

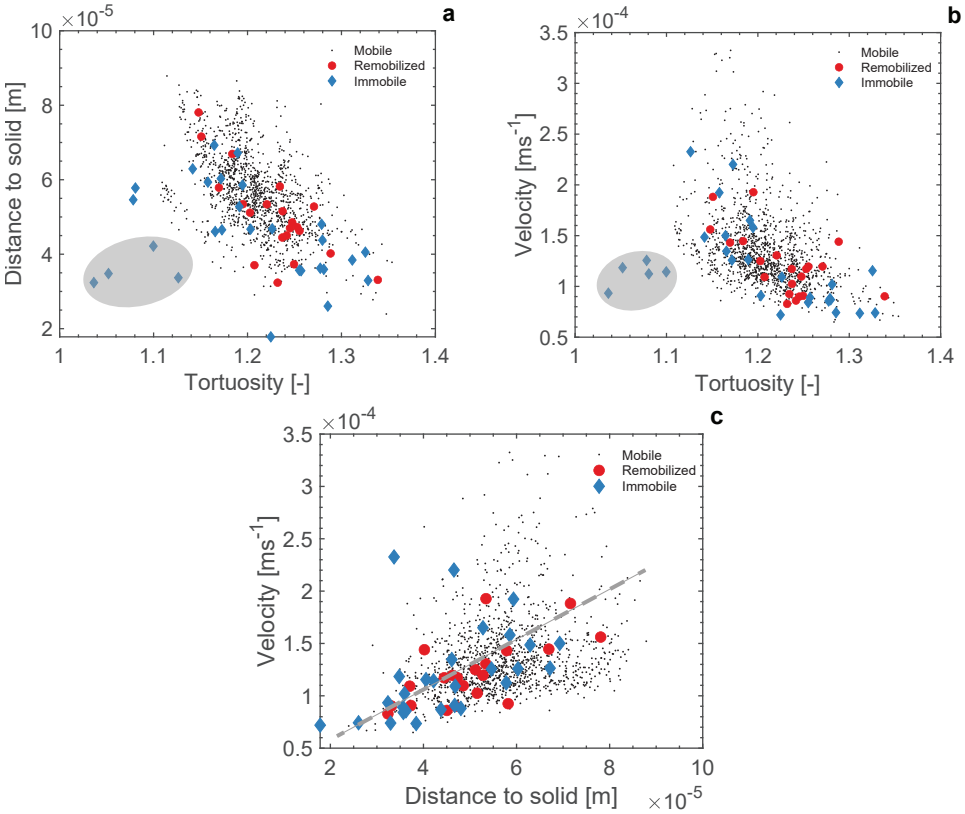

Figure 2.5. Plots showing for each trajectory a) the average distance normal to the grain surfaces versus the tortuosity. b) average velocity versus tortuosity. c) average velocity versus the normal distance to the grain surfaces. Parameters for the attached particles (immobile) were calculated until the moment of attachment. The gray highlights indicate colloids that were attached soon after injection and therefore may have not experienced a sufficient fraction of domain pore structure. The probability distributions of the parameters are given in the Supplementary Materials.

remobilization. Below we will explore the average and standard deviation (i.e., sample scale) transport properties and then describe two of the trajectories in more detail. Analysis have been done on the temporal evolution of adsorption using the 1st and the 2nd moments which are given in Appendix A.

The remobilized colloids spent on average of 42.1 (48.5) seconds in the attached state (immobile), with the total time within the porous medium being on average 144.4 (41.74) seconds. This shows that the remobilized colloids spend, on average, 29% of the total residence time attached to the soil grains. This compares with mobile colloid which, on

average, spend 92.4 (27.6) seconds within the domain. Comparing these residence times shows that remobilization requires on average 50% extra time for colloids to arrive at the outlet. The trajectories of these colloids have a higher tortuosity compared to the mobile colloids and they often are transported closer to the solid grains and have lower average velocities. In our experiments, the maximum time that a colloid was immobilized before being remobilized was 208 seconds, with this colloid residing 268 seconds inside the domain.

Typical examples of the colloid velocity and distance to solid against time are given in Figure 2.6. We found that colloid 615 closely followed free flow (i.e., being mobile), while being transported only slightly closer to the walls compared to the completely mobile colloids. Before attachment, the colloids came closer to the collector surface before being immobile for 110 seconds. While being immobile, the colloid showed very little movement although very small fluctuations in the velocity are visible (the velocities fall within the error margin, an assessment is made in Appendix A). Colloid 548 also follows a free flow path before reaching a low-velocity area where it is immobilized for 10 seconds. After remobilization, the colloid shows rolling along the collector surface before it is transported by bulk free flow. Similar behavior was found for the 18 other colloids that showed attachment and remobilization.

In this study only forward flow was applied and the results showed remobilization of colloids, either by local flow velocity perturbations or rolling along the surface at very low rates. While other mechanisms could lead to remobilization as well, i.e.- increased flow

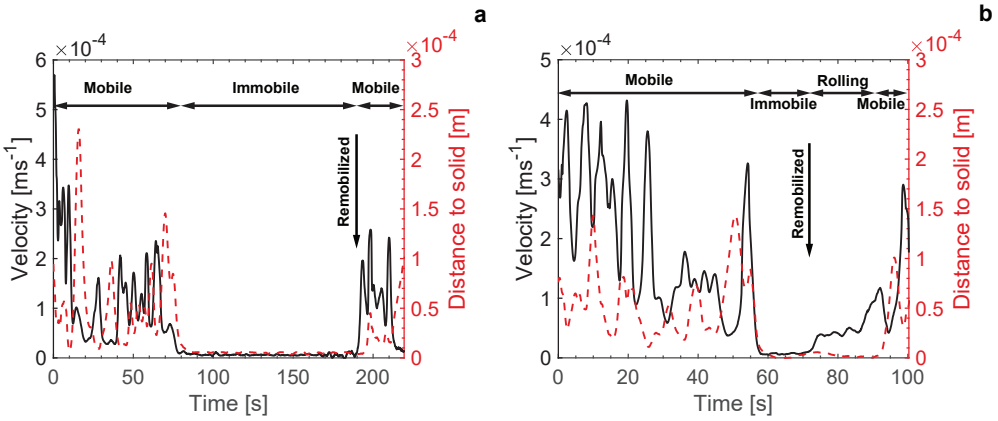

Figure 2.6. Plots showing for colloids 610 (a) and 548 (b) their velocity (left y-axes) and distance to the solid grains (right y-axes) over time. Colloid 615 colloid showed attachment for a duration of 110 seconds before being remobilized and colloid 548 which showed attachment for a total duration of 10 seconds.

velocity (Bradford et al., 2009; Knappenberger et al., 2014), moving interfaces (Aramrak et al., 2011; Zhang et al., 2013), shift in chemical conditions (Mitropoulou et al., 2013; Samari-Kermani et al., 2021), or reversed flow (Reichhardt and Reichhardt, 2018).

Permanently attached colloids. Figure 2.7 shows the location of the attached colloids together with their trajectories (before attachment) inside the transport domain. Additionally, Table 2.3 provides the average properties of the attached colloids. Figure 2.7 shows that although most of colloids were attached to the solid grain walls, some of them were attached to the top or bottom section of the microfluidic. The mean throat size in which colloid attachment has occurred is 0.107 mm (probability density function is given in Appendix A), and the average throat size of the domain is 0.145 mm. Therefore, colloids have shown tendency to become attached within the smaller pores. In several cases, multiple colloids were attached at the same location. When this occurs, the first attached colloid may turn the situation more favorable for the newly arriving colloids to attach (shown by blue markers in Figure 2.7).

The peak arrival time of mobile colloid concentration at the outlet was 90 s. However, a small fraction of colloids became attached at time later than 100 seconds. These colloids mostly attached in regions close to the end of the domain and often had a lower average velocity compared the bulk flow. Travel times much higher than those of the mobile colloids would indicate a high amount of remobilization occurring in the system. However, our results show that the attached colloids were not subject to remobilization prior to permanent attachment. Furthermore, from Figure 2.7 it is evident that several colloids move for some time in close proximity to the collector surface prior to attachment. This behavior shows that the attraction forces are relatively weak to hold the colloids strongly, and that it takes some time for colloids to find an attachment location where the net forces

Table 2.3. Average properties of attached particle trajectories.

Property	Value
Penetration depth [m]	$5.185\ (2.905)\times10^{-3}$
Displacement till attachment [m]	$6.319\ (3.539)\times10^{-3}$
Tortuosity till attachment [-]	1.200 (0.081)
Time till attachment [s]	59.2 (39.7)
Mean pore body size at attachment [m]	$3.183\ (1.102)\times10^{-4}$
Mean pore throat size at attachment [m]	$1.069\ (0.819)\times10^{-4}$

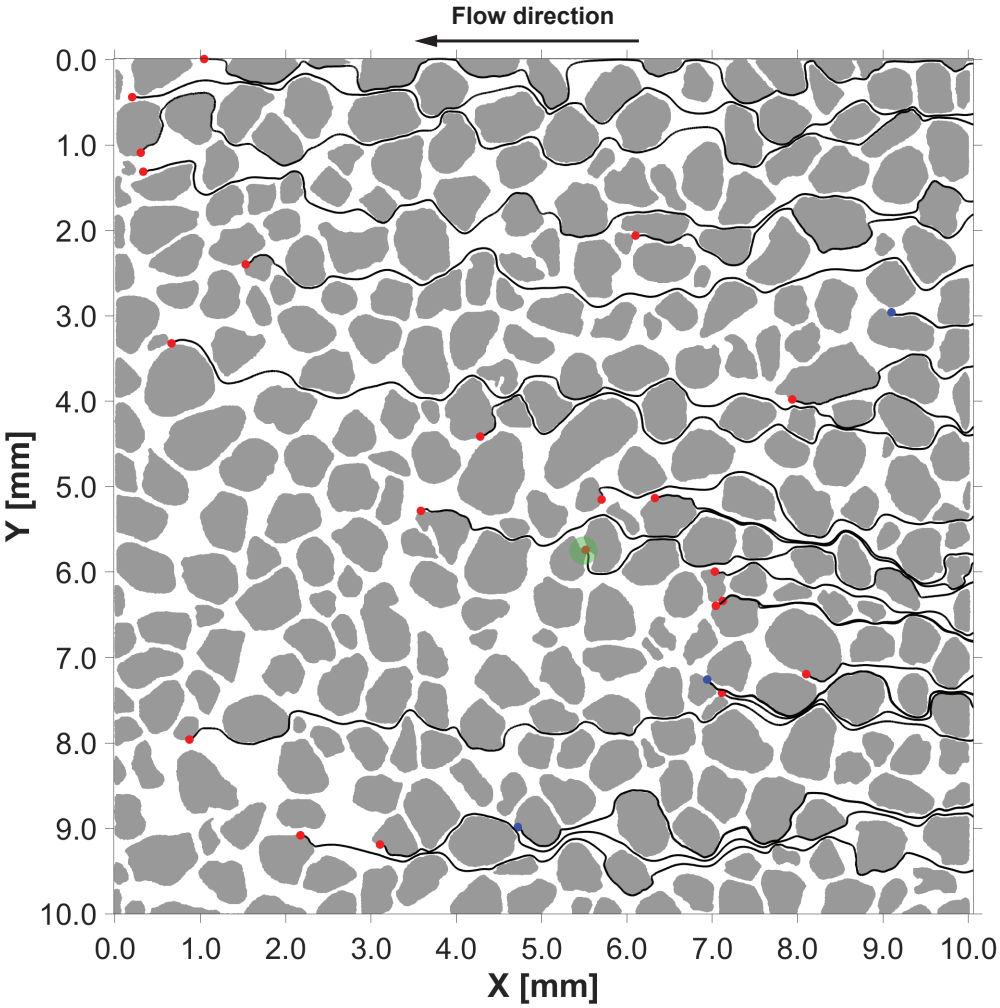

Figure 2.7. Trajectories of the attached colloids. The blue markers indicate locations where more than one colloid were attached, and the red markers locations where a single colloid was attached. The colloid marked by a green circle was attached in a pore orientated perpendicular to the general flow direction.

are favorable for attraction.

Figure 2.8 shows the trajectories of three colloids. Even though colloid 1290 was attached and the other two colloids were mobile throughout the flow domain, however all three had very similar trajectories during most of their flow path. Colloid 1280 reached a low-velocity zone after 100 seconds when it began rolling along the surface for another 70 seconds before attachment. Rolling of the colloid was due to the overall unfavorable conditions for attachment where colloids can attach at a smaller fraction of surfaces when

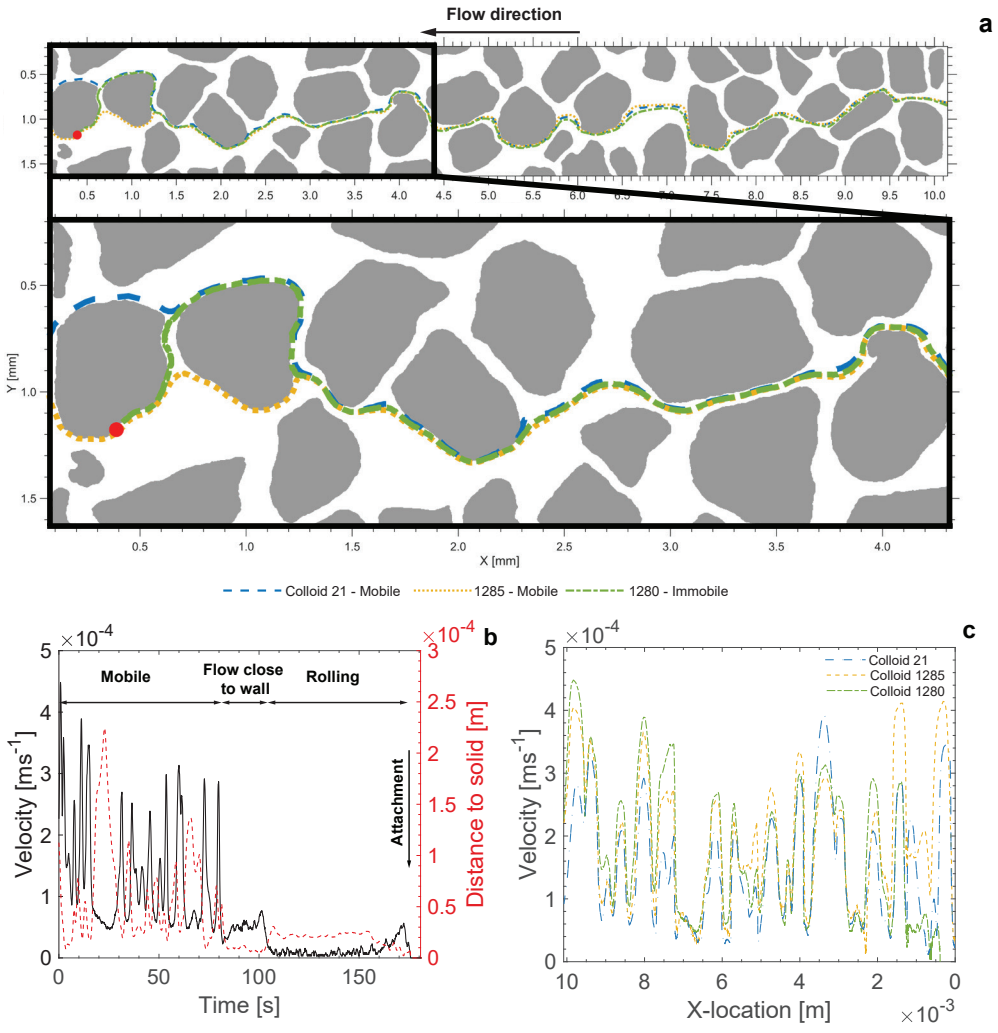

Figure 2.8. a) Trajectories of colloid number 1280 (as an attached (immobile) colloid) and colloids number 1285 and 21 (as mobile colloids), shown in full length as well as a zoomed in section. The two trajectories followed similar pathway through most of the domain, and the trajectory of the attached particle changed near the end of the flow domain where it attached. b) Plots of the velocity and distance to the solid grains against time for colloid 1280, showing that prior to attachment this colloid was rolling over the solid surface. c) Plots of the colloid velocity against location for colloids 1280 (attached) and 1285 and 21 (mobile).

a suitable site is found and the energy barrier is lower due to local roughness, chemical heterogeneities, and/or lower local fluid flow velocities.

Figure 2.8c shows the velocity profile (i.e., along the sample) for an ultimately attached colloid (number 1280) as well as for another two trajectories passing through the whole domain without any deposition. Although the trajectories (shown in Figure 2.8a) were very similar, the velocity distribution was different for each track. Until 9.5 mm, there was no indication that track 1278 would become attached. At 9.5 mm, the particle stagnates and rolled until becoming attached. This observation reveals the challenge of using the location and shape of a trajectory to predict whether an attachment event will occur.

Bridging. Colloid sizes and surface properties together with a relatively low input concentration of colloids (which is often the case in subsurface environments) used in this study resulted in no straining, clogging, or aggregation in our experiments. However, local colloid bridging was observed at three locations where attachment took place in proximity of a previous attached colloid. We should note that as bridging happens and more colloids attach at the same location, the emission from the fluorescence particles intensifies, but the resolution limit makes it difficult to distinguish each particle after they are attached. Nevertheless, because of the trajectory that leads exactly to the previously attached particle (see Figure 2.7, blue dots and their trajectories), we could detect the bridging process. Figure 2.9 shows the velocity of this category of colloids versus the longitudinal distance. While the three trajectories were similar, the transport velocities were different between these trajectories. At location 0.25 mm, we observed the highest velocity reached by colloid 402, and followed by colloids 883 and 1246. While at location 2.1 mm we observed the highest velocity reached by colloid 1246, and subsequently by 883 and 402. This indicates that the correlation of transport velocity between pores is relatively low, which is often assumed to occur up to one pore (Alim et al., 2017; Miele et al., 2019). It is difficult to foresee if a particle will bridge to another particle, although the trajectories indicate that the flow velocities do not differentiate much between the trajectories. This also indicates that the colloids were probably being transported at similar depth inside the micromodel, and thus making it more likely to bridge to a previously attached colloid.

Breakthrough curves. A major aim of this study was to capture full colloid trajectories throughout the domain, as well as colloid concentrations at the outlet to provide insight into the breakthrough curves. Our micromodel was designed to have a uniform flux at the inlet of the sample. However, small discrepancies between the inlet channels were inevitable. This will cause slight local differences in the velocity field and fluctuations in arrival times of colloids at the start of the pore network. Moreover, hydrodynamic dispersion will likely occur also inside the inlet tube, as well as inside the inlet channels of

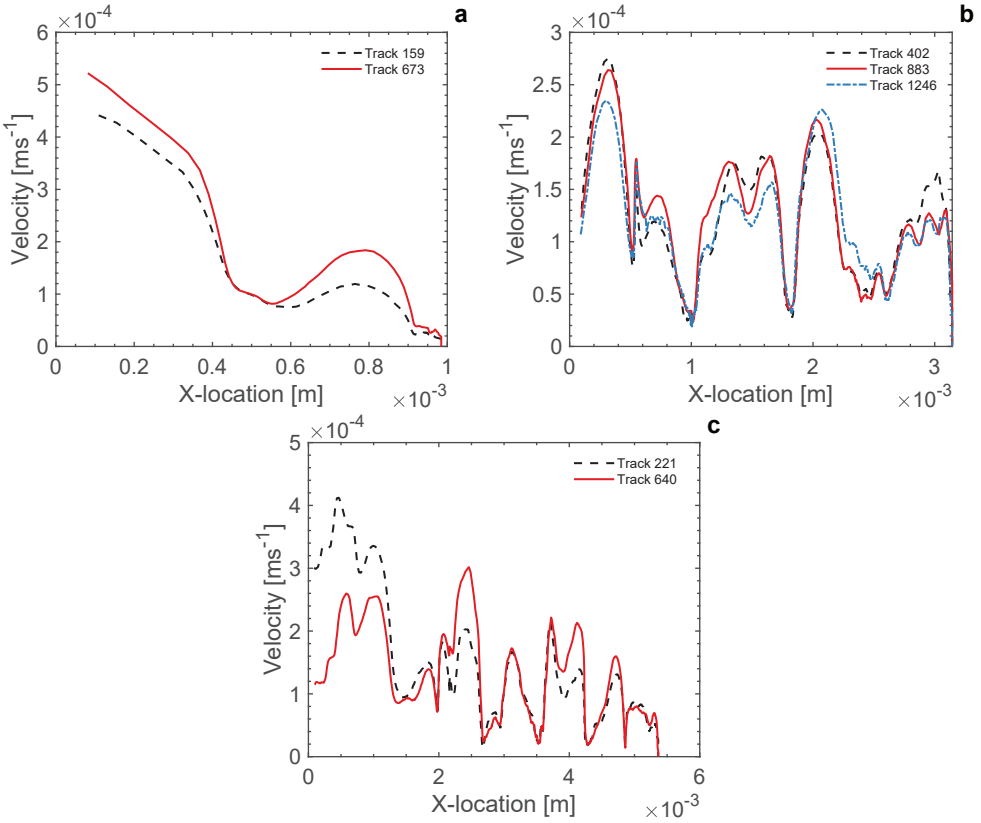

Figure 2.9. Colloid velocities along the longitudinal distance for colloids that were attached (immobilized) at the same location. a) Colloids 159 and 673, b) colloids 402, 883, and 1246, c) colloids 221, and 640

the micromodel. These factors will turn the pulse input into a distributed and often skewed input concentration which may fluctuate over time. However, since the whole pore space was imaged, the arrival time of each individual colloid at the start of the pore domain and when they surpass the outlet, which corresponds to the residence time in the pore network of the colloid. We can normalize colloid entrance times and construct a Dirac delta input (i.e., in the normalized form all the particles enter the domain instantaneously at t=0) which is equal to the probability density function of the residence time. Constructing the breakthrough curve in this way would assure that colloids migrate and interact with the solid grain individually (i.e., no dominant colloid-colloid interaction) which is valid for our experiments based on our observations of colloid trajectories. Having the information of full trajectories for different categories of colloids, we can construct various breakthrough curves from one dataset, such as BTC of all colloids entered the system, BTC of mobile colloids, and BTC of colloids only with detachment and/or remobilization events. This

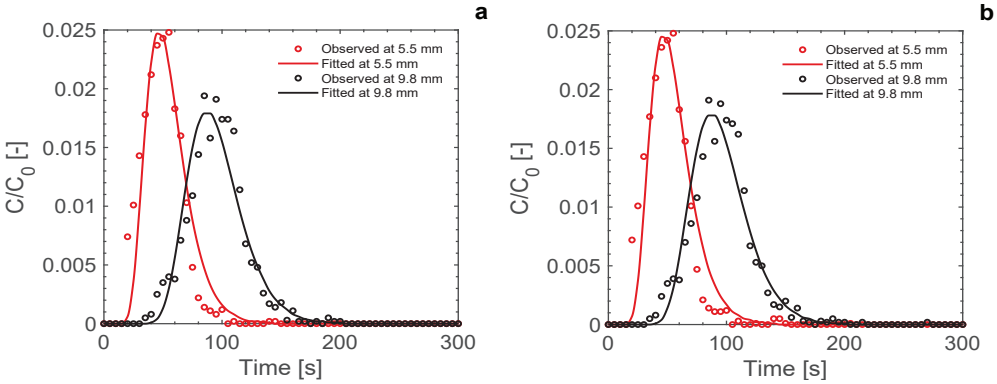

Figure 2.10. Dirac delta input breakthrough curves and the multi-fit results. a) Colloids that were mobile during their transport through the pore domain, breakthrough at multiple locations (mm) through the domain. b) All Colloids that were transported through the pore domain, breakthrough at multiple locations (mm) through the domain.

will a much better understanding of the influence of attachment and remobilization on the breakthrough curves.

Figure 2.10 shows the normalized average concentration breakthrough curves (BTCs) for colloids that were mobile in the domain and for all colloids. The progression of colloids within the domain in form of concentration BTCs are given in Appendix A. Due to the small number of particles with attachment and detachment events (compared to the bulk flow) we see little influence on the shape of the obtained breakthrough curves. All curves are only slightly asymmetrical which is due to the preferential (nonequilibrium) flow paths, with colloid attachment/detachment causing slight increase in late-time tailing of the BTCs. When we exclude these processes, one can analyze the obtained BTCs in terms of the classic Advection-Dispersion Equation, ADE ($\frac{\partial c}{\partial t} = D\frac{\partial^2 c}{\partial x^2} - v\frac{\partial c}{\partial x}$), where C represents the colloid concentration, v denotes the pore water velocity, D is the dispersion coefficient, t is time, and x is the spatial coordinate as before. It is also possible to use a Advection-Dispersion-Sorption equation, for example a one-site or two-site kinetic model, to account for the sorption and desorption of colloids to and from the solid wall (Schijven and Šimrunek, 2002; Molnar et al., 2015). For example, if the fraction of remobilized and attached colloids would increase, which have longer residence time than the mobile colloids, then the traditional ADE would not suit for the observed BTC. In this case, we chose to analyze both trajectory categories using the equilibrium ADE as its was adequate to describe the observed attachment/detachment processes. Figure 2.10 shows the multi fitted BTCs (single fit results are provided in Appendix A) and Table 2.4 provides the optimized transport parameters (D, v, and the dispersivity, $\alpha = Dv$)

Table 2.4. Optimized ADE transport parameters for mobile colloids and all colloids combined. The single fit belongs to the breakthrough curve at 9.5 mm, and the multi-fit for simultaneous analysis of the breakthrough curves at 5.5 mm and 9.8 mm.

Trajectory type	Mobile colloids		All colloids	
Fitting Method	**Single fit**	**Multi fit**	**Single fit**	**Multi fit**
V [ms^{-1}]	1.02×10^{-4}	1.06×10^{-4}	1.02×10^{-4}	1.06×10^{-4}
D [m^{2}s^{-1}]	2.58×10^{-8}	3.23×10^{-8}	2.64×10^{-8}	3.27×10^{-8}
α [m]	2.53×10^{-4}	3.05×10^{-4}	2.59×10^{-4}	3.10×10^{-4}
R^2	0.964	0.941	0.964	0.940

obtained by CXTIFIT code in STANMOD (Šimůnek et al., 1999), as well the R^2 values for a single fit at only the location of 9.8 mm and a multi-fit where the transport parameters were optimized simultaneously for BTCs at two locations (i.e., x = 5.5 and 9.8 mm). The single fits performed slightly better indicated by the R^2 value, and the fitted velocities are marginally lower than those obtained using the multi-fit. The fitted velocities are slightly lower than the estimated values as shown in Table 2.2. The underestimation can be caused by the presence of the preferential flow paths. The dispersion coefficient for multi-fit optimization is higher than the single fit which is due to the stronger bell shape of the fitted BTCs (Appendix A). Results show the influence of the attachment, attachment/detachment trajectories on the BTCs as slightly higher estimated dispersion coefficient, and hence also the dispersivity value.

2.4. Conclusions

In this study we have developed a new microscopy setup to perform colloidal experiments at the cm scale, while simultaneously observing transport, attachment, and remobilization of all individual colloids at the micrometer scale. For each individual colloid that was transported through the domain, the trajectory was captured and analyzed to explore the attachment. We found that even under unfavorable conditions, based on the DLVO interactions, colloids were attached due to fluctuations in the local flow velocity (i.e., fluctuating hydrodynamic forces and local roughness affecting local DLVO forces). The observed trajectories were normalized into single breakthrough curves and fitted using analytical solutions which describes colloids transport as 1D macroscopic process along the general flow direction. This study as particularly showed that:

- The trajectory of the remobilized and permanently attached colloids overall passed

close to the grain surfaces with a lower average velocity compared to the velocity of the bulk flow.

- Due to low input concentration no colloid aggregation was observed and therefore straining was not observed due to the low ratio in particle size versus the pore sizes. A few instances of bridging were observed, this retention processes, as well as straining would be expected to be a higher contributor to retention at higher input concentrations.
- The remobilized colloids spent, on average, 29% of the total residence time in the attached state at the soil grains.
- After remobilization, some colloids show rolling along the collector surface before being transported into the bulk free flow.
- Colloids with very similar trajectories (i.e., transportation in close vicinity of each other) could show different attachment behaviors and different flow velocities along their respective trajectories.
- Attached colloids showed clear rolling over the solid grains, due to the overall unfavorable conditions for attachment before their depositions.
- Attachment and remobilization caused slight increase in estimated dispersion coefficient, and subsequently the dispersivity value of the media, obtained by fitting to the ADE equation.

The developed microscopic set-up demonstrates the potential to further investigate pore-scale behavior at the cm scale by including various chemical conditions, hydrophobicity changes, flow conditions, two-phase flow, colloid size and shape, and different pore structure topologies. Furthermore, the set-up can be extended with an additional camera and light source to be able to observe two different species of colloids simultaneously, or of colloids together with a fluorescent dye to capture their interactions.

Chapter 3

Fluid Flow and Solute Transport Experiments in Dual-Porosity Samples

Direct Pore-Scale Observation in Saturated Micromodels

Abstract

In this study we examined how different fractions of soil aggregates affect water flow and solute transport processes in porous media. To do so, we constructed several dual-porosity micromodels and performed systematically several solute transport experiments using direct imaging with the help of fluorescence recovery after photobleaching (FRAP) techniques. In addition to using samples with different aggregate fractions, four different velocities were used to explore the effects of fluid flow. Resulting concentration fields were analyzed in terms of solute front region areas, front-line lengths, mean values of the concentration gradients within the media, and concentration breakthrough curves at the micromodel exit. Direct pore-scale observations revealed that higher fractions of aggregates lead to larger front region areas and increased front lengths, while relatively minor variations were apparent for the solute gradients within the samples. Increased flow velocities did lead to an increase in front length and larger concentration gradients, while no major differences were observed in the concentration front region. Concentration breakthrough curves showed early arrival times when more aggregates were present. Pore-scale observations indicated a clear effect of aggregation on the internal distribution of solutes and their transport, while the effect was less visible on average macroscopic (continuum scale) transport parameters.

3.1. Introduction

Intense soil usage is causing groundwater and environmental problems by soluble chemical components at an ever-growing rate (Corapcioglu et al., 1997). Agricultural activities, including the application of pesticides and fertilizers, and the use of landfills and other waste sites (Kjeldsen et al., 2002) cause soil and water pollution, while we simultaneously face increasing demands for freshwater in industry and agriculture (Vitousek et al., 1997; Vorosmarty, 2000). Contaminant transport also has become an active area of research due to increased use of pharmaceutical and personal care products and their associated threat to drinking water resources (Kolpin et al., 2002; Ma et al., 2018; Hill et al., 2019; Luque-Espinar and Chica-Olmo, 2019).

Accurate predictions and effective management of subsurface contaminant transport is complicated by cause of many physical and biogeochemical processes affecting contaminant fate. Especially challenging in the vadose zone, is the presence of multiple porosities in the form of inter-aggregate and intra-aggregate pores. Soil aggregates form a key component of soil structure and cause spatial heterogeneity at relatively small and intermediate spatial scales, together with crucial impact on the development of healthy microbial communities within a soil profile (Rillig et al., 2017). Aggregation also provides preferential flow paths which can facilitate the accelerated transport of contaminants towards underlaying groundwater (Brusseau, 1993; Flury et al., 1994; Allaire et al., 2009).

Soils with a dual-porosity system have two distinct pore networks consisting of macropores and micropores and therefore have a bi-modal pore size distribution. Earthworm activity, old plant roots, drying cracks, rock fissures and/or the general existence of aggregates causes the creation of bi-modal (or sometimes multi-modal) pore size distributions (Kohler-Milleret et al., 2013; Martinez et al., 2015). Dual-porosity features often prevail in man-made products such as printing paper (Aslannejad et al., 2018), catalysts (Linares et al., 2012), and concrete (Chindaprasirt et al., 2008; Jenni et al., 2017). Preferential flow though soil macropores may cause early arrival time of surface applied contaminants in groundwater. Complex microporosity systems may promote slow back diffusion of contaminants into the preferential flow paths which may lead to long tailing of breakthrough curves (Mehmani and Prodanovic, 2014) or to secondary concentration peaks (Zhou et al., 2014). The resulting non-Fickian behavior of dual-porosity systems complicates predictive modeling.

Traditionally, laboratory column and field experiments have been used to obtain solute breakthrough curves (BTCs), from which various transport parameters such as the solute dispersivity can be estimated (Klotz et al., 1980; Gerritse and Singh, 1988). Although this approach is very useful to estimate travel times and the integrated behavior of concentration plumes, the exact contribution of different underlying processes forming the BTCs often remains unclear, leading to considerably uncertainty when extrapolating results to other sites or experimental conditions. Pore-scale investigations may help to better identify the basic processes governing contaminant transport.

Direct measurement of pore-scale processes can be carried out using various techniques, including through the use of microfluidic devices. This method provides an opportunity to directly observe the underlying pore-scale processes and how they relate to macroscopic behavior. Micromodels have been used extensively the last several decades to demonstrate various pore-scale processes including single- and two-phase flow (Zarikos et al., 2018), the transport of solutes (Corapcioglu et al., 1997; Karadimitriou et al., 2016; Jiménez-Martinez et al., 2017) and colloids (Zhang et al., 2013, 2014, 2015; Liu et al., 2019), reactive transport (De Anna et al., 2013), enhanced oil recovery (Jiménez-Martinez et al., 2016), as well as for organ-on-a-chip applications (Helm et al., 2016). Commonly, microfluidic studies apply an idealized design such as a structured/periodic system of uniformly placed and similarly sized pillars (Auset and Keller, 2006; Willingham et al., 2008; Zarikos et al., 2018). Such idealized systems, however, limit system behavior and provides local fluid velocity distributions that may not represent flow in real porous media where complex pore structures are always present and often play a critical role.

In this study we use a new method of designing micromodels by combining x-ray tomography-based micromodels with computer generated designs to construct four dual-porosity micromodels. The effect of soil aggregation on transport is studied by systematically replacing certain parts of the soil grains by soil aggregates. Fluorescence recovery after photobleaching (FRAP) was used to provide an accurate non-destructive tracing method to directly observe fluid flow and solute transport in both the macropores and micropores at the same time, and within the entire flow domain (i.e., not only for a small sub-section of the domain). By doing so, changes in the porosity distribution and its influence on solute transport at multiple applied average pore-water velocities is investigated and discussed in detail.

3.2. Experimental approach

Theoretical development. The advection dispersion equation (ADE) is traditionally used to describe the transport of solutes in relatively homogeneous porous media. The equation accounts for solute spreading due to local variations in the flow velocity, including velocity variations caused by tortuous flow paths depending upon the topology of the medium. The one-dimensional ADE as based on Fick's law for diffusion and Darcy's law for fluid flow is given by:

$$\frac{\partial \bar{c}}{\partial t} = D\frac{\partial^2 \bar{c}}{\partial x^2} - v\frac{\partial \bar{c}}{\partial x} \tag{3.1}$$

where $\bar{c}$ is the average concentration, D is the dispersion coefficient, v is the average pore-water velocity, x is distance and t is time..

Various preferential flow models have been developed over the years to describe systems that are more complex and/or show non-equilibrium behavior. These types of models include a range of dual-porosity, dual-permeability, multi-porosity, multi-permeability, and discrete fracture models (e.g., Altman et al., 1996; Šimrunek and Van Genuchten, 2008). A relatively simple dual-porosity nonequilibrium model assumes that advective transport in the smaller pores can be neglected and hence the water phase is stagnant so molecular diffusion becomes the dominant transport process. Macropores form the major transport pathways, with exchange between the inter-aggregate pores (i.e., the macropores) and intra-aggregate pores (the micropores) which is often being approximated by a quasi-empirical first-order rate term proportional to the concentration difference between the domains. This assumption holds for two-phase systems where the water phase is trapped (Karadimitriou et al., 2016), or for systems containing dead-end pores. While useful, the approach may not always be fully accurate since intra-aggregate pores commonly show a non-zero permeability indicative of low pore-water velocities. Mobile-Immobile Models (MIMs) of this type can be written as (Coats and Smith, 1964; Van Genuchten and Wierenga, 1976):

$$\phi_m \frac{\partial \bar{c}_m}{\partial t} = \phi_m D_m \frac{\partial^2 \bar{c}_m}{\partial x^2} - v\frac{\partial \bar{c}_m}{\partial x} - \alpha\left(\bar{c}_m - \bar{c}_{im}\right) \tag{3.2}$$

$$(1-\phi_m)\frac{\partial \bar{c}_{im}}{\partial t} = \alpha\left(\bar{c}_m - \bar{c}_{im}\right) \tag{3.3}$$

where the subscripts m and im refer to the mobile and immobile regions, $\bar{c}$ is the average concentration, ϕ_m is the mobile water fraction, D_m is the dispersion coefficient, and α

represents a first-order mass transfer coefficient. Macroscopic (continuum scale) transport parameters were obtained by fitting analytical solutions of the advection-dispersion equation (ADE) and the mobile-immobile model (MIM) to the measured concentration BTCs. The parameter estimation analysis was carried out using CXTIFIT module (Toride et al., 1995) in the STANMOD software package of Simunek et al. (2000). A third-type inlet boundary conditions was used for a semi-infinite domain, the boundary conditions are given in Appendix B.

The average pore water velocity, $\bar{v}$, is calculated as follow:

$$\bar{v} = \frac{qL}{V_f} \tag{3.4}$$

where q is the volumetric fluid flux, L is the characteristic length of the domain being considered, and V_f is the volume of fluids in the domain.

The Peclet number can be used to quantify the relative behavior of advection to molecular diffusion as:

$$P_e = \frac{\bar{v}L}{D_e} \tag{3.5}$$

where P_e is the Peclet number and D_e is the effective diffusion coefficient of the porous medium, taken in this study as 4.36×10^{-10} $m^2 s^{-1}$ (Petrášek & Schwille, 2008).

The characteristic diffusion and advection times can be used to identify the dominant transport process inside the aggregates. These time scales are given by:

$$T_A = \frac{L_a}{\bar{v}} \tag{3.6}$$

$$T_D = \frac{L_a^{\,2}}{D_e} \tag{3.7}$$

where T_A, and T_D, are characteristic times for advection and diffusion, respectively. In case of aggregates, the characteristic length, L_a, is the aggregate radius.

Micromodel Fabrication. We first constructed a non-aggregated base model consisting of a thin slice of sand imaged using x-ray tomography. The model, further referred to as S40/0, had a porosity of 0.40 and contained no aggregates. The physical size of the sample was 10 mm by 10 mm. Next, dual-porosity domains were constructed by replacing various solid grains of sample S40/0 by grains containing micropores to systematically

create microfluidic devices with aggregate fractions of 25, 50, 75, and 100%. The solid grains of the base model were loaded into MATLAB software (as individual polyshapes). Then, within each grain a large number of points were placed which served as trial points for the center of new micro-grains within the resulting aggregate. An estimate was made for the number of points needed to reach an aggregate porosity fraction of 0.50. A grain size distribution was drawn from a truncated lognormal distribution given by (Raoof and Hassanizadeh, 2012):

$$f\left(R_i,\sigma\right)=\frac{\sqrt{2}exp\left[-\left(\frac{1}{2}\right)\left[\ln\left(\frac{R_i}{R_m}\right)/\sigma\right]^2\right]}{\sqrt{\pi\sigma^2}R_i\left\{erf\left[\ln\left(\frac{R_{max}}{R_m}\right)/\sqrt{2\sigma^2}\right]-erf\left[\ln\left(\frac{R_{min}}{R_m}\right)/\sqrt{2\sigma^2}\right]\right\}} \quad (3.8)$$

where R_{min}, R_{max}, and Rm are the minimum, maximum, and mean of the distribution, and σ^2

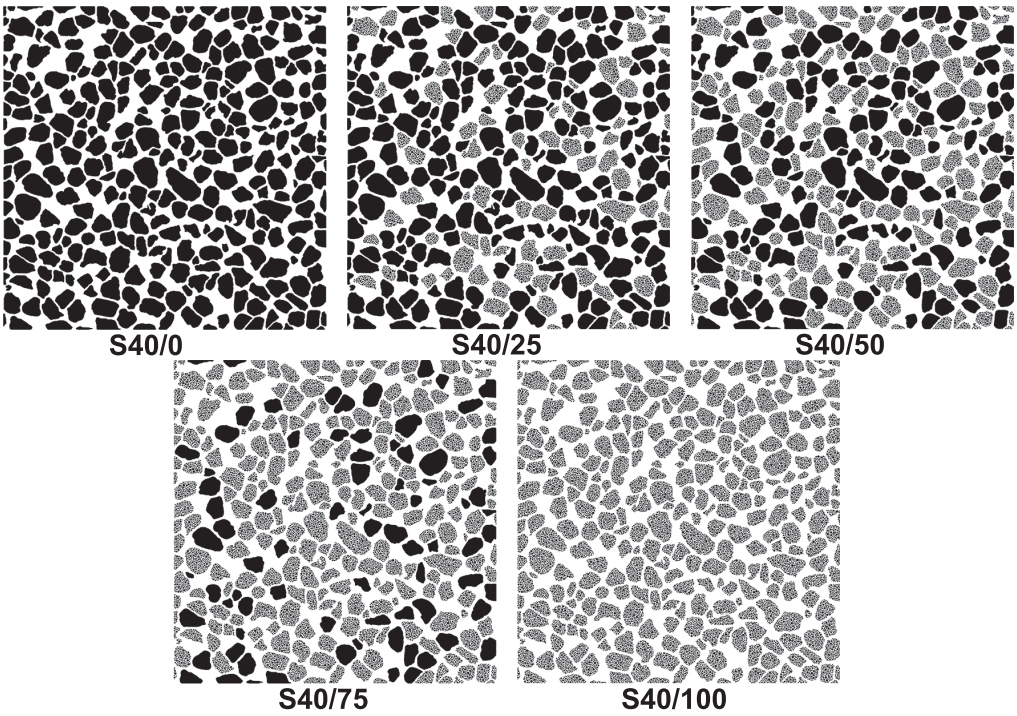

Figure 3.1. The original reference micromodel together with its aggregated variations from 0% , 25%, 50%, 75%, to 100% aggregation based on total grain number in the sample.

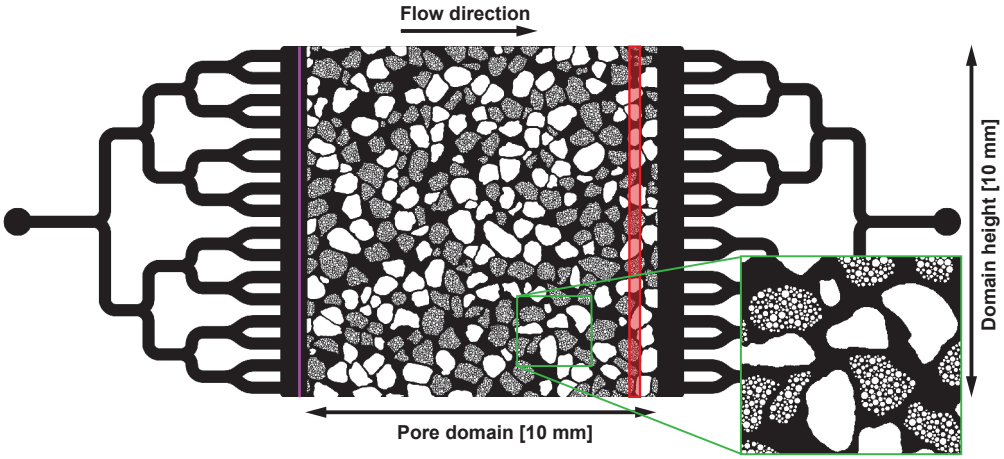

Figure 3.2. Micromodel composed of solid and aggregated (microporous) grains. The purple line on the left side indicates the location of the laser line beam used for bleaching and the red area on the right the position used to measure the breakthrough curves. The green area shows the location of a zoom-in section of the domain.

is the variance of the distribution. The following parameters were used to generate a grain size distribution for the micro-grains (μm): R_{min}=5.0, R_{max}=40.0, R_m=18.0, and *std*=8.0. The distribution was sorted from large to small values in order to achieve a tight packing of the micro-grains next to each other. The algorithm iterated through the generated points to assemble micro-grains that fitted within each domain, while keeping a predetermined minimum distance between the micro-grains. The minimum distance was taken as 5.0 μm in this study to avoid any problem with the soft lithography procedure of the micromodel.

Our intent was to have identical macropore structures of the micropore models. This means that a single aggregate in one model must have exactly the same pore structure as the duplicate aggregate in another model. To achieve this, we first generated the 100% aggregate model (S40/100) as described earlier, after which the original grains of S40/0 were placed back to obtain the other models (25, 50, and 75%), thus deactivating the micro-grains there. This resulted in 5 micromodels with porosities ranging from 0.40 to 0.70. S40/0 has 317 grains and 467 pore bodies, while S40/100 had almost 28000 grains and more than 28000 pore bodies. Properties of the micromodels are given in Table 3.1, the grains that were displaced can be found in can be found in Figure 3.1, and the complete S40/50 micromodel, including the inlet and outlet structures, in Figure 3.2.

A CAD file was generated of the samples, as well as a photomask was produced, which we used to manufacture the SU8-2025 molds in a multiscale porous media lab cleanroom by following traditional photolithography procedures. The micromodels had a uniform

Table 3.1. Solid phase and pore space properties of the 5 S40 micromodels. For the samples with micro-porosity, the larger grains were excluded in calculations of grain and pore element radii.

	Sample	S40/ 0	S40/ 25	S40/ 50	S40/ 75	S40/ 100
Solid phase	Number of grains	317	7000	13375	20260	27999
	Average grain radius [μm]	236.5	17.3	17.2	17.2	17.2
Pore space	Number of pore bodies	467	7579	13496	20668	28687
	Number of pore throats	705	12327	24605	34964	48511
	Pore body radius [μm]	107.1	10.3	10.8	10.7	10.7
	Pore throat radius [μm]	70.1	8.2	8.3	8.6	8.6
	Total porosity: $\theta_t=\theta_{agg}+\theta_{macro}$ [-]	0.40	0.48	0.55	0.62	0.70
	Contribution of aggregates to porosity: θ_{agg}/θ_t	0	0.17	0.27	0.36	0.43

depth of 20 μm, with the complete model including the inlet and outlet being 10 mm wide and 27 mm long. Prints of the mold were made using Polydimethylsiloxane (PDMS); the micromodels were bonded onto a round glass cover coated by a thin layer of PDMS.

Experiment set-up. For our study we constructed a Fluorescence Recovery After Photobleaching (FRAP) set-up that included a laser module and an imaging module. The set-up consisted of a series of optical elements to guide the laser dot beam into a belt-shape beam to enable photobleaching along the inlet section of the micromodel in the form of a line source. The micromodel was mounted on a stereo microscope, which had a camera fitted to image the photobleaching induced concentration (PIC). The laser and imaging modules are described below.

Laser module. The laser pump was from Spectra-Physics Explorer One-355-1W with main power of 800 mW at 50 kHz and a wavelength of 355 nm. The laser beam is guided by a UV enhanced mirror through a shutter unit, with the shutter being controlled by Arduino Mega 2560 to define the precise timing of photobleaching. The laser beam was then guided through another mirror to a cylindrical lens (f=200mm), and subsequently through a convex lens (f=50mm) to shape the laser dot beam into a line-shaped beam. Note that due

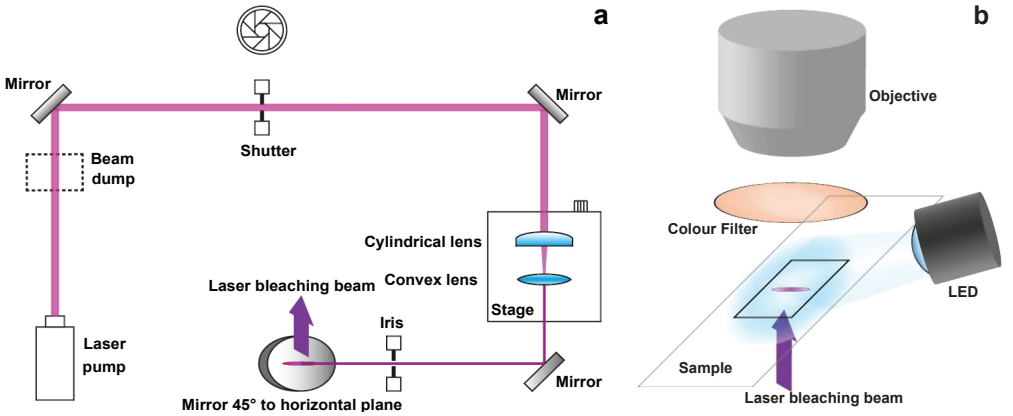

Figure 3.3. a) Schematic of the laser module, and b) the imaging module of the set up.

to the Gaussian shape of the laser spot beam, also a Gaussian line beam exists; due to the power of the laser the effect is minimal. The lenses were placed on a linear translation stage to be able to precisely focus the beam onto the micromodel at the desired location. Next, the line-shaped beam was guided through an iris to cut off undesired scatter light and control the final width of the laser beam. Finally, the beam was guided onto the last mirror to be directed onto the micromodel. The whole laser module was placed below the imaging module described. A schematic of the laser module is shown in Figure 3.3a.

Imaging module. The imaging module, fitted above the laser module, consists of a stereo microscope (Nikon SMU-Z, lens: 0.75× to 7.5× pancreatic magnification, and a 0.45 camera lens), a camera (iDS UI-3180CP-M-GL monochrome camera), and multiple optical components. The complete pore space of 10 mm ×10 mm was imaged at a resolution of 4.8 µm. The camera was also triggered by the Arduino Mega 2560 to precisely control the interplay between laser and imaging module. The fluorescein solution was excited by a collimated blue LED with a peak wavelength of 470 nm (Thorlabs M470L3), with a short pass filter of 500 nm fitted. Emitted light of the fluorescein (peak 515 nm) passes then through a long pass filter mounted between the sample and the lens. The emitted light passes then through the lenses and is captured by the camera. Similarly, as the shutter and camera, the LED is triggered by the Arduino in order to only illuminate the sample while an image is taken by the camera. A schematic of the imaging module is given in Figure 3.3b.

Experimental procedure. The micromodel was initially saturated by injecting first an ethanol solution and subsequently a fluorescein-water solution. The laser was positioned along the inlet as shown in Figure 3.2 and the desired flow rate was set using a syringe pump (Harvard apparatus Pump 11 Pico Plus Elite). To create a step concentration input (i.e., providing a third-type boundary condition) and to image solute spreading inside

Table 3.2. Volumetric fluid flow rates, q, into the micromodels to achieve target average pore water velocities, v, and the corresponding Peclet number, time of advection, and time of diffusion, assuming equal characteristic lengths, T_D.

Velocity [m day^{-1}]	S40/ 0	S40/ 25	S40/ 50	S40/ 75	S40/ 100	Pe [–]	T_A [s]	T_D [s]
2 .0	6.67*	7.95	9.08	10.3	11.7	6.18	42.6	132
5.0	16.7	19.9	22.7	25.8	29.2	12.4	21.3	
12.0	40.0	47.7	54.5	61.9	70.1	24.7	10.64	
20.0	66.7	79.5	90.8	103.2	116.8	61.8	4.25	

*Volumetric flow rates are in unit of $\mu l\ hr^{-1}$

the flow domain, some compromises had to be made as described below. To increase the imaging quality, we programmed the laser light (used for bleaching) and the camera (used for capturing the concentration field) to function in cycles of 1000 milliseconds. A programming script was used so that the fluorescein solution at the inlet was bleached for 800 ms followed by a buffer time of 10 ms. The sample was next illuminated for 170 ms during which an image was captured using an exposure time of 70 ms. Before the next cycle, another 30 ms buffer time was programmed. This procedure was repeated until a total of 3.0 Pore Volumes (PV) of fluorescein solution was bleached and transported through the micromodel. The experiment was repeated four times for each model to impose 4 different averaged pore water velocities, v (i.e., 2.0, 5.0, 12.0 and 20.0 m day^{-1}). The corresponding volumetric flow rates for each micromodel were calculated using Equation 3.4 and are listed in Table 3.2.

Imaging post processing. The camera recorded images in 8-bit grayscale (i.e., ranging in grayscale values from 0 until 255). Before starting the bleaching procedure, the micromodel was first fully saturated with a fluorescein solution and illuminated using a blue LED to obtain an image of the pores space. This image was used to create a mask of the solid grains, to be used as a reference for subsequent images during the experiments to exclude the image pixels belonging to the solid phase. The intensity values (PICs) decreased during photobleaching, indicating higher concentrations, while the original intensity was considered to be the zero concentration value. A normalization step was needed to convert the grayscale images to concentration fields. The normalization step is given as:

$$C_n = -\frac{I - I_0}{I_0 - I_b} \tag{3.9}$$

where C_n is the normalized concentration, I is the measured grayscale value, I_0 is the peak intensity measured before photobleaching, and I_b is the minimum intensity measured at the end of the experiment. For the breakthrough curve (BTC) the average of concentration values contained in the red box were used shown in Figure 3.2, located at a distance of 9.4 mm from the inlet.

Solute Front Region. The solute front region provided information about the temporal development of the concentration front inside the pore network. Experimental conditions often cause a level of noise in the data (e.g., noise generated by small inaccuracies of the filter, or noise present in the images). To provide accurate results, we performed sensitivity analyses to find the optimum concentration margins that could be used for the front region. By varying the concentration in ranges of 0.4-0.6, 0.3-0.6, and 0.2-0.6, we found that concentration margins between 0.2 and 0.6 provided the most accurate and repeatable results. This range hence was used to extract target regions within the flow sample over time. Next, the average value of the concentration gradient was calculated in these regions for each time step to explore the temporal evolution of the concentration field. These properties characterize mixing and diffusion processes at the pore scale, and how the gradients evolve under different flow velocities and for porous media with different aggregate fractions.

Front line. The solute concentration front was defined as the contour line of 0.5 concentration perpendicular to the general flow direction. Since solutes are only present inside the pores, the isolines will be discontinuous at the grain locations, especially when handling dual-porosity domains with large areas occupied by the smaller grains. Our algorithm assumed that the contour line at the location of grains will follow the grain contour which had the shortest path to the next concentration contour line. The continuous contour line obtained in this manner enabled us to track the form of the concentration front over time at the pore scale.

3.3. Experimental results and analysis

In total 20 microfluidic transport experiments were performed. Experiments were carried out using a total of 5 microfluidic structures, each having different fractions of aggregates ranging from 0% (non-aggregated domains) to aggregate fractions of 100% (fully aggregated domains). The concentration front area, gradient, and length were calculated from where the solute entered the domain until solute left the domain. Results were categorized based on the applied average pore-water velocities (with values of 2.0, 5.0, 12.0, and 20.0 m day^{-1}) and aggregate fractions (0, 25, 50, 75, 100%).

Influence of flowrate on concentration front area, gradient, and front-line length. Figure 3.4 shows the transport of solute through the flow domain (S40/50) using an applied average pore water velocity of 12.0 m day^{-1}. As soon as solute entered the domain fingers were formed in response to the heterogeneous flow velocity distribution. Preferential pathways were visible for all flow rates (experimental results for the other samples were provided in Appendix B).

A quantitative analysis of the results is provided in Figure 3.5, which shows differences between the experiments carried out at the applied averaged pore-water velocities. Figure 3a shows the temporal evolution of the concentration front. As soon as solute entered the flow domain, a drastic increase in the front length occurred due to the immediate formation of solute fingers. After injection of 0.3 PV, the front length stabilized and then fluctuated around a stable value in balance with the local heterogeneity of the pore space. The solute front length stabilized by diffusive fluxes present in the system, which alleviated solute fingers and hindered their growth. When the flow rate was increased, advection became more dominant, with concomitant increased Peclet number. This leads to a new equilibrium state of the solute front where solute fingers became more influential (i.e., a larger front length was observed with increased velocity). At 2.0 m day^{-1} we observed a stable front length of 2.2 $\times 10^{-2}$ m, while at 20.0 m day^{-1} the front length was much larger (3.6 $\times 10^{-2}$ m).

Figure 3.5b shows the development of the mean gradient in sample S40/50. As with the solute finger development, we observed a relatively steep decrease of the mean gradient value when solute entered the pore network, reaching a velocity-specific stable mean gradient after approximately 0.5 PV for all flow rates. At 20.0 m day^{-1} an asymptotic value of 0.1 was reached, while a gradient of 0.05 was reached at 2.0 m day^{-1} indicating a less sharp front. The higher velocities hence produced more dispersion consistent with the higher observed gradients in the system. Concentration gradients within the sample were especially higher initially (until about 0.2 PV) for the high flow rates, q.

Figure 3.5c shows the evolution of the concentration front area between concentrations of 0.2 and 0.6. The area of the solute front increased over time until about 0.8 pore volumes. The front area then started to decrease since the solute fingers had reached the end of the domain, which impacts the measured area. The flow rate had only a minimal effect on the area of the solute front, even though an increase in the front length and mean gradient were observed. A higher applied flow rate did lead to an increased front length due to enhanced dispersion (higher surface area), with the gradient become larger due to the lower diffusion times (which lowers the surface area). On the other hand, lower applied flow rates lowered the front length and gradients, causing the opposite effect on the front

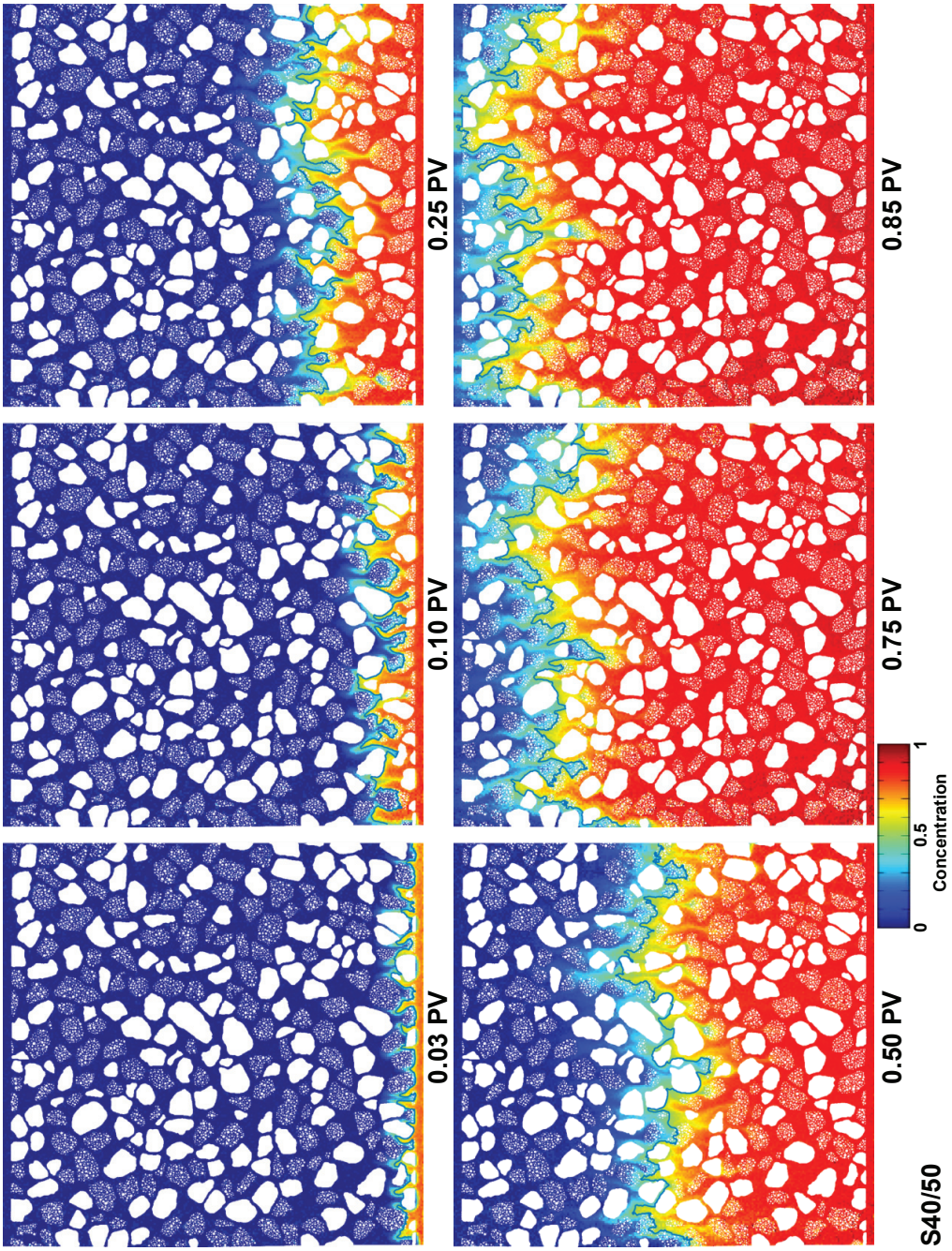

Figure 3.4. Concentration fields showing the front development over time for sample S40/50 subjected to an average pore water velocity of 12.0 m day^{-1}. The plots belong to 0.03, 0.1, 0.25, 0.5, 0.75 and 0.85 injected Pore Volume(PV). The contour line shows the solute front at 0.5 concentration.

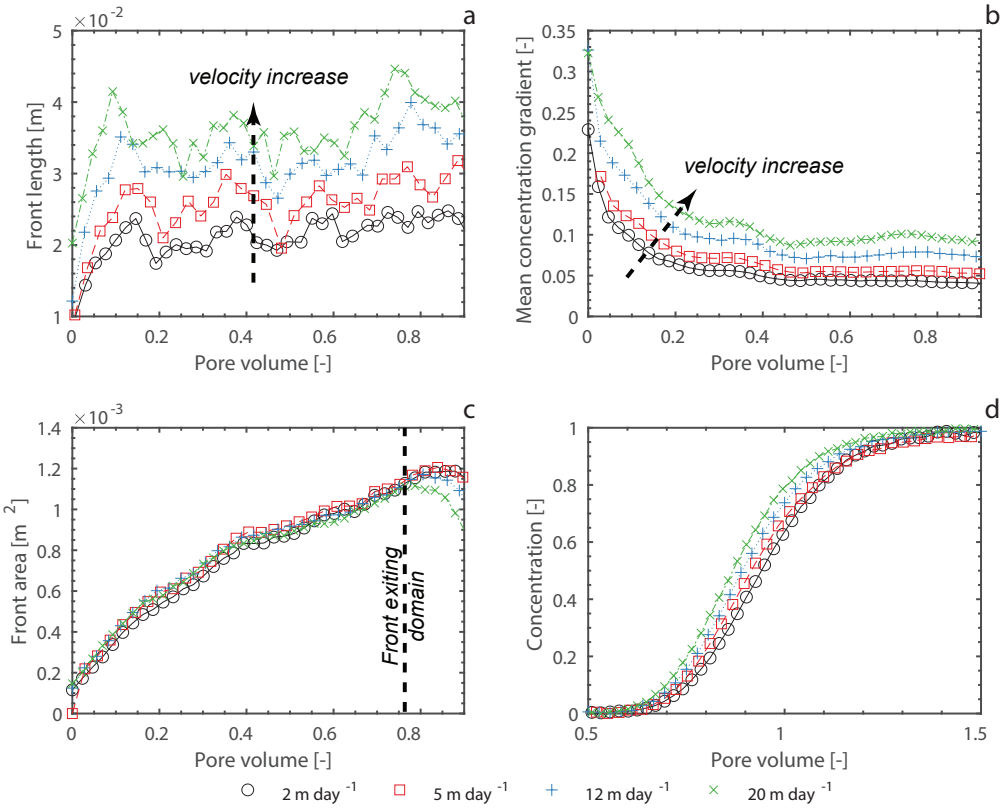

Figure 3.5. Effects of the applied flow rate, *q*. a) Front length (calculated as the length of the 0.5 concentrate isoline) over time, b) mean concentration gradient in the solute front area, c) concentration front area plotted against pore volume and d) breakthrough curve measured at the outlet for S40/50 (sample S40 with 50% aggregation). Results for the other samples are displayed in Appendix B. The data were subsampled due to the high number of data points.

area described above for high flow rates. Therefore, overall results show only minimal differences in the observed front surface areas when varying the flow rate.

Influence of flowrate on the breakthrough curves. Figure 3.5d shows the solute breakthrough curves at the four applied flow rates for S40/50. While minimal, the slope of the rising limb increased with the flow velocity, thus showing the effect of the Peclet number on the BTCs. Compared to the significant differences found for the pore-scale observations on the front length and mean gradient, the effects on the average BTC concentration were relatively small.

Influence of aggregation on concentration front area, mean gradient, and front line length. Figure 3.6 shows concentration distributions after injecting 0.5 pore volume for the all samples, at 12.0 m day^{-1} average pore-water velocity. The front line (i.e., the isoline of 0.5 concentration) is also provided. Increased aggregate fraction led to development of large solute fingers and therefore a more stretched solute front. In the presence of aggregates, the created micropores influenced the local pressure field, leading to variations in the velocity distributions. This effect resulted in a wider velocity distribution, and hence more preferential flow and an increase in the extent of the solute fingers. As the fraction of aggregates increased, the interaction between the aggregates also slowly increased (i.e., the aggregates at first interacted mostly with the macropores but then increasingly exchange solute with one another, as well with the macropore domain). When aggregates are positioned in close proximity to each other, solute will reside and transported within the aggregate domain for a longer time.

The results in Figure 3.7a showed the effects of the applied average pore-water velocity on front length, mean concentration gradients, front area and BTC concentration. Figure 5 shows the effects of the fraction of aggregates on those same properties, with Figure 5a showing the temporal development of the front length for all samples at 12.0 m day^{-1}. Similar plots for the other velocities are provided in Appendix B. All fronts in Figure 5a were found to develop within 0.2 pore volumes. The solute front length increased by about 2.5 times higher from the single porosity domain to the fully aggregated domain, mainly caused by the increase in solute fingers due to changes in the local flow velocity distributions.

The mean concentration gradient at 12.0 m day^{-1} for all samples are given in figure 3.7b. The samples reached an asymptotic value of approximately 0.1 at 0.5 pore volume, although small differences remained. Before reaching an asymptotic value, samples S40/0 and S40/25 showed a slightly steeper decrease in the solute gradients. These samples generated fewer or less extensive solute fingers, thereby reducing the initially

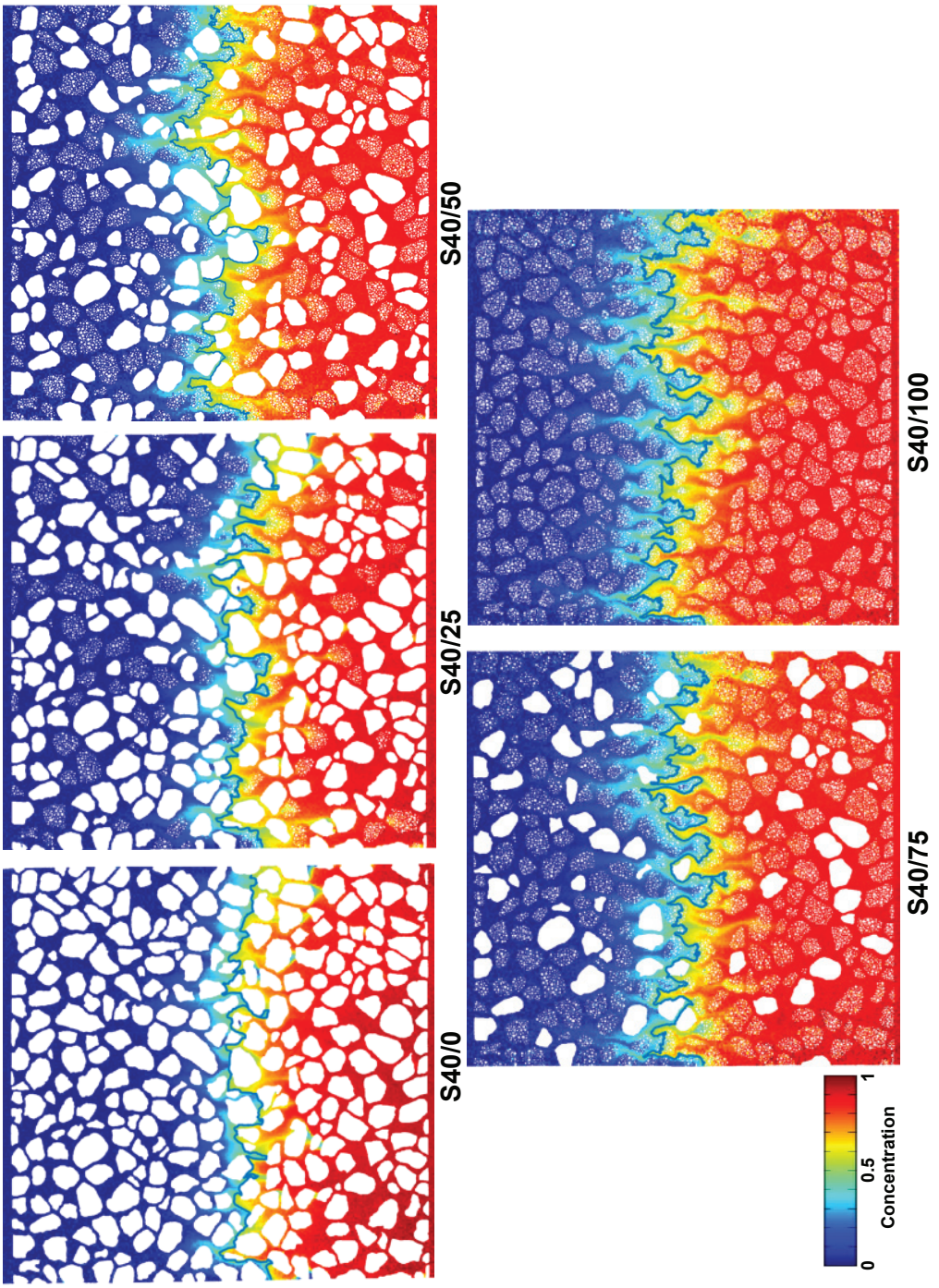

Figure 3.6. Solute concentration distributions in S40/0, S40/25, S40/50, S40/75, and S40/100 after injection of 0.5 PV. The applied average pore water velocity is 12.0 m day^{-1}.

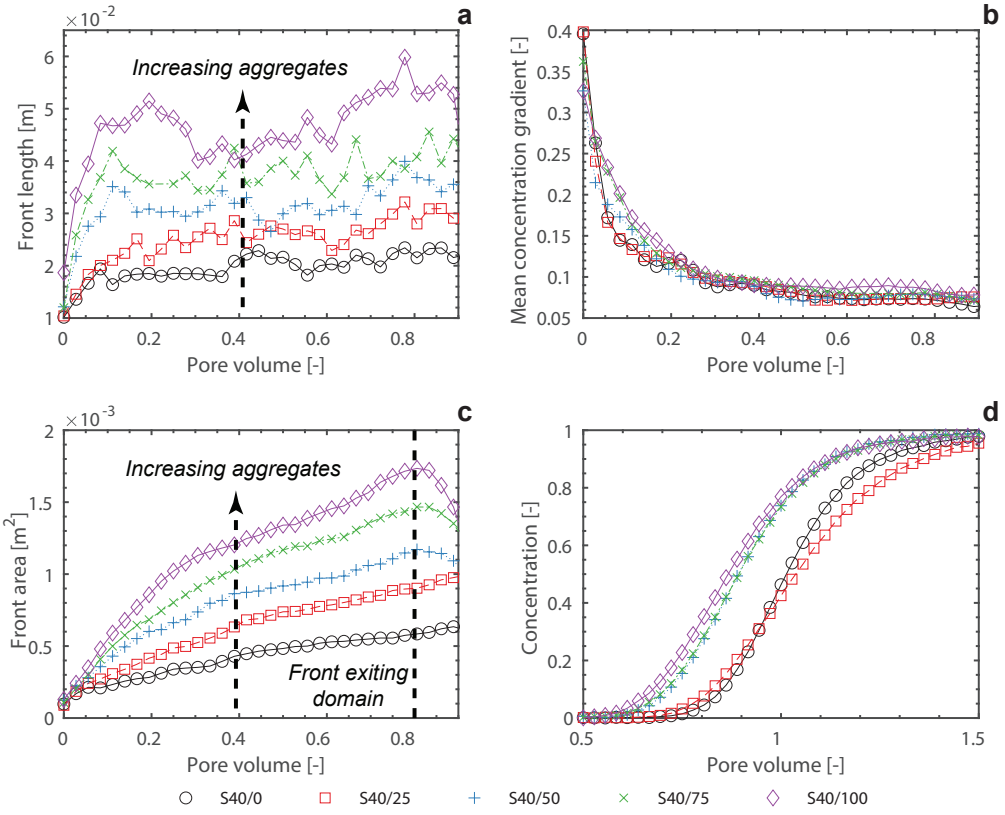

Figure 3.7. Effects of the fraction of aggregates. a) Front length (calculated as the length of the 0.5 concentrate isoline) over time, b) mean concentration gradient of the concentration front area, c) concentration front area plotted against pore volume and d) breakthrough curves measured at the outlet of the samples. Results are for a average pore water velocity of 12.0 m day^{-1}. Results for the other velocities are displayed in the Appendix B. The data were subsampled due to large number of data points.

high gradients quicker to the stable values as compared to samples with high fraction of aggregates.

Figure 3.7c shows that the concentration front area of all samples at 12.0 m day^{-1} increased over time. Samples S40/50, 75, and 100 showed a decrease after 0.8 pore volume due to the front reaching the outlet of the flow domain. No decrease in the front area was observed for samples S40/0 and S40/25, which indicates that the more aggregated samples were subject to more preferential flow, leading to the curves in Figure 3.7a. Sample S40/100 with the highest aggregate fraction did lead to a much higher front area, nearly triple of the front area of sample S40/0. This shows the key impact of the physical structures on the solute front area.

Influence of aggregation on the breakthrough curves. Figure 3.7d shows the concentration distributions of the different samples at a flow rate of 12.0 m day^{-1}. A clear difference was observed between samples S40/0 (i.e., the domain with no aggregates) and S40/25, and the other samples. We observed that arrival times (defined by 0.5 C_n) were shorter at around 0.85 PV for domains with more than 50% aggregates (i.e., the S40/50, S40/75 and S40/100 domains), while for S40/0 and S40/25 solutes arrived mostly after one pore volume. Sample S40/25 had a lower slope of the rising limb than S40/0 due to changes in the local flow velocities, resulting in an increase in hydrodynamic dispersion, while S40/50 and S40/100 showed a clear shift to early arrival times. These differences are a consequence of the different makeups of the micropore systems. For example, the micropore system of sample S40/25, is composed of several isolated aggregates that are placed are relatively far apart from each other, which caused a shift in the S40/25 data relative to those of the samples with higher aggregate fractions.

A key aspect of the effects of aggregate fraction is that the lack of effective connection between individual aggregates has little impact on the flow velocity distribution within the samples. However, samples S40/50, S40/75 and S40/100 show clear percolation pathways through the connected pore system, leading to more impact of the flow velocity and its distribution on the transport of solutes across the domain. Between these two distinct regimes involving low and high aggregate fractions, a transition zone developed with only minor changes in the rising limbs of the BTCs (i.e., slightly later arrival times with the lower aggregate fractions). This shows that the internal physical condition of a porous system can have a significant influence on macroscopic behavior as commonly observed macroscopically such as by a breakthrough curve. This type of spreading may a have significant impact on mixing and reactive transport (De Anna et al., 2013). Our results show the creation of considerable concentration gradients within the pore network and by the introduction of aggregates the front area and front length (two and three times,

Table 3.3. Fitted values of the ADE transport parameters for all samples (*v,* is the pore-water velocity, *D,* the longitudinal dispersivity).

Sample	S40/0	S40/25	S40/50	S40/75	S40/100
v_2 [m s^{-1}]	2.16×10^{-5}	2.09×10^{-5}	2.33×10^{-5}	2.38×10^{-5}	2.50×10^{-5}
v_5 [m s^{-1}]	5.35×10^{-5}	5.19×10^{-5}	5.97×10^{-5}	6.02×10^{-5}	6.24×10^{-5}
v_{12} [m s^{-1}]	1.31×10^{-4}	1.27×10^{-4}	1.47×10^{-4}	1.48×10^{-4}	1.53×10^{-4}
v_{20} [m s^{-1}]	2.26×10^{-4}	2.18×10^{-4}	2.53×10^{-4}	2.53×10^{-4}	2.52×10^{-4}
λ_2 [m]	1.11×10^{-4}	1.59×10^{-4}	1.52×10^{-4}	1.38×10^{-4}	1.43×10^{-4}
λ_5 [m]	1.14×10^{-4}	1.92×10^{-4}	1.73×10^{-4}	1.53×10^{-4}	1.83×10^{-4}
λ_{12} [m]	1.11×10^{-4}	1.88×10^{-4}	1.53×10^{-4}	1.69×10^{-4}	1.98×10^{-4}
λ_{20} [m]	9.45×10^{-5}	1.78×10^{-4}	1.48×10^{-4}	1.49×10^{-4}	1.92×10^{-4}

respectively) was increased, which could lead to more reactivity.

Advection-Dispersion equation and Mobile-Immobile equation. Macroscopic transport parameters were obtained by fitting solutions of the ADE and the (MIM) to the BTCs. Table 3.3 provides the fitted velocity and the longitudinal dispersivity value ($\lambda = \frac{D}{v}$) for the ADE and Table 3.4 shows the fitted values for the MIM model (the BTCs were fitted once by including velocity and once by fixing velocity and only fitting the dispersion coefficient). We have observed a difference between the estimated velocity (approximated using the applied flow rates in experiments) and the velocity obtained by fitting. One way to obtain the average velocity is using the applied inflow volumetric rate during the experiment and divide it by the pore-space surface area normal to the flow direction. This velocity provides an estimation of the real average velocity that the solute is traveling with. The real and more accurate average velocity depends however on the tortuosity of the pore space. The observed longitudinal dispersivity values do not show functionality on velocities under the range of Peclet numbers applied in this study.

Figure 3.8a shows average values of the longitudinal dispersivity of the S40 samples. No reasonably good fits of the MIM were obtained for S40/0 and S40/25 without also fitting the pore water velocity, v (the "MIM no velocity" cases in Figure 3.8), while the other samples showed near-perfect fits with R^2 value of 0.999 or more. The MIM results with velocities optimized reproduced BTCs of Samples S40/0 and S40/25 very well, with the mobile water fraction (especially for the latter case) being close to 1.0. This shows that

Table 3.4. Fitted values of the MIM transport parameters for all samples assuming the pore water velocity to be unknown (top part of table) and known at the imposed value (bottom part). Unacceptable results were obtained for some of the cases where the velocity was fixed.

	Sample	S40/0	S40/25	S40/50	S40/75	S40/100%
Velocity	v_2 [m/s]	2.13×10^{-5}	2.09×10^{-5}	2.30×10^{-5}	2.34×10^{-5}	2.46×10^{-5}
	v_5 [m/s]	5.30×10^{-5}	5.09×10^{-5}	5.85E-05	5.67×10^{-5}	6.13×10^{-5}
	v_{12} [m/s]	1.29×10^{-4}	1.29×10^{-4}	1.46×10^{-4}	1.46×10^{-4}	1.50×10^{-4}
	v_{20} [m/s]	2.24×10^{-4}	2.21×10^{-4}	2.51×10^{-4}	2.09×10^{-4}	2.48×10^{-4}
Dispersivity	λ_2 [m]	9.02×10^{-5}	1.60×10^{-4}	1.41×10^{-4}	1.35×10^{-4}	1.36×10^{-4}
	λ_5 [m]	8.43×10^{-5}	1.11×10^{-4}	1.37×10^{-4}	1.50×10^{-4}	1.58×10^{-4}
	λ_{12} [m]	7.62×10^{-5}	2.04×10^{-4}	1.30×10^{-4}	1.47×10^{-4}	1.68×10^{-4}
	λ_{20} [m]	9.05×10^{-5}	1.89×10^{-4}	1.40×10^{-4}	1.48×10^{-4}	1.70×10^{-4}
Mobile water	ϕ_{m2}	0.97	1.00	0.98	0.98	0.99
	ϕ_{m5}	0.96	0.92	0.96	0.94	0.98
	ϕ_{m12}	0.96	1.00	0.98	0.98	0.97
	ϕ_{m20}	0.99	1.00	0.99	0.82	0.98
Mass transfer	α_2 [cm^{-1}]	1.07×10^{-4}	0.10	2.92×10^{-5}	8.39×10^{-6}	2.27×10^{-5}
	α_5 [cm^{-1}]	5.27×10^{-4}	1.40×10^{-3}	3.55×10^{-4}	1.90×10^{-5}	3.07×10^{-4}
	α_{12} [cm^{-1}]	1.48×10^{-4}	0.62	9.90×10^{-4}	5.72×10^{-4}	6.81×10^{-4}
	α_{20} [cm^{-1}]	1.23×10^{-4}	1.06	2.61×10^{-4}	1.75×10^{-5}	9.03×10^{-4}
No velocity fit						
Dispersivity	λ_2 [m]	No fit	No fit	1.42×10^{-4}	1.35×10^{-4}	1.39×10^{-4}
	λ_5 [m]			1.42×10^{-4}	1.35×10^{-4}	1.39×10^{-4}
	λ_{12} [m]			1.50×10^{-4}	1.64×10^{-4}	1.89×10^{-4}
	λ_{20}[m]			1.45×10^{-4}	1.48×10^{-4}	1.85×10^{-4}
Mobile water	ϕ_{m2}	No fit	No fit	0.99	0.97	0.93
	ϕ_{m5}			0.96	0.96	0.93
	ϕ_{m12}			0.94	0.94	0.91
	ϕ_{m20}			0.92	0.91	0.92
Mass transfer	α_2 [cm^{-1}]	No fit	No fit	3.04×10^{-5}	7.21×10^{-6}	7.52×10^{-6}
	α_5 [cm^{-1}]			2.34×10^{-4}	2.02×10^{-5}	2.52×10^{-5}
	α_{12} [cm^{-1}]			3.96×10^{-5}	5.97×10^{-5}	9.34×10^{-5}
	α_{20} [cm^{-1}]			5.52×10^{-5}	1.94×10^{-5}	1.02×10^{-4}

the ADE model was sufficient for most or all the experiments. The lowest dispersivity values for the ADE and MIM were found for S40, and the highest values for S40/25 and S40/100 (1.8×10^{-4} m for the ADE). For the MIM model, the highest mean dispersivity was for S40/25. However, the quality of the fit was relatively poor for this case. The mean MIM dispersivities (both MIM and MIM no velocity) of the S40 samples were found to increase with aggregate faction for aggregate fractions of 50% and larger, but not when the ADE was used. When using a fixed velocity, optimized dispersivity values were slightly larger.

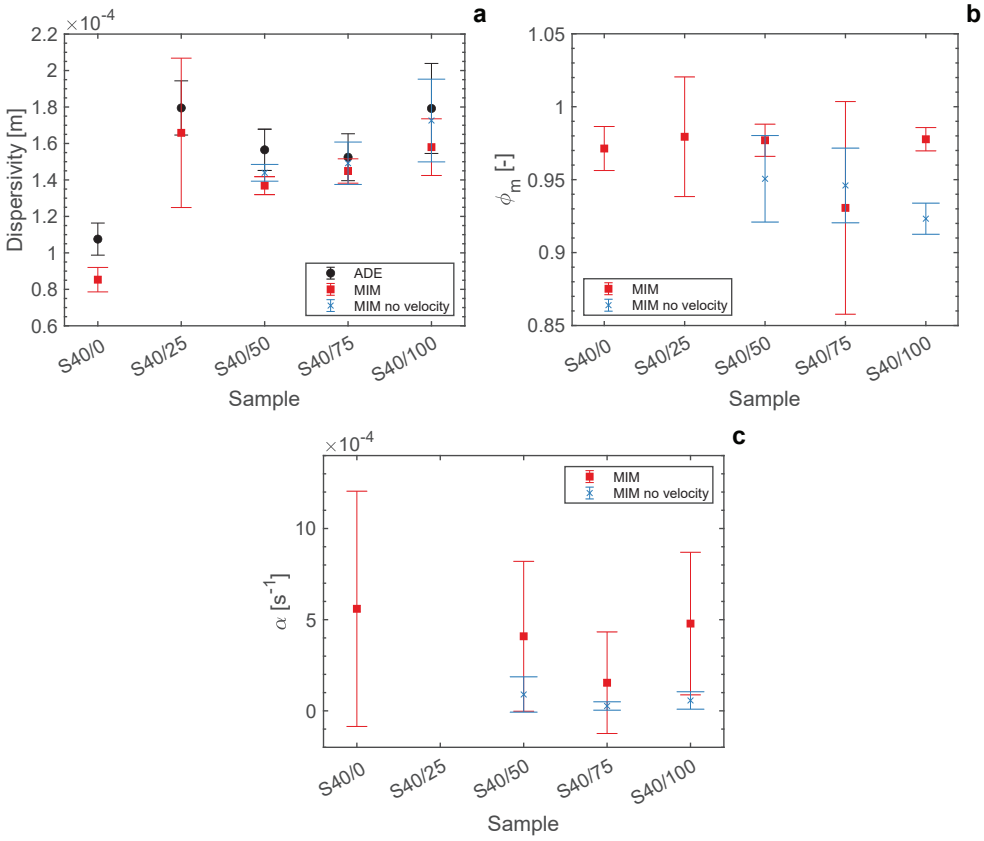

Figure 3.8. a) The mean fitted dispersivity values for each sample for multiple fitting methods (averaged over all applied velocities), b) mean mobile water fraction (ϕ_m) for MIM and MIM with fixed velocity, and c) mean fitted mass transfer coefficients (α) for MIM and MIM with fixed velocity.

Figure 3.8b shows values of the mobile water fraction (ϕ_m) for the MIM and MIM with fixed velocity cases. For MIM we found ϕ_m to be around 0.975, except for S40/75 which had a much lower mean of 0.82. For MIM with fixed velocity, the average values were 0.95, 0.945, and 0.92 for samples S40/50, S40/75 and S40/100, respectively. This is in accordance with the increased contribution of aggregate micropores to the overall porosity, although the optimized values of ϕ_m were much higher than the actual macropore fractions (ϕ_{macro}/ϕ_t) of the micromodel as constructed (which were 0.51, 0.42, and 0.38 samples S40/50, S40/75 and S40/100, respectively). These results indicate that the transport regime was mainly advection dominated. Our results also show that the observed outlet BTCs of the average concentrations could not clearly reflect the specific pore-scale conditions of the experiments (like fingering, concentration gradients, front areas, and front lengths), but merely lumped those processes into overall behavior. However, the outlet BTCs still may be used to distinguish internal distributions for samples having larger aggregates or higher internal aggregate porosities compared to those used in this study. For example, a study by (De Vries et al., 2017) showed that an increase in aggregate porosity should be considered in combination with the aggregate permeability relative to the permeability of the macropore region. Highly porous aggregates may sometimes have narrow pore throats internally between the micropores, as well as on their outside surfaces (e.g., clay particles or coatings), that may materially lower the overall aggregate permeability and/or the connectedness with the macropore domain.

The mean fitted mass transfer coefficients (α) are given in Figure 3.8c. Similarly, as parameter ϕ_m, the α value of sample S40/75 deviated from those of samples S40, S40/75 and S40/100, while S40/25 was left out because of its unsuitable fit. For samples S40/50 and S40/100, we found similar values of approximately 4.2×10^{-4} s^{-1}, although the range between the applied flow velocities is more substantial than for ϕ_m. For MIM (no velocity) the α values are more similar at a value of about 0.5×10^{-5} s^{-1}, and with more fluctuations between the applied velocities.

3.4. Conclusion

In this study we explored the dual-porosity effects of aggregation on the transport and spreading of solutes in constructed micromodels with distinct differences the inter-aggregate and intra-aggregate pore spaces. A total of 20 FRAP experiments were performed using a custom-build optic setup that could image the transport of solutes within the entire pore space with sufficient resolution to obtain concentrations inside both the macropore and micropore domains. The acquired images over time were used to obtain concentration fields across the domain and to construct breakthrough curves at the outlet of the samples. The obtained concentration fields were used to investigate front line

length, front area, and the mean gradient of the solute front.

We observed only relatively small effect of the flow velocity on the BTCs at the macroscopic (continuum) scale, while at the pore-scale an increase occurred in the front-line length and a decrease in the mean gradient of the front, while only small variations in the concentration front area of the front were observed due to the interplay between dispersive and diffusive fluxes. Higher aggregate fraction produced a shift in the breakthrough curves to early arrival times for the more aggregated samples (S40/50, S40/75 and S40/100) due to increased preferential flow. More aggregation did lead to an increase in front line length and concentration front area at the pore scale, but only small variations in the observed average concentration gradient (note that the applied velocities were chosen such that the same Peclet numbers were obtained in different samples). Direct observations as presented in this study provide insight into how underlying pore scale processes affect traditionally observed concentration BTCs at the larger column scale (or even field scale). Uncertainty at the larger continuum scale are dues to fact that different internal conditions in a pore-scale system can cause similar macroscale observations. This may include reactive geochemical conditions leading to retardation, while physical conditions inside the model can cause similar observations. While these types of situations could be investigated in future research, some examples are given below.

In this study we used similar aggregates (i.e., having the same micropore makeup and size) in the various samples, with only the fraction of aggregates in the micromodel being altered. Many more forms of aggregates, as well as other dual-porosity systems exists in natural and synthetic porous media. Higher macropore/micropore flow velocity ratios could be achieved by introducing smaller pores inside the aggregates, while larger aggregate porosities could be created by using larger micropores and/or varying the aggregate packing method. These changes will affect the storage capacity of solute within the aggregates, leading to a more exchange between the inter-aggregate and intra-aggregate domains, as well as possibly to long-tailed BTCs.

Chapter 4

Multi-Scale Modeling of Flow and Transport in Dual-Porosity Porous Media

A Computational Pore-Scale Study for Flow and Solute Transport

Abstract

Many environmental and agricultural applications involve the transport of water and dissolved constituents through aggregated soil profiles, or porous media that are structured, fractured, or macroporous in other ways. During the past several decades, various process-based macroscopic models have been used to simulate contaminant transport in such media. Many of these models consider advective-dispersive transport through relatively large inter-aggregate pore domains, while exchange with the smaller intra-aggregate pores is assumed to be controlled by diffusion. The exchange of solute between the two domains is often represented using a first-order mass transfer coefficient, which is commonly obtained by fitting to observed data. This study aims to understand and quantify the solute exchange term by applying a dual-porosity pore-scale network model to relatively large domains, and analyzing the pore-scale results in terms of the classical dual-porosity (mobile-immobile) transport formulation.

We examined the effects of key parameters (notably aggregate porosity and aggregate permeability) on the main dual-porosity model parameters, i.e., the mobile water fraction (ϕ_m) and the mass transfer coefficient (α). Results were obtained for a wide range of aggregate porosities (between 0.082 and 0.700). The effect of aggregate permeability was explored by varying pore throat sizes within the aggregates. Solute breakthrough curves (BTCs) obtained with the pore-scale network model at several locations along the domain were analyzed using analytical solutions of the dual-porosity model to obtain estimates of ϕ_m and α. An increase in aggregate porosity was found to decrease ϕ_m and increase α, leading to considerable tailing in the BTCs. Changes in the aggregate pore throat size affected the relative flow velocity between the intra- and inter-aggregate domains. Higher flow velocities within the aggregates caused a change in the transport regime from diffusion dominated to more advection dominated. This change increased the exchange rate of solutes between the mobile and immobile domains, with a related increase in the value of the mass transfer coefficient and less tailing in the BTCs.

4.1. Introduction

Soil and groundwater pollution by a broad range of industrial and agricultural contaminants is an ever-increasing problem worldwide. One issue exacerbating effective management of the subsurface is the problem of preferential flow of surface-applied chemicals such as fertilizers, pesticides, trace elements, and pathogenic microorganisms. Much evidence exists that preferential flow through especially the vadose zone is contributing to surface and subsurface pollution problems (e.g., Flury et al., 1994; Abbaspour et al., 2001; Hendrickx and Flury, 2001; Allaire et al., 2009, Vogel et al., 2010; Mahmoodlu et al., 2013, 2014; Zhang et al., 2013). In attempts to describe and quantify the basic processes leading to preferential flow, a large number of dual-porosity, dual-permeability, multi-porosity, and multi-permeability models and related approaches have been developed and verified. Comprehensive reviews of alternative modeling approaches are provided by NRC (2001), Šimunek et al. (2003), Gerke (2006), Jarvis (2007), Šimunek and Van Genuchten (2008), and Köhne et al. (2009).

A commonality of many preferential flow models is the assumption that the liquid phase can be divided into relatively mobile and immobile parts representing the macropore (or inter-aggregate or fracture) domain, and the micropore (or intra-aggregate or soil matrix) domain, respectively, together with appropriate coupling terms to account for the exchange of water and/or dissolved constituents between the two domains. The simplest formulation arises when no flow occurs in the micropore domain, and a first-order macropore/micropore solute exchange term is used, to lead to mobile-immobile (MIM) type dual-porosity models of the form (Coats and Smith, 1964; Van Genuchten and Wierenga, 1976):

$$\phi_m \theta \frac{\partial \overline{c}_m}{\partial t} = \phi_m \theta D_m \frac{\partial^2 \overline{c}_m}{\partial x^2} - q \frac{\partial \overline{c}_m}{\partial x} - \alpha \left(\overline{c}_m - \overline{c}_{im} \right) \tag{4.1}$$

$$(1 - \phi_m) \theta \frac{\partial \overline{c}_{im}}{\partial t} = \alpha \left(\overline{c}_m - \overline{c}_{im} \right) \tag{4.2}$$

where the subscripts *m* and *im* refer to the mobile and immobile region, $\overline{c}$ is the average concentration, θ is the volumetric water content, ϕ_m is the mobile water fraction defined as θ_m/θ, D_m is the dispersion coefficient, q is the volumetric fluid flux, and α is a first-order mass transfer coefficient.

The dual-porosity model given by Eqs. (4.1) and (4.2) involves several assumptions, the most important being that advective transport in the smaller intra-aggregate pores can be neglected. This implies that the overall pore water velocity distribution within the porous medium is approximated by the step function, with one part of the medium having an average pore water velocity equal to $v_m=q/\theta_m$, while water in the other part is completely stagnant. This assumption is generally not met since the intra-aggregate (soil matrix) region often has some non-zero permeability, even if small compared to the inter-aggregate (or fracture) region.

Another simplifying assumption of Eqs. (4.1) and (4.2) is that solute exchange between the mobile and immobile regions can be described using a quasi-empirical first-order rate term proportional to the difference between the average concentrations of the mobile and immobile regions. Various attempts have been made to obtain a more physical basis of the mass transfer coefficient, α, in terms of such parameters as the diffusion coefficient and the shape and size of the aggregates or soil matrix. This has led to a number of analytical models that explicitly considered diffusion from the inter-aggregate region into immobile intra-aggregate regions of various shapes (e.g., Rasmuson and Neretnieks, 1980; Tang et al., 1981; Sudicky and Frind, 1982; Van Genuchten et al., 1984; Van Genuchten, 1985). These and related studies also allowed derivation of approximate relationship for the mass transfer coefficient, including through the use of Laplace transforms or moment analyses, as exemplified in studies by Bolt (1979), Barker (1985), Van Genuchten and Dalton (1986), Parker and Valocchi (1986), Goltz and Roberts (1987), and Hantush and Mariño (1998).

Another approach for estimating the parameters ϕ_m and α in Eqs. (4.1) and (4.2) is by direct measurement (e.g., Clothier et al., 1992; Jaynes and Shao, 1999), or by analyzing a large number of previously published data such as shown by Maraqa (2001). A latter study revealed an approximately linear relationship between the mass transfer coefficient and the residence time of the solute in the transport domain (Pontedeiro et al., 2010).

Both of the above assumptions (i.e., negligible advection within the aggregates, and the use of a first-order exchange term) require more research. This includes how best to account for aggregate shape and size, which are known to vary widely and may involve various spherical, blocky, columnar, and prismatic geometries, or mixtures thereof (e.g., Tisdall and Oades, 1982; Hillel, 2003). Imaging techniques can be of great value for determining the size and shapes of aggregates, and hence can reduce the dependency on using idealized shapes (Bultreys et al., 2015, 2016). The mass transfer coefficient is, in actuality, a more complex integrated parameter whose value depends on many porous media characteristics including pore and aggregate geometry, the solute diffusion coefficient,

the intra-aggregate permeability, the relative magnitude of the mobile and immobile region, as well as the dynamics of the overall system such as the concentration gradients and the applied flow velocity. At relatively low pore water velocities, the time scale of solute diffusion into aggregates may be comparable with the transport time scale within the macropore domain, in which case a larger fraction of the solutes may diffuse into or out of the aggregates, thus limiting any tailing in observed BTCs. At the other extreme, at relatively high pore water velocities, macro-and micropores may become essentially disconnected, leading to negligible solute exchange and the possibility of dual peaks in the BTCs (Zhou et al., 2014).

The value of the mass transfer coefficient, α, is commonly obtained by fitting macroscopic models to observed solute BTCs (Toride et al., 1995). Since BTCs often show tailing, this approach may be very time-consuming in terms of getting an appropriate resolution in the data. Moreover, the BTC data then provide information only of the macroscopic concentrations at selected observation points within the medium, or from column outflow experiments, thus providing little insight into the internal concentration distributions and interactions between the mobile and immobile zones. This makes it difficult to estimate the contribution of different transport processes into the BTCs and extrapolate such BTC data to other transport regimes. Methods are hence needed to provide information in a systematic manner about the internal state of aggregated media, including quantification of the basic transport processes operating at the microscopic level. An alternative would be to obtain the BTCs using pore-scale modeling (Raoof et al., 2010; Raoof and Hassanizadeh, 2013). For transport in unsaturated non-aggregated media, Raoof and Hassanizadeh (2013) used pore network modeling to obtain several BTCs in this manner, which would be difficult and time-consuming to obtain experimentally.

Advanced 3D X-ray microtomography and related imaging techniques are now being increasingly used to obtain non-destructive visualizations of pore structures (Allaire et al., 2009; Ferro et al., 2013; Mangalassery et al., 2013; Zhou et al., 2013; Martinez et al., 2015). This includes studies of dynamic processes such as fluid flow and structural dynamic processes (Cnudde and Boone, 2013; Wildenschild and Sheppard, 2013). Soil aggregates for such studies could be imaged and analyzed individually to collect data on pore morphology and connectivity (Ferro et al., 2013; Zhou et al., 2013), or direct fluid flow experiments could be performed on a dual-porosity medium. The resulting information can then be utilized to construct pore network structures needed for pore-scale flow and/or transport models.

Various pore-scale modeling approaches are now being pursued, with differences pertaining to the specific mathematical formulation such as the use of direct numerical solutions (Bijeljic et al., 2013; Fathi et al., 2017a, 2017b), Lattice Boltzmann methods (Jafari et al., 2011) or pore network modeling (Raoof et al., 2013), including differences in the invoked modeling resolution and required computational time (Sahimi, 2011; Bultreys et al., 2016). Multi-scale pore network modeling has been applied for simulating two-phase flow (Jiang et al., 2013; Prodanovic et al., 2014; Bultreys et al., 2015) as well as solute transport (Bijeljic et al., 2013). Furthermore, grain-filling and pore-filling methods were developed to construct multi-scale pore network models (Mehmani and Prodanovic, 2014).

Our study aimed to use a pore-scale network model to simulate flow and transport in dual-porosity domains containing a large number of aggregates. The pore network modeling approach assumes that the porous medium continuum can be divided into pore elements made up of pore bodies representing the larger voids in the medium, and pore throats representing narrow openings connecting the pore bodies (Raoof et al., 2013; Bultreys et al., 2016). Applying mass balance equations, flow and transport are simulated within each individual pore. Averaging over a large number of pores will then allow estimation of the macroscopic transport properties for porous media containing unimodal pore sizes (Raoof et al., 2010, 2013), or for multi-scale media with multimodal pore size distributions (Bultreys et al., 2015; Mehmani and Prodanović, 2014; Mehmani et al., 2015). The obtained information at the pore-scale makes it possible to relate macroscopic transport properties to the underlying physical pore-scale processes and pore size distributions, and their connectivities (Raoof et al., 2010; Raoof and Hassanizadeh, 2013). Using such multi-scale porous media requires a description of the connectivity between the macro- and micro-porosity domains, which computationally can be particularly challenging for heterogeneous multimodal pore-scale domains.

Our objective is to develop a dual-porosity pore structure to represent an aggregated medium and to use this structure to simulate flow and transport within the composite medium in order to obtain pore-scale distributions of the solute concentration. The resulting solute breakthrough curves are then compared with solutions of the macroscopic equations given by Eqs (4.1) and (4.2) to obtain estimates of the fraction of mobile water (ϕ_m), and the mass transfer coefficient (α). A large number of simulations will be carried out to obtain dependencies of ϕ_m and α on such soil aggregate properties as porosity and internal permeability. The resulting insight may be useful for field-scale models to improve predictions needed at the larger scales for evaluating alternative management or contaminant remediation strategies, as well as industrial porous media applications.

4.2. Theoretical Development

In this section, we describe the pore-scale network model that was used to simulate flow and transport in the aggregated dual-porosity pore structure. After a brief review of the pore-scale network modeling approach in general, details are provided on how the pore-scale model was used to generate pore structures and conduct simulations for an aggregated medium.

Pore network model. Pore network modeling considers a porous medium as a system of pore elements composed of pore bodies and pore throats. While pore bodies, due to their larger size, mainly control the porosity of the medium, the smaller pore throats determine the hydraulic conductivity. The complete pore structure of an aggregated soil requires the use of two types of pore spaces with different sizes. The aggregated medium in our study was obtained by first generating a macropore domain. Since pore connectivity is an important topological property of the medium, we used a pore network model with random pore connectivity (Raoof & Hassanizadeh, 2012) to represent the randomness of real porous media. Once the macropore domain was generated, several aggregates were superimposed within the overall domain. Each aggregate of a certain size was assumed to contain a large number of micropores. Algorithms were developed to connect the collection of pores located at the outer surface of the aggregates to their adjacent macropores. We generated for this purpose several domains with different aggregate fractions, with the aggregates themselves randomly placed within the medium. An example is shown in Figure 4.1. Once the pore structures were constructed, flow and transport processes were simulated within the pore network domain using the PoreFlow package developed by Raoof et al. (2013), which is capable of simulating saturated and variably-saturated flow, as well as multi-component reactive transport, within arbitrary pore structures.

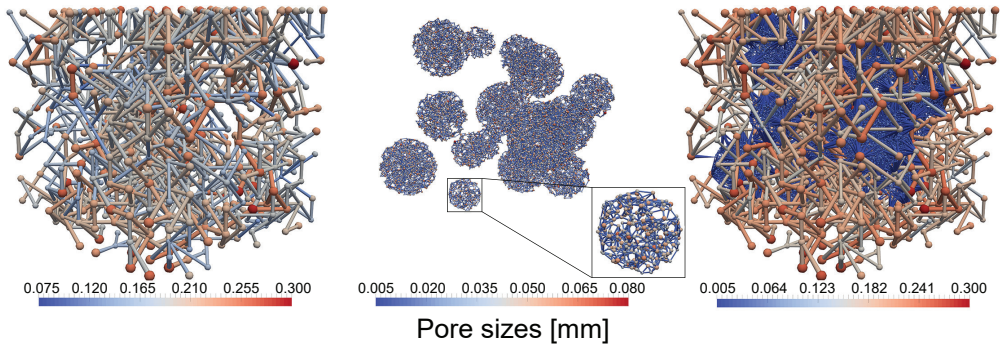

Figure 4.1. Construction of the aggregated domain: macroscopic pore domain (the left plot), as well as the aggregate domain (the middle plot) are created and superimposed to provide the ultimate multi-scale domain (the right plot).

Since the adopted pore-scale model has been explained in detail elsewhere (Raoof and Hassanizadeh, 2010, 2012; Raoof et al., 2010, 2013), only a brief overview is provided here of the main equations governing flow and transport within the porous medium. Assuming laminar flow, the volumetric flow rate within each pore was obtained using the Hagen-Poiseulle equation:

$$q_{ij} = g_{ij}\left(p_j - p_i\right) \tag{4.3}$$

where q_{ij} is the volumetric volume rate through the pore throat between two adjacent connected pore bodies i and j, p_i and p_j are pressures of the two adjacent pore bodies, and g_{ij} is the conductance of the pore throat which, for a pore throat with a cylindrical cross-section, is given by:

$$g_{ij} = \frac{\pi R_{ij}^4}{8\mu l_{ij}} \tag{4.4}$$

where R_{ij} is the pore throat radius, l_{ij} is the throat length, and μ is the fluid dynamic viscosity.

Considering incompressible flow, the continuity equation for flow is applied at pore junctions:

$$\sum_{j=1}^{z_i} q_{ij} = 0; \quad j = 1, 2, \ldots, z_i, \tag{4.5}$$

where q_{ij} is the volumetric flow rate within a pore throat from pore body i to pore body j, and z_i is the pore coordination number of pore i.

Combining Eqs. (4.3), (4.4) and (4.5) for all pores result in a linear system of equations with a sparse, symmetric, and positive-definite coefficient matrix, which is to be solved for the pore body pressures. Considering the sample as a representative elementary volume (REV), the average pore water velocity, $\overline{v}$, can be calculated as (Raoof et al., 2013):

$$\overline{v} = \frac{Q_{tot} L}{V_f} \tag{4.6}$$

where Q_{tot} is the total discharge rate through the pore network, which can be determined at the inlet or outlet of the pore network as the sum of all fluxes, L is the length of the pore network, and V_f is the total volume of the fluid phase within the pore network.

The intrinsic permeability, κ, of the sample can be determined using Darcy's law:

$$\kappa = \frac{\mu Q_{tot} L}{A \Delta P} \tag{4.7}$$

where μ is the dynamic viscosity, ΔP is the pressure difference between the inlet and outlet pores, and A is the cross-sectional area of the pore network.

Solute transport through the pore network was described for the general case involving both advective transport and diffusion (Vasilyev et al., 2012). Calculations were done by considering each pore element (i.e., a pore body or a pore throat) as the control volume. We used a backward Euler method for the temporal discretization and first-order upwind and central schemes for spatial discretization of the advection and diffusion terms, respectively. For a given pore body i, one can write the following mass balance equation:

$$V_i \frac{dc_i}{dt} = \sum_{j=1}^{N_{in}^{throat}} q_{ij} c_{ij} - Q_i c_i + \sum_{j=1}^{z_i} D_0 A_{ij} \frac{\left(c_{ij} - c_i\right)}{l_{ij}}, \tag{4.8}$$

where V_i is the volume of the pore body, Q_i is the total volumetric rate going out of the pore body, A_{ij} is the cross-sectional area of the pore throat, D_0 is the ionic or molecular diffusion coefficient, c_i is the concentration in the pore body, c_{ij} is the concentration in the pore throat, l_{ij} is again the length of the throat, while N_{in}^{throat} represents the number of pore throats flowing into pore body i.

Similarly, the mass balance equation for solutes in a pore throat ij may be written as:

$$V_{ij} \frac{dc_{ij}}{dt} = q_{ij} c_j - q_{ij} c_{ij} + D_0 A_{ij} \frac{\left(c_j - c_{ij}\right)}{l_{ij}} + D_0 A_{ij} \frac{\left(c_i - c_{ij}\right)}{l_{ij}} \tag{4.9}$$

which assumes that pore body j is the upstream node. Eqs. (4.8) and (4.9) were solved using a fully implicit scheme available in the PoreFlow software package (Raoof et al., 2013). Flux-averaged breakthrough curves at selected points were obtained by averaging concentrations over the network cross-section at successive times as follows:

$$c\left(x,t\right) = \left[\frac{\sum_i^{N_t^x} c_i\left(x,t\right) Q_i}{\sum_i^{N_t^x} Q_i} \right] \frac{1}{c_0} \qquad i = 1,2,\ldots,N_t \tag{4.10}$$

where $c(x,t)$ is the normalized average concentration at location x and time t, N_t^x refers to the total number of pores at location x, and c_0 is the input concentration of the solute.

Application to aggregated media. Imaging techniques such as X-ray microtomography are being increasingly used to visualize the inner structures of aggregates and to provide information on pore size distribution, aggregate porosity, and aggregate size and shape (Ferro et al., 2013; Mangalassery et al., 2013; Zhou et al., 2013; Martinez et al., 2015). We note that studies using only X-ray microtomography often show lower aggregate porosities as compared to studies using multiple measuring techniques (Ferro et al., 2012, 2013; Czachor et al., 2015). The resolution of X-ray tomography has been shown to be a limiting factor since it tends to neglect the presence of below-resolution pores. Additional techniques such as mercury intrusion hence are often used to obtain a more realistic value for the porosity of the aggregates (Ferro et al., 2013). Focused ion beam-scanning electron microscopy (FIB-SEM) can provide much higher resolution images, as compared to X-ray tomography, for analyzing microporosity (Hemes et al., 2015). Using a combination of multiple techniques applicable to different scales will be most valuable for multi-scale pore topology applications such as in this study. Table 4.1 shows aggregate sizes, pore sizes, and aggregate porosities as obtained from the literature. We used these data to establish as realistic ranges of properties as possible for the aggregates used in our calculations.

Table 4.1. Selected literature on aggregate properties: aggregate diameters, pore sizes, and porosities.

Reference	Aggregate diameter [mm]	Pore size [µm]	Mean aggregate porosity [-]	Imaging method
Czachor et al. (2015)	3-4	2.5-100	0.35	X-ray microtomography and paraffin intrusion
Dal Ferro et al. (2012)	1-2	0.074-100	0.37	X-ray microtomography and mercury intrusion
Dal Ferro et al. (2013)	5-6	12.5-200	0.11	X-ray microtomography
Khan et al. (2012)	1-5	1-85	0.40	Synchrotron-based nano-CT
Peth et al. (2008)	3-5	5-50	0.13	X-ray microtomography
Rabbi et al. (2015)	2-4	5.2-60	0.048	X-ray microtomography
Zhou et al. (2013)	1.5-2	10-500	0.14	X-ray microtomography

Transport processes within the aggregated media we considered were studied by first creating a reference model. The reference model was then modified to consider i) domains with different aggregate porosities by changing pore body sizes, and ii) domains with different aggregate permeabilities by changing pore throat sizes to explore the effects of flow velocity differences between the macro-and aggregate domains. The reference model had a physical size of 100×20×20 mm^3 and contained a total of 1000 aggregates. The mean distance between pore bodies in the aggregates was taken to be 0.1 of the separation distance between the macropores, while the mean coordination number was taken to be 5. The minimum and maximum aggregate diameters were set to 1.0 and 3.0 mm, respectively. Pore body sizes and aggregate throat sizes were assigned from a truncated log-normal distribution given by (Raoof and Hassanizadeh, 2012):

$$f\left(R_i,\sigma\right)=\frac{\sqrt{2}exp\left[-\left(\frac{1}{2}\right)\left[\ln\left(\frac{R_i}{R_m}\right)/\sigma\right]^2\right]}{\sqrt{\pi\sigma^2}R_i\left\{erf\left[\ln\left(\frac{R_{max}}{R_m}\right)/\sqrt{2\sigma^2}\right]-erf\left[\ln\left(\frac{R_{min}}{R_m}\right)/\sqrt{2\sigma^2}\right]\right\}} \tag{4.11}$$

where R_{min}, R_{max}, and R_m are the minimum, maximum, and mean of the distribution, and σ^2 is the variance of the distribution. The macropore and micropore bodies each had their own size distribution. The macropore throat sizes were set as the smallest of the adjacent pore body sizes. The throat lengths were calculated by determining the length between the center points of two adjacent pore bodies of the throat while subtracting the radii of the two pore bodies.

Table 4.2 provides the pore size statistics used for the calculations, with Cases I-3 and II-2 serving as the reference models. Case I calculations were meant to show the effects of aggregate porosity, and Case II calculations the effects of aggregate permeability. Based on the data in Table 4.1, the single aggregate porosity (Case I in Table 4.2) was varied between 0.082 and 0.700 in 6 steps by changing the aggregate pore body size distributions. The aggregate throat radii, as well as the macropore sizes, were kept constant in these simulations to examine the effects of varying aggregate porosities on flow and transport. For the Case II simulations (Table 4.2), the aggregate permeability was varied by changing the aggregate throat sizes in 4 steps, while the aggregate body and macropore body/throat sizes were kept constant. Simulation II-1 had smaller throats, and simulations II-3 and II-4 larger throats, compared to the reference model (Case II-2).

Table 4.2. Minimum (R_{min}), maximum (R_{max}) and mean (R_m) pore body radii (Case I) and pore throat radii (Case II), as well as standard deviations (σ), of the pore-size distributions used in the calculations.

	Case	R_{min} [mm]	R_{max} [mm]	R_m [mm]	σ [mm]
Porosity effects	Pore body radii				
	I-1	0.0375	0.050	0.045	0.0025
	I-2	0.050	0.070	0.060	0.0030
	I-3 (Reference model)	0.055	0.075	0.065	0.0030
	I-4	0.070	0.090	0.080	0.0030
	I-5	0.075	0.100	0.090	0.0040
	I-6	0.090	0.120	0.100	0.0040
Permeability effects	Pore throat radii				
	II-1	0.001	0.010	0.005	0.0015
	II-2 (Reference model)	0.010	0.020	0.015	0.0015
	II-3	0.020	0.030	0.025	0.0015
	II-4	0.040	0.050	0.045	0.0015

The presence of macropores and aggregates with distinctly different micropore sizes created various pore systems. To explore the contribution of the different pore systems, porosities were calculated separately for the macropores and aggregates. Pore bodies were presumed to be spherically shaped, and pore throats to be cylindrical capillaries. Using the pore volumes of each domain, the domain porosities could be obtained, with the total porosity of the dual-porosity medium being simply the sum of the macropore and micropore domain porosities. For all simulations, we kept the mean pore water velocity constant at a value of 1.50×10^{-5} m/s. The molecular diffusion coefficient, D_0, was set at 1.6×10^{-9} m^2/s, the viscosity at 0.001 Pa s, and the fluid density at 1 g/cm^3.

For all simulations, we injected into the pore network a pulse of one pore volume (equivalent to 66 min) of a tracer having a relative concentration of 1.0. BTCs of the average concentrations as obtained with the pore network model were analyzed using the CXTFIT program (Toride et al., 1995) within the STANMOD software of Šimunek et al. (1999), leading to estimates of the solute dispersivity, $\lambda=D_m/v$, the fraction of mobile

Table 4.3. Statistics of the generated aggregates.

Property	Value*
Number of aggregates	1000
Mean aggregate diameter [mm]	2.141 (0.475)
Aggregate pore bodies in domain	965,985
Mean pore bodies per aggregate	966 (578)*
Aggregate pore throats in domain	2,391,040
Mean pore throats per aggregate	2391 (1424)*
Mean coordination number	4.95

*values in in parenthesis indicate standard deviations

water, ϕ_m, and the mass transfer coefficient, α, in Eqs. (4.1) and (4.2). This in turn also produced values of the mobile water content, θ_m, and the immobile water content, θ_{im}. The intrinsic permeability was determined for the domain as a whole, as well as for the macropore domain separately (i.e., excluding the presence of the aggregates). In addition, simulations were performed to obtain the intrinsic permeability of the single aggregates. For the Case II simulations, based on the simulated pore velocities, the characteristic time scales of diffusion and advection were calculated to explore the effects of the porewater velocity ratio between the macropore and aggregate domains on the calculations.

4.3. Results and analysis

Before presenting the results of the various pore network calculations, we first summarize the pore network that was used for the reference simulations.

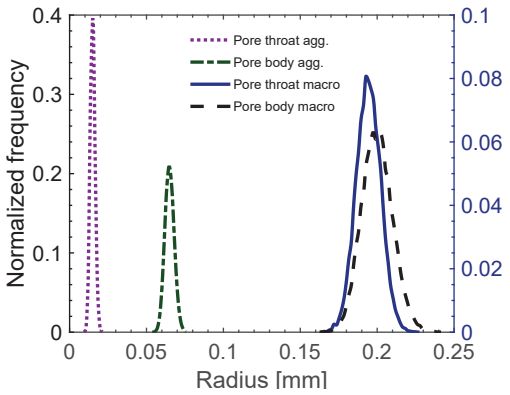

Figure 4.2. Pore body (the right vertical axis) and pore throat (the left vertical axis) size distributions used for the macropore and aggregate domains of the reference model.

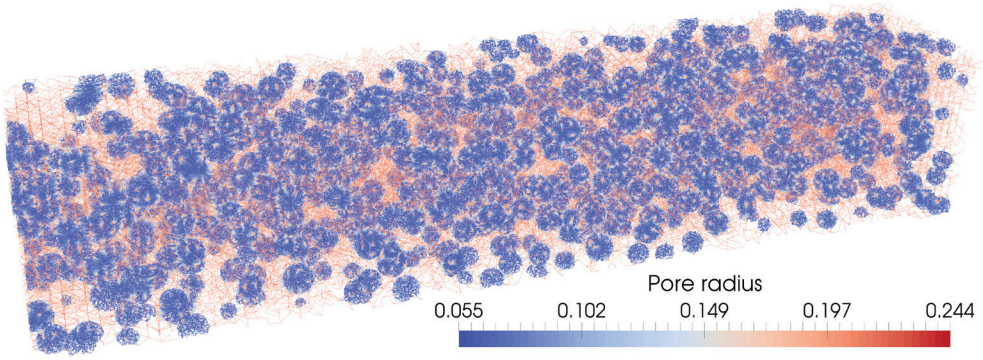

Figure 4.3. Pore radii of the constructed pore network containing 1000 aggregates and composed of a total of 3,357,025 pores.

4.3.1. Reference model

The structured macropore network consisted of 12,929 pore throats connected to each other at 6850 junctions serving as the pore bodies, while the mean pore coordination number was 3.7. A total of 1000 aggregates were randomly placed within the macropore network. Statistics of the generated pore network are given in Table 4.3. The total number of pores within the created computational domain was 3,357,025. The macropore domain porosity was 0.198, and the mean porosity of the single aggregates 0.204. Figure 4.2 shows the generated pore body and pore throat size distributions of the reference model, while Figure 4.3 shows the generated dual-porosity pore network.

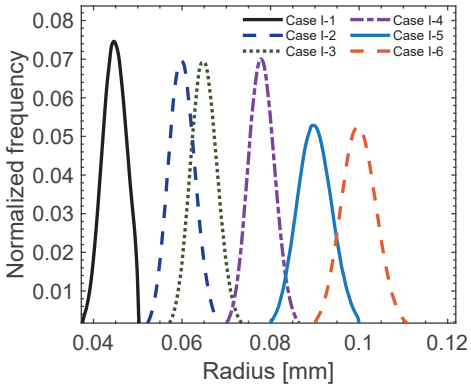

Figure 4.4. Aggregate pore body size distributions for the Case I pore network calculations. The corresponding porosity values are provided in Table 4.4.

Table 4.4. Micro- and macro-porosities for the Case I calculations with variable aggregate porosities.

	Case	Totaldomain porosity $\phi_t=\phi_{ag}+\phi_{macro}$	Porosity of single aggregate ϕ_{sa}	Contribution of aggregates to total porosity ϕ_{ag}/ϕ_t
Porosity effects	I-1	0.214	0.082	0.078
	I-2	0.227	0.163	0.131
	I-3	0.234	0.204	0.156
	I-4	0.260	0.362	0.239
	I-5	0.284	0.510	0.304
	I-6	0.315	0.700	0.372

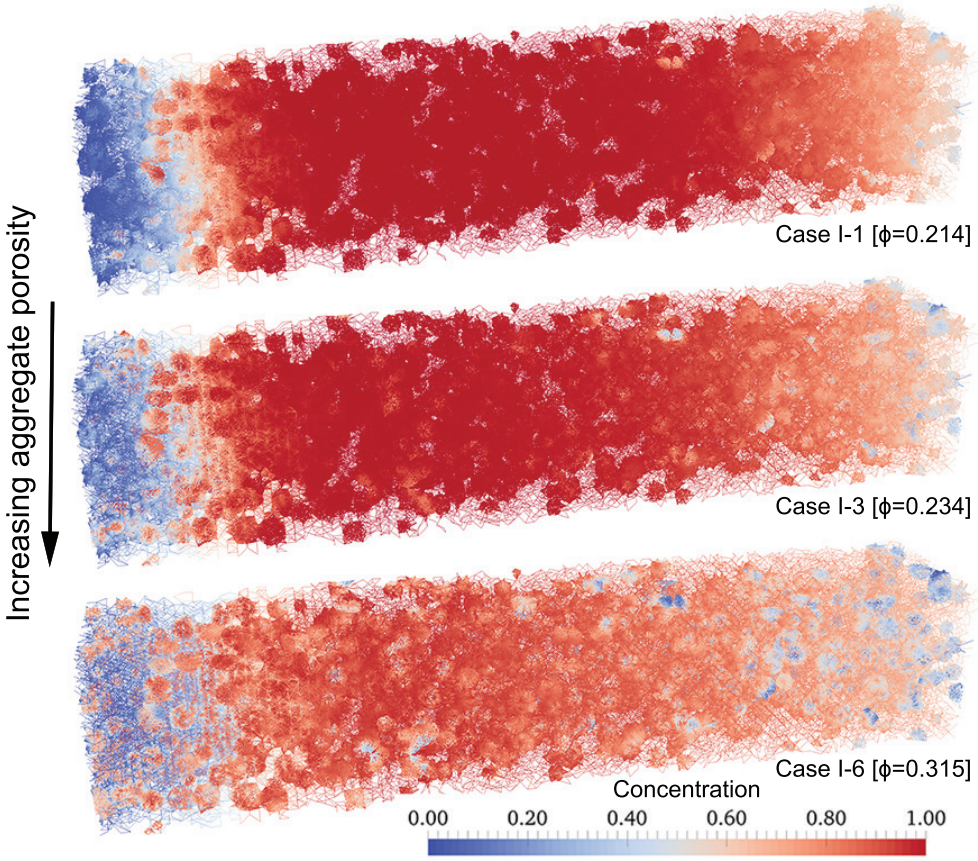

Figure 4.5. Progress of advective transport and dispersion into the domain for Cases I-1, I-3 and I-6 after 1.1 pore volumes. A total of 1.0 pore volumes of tracer was injected.

4.3.2. Case I: porosity effects

Based on the information in Table 4.1, six different pore body size distributions were generated as displayed in Figure 4.4. Table 4.4 summarizes the porosities of the micropore and macropore domains for the Case I simulations. The porosity of the single aggregates ranged from very small (0.082) to very large (0.700). The aggregate domain porosity ranged from 0.013 to 0.114, and the total domain porosity (micropore and macropore domains combined) from 0.214 to 0.315 (the porosity of the macropore domain was kept constant at 0.198).

Figure 4.5 shows the simulated solute concentration distributions for Cases I-1, I-3, and I-6 after injecting 1.0 pore volume of solute into the medium. The distributions are given at T=1.1 pore volume, with pore volume defined as $T=qt/(\phi_t L)$, where L is the length of the medium (100 mm). Concentration distributions at other times are provided in Appendix C, as well as a video clip showing the effect of aggregate porosity. A pulse injection was used to show both solute diffusion into the aggregate domain and subsequent back diffusion from the aggregate domain into the macropore domain. The plots in Figure 4.5 show increased solute spreading as the porosity of single aggregates increased. Case I-6 with its very high single aggregate porosity (ϕ_{sa}=0.700) was included as a mere limiting case. The other extreme would be if no aggregate porosity were to be present (ϕ_{sa}=0), in which case no intra-aggregate diffusion would take place and the standard advection-dispersion equation presumably would apply.

Figure 4.6 shows calculated BTCs (indicated by symbols) obtained with the pore network model at 30, 60, and 90 mm distances from the inlet for all Case I scenarios. Also included are the fitted curves obtained with the macroscopic mobile-immobile (MIM) dual-porosity model given by Eqs. (4.1) and (4.2). We optimized for this purpose the parameters (λ_m, ϕ_m, and α) simultaneously to the three curves (i.e., at x=30, 60, and 90 mm) obtained for each domain with a particular porosity of single aggregates. R^2 values for all Case I calculations, as well for the various Case II examples to be discussed later, were always higher than 0.9995, thus reflecting excellent descriptions of the pore-scale modeling results using the macroscopic formulation. Figure 4.7 shows the fitted BTCs at 90 mm for all six scenarios. Similar BTCs at 30 and 60 mm are provided in Appendix C.

The results in Figures 4.6 indicate increased spreading of the BTCs obtained at larger distances. Also, while the BTCs of Case I-1 were nearly symmetrical, Case I-6 with its highest porosity of single aggregates produced far more asymmetry and tailing in the distributions. Higher porosities of single aggregates (and hence more relatively immobile water) enhanced the extent of preferential flow as exhibited by early breakthrough and

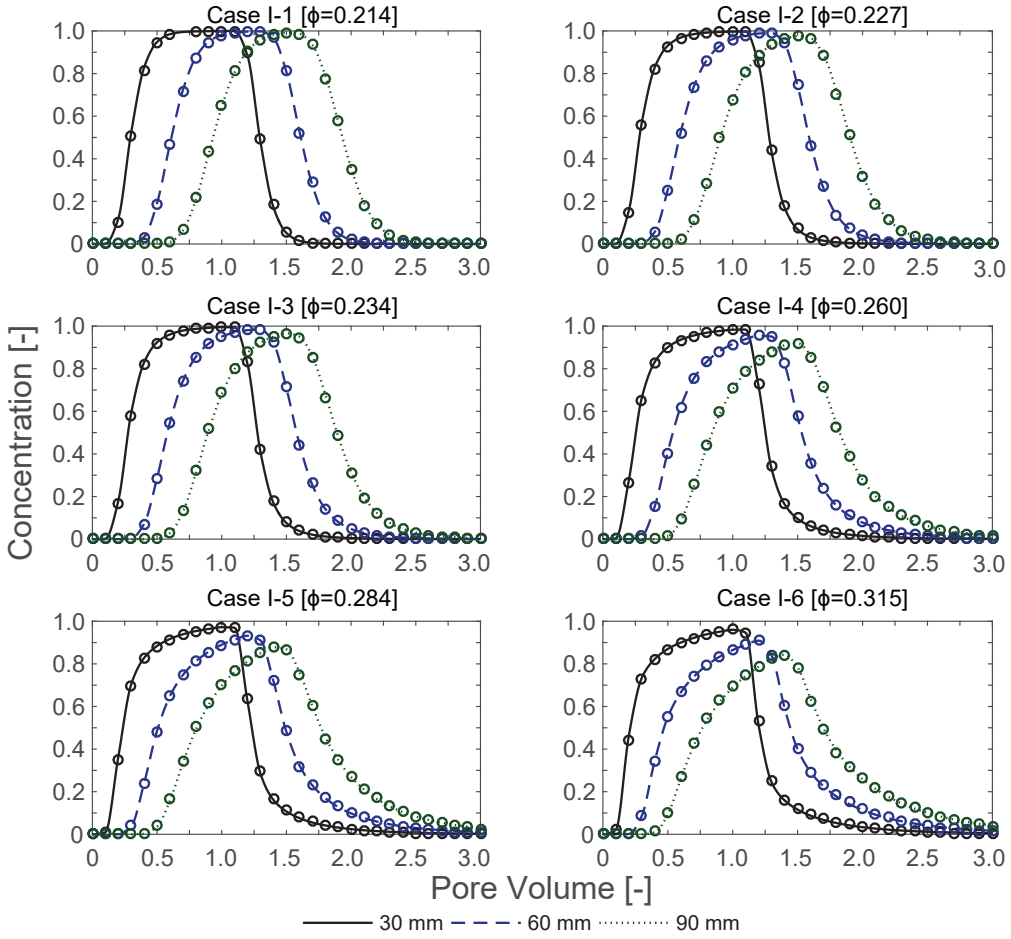

Figure 4.6. Aggregate porosity effects: BTCs obtained with pore network modelling (symbols) and the fitted MIM transport BTCs (solid lines) for the Case I simulations.

Table 4.5. Optimized MIM transport parameters for the Case I simulations.

	Case	v [mm min^{-1}]	λ [mm]	ϕ_m [-]	α [min^{-1}]	θ_m [-]	θ_{im} [-]
Porosity effects	I-1	1.44	1.47	0.967	1.52×10^{-5}	0.207	0.007
	I-2	1.46	1.58	0.930	1.74×10^{-5}	0.211	0.016
	I-3	1.46	1.63	0.908	2.03×10^{-5}	0.213	0.022
	I-4	1.45	1.78	0.822	3.48×10^{-5}	0.210	0.043
	I-5	1.48	1.86	0.747	3.79×10^{-5}	0.212	0.072
	I-6	1.47	1.84	0.661	4.81×10^{-5}	0.208	0.107

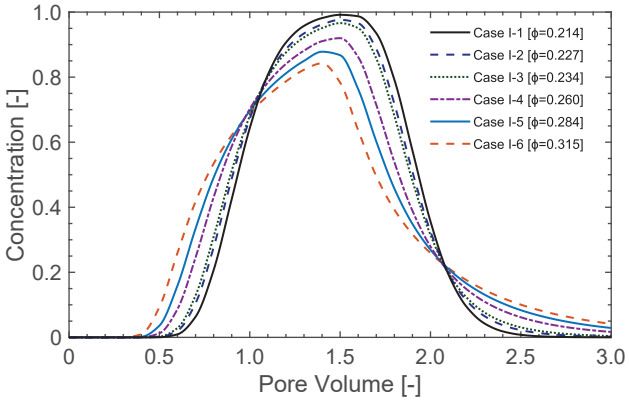

Figure 4.7. BTCs obtained with the macroscopic MIM model as fitted to the pore network modelling results at 90 mm for Case I simulations.

late-time tailing of the curves in Figure 4.7. This agrees with a previous study done on highly heterogenous rocks by Mehmani et al. (2015) who showed that an increasing fraction of microporosity causes more tailing of the observed solute plume. Our findings are also consistent with several other previous studies (e.g., Van Genuchten and Wierenga, 1976; Brusseau, 1993; Shukla, 2013). Table 4.5 provides the transport parameters obtained for the six Case I calculations. Results indicate that a higher aggregate porosity caused a decrease in the mobile water fraction, ϕ_m, and an increase in the mass transfer coefficient, α. The mobile water content, θ_m, was found to be approximately 0.21 for all Case I simulations, which is slightly higher than the macroporosity of 0.198. For all of the simulations, the mobile water content was slightly larger than the macro domain porosity. This is because the calculated fraction of mobile water (ϕ_m) at the macroscopic level is determined by the flow lines affected by the presence of both macropores and aggregates. Figure 4.8 shows that a clear relationship exists between the mobile water content, ϕ_m, and the fraction of macropores. As compared with the porosity of macropores, the fraction of mobile water content using the fitting resulted in 5 to 10 % larger values.

Figure 4.9 shows the relationship we found between the mass transfer coefficient, α, and the porosity of single aggregates, ϕ_{sa}. The mass transfer coefficient increased with aggregate porosity as more solute mass could be transported into aggregates having higher porosity values and higher permeabilities as discussed next.

To further analyze and interpret the pore-scale modeling results, we calculated the permeability (K) of the macro domain and the aggregate domain, as well as the permeability ratio between the aggregates and the macropore region (K_{agg}/K_{macro}). The permeability of the macropore domain was found to be 2.24×10^{-4} mm^2, with the results for K_{agg} and K_{ratio}

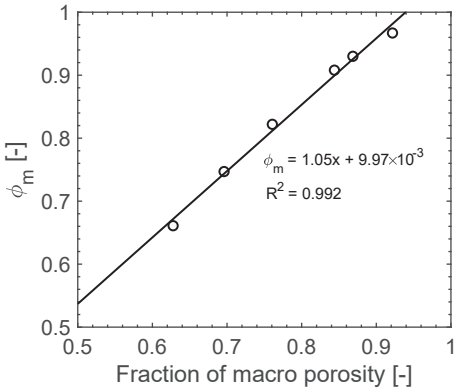

Figure 4.8. Plot of the mobile water content (ϕ_m) against the fraction of macroporosity for Case I simulations. A value of 1 for ϕ_m would mean the absence of any aggregates.

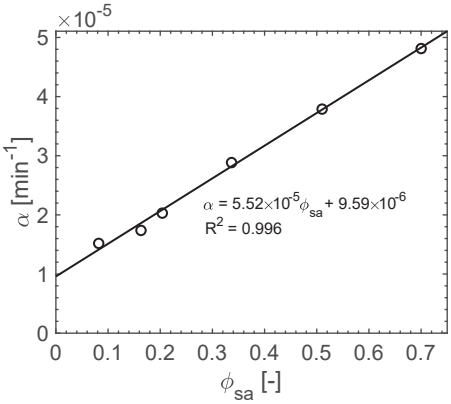

Figure 4.9. Plot of the mass transfer coefficient (α) against the porosity of single aggregates (ϕ_{sa}) for Case I.

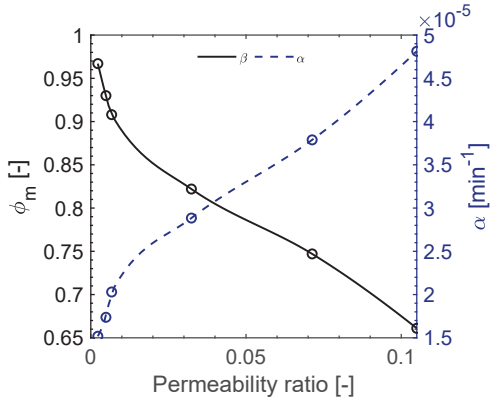

Figure 4.10. Values of the mobile water fraction (ϕ_m) and the mass transfer coefficient (α) plotted against the permeability ratio (K_{agg}/K_{macro}) for Case I.

Table 4.6. Calculated permeability values for the aggregates, and the permeability ratio (K_{agg}/K_{macro}) for Case I.

	Case	K_{agg} [mm^2]	K_{ratio} [-]
Porosity effects	I-1	5.06×10^{-7}	2.26×10^{-3}
	I-2	1.09×10^{-6}	4.87×10^{-3}
	I-3	1.50×10^{-6}	6.71×10^{-3}
	I-4	7.25×10^{-6}	3.24×10^{-2}
	I-5	1.60×10^{-5}	7.13×10^{-2}
	I-6	2.35×10^{-5}	1.05×10^{-1}

given in Table 4.6. When the porosity of the single aggregates increased, pores come to be closer to each other, which resulted in higher aggregate permeability values and larger permeability ratios. With a larger permeability, more fluid may flow into and through the aggregates, leading to higher α and lower ϕ_m values (Figure 4.10).

4.3.3. Case II: aggregate permeability effects

Utilizing the input parameters from Table 4.1, pore body size distributions were generated for the various examples. We used domains with four different pore-throat size distributions for the aggregates (Figure 4.11). Flow and solute transport simulations were carried out for each pore size distribution. Note that the reference model is Case II-2, which corresponds to Case I-3 of the first set of simulations. Table 4.7 provides the porosity values for the Case II simulations. The data show that an increase in the pore throat radii increased the single aggregate porosity as well as the total porosity. The progress of one

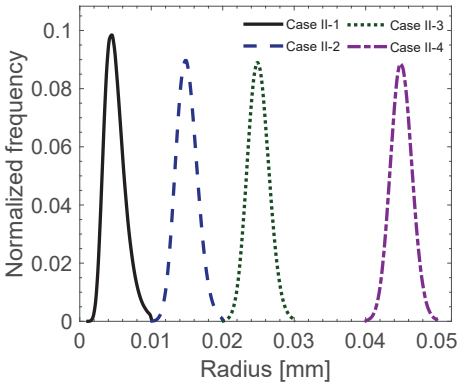

Figure 4.11. Aggregate pore throat size distributions for Case II pore network calculations. The corresponding porosity values are provided in Table 4.7.

Table 4.7. Micro- and macro-porosities for the Case II calculations with variable aggregate permeability.

	Case	Total domain porosity $\phi_t=\phi_{ag}+\phi_{ma}$	Porosity of single aggregate ϕ_{sa}	Contribution of aggregates to total porosity ϕ_{ag}/ϕ_t
Permeability effects	II-1	0.229	0.193	0.137
	II-2	0.234	0.202	0.141
	II-3	0.242	0.219	0.147
	II-4	0.272	0.281	0.166

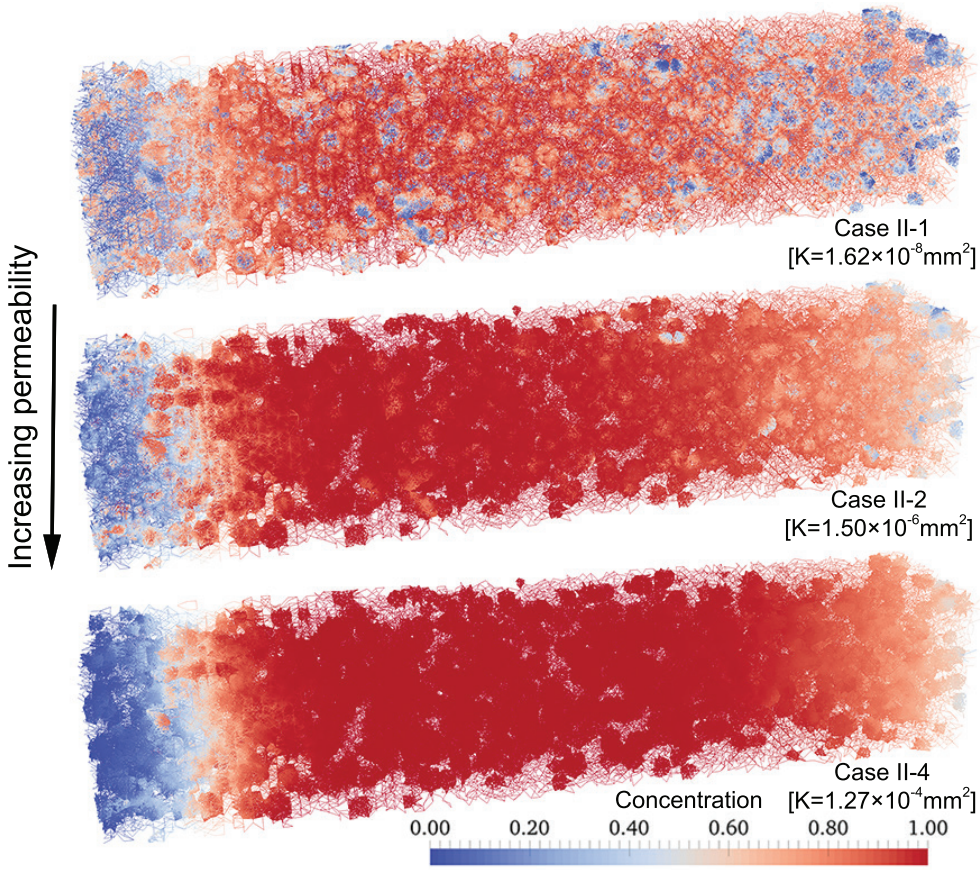

Figure 4.12. Progress of advective transport and dispersion into the domains of Cases II-1, II-2, and II-4 after 1.1 pore volumes. A total of 1.0 pore volumes of tracer was injected.

pore volume of solute moving through and dispersing into the domains of Cases II-1, II-2, and II-4 at 1.1 pore volumes are shown in Figure 4.12. Similar visualizations at multiple time levels are provided in Appendix C, as well as a video clip showing the effect of aggregate permeability. The flow of solute-free water after entry of the concentration pulse into the domain shows that solutes moved much faster into and through the macropore domain for Case II-4, while the residence time of solutes in the aggregates was higher for Case II-1. These results indicate that the exchange rate of the solute tracer between the aggregate and macropore domains for Case II-1 was lower than for Cases II-2 and II-4. A higher solute exchange rate was observed especially for Case II-4 due to the fact that solutes in the aggregates were almost instantly leached back into the macropore domain (also see Appendix C).

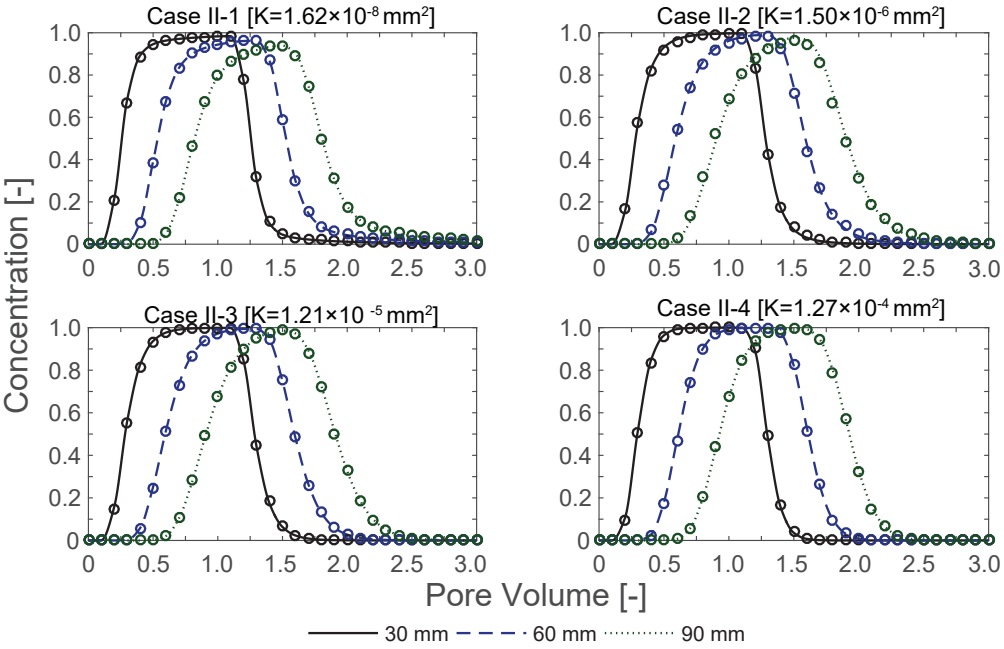

Figure 4.13. Aggregate permeability effects: BTCs obtained with pore network modelling (symbols) and the fitted MIM transport BTCs (solid lines) for the Case II simulations.

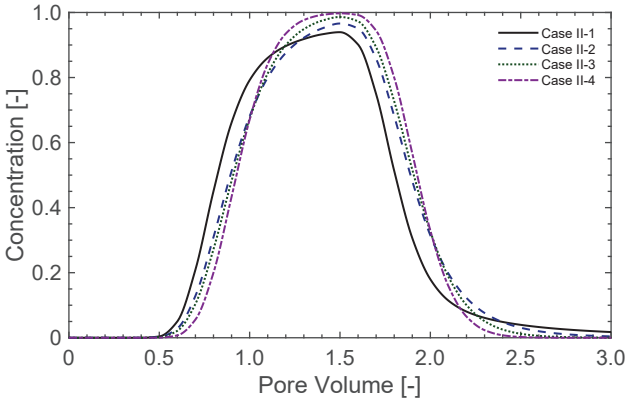

Figure 4.14. BTCs obtained with the macroscopic MIM model as fitted to the pore network modeling results at 90 mm for Case II.

Table 4.8. Optimized MIM transport parameters for the Case II simulations.

	Case	v [mm min^{-1}]	λ [mm]	ϕ_m [-]	α [min^{-1}]	θ_m [-]	θ_{im} [-]
Permeability effects	II-1	1.51	1.47	0.891	7.31×10^{-6}	0.204	0.025
	II-2	1.46	1.63	0.908	2.03×10^{-5}	0.212	0.021
	II-3	1.46	1.37	0.878	6.93×10^{-5}	0.213	0.030
	II-4	1.46	1.24	0.789	1.27×10^{-3}	0.215	0.057

Figure 4.13 compares the BTCs for the individual simulations, while Figure 4.14 shows a comparison of the different simulations for Case II at a longitudinal distance of 90 mm. BTCs obtained at 30 and 60 mm are provided in Appendix C. The plots show that reduced pore throat sizes lead to an earlier breakthrough of solute, increased attenuation of the peak concentration, and more positive skewness of the BTCs in the form of tailing (e.g., Case II-1). Increasing pore throat sizes, on the other hand, resulted in delayed breakthrough curves with less tailing and more symmetrical BTCs. This is consistent with the visualizations in Figure 4.12 and in Appendix C, which show a more uniform solute front for Case II-4 as compared to Case II-1. The latter case exhibits more preferential flow and more pronounced tailing.

Utilizing the BTCs, transport parameters were again obtained for each simulation using the CXTFIT program. The results are given in Table 4.8. The obtained mobile fraction, ϕ_m, was found to be higher than the volume fraction of macropores for Cases II-1, II-2, and II-3, while ϕ_m was lower than the volume fraction of macropores for Cases II-4. These results are due to the hydrodynamic effects caused by the presence of aggregates in the domain. Smaller pore throats create relatively impermeable aggregates, which causes the overall fluid flow path through the macropores to become more tortuous, leading to higher immobile fractions at the macroscopic scale. On the other hand, the presence of aggregates with larger pore throats causes a less tortuous flow path as aggregates provide

Table 4.9. Mean pore water velocities in the macropore and aggregated domains for Case II.

		Pore Bodies[mm min^{-1}]			Pore Throats[mm min^{-1}]		
	Case	v_{agg}	v_m	$v_{agg/m}$	v_{agg}	v_m	$v_{agg/m}$
Permeability effects	II-1	2.32×10^{-4}	5.40	4.30×10^{-5}	1.51×10^{-2}	2.99	5.05×10^{-3}
	II-2	1.67×10^{-2}	5.48	3.05×10^{-3}	1.19×10^{-1}	3.04	3.92×10^{-2}
	II-3	1.24×10^{-1}	5.58	2.22×10^{-2}	3.19×10^{-1}	3.09	1.03×10^{-1}
	II-4	1.02	5.79	1.75×10^{-1}	8.06×10^{-1}	3.10	2.60×10^{-1}

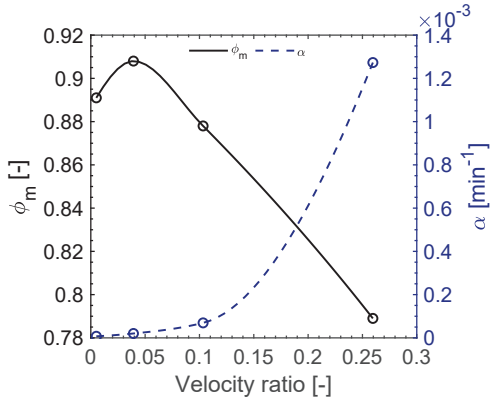

Figure 4.15. Values of the mobile water fraction (ϕ_m) and the mass transfer coefficient (α) plotted against the velocity ratio (v_{agg}/v_{ma}) for Case II.

a noticeable contribution to the total flow, leading to lower immobile water fractions at the macroscopic scale. The mass transfer rate, α, was lowest for Case II-1 and highest for Case II-4. This is in agreement with our earlier observations about the visualizations.

Table 4.9 shows calculated pore water velocities of the macropore and micropore (aggregate) domains. The data indicate that larger pore throat sizes lead to higher pore water velocities. Figure 4.15 shows plots ϕ_m and α against the velocity ratio, v_{agg}/v_{ma}. The mass transfer rate, α, decreased with a lower velocity ratio. In contrast with Case I, an increase in α did not lead to longer tailing but produced more symmetric BTCs. Increasing the aggregate pore water velocities caused the dominant transport process in the micropore domains to change from diffusion dominated to advection dominated. Interactions between the aggregate and macropore domains consequently increased, leading to higher values of the mass transfer coefficient, α. We note here that the two-region mobile-immobile model (MIM) considers the immobile domain to be completely diffusion dominated, which likely contributed to the fluctuations in ϕ_m with the velocity ratio.

When solute-free water is injected and the transport regime in the aggregate domain is diffusion dominated, then the characteristic time for solutes to diffuse back into the macropore domain is given by $t_{dif} = l^2/D_m$, where l is the effective length of the aggregates and D_m the molecular diffusion coefficient. For an advection dominated transport regime, on the other hand, the characteristic transport time is described by $t_{adv} = l/\overline{v}$, where l is now the domain length. These time scales are characteristic for the extent of BTC tailing when the amount of mass stored in the aggregates is noticeable, and when the velocity ratio is low. The advection and diffusion time scales for the aggregate and macropore

Table 4.10. Characteristic advection and diffusion times (in minutes) for the Case II simulations.

	Case	$t_{adv,ma}$	$t_{adv,agg}$	$t_{dif,agg}$	Transport regime
Permeability effects	II-1	23.86	139.69	19.10	diffusive
	II-2	23.49	15.77	19.10	advective
	II-3	23.08	4.83	19.10	advective
	II-4	22.48	1.18	19.10	advective

domains are listed in Table 4.10. For these calculations, we used the mean fluid velocity in the pore bodies and throats, while for the characteristic length of the aggregates we used the mean aggregate radius.

We used the transport time scales to identify the dominant transport mechanism in the aggregate domain. When $t_{adv,agg}<t_{dif,agg}$, transport in the aggregate domain is primarily advection dominated, but when $t_{adv,agg}>t_{dif,agg}$ the aggregated domain becomes more dominated by diffusion. The data in Table 4.10 indicate that Case II-1 was very much diffusion dominated, while the experiments towards Case II-4 became increasingly more advection dominated. Tailing will be observed when the characteristic time for diffusive transport in the aggregates is similar or becomes less in comparison to the advection time scale in the macropore domain.

For Case II-1, when the transport domain is leached, the amount of solute tracer remains relatively high in the micropore domain since the time of solute tracer to be transported back into the macropore domain is much lower than the front of the solute-free water passing through the domain. This effect becomes less visible for Case II-2, and is almost absent for Case II-4. Extensive tailing is observed when the transport regime in the aggregates is diffusion dominated and the transport regime in the macro domain is advection dominated. For flow conditions when the velocity ratio between the two domains

Table 4.11. Calculated permeability values for the aggregates, and the permeability ratio (K_{agg}/K_{macro}) for Case II.

	Case	K [mm^2]	K_{ratio} [-]
Permeability effects	II-1	1.62×10^{-8}	7.24×10^{-5}
	II-2	1.50×10^{-6}	6.71×10^{-3}
	II-3	1.21×10^{-5}	5.40×10^{-2}
	II-4	1.27×10^{-4}	5.65×10^{-1}

is close to 1, fluid passes through the aggregates as well as through the macropore domain, leading to relatively symmetrical BTCs. Fluid flow at lower velocity ratios is relatively much slower in the aggregates, leading to long tails in the BTC. These findings agree with other studies, such as those by Brusseau (1993) and Bijeljic et al. (2013), who found that the degree of non-equilibrium and dominance of the velocity variations between the inter-aggregate and intra-aggregate pores influence the severity of tailing. Values of the calculated permeabilities are listed in Table 4.11. With increasing pore throat sizes, the permeability increased, with the permeability ratio increasing from a value of 7.24×10^{-5} for Case II-1 to 0.56 for Case II-4. This means that for Case II-4 the fluid penetrated into aggregates almost as easily as it passed through the macropores. For Case II-1 the ratio is very low, meaning that fluid flow now takes place much less through the aggregate pores as compared to the macropores. This is consistent with the fact that considerable tailing was observed in the BTCs of Case II-1, while Case II-4 produced more symmetrical BTCs.

4.4. Conclusions

We investigated the effects of multi-scale pore sizes in a dual-porosity porous medium on fluid flow and solute transport processes. Several dual-porosity pore networks were constructed by placing a large number of aggregates into the macropore domain. After construction of the aggregate domains, fluid flow and solute transport were simulated using the PoreFlow (Raoof et al., 2013) pore network model to obtain three-dimensional flow fields and solute distributions, as well as the BTCs at several locations along the flow path. The resulting BTCs were fitted analyzed in terms of the conventional macroscopic dual-porosity (MIM) transport model to estimate several key macroscopic transport parameters. The use of pore-scale modeling provided information to link the transport properties to the underlying pore-scale processes, which would be very difficult and time-consuming to do using only experimental methods.

A pore network model consisting of 1000 aggregates, each having an average of 966 intra-aggregate pores, was generated to produce a domain with a total of 3,357,025 pores. By varying the pore sizes, different aggregates with porosity values between 0.082 and 0.700 were obtained. We showed that increasing aggregate porosities did lead to higher values of the mass transfer coefficient and more tailing in the BTCs. Higher fluid velocities within the aggregate domain also increased the mass transfer coefficient but produced less tailing in the calculated BTCs. On the other hand, lower pore water velocities in the micropore domain produced lower mass transfer coefficients but more extensive tailing in the BTCs. The velocity ratio between the aggregated and macro domain could explain the magnitude of tailing observed in the BTCs.

We showed that dual-porosity pore network models are attractive tools for investigating the basic processes governing solute interactions between the macropore domain (containing interaggregate pores) and the micropore or aggregate domain (containing intra-aggregate pores). The developed pore network model provides a flexible means of analyzing the effects of pore-scale transport properties such as aggregate porosity and permeability on macroscopic flow and transport parameters of dual-porosity porous media. While in this study we focused on the effects of aggregate porosity and permeability on macroscopic transport, further studies are needed to better understand all of the pore-scale properties of aggregates. In our work, we varied the aggregate porosity by varying the size of the pore bodies. The aggregate porosity can vary also as a result of changes in the number of pore bodies, the pore coordination number, and the size of the throats. The influence of the range, variance, skewness, and kurtosis of the pore size distribution on the mass transfer coefficients must also be investigated further. We note also that aggregate domain porosity can be influenced by the size and number of aggregates, which have been kept constant in this study. We furthermore did not consider any direct connections between the aggregates. These connections will have an influence on the residence time of the solute in the aggregated domain. They very likely will influence the magnitude of transferred mass, and how solutes are exchanged between the micropore and macropore domains. The use of suitable imaging techniques remains indispensable in all of this to most accurately obtain the exact micropore structures of the aggregates and the porous medium as a whole.

Chapter 5

Fluid Flow and Colloid Transport Experiments in Dual-Porosity Samples

Role of Micro-Porosity on the Transport Behavior of Colloids

Abstract

The remarkable increase in the use of natural and engineered colloids and nanoparticles in agriculture, industry, and for consumer products is leading to more exposure of these particles to the environment. Colloid transport in the subsurface is becoming especially a concern since they are being detected in drinking water supplies, thereby posing health threat. Preferential flow in aggregated soil profiles, or porous media that are structured or fractured in other ways, is a major cause of the transport of pollutants between the earth surface and underlying soils and groundwater. Unfortunately, the effect of soil aggregation on colloid transport is still poorly understood.

In this study, we constructed PDMS micromodels based on x-ray tomography of real soil samples and transformed solid grains into porous aggregates. We replaced 25, 50, 75, and 100% of the solid grains with porous aggregates. The micromodels provided distinct inter-aggregate and intra-aggregate pores. We could track the full trajectory of a large number of colloids moving through pore structures, and hence follow their dynamics in space and time. Colloids were divided into four categories based on their flow paths (trajectories): mobile colloids in the macropores, mobile colloids in the micropores, immobilized colloids, and remobilized colloids. We used 4-µm sized colloids and applied an average velocity of 12.0 m $day^{-1}$to the different samples. For one sample, we additionally applied different velocities (1.0, 5.0, and 20.0 m day^{-1}) to investigate the flow velocity effects.

During all experiments over 1500 colloid trajectories were observed. While chemical conditions during the experiments were unchanged, we found an increase in immobilized particles from almost 0% for the sample without aggregates to 40% retention for the fully (100%) aggregated sample. Remobilization rarely occurred in all micromodels. The trajectory tortuosity decreased from 1.21 to 1.15 due to shorter flow paths in the fully aggregated micromodels. Introducing more aggregates was found to considerably increase the chance of colloids to be transported through the smaller intra-aggregate pores, and hence for the colloids to interact with solid surfaces (i.e., collectors) and become attached. Lower flow velocities within the aggregates also contributed to attachment due to lower hydrodynamic forces. Concentration breakthrough curves (BTCs) could be constructed within the micromodels and near the exit. The pore-scale information provided major insight into the measured BTCs in terms of explaining observed sample-scale BTCs of larger systems like those of column and field-scale experiments.

5.1. Introduction

Soil and groundwater pollution by a broad range of industrial and agricultural contaminants is an ever-increasing global problem. The increased use of pesticides (Hantush et al., 2000, 2002), man-made nano-colloids (Baalousha et al., 2009; Gottschalk and Nowack, 2011; Neukum et al., 2014; Braun et al., 2015), micro-plastics (Engdahl, 2018; Xu et al., 2019; Li et al., 2020), landfills (Kjeldsen et al., 2002), and pharmaceuticals (Kolpin et al., 2002; Hill et al., 2019; Luque-Espinar and Chica-Olmo, 2019) is causing major soil and groundwater pollution problems. The applied chemicals are known to contribute especially to subsurface problems when subject to preferential flow through the vadose zone caused by local soil heterogeneities (Flury et al., 1994; Abbaspour et al., 2001; Hendrickx and Flury, 2001). These heterogeneities cause colloids and other contaminants to travel deeper and faster through the media.

Preferential flow may result from the bimodal pore size distribution of an aggregated soil. Soil pores then can be divided into macropores (inter-aggregate pores or fractures), and micropores (intra-aggregate or matrix pores) (Mehmani and Prodanovic, 2014; Martínez et al., 2015). The liquid is then often assumed to be mobile only within the inter-aggregate pores and immobile in the intra-aggregate pores (Gerke and Van Genuchten, 1993; Šimůnek et al., 2003). During transport, the dissolved solute phases are generally assumed to be freely dispersible in the water due to Brownian motion. However, colloids with sizes >1µm are less affected by Brownian motion, thus causing diffusion generally to be minimal (Bales et al., 1989). Studies have shown that colloids can move through natural porous media up to 50% faster than dissolved solute tracers (Kretzschmar et al., 1999; Bai et al., 2018).

Multiple factors may lead to lower transport times of colloids in porous media. One factor is the presence of repulsive forces between the porous medium and colloidal particles that force particles away from the solid surfaces into the pore bulk regions with higher velocity streamlines (Zvikelsky and Weisbrod, 2006). A second factor is the size exclusion effect whereby colloids try to surpass small pores resulting in a smaller effective available pore space for particle transport in comparison to dissolved solute tracers (Kretzschmar et al., 1999; Sirivithayapakorn and Keller, 2003; Bai et al., 2018). In a study using pore-scale micromodels, Sirivithayapakorn and Keller (2003) showed that size exclusion could cause colloid velocities to be 4 - 5.5 times larger than the estimated average pore-water velocities. Size exclusion is assumed to reduce the retention of colloids due to their faster transport in pores with higher velocities and bypassing the smaller pores (Zvikelsky and Weisbrod, 2006; Pang et al., 2008; Jiang et al., 2010; Neukum et al., 2014; Bai et al., 2016).

However, the intra-aggregate pores have at the same time a potential for colloid retention due to the smaller pore spaces with their lower hydrodynamic forces, leading to more interaction with solid surfaces (Wang et al., 2013; Bai et al., 2018).

Several processes are known to play a major role in the transport and retention of colloids in homogenous media. For example, high ionic strength can lead to a more compact electric double layer to make attachment more likely (Mitropoulou et al., 2013; Wang et al., 2013, 2016; Mohanty et al., 2016), while an increase in pH can lead to less colloid attachment by providing more stable solutions (Roy and Dzombak, 1997; Kumahor et al., 2015). Other factors that affect colloid transport are chemical surface heterogeneities and surface roughness, which can lead to more preferred attachment locations and sites (Mitropoulou et al., 2013; Argent et al., 2015; Bradford and Torkzaban, 2015).

Past studies of colloidal and microorganism transport in porous media during preferential flow have focused mostly on packed columns with a mixture of lenses of fine sand surrounded by coarser sands (Bradford et al., 2004; Wang et al., 2013), fractured media (Bales et al., 1989; Zvikelsky and Weisbrod, 2006; Mohanty et al., 2015, 2016), heterogeneous undisturbed soil samples (Rousseau et al., 2004; Jiang et al., 2010; Braun et al., 2015), and media with a limited presence of aggregates (Bai et al., 2018). Leij and Bradford (2013) studied colloid transport in a column consisting of an inner core and an outer ring, with the inner core representing the soil matrix (filled with small grains) and the outer ring the preferential flow part (filled with coarser grains), and then also with the two parts interchanged. The setup was used to study the effect of dual-porosity systems on colloid transport and the associated preferential pathways and phase exchange. While their method provided a system without individual aggregates, it allowed them to study the effect of particle and colloid size on transport. They found higher retention rates when smaller grain sizes were used but were not able to link the observed behavior to pore-scale processes. Bai et al. (2018) performed colloid transport experiments using columns consisting of heterogenous sand and an aggregated medium. They observed more preferential flow in the aggregated media compared to the sand and linked this difference to size exclusion. While they expected preferential flow to lead to less retention, they observed the opposite in that more retention occurred during saturated flow in the dual-porosity media. The micropores of the aggregates contributed to the preferential flow of colloids while also providing an additional deposition site for colloid attachment due to their high surface area. At the microscopic scale, there is only limited knowledge on colloidal movement in dual-porosity media, with most studies focusing on breakthrough curves at larger scales.

In this study, we used solutions with low ionic strength (deionized water) and a neutral pH. The colloids we used, as well as the pore structure surfaces, were negatively charged. which results in unfavorable conditions for attachment. Each individual aggregate in our system was a cluster of several smaller grains to serve as a micropore structure. The pore networks within the aggregates created relatively low flow velocities compared to the main macropore domains. Using a custom-built optic setup, we could track each individual colloid and its movement through the porous media containing both macro- and micropore spaces, to obtain full colloid trajectories needed to describe the transport processes in detail. Having images from the whole domain at successive times, breakthrough curve (BTC) of colloid arrivals at given longitudinal distances from the inlet were also obtained.

The micromodel setup provided an ideal system to explore colloid transport under unfavorable conditions where attachment is not very likely, and with the overall domain showing most or all colloid transport processes that can take place within the sample. The solution chemistry was kept unchanged between the various experiments to provide a very systematic study with several samples having increasing fractions of aggregates. We furthermore performed for one sample several experiments with different flow velocities to explore the effects of fluid flow on colloid transport in aggregated media.

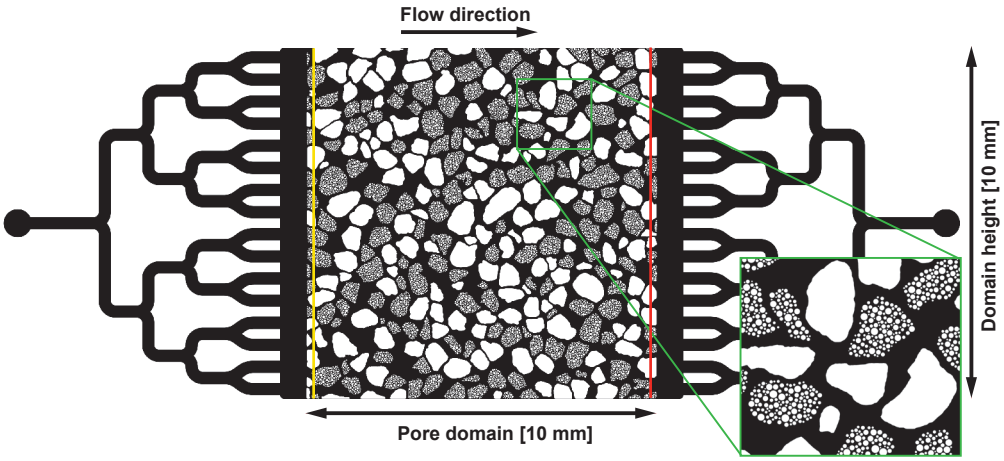

Figure 5.1. Schematic of the micromodel S40/50 pore structure where 50% of the solid particles were transformed into aggregates. Colloids could be tracked in the domain between the yellow and red lines, with the red line showing the location where the breakthrough curves were measured. A zoomed-in section is presented to show the inter-aggregate (macro-) and intra-aggregate (micro-) pores. The flow direction was from left to right, with the flow domain having a physical size of 10×10 mm^2 with a depth 20 μm.

Experimental approach

Pore space topology. The reference pore structure domain was constructed using x-ray tomography to obtain an as realistically as possible pore network. The reference sample was used to embed aggregates within the pore spaces using an in-house numerical MATLAB code. Construction of the micromodels is described in detail in Chapter 3. Figure 5.1 shows the S40/50 micromodel. Colloids were tracked between the yellow and red lines. The red line shows the location where the breakthrough curves (BTCs) were measured. A zoomed-in view of the aggregated medium is also presented.

Poly-Di-Methyl-siloxane (PDMS) micromodels are optically transparent between wavelengths of 240 and 1100 nm, while having a quasi-2D structure. The micromodels are hydrophobic and are negatively charged (Sze et al., 2003; Kirby and Hasselbrink, 2004; Almutairi et al., 2012). PDMS micromodels have been used in studies for two-phase flow (Karadimitriou et al., 2013; Zarikos et al., 2018), as well for solute transport (Corapcioglu et al., 1997), reactive transport (De Anna et al., 2013; Jiménez-Martinez et al., 2015), and colloid transport (Auset and Keller, 2006; Zhang et al., 2014, 2015).

The microscopy setup and the experimental procedure.

The basic microscopy set-up was described in detail in Chapter 2. The experimental procedure was modified as outlined below. The pore network was initially fully saturated using CO2 gas. Next, we injected 100 pore volume s (PVs) of a colloid-free solution into the samples to fully saturate all pore spaces, including the removal of CO2 from poorly accessible and dead-end pores. The large volume (i.e., 100 PV) was enough to return the pore fluid pH to neutral. The experiments continued by injecting 5 PV of a solution containing colloids to allow for colloid transport and retention, followed by injecting 20 PV of a colloid-free solution (4-μm FluoSpheres™ Sulfate Microspheres (580/605), ThermoFischer) to explore subsequent transport and detachment/ remobilization of the colloids. Since the porosity of the domains changed when including different fractions of aggregates, we adjusted the flow rate for each domain to reach an average pore-water velocity of 12.0 m day^{-1} for all samples; this to investigate in a consistent manner the influence of flow rate and soil aggregation on colloid transport. Additional experiments were performed with sample S40/50 to examine how different flow velocities (1.0, 5.0, and 20.0 m day^{-1}) would affect colloid transport and attached/remobilization inside the aggregates. The average flow velocity was converted to flow rate using:

$$q = \frac{\bar{v} n V}{L} \tag{5.1}$$

where q is the flow rate [L^3T^{-1}], v is the average velocity [LT^{-1}], V is the volume of the domain [L^3], and n is porosity [-].

Pore volume is the ratio of cumulative discharge over media volumetric capacity. This dimensionless time, also known as the hydraulic residence time (Fetter et al., 2017), is given by:

$$PV = \frac{qt}{Vn} = \frac{\bar{v}t}{L} \tag{5.2}$$

where t is time [T] and L is the length of the domain [L]. The input parameters and porosities of the micromodels are given in Table 5.1.

The imaging processes. For each experiment, a reference image was created to identify the inter-aggregate pores (macropores) and intra-aggregate pores (micropores). This was done by injecting a fluorophore solution inside the micromodel to capture a bright-field image of the pore space. The reference image was subsequently used to identify with high accuracy when a colloid was transported through the intra-aggregate pores, as well the duration, the average travel velocity inside the aggregates, and the frequency of a colloid passing through different aggregates along its full trajectory. The experiments at an average velocity of 12.0 m day^{-1} were recorded at 10 frames per second, while the second set (those with varying velocities) was recorded at 2, 10, and 20 frames per second, respectively, to provide the needed time resolutions. Using image analysis, each colloid could be tracked through successive images. We used for this purpose the Trackmate package of ImageJ

Table 5.1. Volumetric fluid flow rates, q, for all experiment to achieve a target average pore-water velocity, v, of 12.0 m day^{-1}, and for sample S40/50 subjected to velocities of 1.0, 5.0, 12.0 and 20.0 m day^{-1}.

Applied to all samples: aggregate fraction effect

Sample	**S40/0**	**S40/25**	**S40/50**	**S40/75**	**S40/100**
***n* [-]**	0.4	0.48	0.55	0.62	0.70
***q* [µL hr^{-1}]**	40.0	47.7	54.5	61.9	70.1

Applied to Sample S40/50: velocity effect

***v* [m day^{-1}]**	**1.0**	**5.0**	**12.0**	**20.0**
***q* [µL hr^{-1}]**	4.54	22.7	54.5	90.8

(Tinevez et al., 2017). Colloid trajectories were exported and further analyzed using in-house developed MATLAB algorithms. More details can be found in Chapter 2.

Categorizing colloids based on their individual behavior. We grouped the colloids based on their individual behavior during their transport through the pore networks of the micromodel. The approach categorizes colloids as:

i) colloids that were transported only through the inter-aggregate pore spaces (i.e., the macropores) without retention, indicated as: Mobile in macropores

ii) colloids that were transported through both the inter-aggregate and intra-aggregate pore spaces, and experienced retention and subsequent remobilization (i.e., they remobilized after initially being attachment during the experiments), indicated as: Remobilized

iii) colloids that were permanently attached and retained within the pore network (i.e., attached, but did not remobilize afterward), indicated as: Immobile

iv) colloids that were transported through one or more aggregates (i.e., intra-aggregate pores) without any retention, indicated as Mobile in aggregates

For each colloid trajectory, the following parameters were determined: tortuosity of the colloid trajectory, residence time, 1st moment (representing the penetration depth), average velocity, and frequency and fraction of the residence time of a colloid passing through different aggregates during its transport. The methods and approaches used to determine these parameters are described in Chapter 2.

Constructing of Breakthrough Curves (BTCs). BTCs are traditionally constructed using effluent concentration data collected at the outlet of a sample over the duration of the experiment, leading to flux-averaged concentrations when an analytical solution of the transport equation for a semi-infinite medium is used (e.g., Van Genuchten and Parker, 1984). In our experiments, using the pore-scale information we collected during the experiments, the time for each colloid to move from the inlet to the outlet is known. Since the colloid concentrations were very low, we could assume that they did not interact with each other during their transport through the samples. Their injection time as subsequently normalized to an input time of t=0 to obtain a Dirac delta input form. To obtain normalized concentrations, the number of colloids passing through the outlet line during a given time period were counted and divided by the total number of colloids injected into the porous system. The breakthrough curves were constructed at 9.8 mm from the inlet.

Table 5.2. Number and mass fraction of colloids in the different samples as categorized according to their transport behavior.

		Mobile in macropores		Remobilized		Immobile		Mobile in aggregates	
Sample	**Total colloid trajectories**	**Number of colloids**	**Mass fraction**	**Number of colloids**	**Mass fraction**	**Number of colloids**	**Mass fraction**	**Number of colloids**	**Mass fraction**
S40/0	1579	1555	0.985	13	0.008	11	0.007	-	-
S40/25	1861	696	0.374	51	0.027	325	0.175	833	0.448
S40/50	2250	303	0.135	49	0.022	693	0.308	1250	0.556
S40/75	2568	206	0.08	45	0.018	992	0.386	1369	0.533
S40/100	2870	109	0.04	66	0.023	1226	0.427	1533	0.534

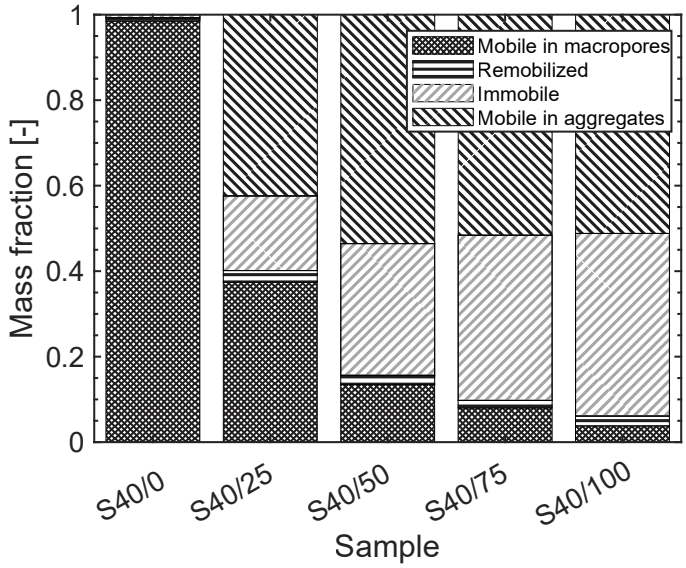

Figure 5.2. Mass fractions of colloids that contributed to the four transport categories.

5.2. Experimental results and analysis

5.2.1. Aggregation effect

A total of five experiments were performed at an average applied flow velocity of 12.0 m day^{-1}. During each experiment, a total of 5 PV was injected, which allowed us to follow a total of between 1579 and 2870 colloid trajectories. Because each micromodel had a different porosity (due to differences in aggregation), the fluid contents and pore water velocities of the various experiments were not the same, leading also to differences in the number and type of the colloid trajectories. Table 5.2 provides the number and mass

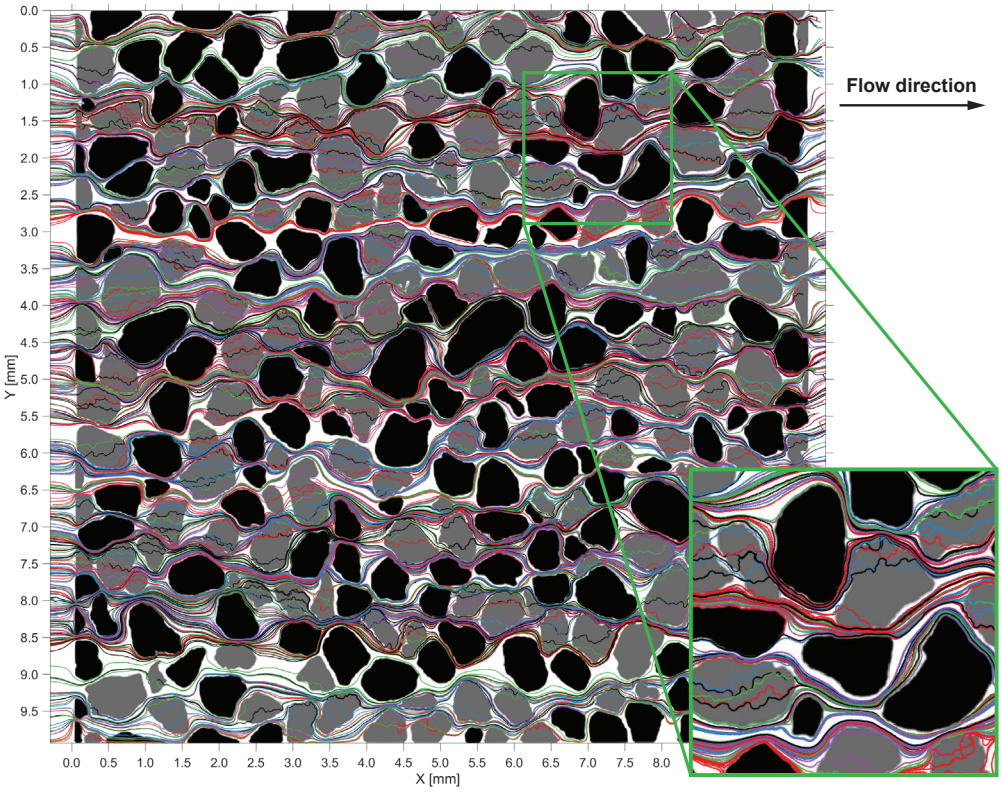

Figure 5.3. Trajectories of colloids which passed through the intra-aggregate pores of sample S40/50 at a velocity of 12.0 m day^{-1}. Solid grains are shown in black, the aggregates in gray, and the various colloid trajectories by different colors. Colloid trajectories of the other samples are given in Appendix D.

fraction of colloids transported as grouped in terms of their transport behavior, while Figure 5.2 shows the contribution of each transport process to overall colloid transport.

The fraction of colloids that were attached during their transport ranged from 0.007 for S40/0 to a value of 0.427 for S40/100. The fraction of remobilized colloids was low (only around 0.02) for all samples. The fraction of colloids passing through at least one aggregate was 0.448 for sample S40/25, but increased to 0.534 for sample S40/100. Consistent with these results, the faction of colloids that were transported only through the macropores and were not attached, decreased with the number of aggregates present in the domain. This shows the important effect of aggregation on the flow paths by increasing the chance of a colloid to find a collector surface with conditions for attachment. An example of the trajectories of colloids transported through the intra-aggregate pores in S40/50 is shown in Figure 5.3. The exact trajectories through the inter-aggregate pores, and the trajectories

of the attached colloids as well as those being remobilized of all samples are given in Appendix D.

Penetration depth of the adsorbed mass. The attachment of colloids created a spatial distribution of the attached mass. This spatial distribution mass changed over time as newly arrived colloids did attach at other locations. Figure 5.4 provides the 1st moment of the attached mass. The figure shows how the mean penetration depth of the attached mass changes over time for all samples (i.e., S40/25-100), except for sample S40/0 which was excluded since only 11 colloids had attached. Our results indicate that the attached mass initially is limited to the first part of the domain, but later becomes more evenly distributed over the entire domain. The ultimate mean values of the attached mass were equal to 5.17×10^{-3} m (2.57), 5.14×10^{-3} m (2.89), 4.38×10^{-3} m (2.68), and 4.73×10^{-3} m (2.80), for the four domains having an increasing number of aggregates (standard deviations are given in brackets). The final states of the attached colloids are given in Appendix D. Figure 5.4 shows that although the fraction of aggregates affects the center of mass of the attached particles, there is no monotonic relation between these two. From these observations, we may conclude that the size of the aggregates and their microporous structure, as well their location, are major parameters controlling attachment behavior these they affect local pressure distributions and colloid passage into across the intra-aggregate pores.

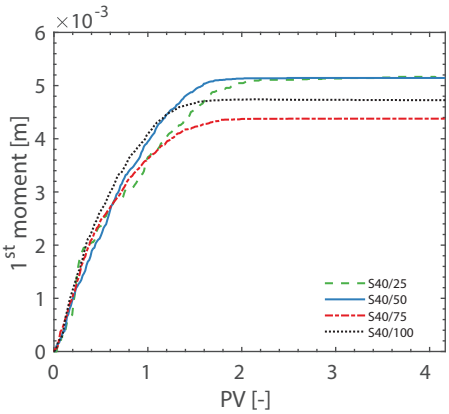

Figure 5.4. Values of the 1st moment of the penetration depth of attached colloids (i.e., the distributed attached mass) against pore volume. Results for S40/0 were not displayed because of limited data.

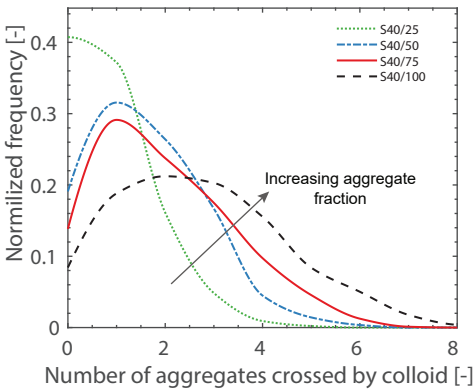

Figure 5.5. Frequency of colloids that crossed an aggregate. The figure shows how many times a colloid entered and exited an aggregate.

Frequency appearance in aggregates. For each colloid trajectory, we counted the frequency of its entrance into and exit from the different aggregates. Figure 5.5 shows a clear increase in the number of passages of colloids through aggregates when there are more aggregates inside the micromodel. This shows that the effect of aggregation on colloid transport increases with the number of aggregates inside the domain. For example, in the domain with 100% aggregates, colloids crossed up to eight aggregates on their way towards the sample outlet. For sample S40/25, over 40% of the colloids were not influenced by the aggregates, and hence moved only through the inter-aggregate pores, while almost an even fraction of colloids was transported through one aggregate. This sample showed a maximum in terms of a single colloids passing through five aggregates. Most of the colloids in samples S40/50 and 75 passed through only one aggregate, while a few of passed through up to six aggregates. By comparison, most of the colloids in sample S40/100 were transported through two aggregates, with a maximum passage through eight aggregates, thus showing the important effect of complete aggregation.

Average colloid velocities. Figure 5.6 shows the average transport velocity of the colloids in the different transport categories. The average values were obtained by analyzing the full length of the colloid trajectory for each particle. Colloid transport velocities clearly

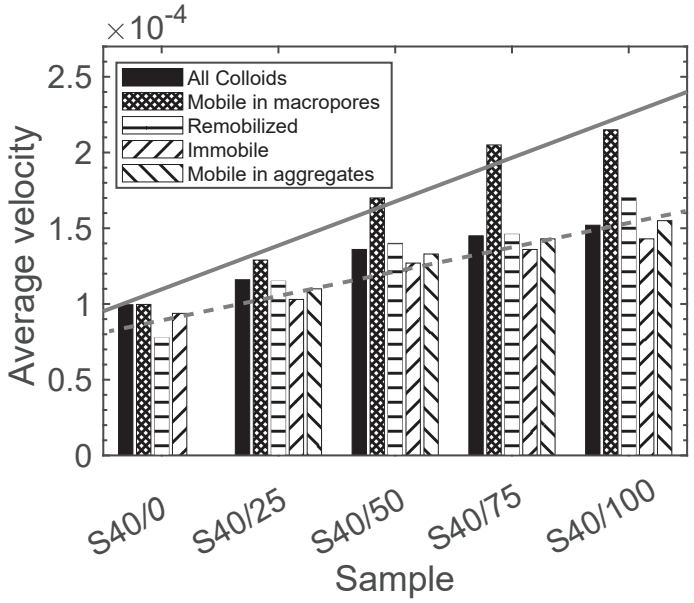

Figure 5.6. Average velocity of colloids for each sample as categorized based on their transport behavior, together with fitted linear trends for the categories of mobile colloids in the macropores (solid-line) and mobile colloids in the aggregates (dashed-line).

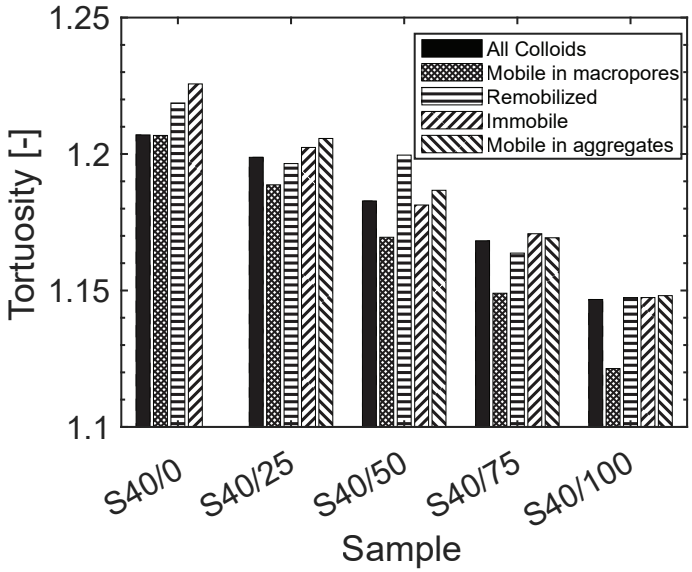

Figure 5.7. Average tortuosity of the colloid transport trajectories for each sample as categorized in terms of their transport behavior.

increased when the fraction of aggregates increased. Note that we imposed fluid fluxes on the different domains so that we had the same average velocity irrespective of the level of aggregation. The data in Figure 5.6 show that the presence of aggregates impacts the distribution of colloid flow velocities possibly through the impacts of tortuosity and residence time as discussed in the next sections. The linear trends indicate that the velocity increase is higher for colloids transported through the inter-aggregate pores compared to the other colloids.

Tortuosity of colloid transport paths. Figure 5.7 shows the average tortuosity of the colloid trajectories for each sample as categorized based on colloid behavior. The tortuosity decreased with increasing aggregation, which shows that the colloids are moving increasingly through the aggregates leading to shorter displacement lengths. This is contradictory to the more tortuous path observed for the intra-aggregate pores (Figure 5.3), although the transport path is shorter through the aggregate than around the contour of the grains. Figure 5.7 shows that the strongest decrease in the trajectory tortuosity occurred for colloids transported through the inter-aggregate (macro) pores. Remobilized and attached colloids show a higher tortuosity compared to colloids transported through the macropores since they are moving at lower velocities and closer to the grain surfaces, leading to higher displacement lengths. The trajectories are given in Appendix D, indexed according to their behavior.

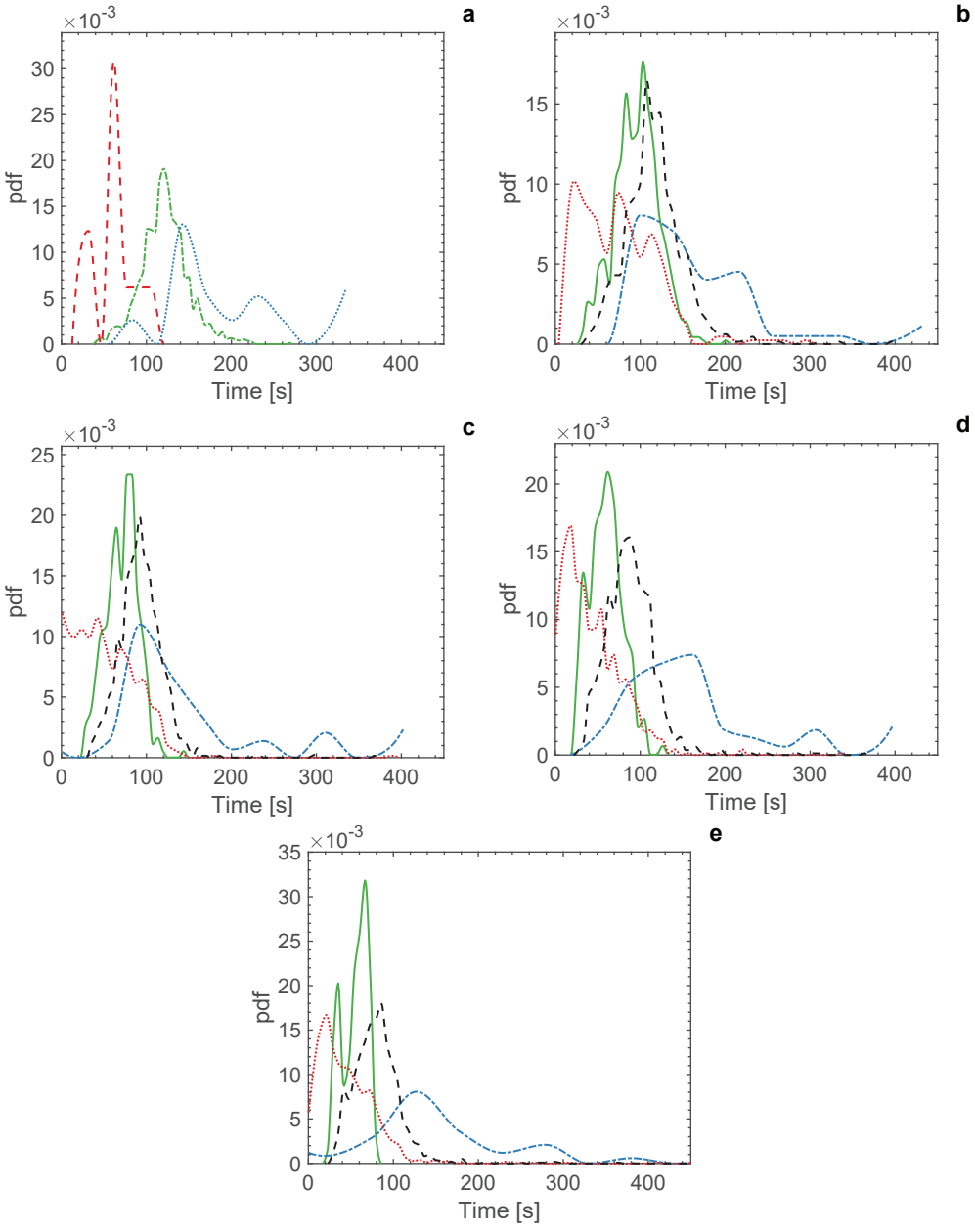

Figure 5.8. Probability density functions (pdfs) of colloid transport time in the four domains for a) S40/0, b) S40/25, c) S40/50, d) S40/75, and e) S40/100. The colloids were indexed based on their transport category. For the attached colloids, the distributions shows the time duration up to their attachment.

Table 5.3. Average times spent in the various domains normalized in terms of pore volume (values in brackets provide the standard deviations).

Sample	Mobile in macropores	Remobilized	Immobile	Mobile in aggregates
S40/0	1.69 (0.39)	2.52 (0.82)	0.84 (0.36)	-
S40/25	1.33 (0.36)	2.28 (0.90	1.02 (0.65)	1.61 (0.48)
S40/50	0.99 (0.26)	2.02 (0.95)	0.74 (0.50)	1.30 (0.39)
S40/75	0.83 (0.27)	2.16 (0.99)	0.61 (0.47)	1.22 (0.41)
S40/100	0.76 (0.20)	2.22 (1.22)	0.64 (0.58)	1.13 (0.46)

Colloid residence time. Figure 5.8 shows the travel times (from the inlet to the outlet) spent by the colloids in the inter-aggregate and intra-aggregate parts of the microdomain samples. For the attached colloids, the times were calculated from their entry into the sample up to the time of attachment. By increasing the number of aggregates in the system, the trajectories through the inter-aggregates (macropore) show a reduction in residence time. This trend reflects the impact of the longer preferential flow paths through the inter-aggregate (macro-) pores induced by intra-aggregate (micro-) pores as seen also by reductions in their tortuosity. At the same time, we see a shift to the right (i.e., increasing travel times) of colloids transported through the aggregates for all samples. This means that aggregates increase the residence time of colloids in the domain due to the lower velocity values created inside the intra-aggregate pores. The remobilized colloids very often cause considerable delay in travel times, with the magnitude of this impact varying among the different samples.

The most frequent residence times (i.e., the distribution peaks in Figure 5.8) of samples S40/25 and 50 occurred around at the same times as the peaks of the trajectories through the aggregates. However, for the remobilized colloids of the other samples the peaks shifted towards higher residence times. Table 5.3 shows normalized travel times for the five samples in the form of dimensionless pore volumes. Colloids transported through the macropores had travel times of 1.69, 1.33, 0.99, 0.83, and 0.76 PV for the five samples ordered by an increasing fraction of aggregates. In a similar trend as tortuosity, the average travel time decreased for both the macropores and aggregates when aggregation increased. Our results show that the time to attachment for the attached colloids was lowest (0.61 PV) for sample S40/75 and highest (1.02 PV) for sample S40/25.

Flow velocities in micro-and macropores. Figure 5.9 shows velocity distributions for colloids that crossed at least one aggregate during their full trajectory, and the associated scatter plots. We analyzed the colloid trajectories to obtain two average velocities for each trajectory: one average velocity for part of the trajectory that passed through the intra-aggregate pores and another average flow velocity for the other part of the trajectory (i.e., representing transport in the inter-aggregate pores). Our results show that in most samples the colloid transport velocities were approximately 0.8×10^{-4} m s^{-1} lower in the intra-aggregate pores compared to the inter-aggregate pores. Although higher velocities were observed with an increased aggregate fraction (Figure 5.6), the ratio between the two velocities remained close to each other. Still, we observed more scattering due to the higher rate of velocity increase in the macropores with more aggregation in the domains. One likely reason is that even with the different structures of the overall microdomains, the average pore sizes of the aggregated grains in our study were still very similar.

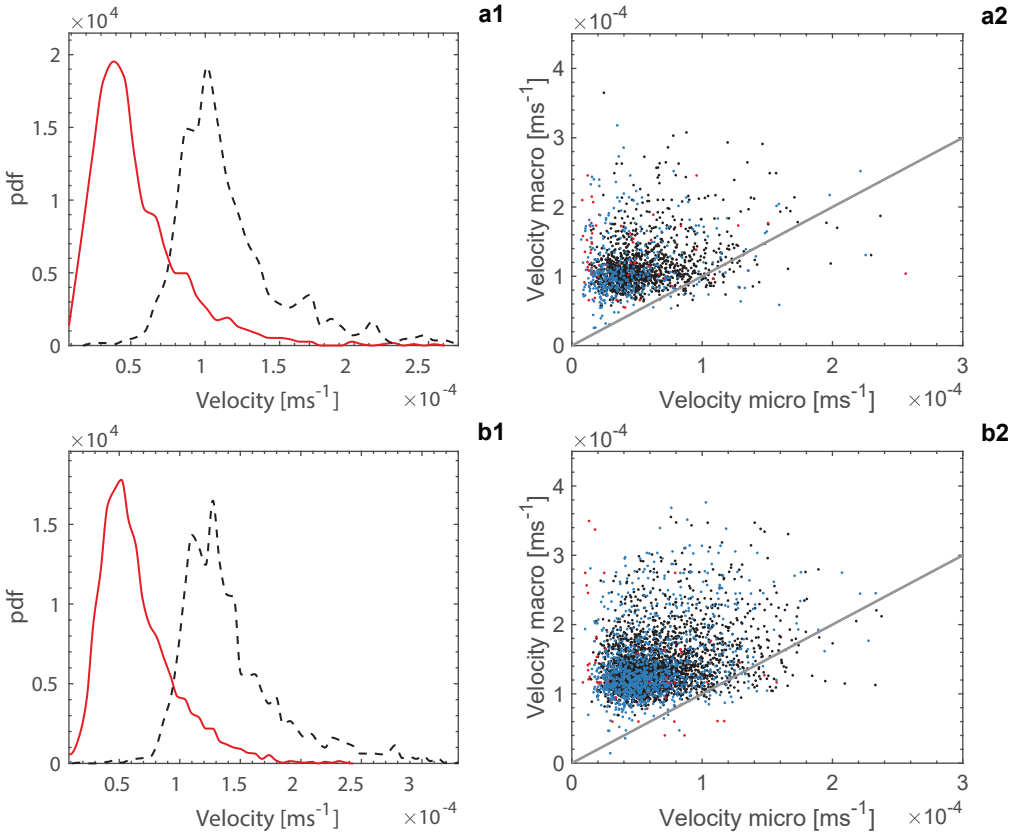

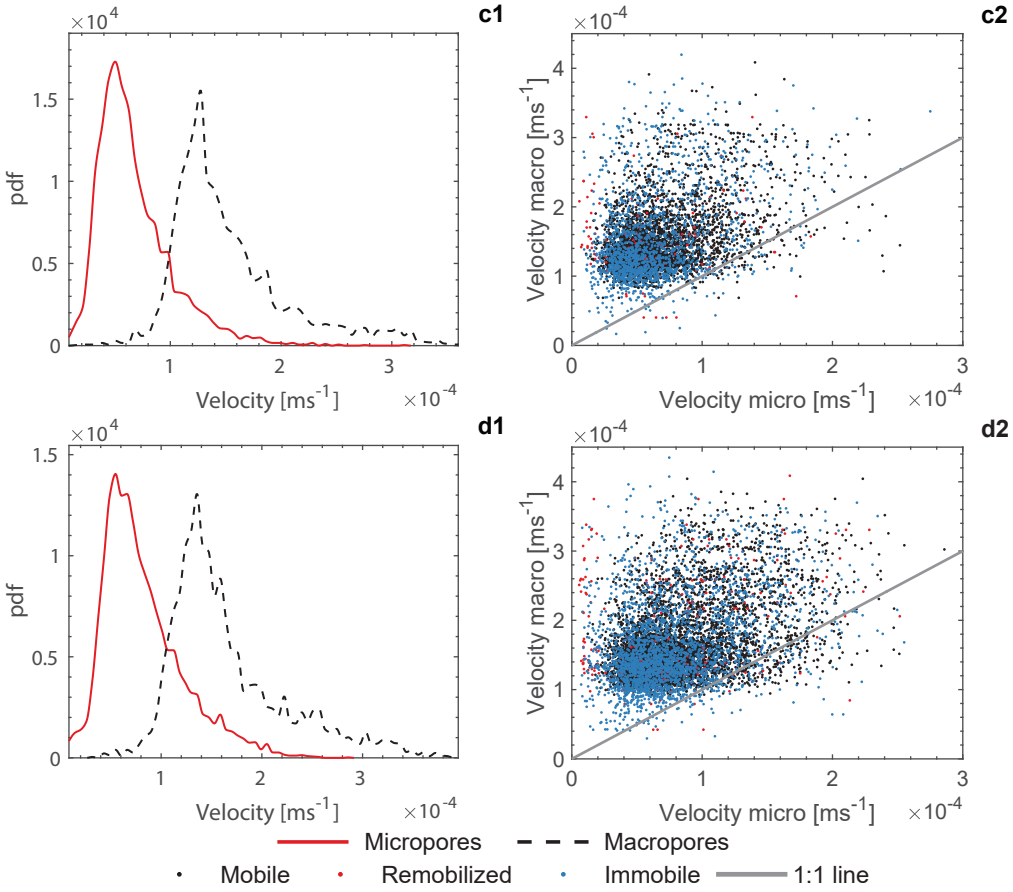

Figure 5.9. Average velocity distributions of colloids (1) moving inside the aggregate micropores (intra-aggregate) and within the macropores (inter-aggregate), and corresponding scatter plots for the a) S40/25, b) S40/50, c) S40/75, and d) S40/100 samples. The average flow velocity was 12 m day^{-1} for all samples.

Residence time in the aggregates. Figure 5.10 shows the average colloid transport velocity against the fraction of time spend by a colloid inside aggregates. Our data show that most colloids spend less than half of their transport time inside aggregates, and that higher fractions of aggregates leads to more time during which a colloid remains inside the aggregates. In general, more time spent inside the intra-aggregate pores leads to a lower average velocity, with this correlation being especially visible for Samples S40/75 and 100.

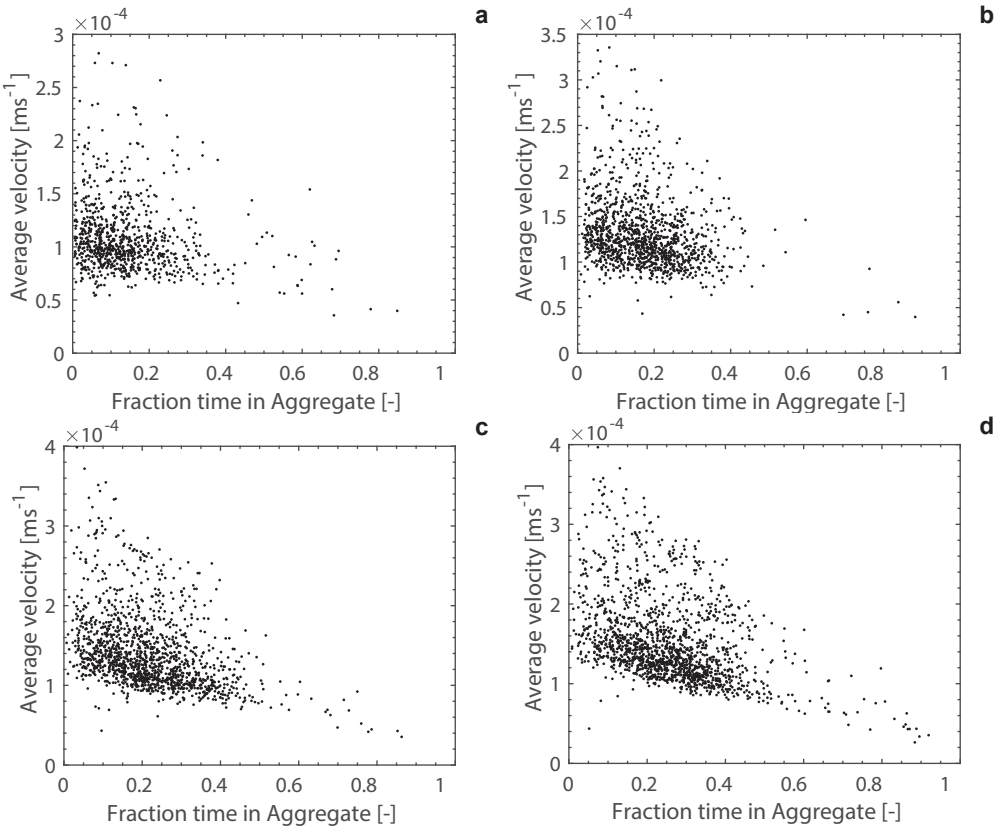

Figure 5.10. Average colloid transport velocity against fraction of time spent in the aggregate micropores. a) S40/25, b) S40/50, c) S40/75, and d) S40/100. The average flow velocity was 12 m day^{-1} for all samples.

Individual behavior of colloids. In this section, we discuss the behavior and trajectories of several individual colloids to show how colloids that are initially in the vicinity of each other may behave differently as they flow through the pore network. Figure 5.11 shows the trajectories of three colloids that entered the micromodel at locations close to each other, together with their corresponding flow velocities against the longitudinal distance. While the three colloids showed similar trajectories because of they entered the sample at approximately the same location, colloid 1 moved mainly through the inter-aggregate pores and entered/existed four aggregates during its transport through the microdomain. Colloid 2 moved through the macropores without any hindrance. By comparison, colloid 3 followed a more complex path, initially transported through the macropores, next through an aggregate, subsequently again through the larger inter-aggregate pores, and then finally moved into an aggregate where the colloid became attached at a micro-grain surface. Of

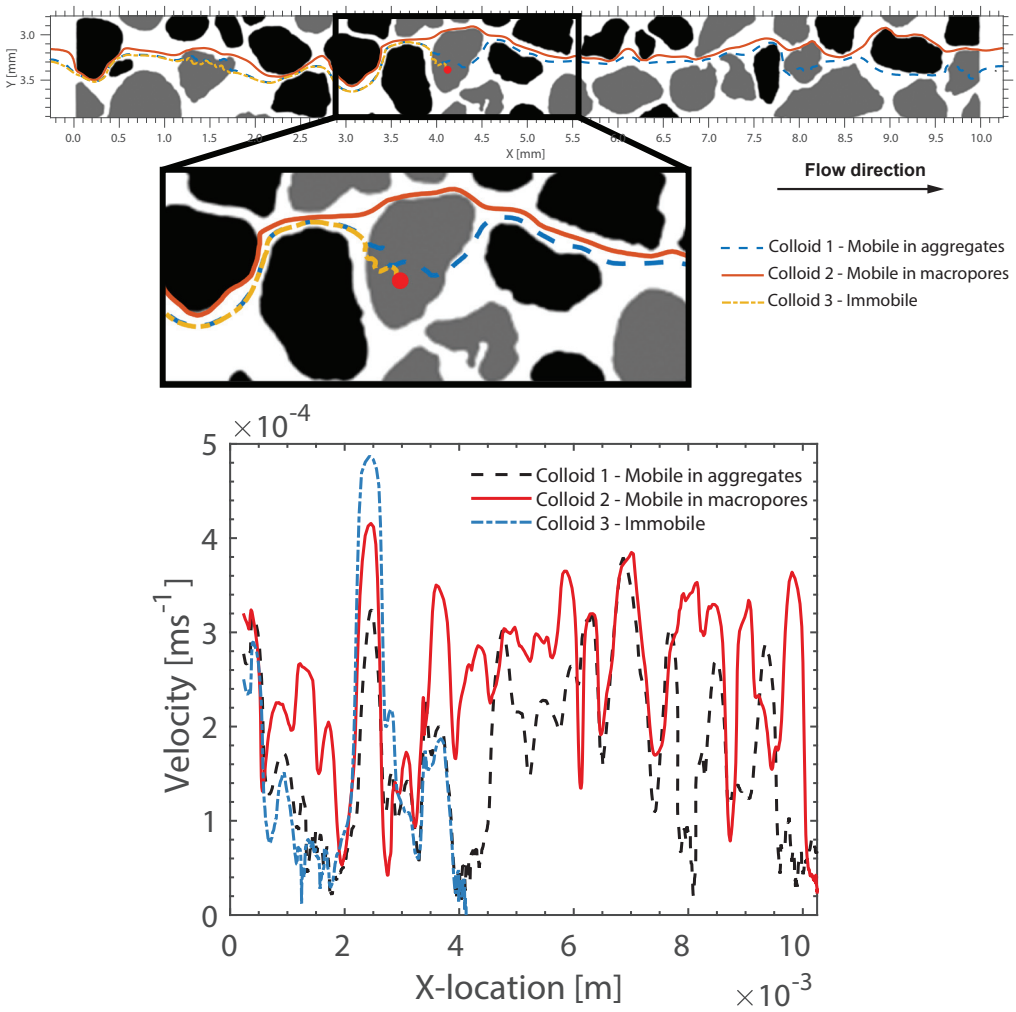

Figure 5.11. Different transport trajectories of three colloids which entered the flow domain close to each other: a) colloid 1 moving through aggregate micropores, with colloid 2 showing unimpeded transport through the macropores, and colloid 3 subject to attachment in an aggregate. Solid grains are shown in black and aggregates in gray, b) local colloid velocities against the longitudinal direction along their flow path.

the three colloids, the highest flow velocity was reached by colloid 3 just after re-entering the macropore domain from the first aggregate it went through. Remarkably, the same colloid also showed the lowest velocity among the three colloids. When the colloids entered the aggregates a significant reduction in their velocities occurred (also shown in Figure 5.9). Major velocity declines also occurred in the macropore trajectories when colloids moved close to the solid grains, although the extent of these velocity reductions

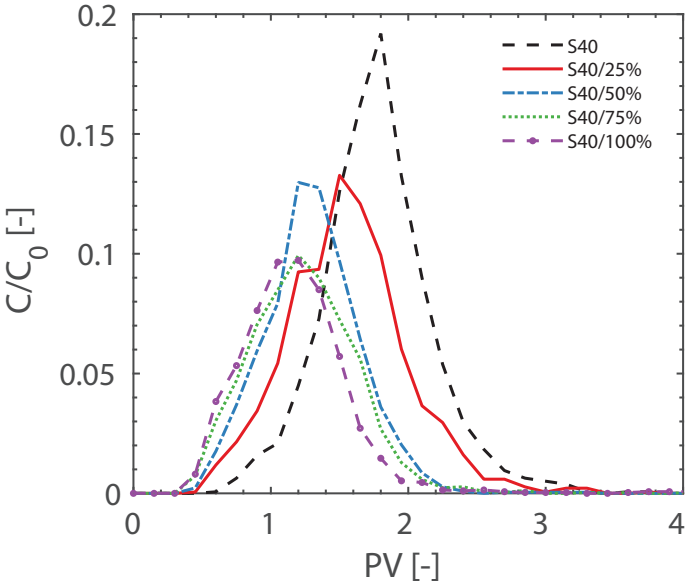

Figure 5.12. Colloid breakthrough curves of the different samples. The average flow velocity was 12 m day^{-1} for all samples.

were much smaller compared to those colloid velocities inside the aggregate pores. The reductions in velocity, together with the increased specific surface area of the micro-grains inside the aggregates, did favor colloid attachment. Since surface chemistries were similar throughout the entire domain, local surface roughness and lower hydrodynamic forces due to the low flow velocities contributed to colloid attachment.

Colloid breakthrough curves. Figure 5.12 shows the colloid breakthrough curves (BTCs) of the different samples. As explained before, the arrival time of each colloid was normalized to the time of their entry into the sample, leading to an equivalent Dirac delta input function for the colloids. The results show that arrival times decreased with higher intra-aggregate pore fractions. Additionally, the peak concentration of the more aggregated samples decreased due to the increased attachment of colloids within the samples. As the micro-porosity increases, and hence then also the inter-link between the intra-aggregate pores, preferential transport becomes dominant, leading to early breakthrough. Due to the low remobilization rate, no long tails were observed within the domain. Changing the solution chemistry (e.g., ionic strength or pH) or flow conditions within the system can lead to remobilization of the attached colloids and extensive tailing. Parameters including the size of the aggregates, the interconnectivity among intra-aggregate pores, and the aggregates pore size distribution, are among factors that impact the spreading of the BTCs.

5.2.2. Flow velocity effect

To explore the effect of flow velocity, several experiments were performed with sample S40/50 using different applied velocities (i.e., 1.0, 5.0, 12.0, and 20.0 m day^{-1}). Results were analyzed, again in terms of their categorization in transport behavior. Results are given in Table 5.4, and graphically visualized in Figure 5.13.

For the lowest velocity, a total of 1466 colloids were transported, and for the higher velocities 2053, 2250, and 2513 colloids (Table 5.4). While in each experiment 5 PV of a solution with colloids was injected, we observe a reduction in the detected mass among experiments. A possible effect can be that for the lower input velocities some of the colloids were attached in the inlet tubing system or in the inlet system of the micromodel itself. However, since we imaged the whole micromodel, the exact (although different) amounts of entering colloids were known as listed in Table 5.4.

For the flow velocities of 1.0 and 5.0 m day^{-1} the fraction of colloids transported through the macropores were 0.247 and 0.255, respectively. At the higher applied velocities, the corresponding values were lower (0.135 and 0.167, respectively). These data show that at lower velocities the main macropore flow paths are preferred, while colloids at the higher velocities are more likely to enter the intra-aggregate pores. This result was confirmed by the colloid fractions that entered at least one aggregate, which were equal to 0.389, and 0.468 at the lower velocities and 0.556 and 0.530 for the higher velocities. The main difference between the two low velocities was the high number of remobilization events at 1.0 m day^{-1}, which occurred mostly inside aggregates. Reducing the flow rate from 12.0 and 20.0 m day^{-1} to 5.0 m day^{-1} caused an increase of 50% in the remobilization events, while three times as many remobilization events were found at 1.0 m day^{-1} than at 20.0 m day^{-1}. At the very low flow rates, it is much harder to detect which colloids were subject to movement, rolling, or attachment. This because of minimal or no colloid displacement within the detection time frames, which we tried to correct by recording at a lower frame rate. Nevertheless, we expected a few false positives, although we could see an increase in the average transport time to about 300 seconds (shown later in Figure 5.17). The highest fraction of attachment of colloids was found for 1.0 m day^{-1}, while the lowest fraction was for 5.0 m day^{-1}. For the high velocities, we did find an almost equal fraction (~0.30) of attached colloids.

Bai et al. (2018) attributed a high attachment rate at low input velocities due to better accessibility of the colloids into the immobile phase. While for the lowest velocity a larger number of colloids moved only through the inter-aggregate pores, where attachment is less, the highest overall attachment occurred in the aggregates. This shows that the intra-

Table 5.4. Number and mass fraction of colloids transported in sample S40/50 at different velocities, as categorized according to their transport behavior.

		Mobile in macropores		Remobilized		Immobile		Mobile in aggregates	
Velocity [m day^{-1}]	**Total colloid trajectories**	**Number of colloids**	**Mass fraction**	**Number of colloids**	**Mass fraction**	**Number of colloids**	**Mass fraction**	**Number of colloids**	**Mass fraction**
1.0	1466	362	0.247	180	0.123	512	0.349	571	0.389
5.0	2053	523	0.255	80	0.040	564	0.275	960	0.468
12.0	2250	303	0.135	49	0.022	693	0.308	1250	0.556
20.0	2513	427	0.167	56	0.022	751	0.299	1333	0.530

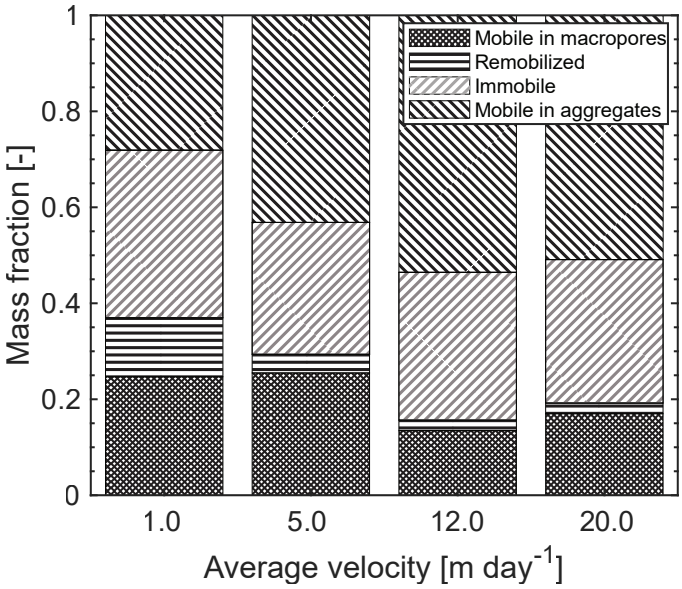

Figure 5.13. Effect of flow rate on the mass fractions of colloids in S40/50 at flow rates of 1.0, 5.0, 12.0, and 20.0 m day^{-1}. The mass fractions were categorized in terms of the four colloid transport groups.

aggregate pores played a vital role in the attachment of colloids and their associated pore velocities.

Penetration depth of the adsorbed mass. Figure 5.14 shows the mean penetration depths (calculated using the spatial coordinates of all attached particles) against pore volume for different input velocities used for Sample S40/50. Steady-state conditions were reached after about 1.8 PV for all samples. The mean penetration depth was approximately 5×10^{-3}m, with slight differences among the different velocities due to colloid attachments

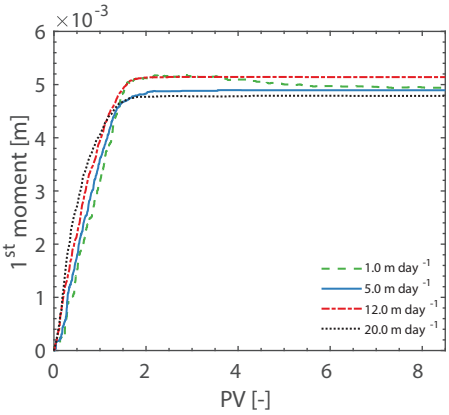

Figure 5.14. Values of the 1st moment of the penetration depth of the attached colloids (i.e., the distributed attached mass) against pore volume for sample S40/50 at flow rates of 1.0, 5.0, 12.0, and 20.0 m day^{-1}.

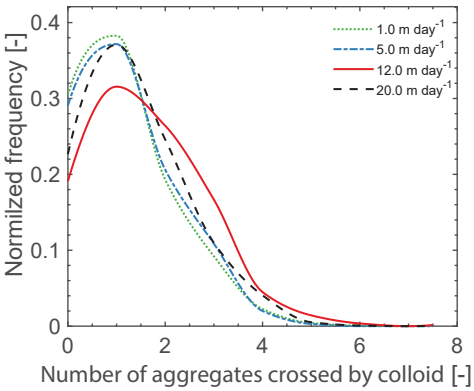

Figure 5.15. Frequency of colloids that crossed an aggregate. The figure shows how many times a colloid entered and exited an aggregate of sample S40/50 at flow rates of 1.0, 5.0, 12.0, and 20.0 m day^{-1}.

in especially the aggregates. However, variations occurred before reaching the steady-state conditions. For example, at 20.0 m day^{-1} more attachment occurred farther away from the inlet, while at 1.0 m day^{-1} attachment began at the beginning of the domain and then spread more gradually over the domain. The end states of the attached colloids are given in Appendix D.

Frequency appearance in aggregates. The frequencies of colloid transport across intra-aggregate pores are shown in Figure 5.15. The distributions were quite similar for the different velocities. For all velocities, most colloids passed through only one aggregate, with the velocity of 12.0 m day^{-1} showing a slightly higher frequency at 3 aggregates. The results in Figure 5.15 indicate that frequency of transport across aggregates is dominated mostly by pore structure and to a lesser extent by the applied flow velocity.

Tortuosity of colloid transport paths. Figure 5.16 shows the average tortuosity values of the colloid trajectories, also categorized based on colloid transport behavior. Individual colloid trajectories are provided in Appendix D. While having considerable similarities among colloid trajectories in macropores, we observed paths that were followed only at the lower velocities, but were inaccessible at higher velocities. This caused variations in the observed tortuosity between the different experiments. At higher velocities, colloids penetrated more aggregates relative to transport at low velocities (Figure 5.13) to lead to a straighter path from the inlet towards the outlet, and hence lower tortuosity values. At lower velocities, the colloid transport paths were more often through the inter-aggregate

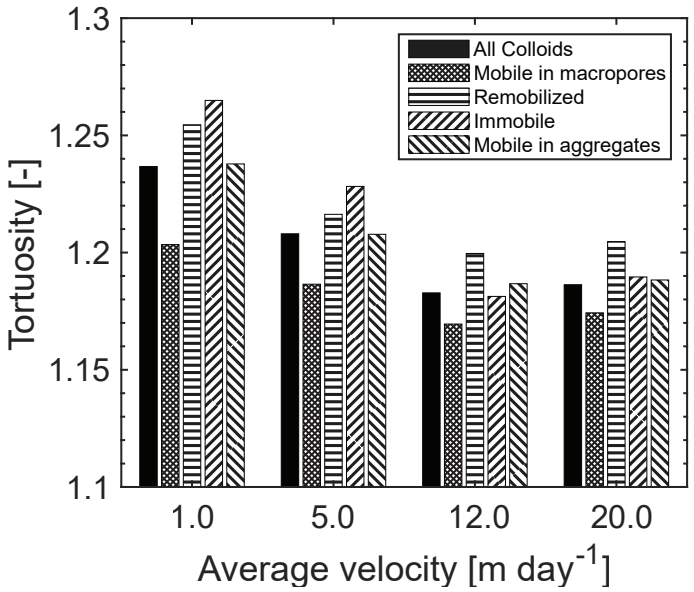

Figure 5.16. Average tortuosity of colloid transport paths at different applied velocities, categorized based on colloid transport behavior.

pores (the flow paths are given in Appendix D). Colloid attachment and remobilization mainly occurred inside the intra-aggregate pores. Hence, while the appearance frequency distributions of the various experiments were similar, observed tortuosity values did showed some differences. For 12.0 and 20.0 m day^{-1} we did not find major differences, which suggests that a velocity threshold may exist after which the tortuosity does not depend any more on velocity. This needs to be investigated further by performing experiments at a wider range of velocities. We did see that for all flow rates the remobilized colloids always had higher tortuosity values than the aggregate tortuosity. This indicates that the remobilized colloids followed a more tortuous path, presumably closer to the grain surfaces, thereby increasing the chance for a colloid to become attached or remobilized. For the flow rates of 1.0, and 5.0 m day^{-1} this was also observed for the attached colloids, while for the higher velocities the attached colloids followed the tortuosity of the colloids in the aggregates.

Colloid residence time. Figure 5.17 shows time durations during which the different colloid categories remained in the samples. Mean and standard deviation values as normalized in terms of pore volume are given in Table 5.5. All experiments (using different velocities) show a slight shift in travel time between the colloids passing through macropores and those passing through the aggregates, with the remobilized colloids

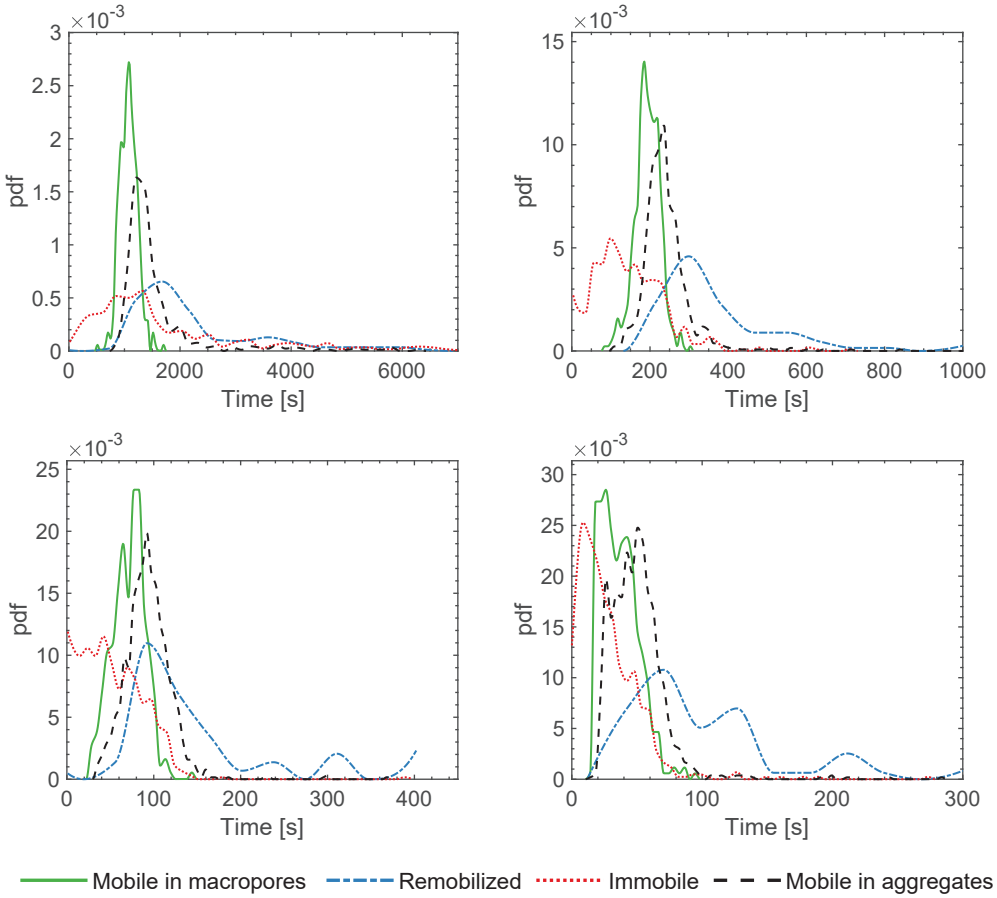

Figure 5.17. Probability density functions (pdfs) of the colloid transport time through sample S40/50 subjected to flow velocities of a) 1.0, b) 5.0, c) 12.0, and d) 20.0 m day^{-1}. The colloids were indexed based on their transport category. For the attached colloids, the distribution shows time durations up to their attachment.

Table 5.5. Average time, normalized in terms of pore volume, spent in sample S40/50 at multiple applied average velocities (values in brackets provide the standard deviations).

velocity [m day^{-1}]	Mobile in macropores	Remobilized	Immobile	Mobile in aggregates
1.0	1.24 (0.18)	2.58 (1.33)	2.06 (1.73)	1.82 (0.92)
5.0	1.12 (0.18)	2.10 (0.90)	0.86 (0.54)	1.40 (0.41)
12.0	0.99 (0.26)	2.02 (0.95)	0.74 (0.50)	1.30 (0.39)
20.0	0.85 (0.33)	2.34 (1.28)	0.65 (0.56)	1.16 (0.50)

showing approximately two times longer travel times compared to transport in the macropores. The attached colloids showed generally a lower travel time (compared to transport in macropores) of around 0.2 PV. An exception occurred at a velocity of 1.0 m day^{-1} for which where we observed an average travel time of as high as 2.06 PV before attachment, which is an increase of 0.82 PV compared to the mobile colloids in the macropores. Direct visualizations showed that this behavior was due to rolling of colloids along solid surfaces for longer times (which was not observed at the higher velocities). These colloids also had higher tortuosity values as shown in Figure 5.16. Different applied velocities provided distinct differences in travel times of colloids in the inter-aggregate pores as shown by the decreasing PV values of 1.24, 1.12. 0.99, and 0.85 with increasing the applied velocities, respectively. These results show that at 1.0 m day^{-1} colloids were transported for a longer time (the equivalent to 0.24 PV) than the calculated average pore water velocity, while for a velocity of 20 m day^{-1} the colloids moved more rapidly, on average by 0.15 PV (mainly due size exclusion effects, either exclusion from smaller pores or more tortuous flow paths), leading to lower tortuosities and lower travel times. Note that for non-reacting tracer solutes one would expect no difference in arrival time, while with colloids of 4 µm we observed a clear reduction in the arrival time with increasing flow velocity.

Flow velocities the in micro-and macropores. Figure 5.18 shows the velocity distributions of colloids transported at least through one aggregate, along with the scatter plots of the velocities in the inter-aggregate and intra-aggregate pores. Velocities were determined based on their transport through the inter-aggregate and intra-aggregate pores. Our results show that at an applied velocity of 12.0 and 20.0 m day^{-1} a more skewed distribution was present at at the higher velocities, which is consistent with the observed decrease in tortuosity and lower transport times of mobile colloids in the aggregates.

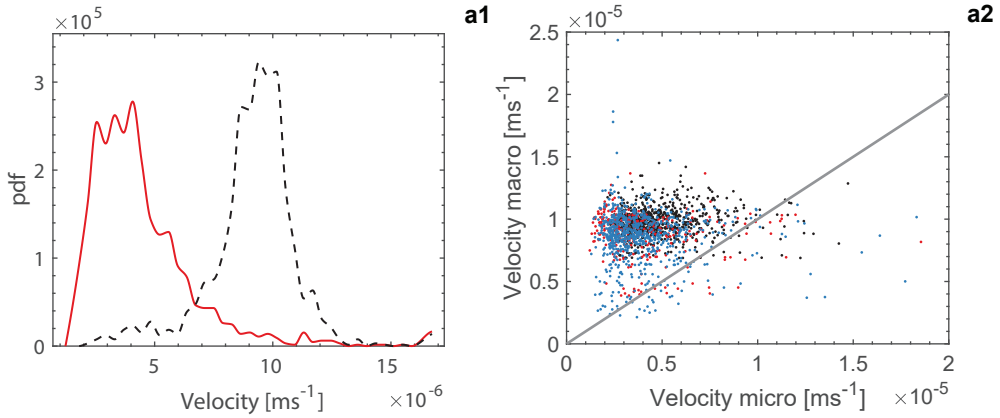

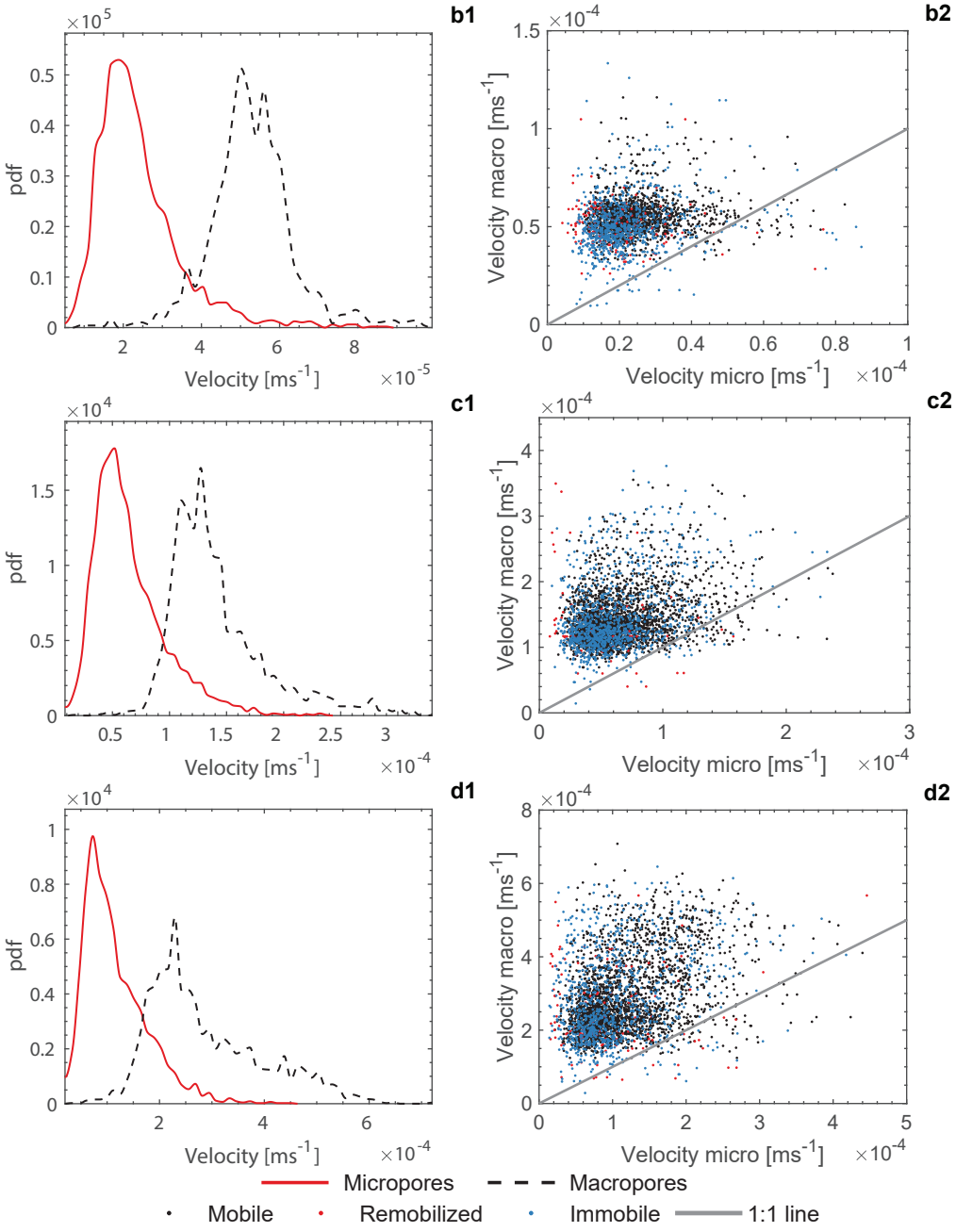

Figure 5.18. Probability density functions of the average velocity (1) for colloids flowing inside the intra-aggregate (micropore) and the interaggregate (macropore) flow domains, and the corresponding scatter plots (2) for a) 1.0, b) 5.0, c) 12.0, and d) 20.0 m day^{-1}.

Less scattering in the macropore against micropore velocities was observed at 1.0 m day^{-1} indicating that colloids entering aggregates had a similar transport trajectory. With increasing velocity more scattering occurred, indicating that at higher velocities colloids with a wider range of trajectories may enter an aggregate as seen in also Figure 5.13 (mass fractions) and Figure 5.14 (frequency appearance).

Residence times in the aggregates. To explore the effects of aggregation on colloid transport, we calculated the fraction of time that each colloid stayed within an aggregate pore network. as well as its average transport velocity. The results in Figure 5.19 show that at a velocity of 1.0 m day^{-1} more colloids have relatively long residence times, with the colloid transport velocity decreasing with increased fraction of time resided within the intra-aggregate pores. We observed exceptions to this general trend. For example, a small group of colloids with a relatively a low flow velocity also showed shorter transport time in the aggregates. At velocities of 12.0, and 20.0 m day^{-1} fewer colloids spent time inside

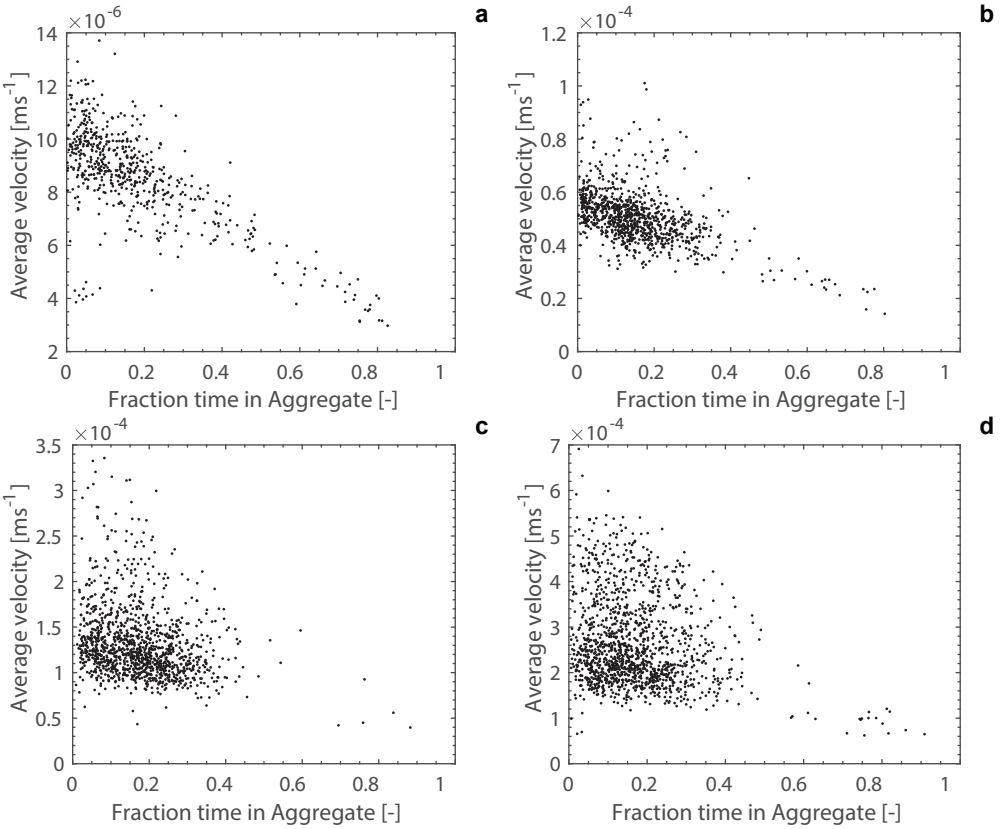

Figure 5.19. Average colloid velocity against fraction of total time spent in aggregates for sample S40/50 at flow rates of a) 1.0, b) 5.0, c) 12.0, and d) 20.0 m day^{-1}.

the aggregate pore spaces, with more spreading in the observed average colloid velocities in the aggregates. This corresponds with our observations that a larger fraction of colloids accesses the intra-aggregate pores, but it became less predictable if a colloid had entered an aggregate or not at high velocities. By comparison, at lower input velocities a correlation existed with the fraction of residence time and average velocity of the trajectory.

Colloid breakthrough curve. Figure 5.20 shows the concentration BTCs for colloid transport in sample S40/50 at four different applied flow velocities. Increasing velocities caused earlier arrival times of the colloids. This was expected due to the lower observed normalized residence times (Table 5.5) as well as in view of lower tortuosities (as shown in Figure 5.16) at the higher flow velocities. The measurements show that the highest peak concentration occurred for the velocity of 5.0 m day^{-1}, and the lowest peak concentration for a velocity of 20.0 m day^{-1}. In our experiments and based on our method to construct the BTCs, we obtained higher concentrations when attachment was low, movement through the macropores is higher, and less movement occurred through the aggregates, leading to a less spreading in the colloid transport residence times. For the experiment at 5.0 m day^{-1}, a high fraction for the colloids moved through the macropores, with relatively low fractions of remobilization, transport in aggregate pores, and colloid attachment (Table 5.4). Furthermore, for the applied velocity of 1.0 m day^{-1}, we observed a low fraction for

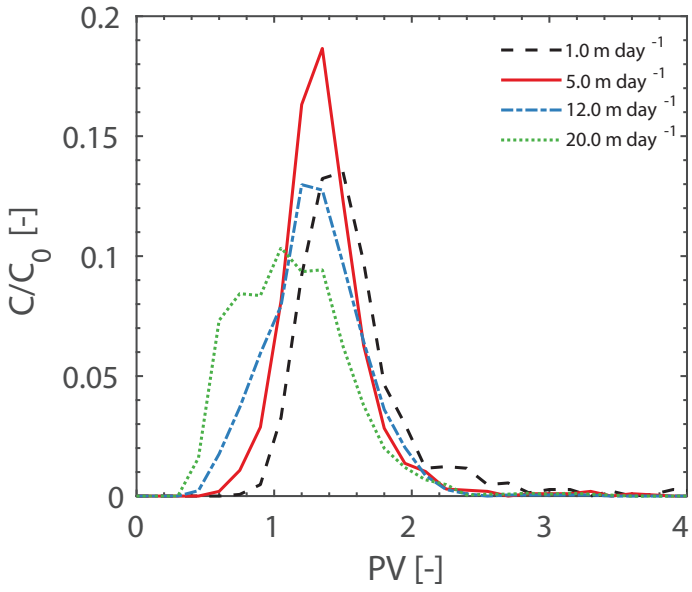

Figure 5.20. Colloid breakthrough for sample S40/50 at flow rates of 1.0, 5.0, 12.0, and 20.0 m day^{-1}.

transport through the aggregate pores, although this behavior was combined with a high fraction of remobilized colloids leading to more spreading in the transport times and lower peak concentrations. Significant BTC tailing occurred at an applied velocity of 1.0 m day^{-1}, while tailing was minimal for other applied velocities. Direct visualization showed that the key process behind tailing at 1.0 m day^{-1} was colloid remobilization which did lead to a high increase (1.34 PV) in residence time compared to colloid transport through the macropores. We also observed an increase in residence time (0.58 PV) for colloid transport in the aggregates, while for the remaining experiments the delay was only approximately 0.30 PV.

The obtained pore-scale information involving different levels of aggregations and applied flow velocities showed much insight in the observed BTCs, and help to explain observed colloid transport processes in other systems such column setups and field-scale experiments.

5.3. Conclusions

The subsurface environment often contains aggregates and porous grains that impact the flow of fluids and the transport of solutes and colloids. In this study, we performed a detailed and systematic study to explore colloid transport processes in several aggregate samples with increasing fractions of aggregate micropores. Novel visualization techniques were applied in the experiments to obtain near-continuous observations of the transport of colloids across the whole domain, including both the macropores and micropores.

Results have shown that aggregates were responsible to up to 40 of the retention of colloids due to transport within the micropore domains. Unique data about the complete trajectories of individual colloids across the entire domain allowed us to focus on the underlying processes contributing to this colloid transport, as well as explaining different pore-scale processes there are behind the observed (integrated) BTCs collected at the outlet of the sample. Integrated BTCs are the common form of data collected when using column and field-scale experiments.

Our direct observations have shown that in presence of intra-aggregate pores a considerable fraction of colloids was transported through the micropores. Upon entrance, transport of colloids in the micropores is affected by the lower flow velocity and prevailing hydrodynamic forces due to the smaller pore sizes. The aggregates also have higher chances of attachment due to increased interactions with their larger surface areas compared to the remainder of the sample (i.e., the macropore spaces). These factors contributed to increased retention of colloids inside the medium, even under unfavorable attachment conditions, and show the importance of the subsurface soil aggregates.

Further research. This study considered the transport, attachment and remobilization of colloids under fully saturated flow conditions. Similar experiments are needed during unsaturated (or two-phase air-water) flow to be more realistic for colloid transport in the vadose zone subject to time-dependent soil surface weather conditions and fluctuating water tables. Future research should also explore the effects of wider pore sizes of the intra-aggregate and interaggregate pores (including those of fractured rock), and transient geochemical conditions.

Chapter 6

Two-phase Flow Drainage and Imbibition Cycles in Dual-Porosity Samples

Role of Micro-Porosity and moving Interfaces on the Retention and Remobilization of Colloids

Abstract

Phase interfaces have shown significant impacts on colloid transport in the vadose zone. This is through drainage and imbibition cycles caused by processes such as rainfall events and irrigation. These events cause interface movements and can contribute to the remobilization of colloids. In this study, we consider a dual-porosity micromodel to represent an aggregated soil. We have observed and measured colloid transport by imaging colloid trajectories and changes in fluid distribution due to two-phase flow and saturation changes. We performed drainage and imbibition cycles after colloids were attached during saturated flow conditions. Our direct observations have shown that colloids were mainly attached in the intra-aggregate pores due to the small pore sizes compared to the inter-aggregate pores. To provide details, we have focused and zoomed into two regions of the micromodel to investigate the remobilization processes during the drainage and imbibition cycle. We have observed colloid remobilization and deposition due to both bulk fluid flows as well as direct contact with interfaces. We have found that bulk fluid flow is the main contributor to remobilization in our experiments. The aggregates have a major impact on the fluid distributions after primary drainage due to the residual saturation within aggregates leading to be the main connectors of fluid during imbibition. Therefore, the aggregates are of great interest due to their influence on flow and transport.

6.1. Introduction

Transport of colloids in the vadose zone is affected by the presence and dynamics of air-water interfaces which may remobilize colloids and facilitate their transport into the deeper sections of the soil and into the groundwater. Rainfall events (Mohanty et al., 2015), irrigation, leaching of pesticides and fertilizers, as well human activities like waste disposal, groundwater pumping, and artificial recharge (Ryan and Elimelech, 1996) cause transient changes in the subsurface flow dynamics as well as the chemical composition of the porewater (Kretzschmar et al., 1999). The known factors affecting colloid retention and mobilization include ionic strength (Mitropoulou et al., 2013), pH (Roy and Dzombak, 1997), colloid properties (Aramrak et al., 2013; Chatterjee and Flury, 2013; Zhang et al., 2014), soil properties (roughness, chemical heterogeneity) (Mitropoulou et al., 2013; Argent et al., 2015; Bradford, Torkzaban, et al., 2015), flow patterns (Bradford and Torkzaban, 2015), flow rate (Knappenberger et al., 2014; Zhang et al., 2015), and colloid concentration (Wang et al., 2012).

In the vadose zone section of soil, under the steady-state condition, the air-water interface repels colloids as both include negatively charged surfaces. However, the solid-air-water contact line can lead to retention due to capillary forces (Flury and Aramrak, 2017). Under transient conditions, the (volumetric) magnitude of phase saturations, as well as movement of air-water interfaces, have major controls on colloid remobilization. The underlying mechanisms are capillary forces and hydrodynamic forces which can succeed the DLVO forces (Sang et al., 2013; Knappenberger et al., 2014; Zhang et al., 2014). At the scale of single pores (i.e., excluding pore connectivity effects), studies have used single channel and pore slit experiments and provided insight into the effect of receding and advancing air-water interfaces (Sharma et al., 2008; Aramrak et al., 2011; Lazouskaya et al., 2011, 2013). To incorporate the effect of pore connectivity, micromodel experiments have been done to incorporate a large number of pores and to explore colloid transport under different saturation levels and removal of colloids by phase interfaces (Zhang et al., 2013). This study however had a limitation of observing only a few pores of the sample in a single image. Very often micromodel experiments of porous samples do not consider moving air-water interfaces in the whole micromodel flow field due to lack of field of view and the required imaging focus. Furthermore, commonly idealized pore shapes were used which does not incorporate the true complexity of porous media like tortuous pore structures and dual-porosity effects.

Several processes contribute to the heterogeneity of soils in the unsaturated zone. They include earthworm activities, plant root degradation, creation of cracks, fissures, and

presence of aggregates (Genuchten, 1985; Martinez et al., 2015). Such soils may show a bi-modal pore size distribution consisting of larger macropores (inter-aggregate pores) and smaller micropores within the aggregates (intra-aggregate pores). The macropores promote preferential flow (Schelde et al., 2002) and may cause size exclusion effect (Kretzschmar et al., 1999; Bradford and Torkzaban, 2008; Bai et al., 2018) where colloids surpass the smaller pores and show early breakthrough curves compared to the behavior of non-absorbing solutes.

In this study, we consider aggregated soils with bi-modal pore size distribution and explore drainage and imbibition cycles. The immiscible fluids used in this study include water and Fluorinert and attachment conditions can be described as unfavorable in the presence of low ionic strength ($<10^{-3}$) and negatively charged medium and colloids. Fluorinert was chosen to provide more accurate observation since an air-water system provides difficulties in control imaging, measurement of the processes due to large reflectance of interfaces, the compressibility of air, and its dissolution in water and in microfluidic materials. To generate the desired two-phase cycles a series of boundary conditions are applied. First, water-saturated conditions are provided to let colloids deposition at the surfaces. Next, a drainage experiment followed by imbibition is performed. This step is repeated for a second time to provide two cycles of drainage and imbibition. A micromodel of size 10×10 mm is used and an optic setup is designed to image the whole pore space domain at once at a rate of 10 frames per second. A major advantage of this setup is that it allows us to track the full trajectory of colloids in real-time and also enables us to observe and record the rather infrequent colloid transport and remobilization processes which may not be captured when only imaging one or few single pores of the domain. As in Chapter 3 colloids mainly attach inside of the aggregates due to the lower flow velocities associated with the smaller intra-aggregate pores. We will focus on how the moving interfaces influence the previously attached colloids retained inside the aggregate pore spaces.

6.2. Experimental approach

Micromodel. A micromodel was designed using real pore geometries obtained from x-ray tomography imaging. To obtain systematic dual-porosity domains (i.e., several domains with varying aggregate fractions) a numerical algorithm is developed to replace and substitute some of the solid grains with aggregates each having a large number of micro grains, and, therefore, micropore sizes with much smaller sizes (intra-aggregate pores) compared to the macropore space (inter-aggregate pores). This complete process of designing and production of the micromodels is described in Chapter 3. The domain utilized in this experiment has 50% of its grains replace with aggregates with micropores.

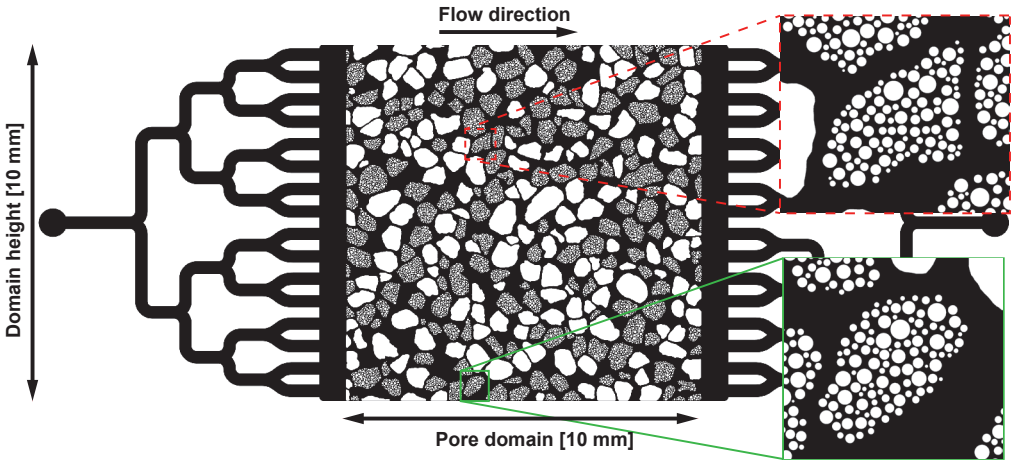

Figure 6.1. Micromodel pore network (i.e., microfluidic mask) including inlet and outlet structures. The red zoom-in section shows the region of interest 1 (A1), and the green color shows the region of interest 2 (A2).

This sample is referred to as S40/50. The total porosity of the domain is 0.55, whereof 27% is intra-aggregate porosity. In the larger (inter-aggregate) portion of the domain, the average pore body radius is 107.1 μm and the average pore throat radius is 70.1 μm. For the smaller (intra-aggregate) pores, these values are equal to 10.8 μm and 8.3 μm, respectively. Figure 6.1 shows the micromodel pore structure as well as the zoom-in sections for two regions of the domain which are discussed in detail to explore colloid remobilization.

Experimental set-up. The details of the base set-up were described in Chapter 2. Adjustments were made to enable detecting two species of fluorophore, a fluorescein-water solution which has an excitation wavelength of 460 nm and emission wavelength of 515 nm, and a fluorescent colloid-water solution. The colloids have a size of 4 μm (FluoSpheres F8858, Thermo Fischer), and have a peak excitation wavelength of 580 nm and a peak emission wavelength at 605 nm. We have used a 470 nm collimated light LED (Thorlabs M470L3) with a short pass filter of 500 nm to excite the fluorescein-water solution. The colloid-water solution is excited using two 595 nm LED's (Thorlabs M595) with band-pass filters of 580 ± 10 nm. During the experiment, the light travels to a mirror and is reflected onto a lens and then the light moves on a longpass dichroic mirror of 550 nm (DMLP550R, Thorlabs). This process divides the wavelengths emitted by the fluorescein and the colloids into two separate cameras (Basler acA5472-17um). An Arduino Uno is used to trigger the cameras simultaneously and to capture images at 10 frames per second. The schematic of the set-up is given in Figure 6.2.

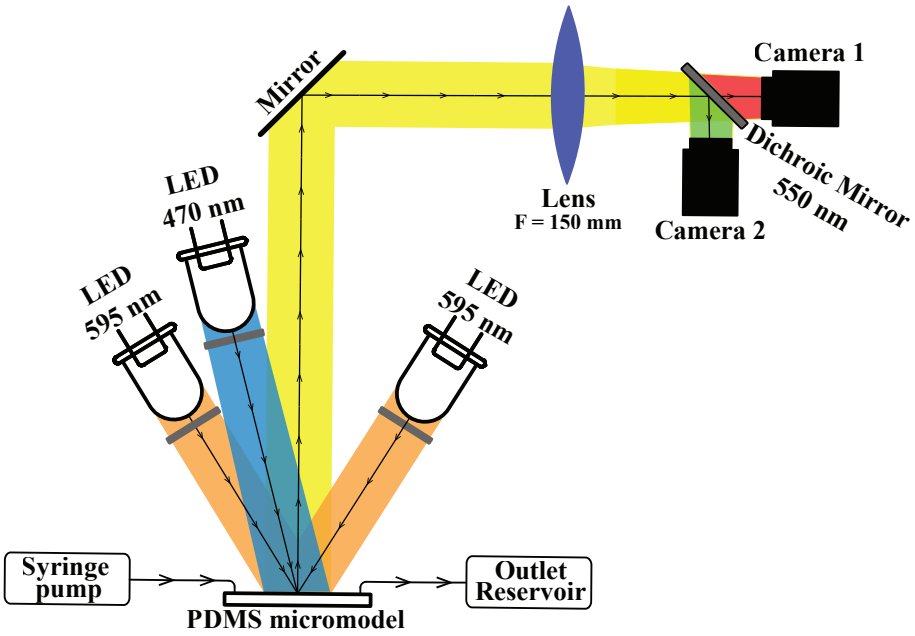

Figure 6.2. Schematic of the optic set-up. Two LEDs at 595 nm are used to excite the colloids, and a 470 nm LED is used to excite the fluorescein. The emitted light by the fluorophores is separated using a dichroic mirror and captured by two cameras. The flow is established by a syringe pump connected to the inlet of the PDMS micromodel and the outlet is connected to a reservoir.

Experimental procedure. First, the PDMS micromodel was silanized using an ethanol-silane solution to obtain uniform surface chemistry. Next, the micromodel was fully saturated by DI-water, by first introducing CO_2 into the pores and injecting water to displace the CO_2 and any residue is dissolved into the water (therefore a completely saturated pore structure was obtained). This process lowers solution pH. Therefore, a large amount of water (>50 pore volume, PV) was injected to bring pH back to its neutral value. At this stage, 7.5 PV of colloid-water solution (SW1) where colloids were dispersed in deionized water is injected using an average velocity of 5 m day^{-1} under a constant flow rate. The capillary number in our experiment has a magnitude of 9.98×10^{-7}. After colloid injection, 15 PV of clean water was injected (SW2), which was followed by injecting 2 PV of Fluorinert (F1) and then 2 PV of clean water (W1). The last two steps were repeated once more (F2, W2). The details are given in Table 6.1. Camera 2 recorded the fluid distribution inside the whole micromodel while camera 1 recorded the transport of colloids. To provide discussions, we will focus on 2 regions of interest (indicated by A1, A2 in Figure 6.1). The TrackMate algorithm (Tinevez et al., 2017) was used to trace colloids during various stages of the experiment.

Table 6.1. Stages of experiment and corresponding PV, volume injected, and time. All stages were injected at a constant velocity of 5.0 m day^{-1}.

Stage	Displacement	PV [-]	Volume [µL]	Time [m]
SW1	Saturated flow with colloids	7.5	8.175	21.6
SW2	Saturated flow without colloids	15.0	16.35	43.2
F1	Drainage without colloids	2.0	2.18	5.8
W1	Imbibition without colloids	2.0	2.18	5.8
F2	Drainage without colloids	2.0	2.18	5.8
W2	Imbibition without colloids	2.0	2.18	5.8
Cumulative	2 cycles	30.5	33.25	87.8

Phase Saturations. Water and Fluorinert saturation were determined from the images captured by camera 2. The images were binarized to calculate water saturation (S_w) and Fluorinert saturation (S_F) as follows:

$$S_F = \frac{\sum I_{255}}{\sum I_{255} + \sum I_0} \tag{6.1}$$

$$S_w = 1 - S_F \tag{6.2}$$

where I_0 represent the black pixels and I_{255} are the white pixels. The main flow paths were determined using colloid movements and fluorescein intensity. When fluorescein-water is stagnant the intensity decreases over time due to decay and intensity increases in the presence of fresh solution. This phenomenon was utilized to determine the main flow paths at stage W2, while at stage W1 the movement of colloids was utilized for determining the main flow paths. The recorded images can be also used to determine the amount of static and moving interfaces as well as curvature size, which is of importance for recently developed models (Zhang et al., 2012; Bradford, Wang, et al., 2015). However, to keep the focus of this study, these steps were not included.

6.3. Experimental results and analysis

After injecting colloids in a water-saturated micromodel, drainage and imbibition cycles were performed. In this process, a change in total saturation and in detail the distribution of phases inside the porous domain were measured. After stages SW1, and SW2 a total of ~692 colloids were retained within the sample. Colloids were predominantly retained within the aggregates, the locations are marked in Figure 6.3. Due to colloid retainment mainly occurred within the aggregates, we will focus on 2 regions of interest and investigate how the colloids behave during the drainage and imbibition cycles. Detail imaging has shown that although the PDMS micromodel is hydrophobic, after initially saturating the domain with water, Fluorinert (FC-43) became the non-wetting fluid. This is clearly visible when water imbibes the small pores and develops water films, pools, and bridges which are features that often the wetting fluid shows (Zhang et al., 2011). Pools are regions that fluid occupies multiple pores, and bridges are locations that water residue exists between pore throats.

Saturation. Figure 6.4 shows the fluid distribution inside the micromodels, together with the main flow paths (i.e., mobile water pathways) at the end of the imbibition stages. The corresponding saturation values, S_w and S_F, are provided in Table 6.2. The experiment began with a fully water-saturated domain (SW1, SW2). At the end of this stage, colloids were often attached in the intra-aggregate pores. Next, in stage F1 (Figure 6.4, plot F1), most of the water phase was displaced from the main pores (inter-aggregate pores) by

Table 6.2. Water and Fluorinert saturation at the different stages of the experiment.

Stage	S_w [-]	S_F [-]	S_{wA1} [-]	S_{wA2} [-]
SW1	1	0	1	1
SW2	1	0	1	1
F1	0.46	0.54	0.76	0.44
W1	0.59	0.41	0.79	0.60
F2	0.49	0.51	0.78	0.44
W2	0.52	0.48	0.79	0.42

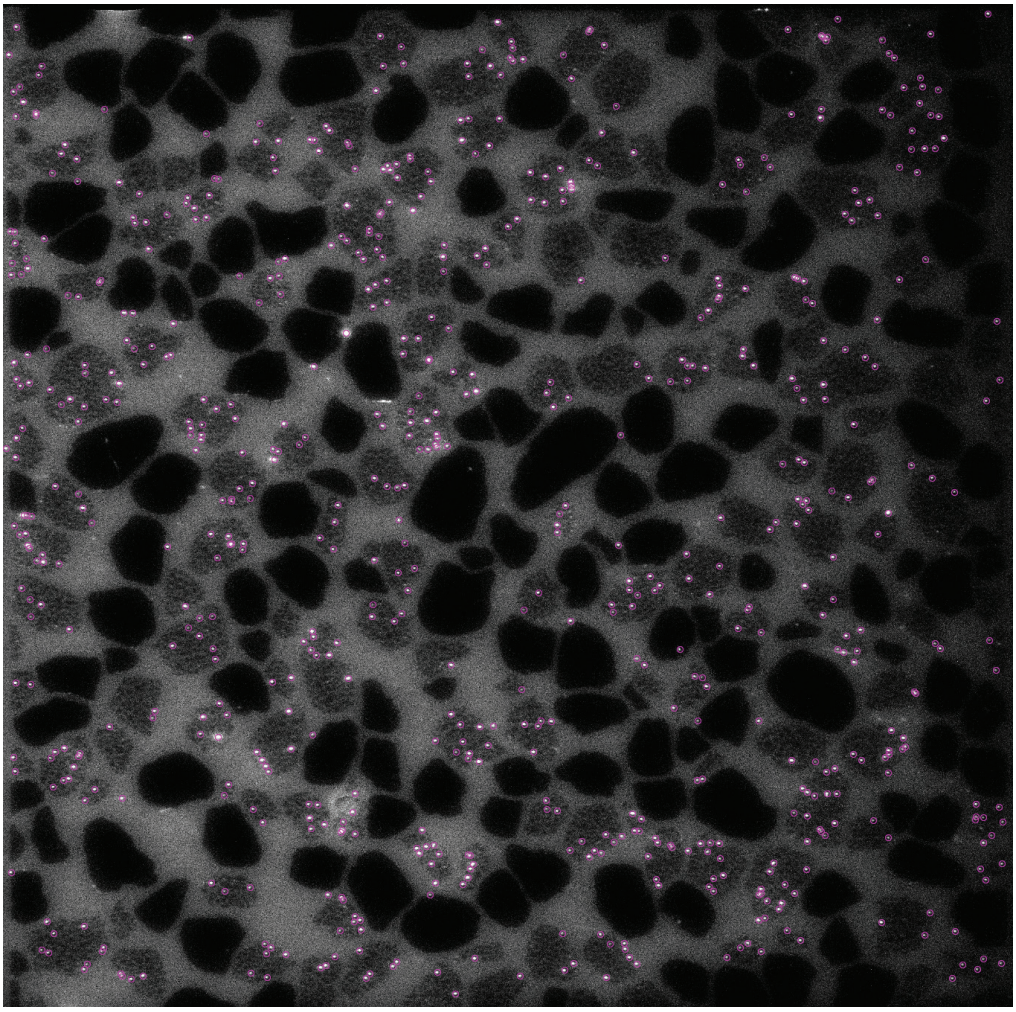

Figure 6.3. Locations of ~692 retained colloids after step CW1, and CW2. The original image is enhanced and the colloids are marked by circles. Black is the solid grains, white is the fluorescein-water solution, representing the macropore spaces, and the aggregates are a black/white combination due to the fluorescein-water solution in between the small solid grains.

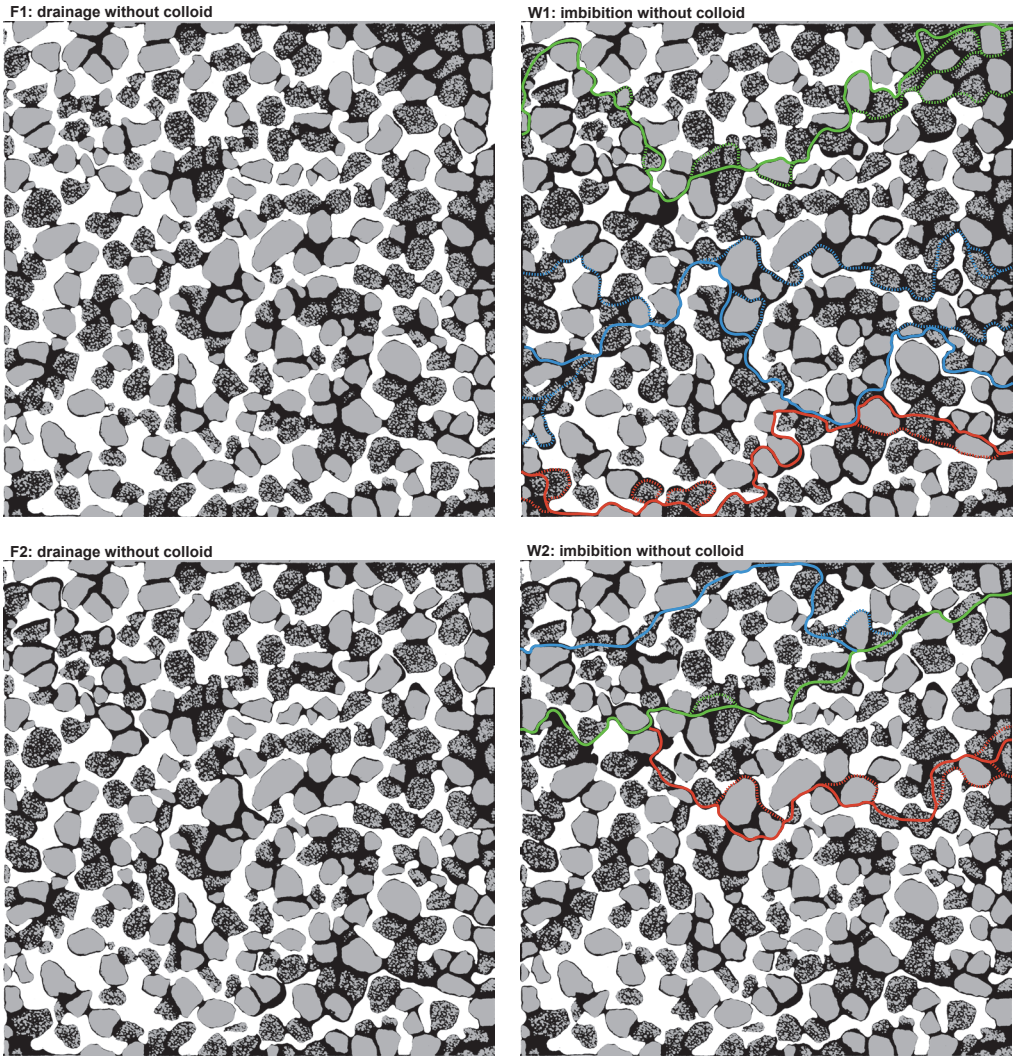

Figure 6.4. Drainage and imbibition cycles. Fluid distribution of stages F1, W1, F2, and W2 as well the main flow paths (mobile water) for W1 and W2. Water saturation: 0.46, 0.59, 0.49, and 0.52 respectively. Black: water phase, White: Fluorinert phase, gray: solid phase. The main water flow paths are indicated using solid color lines, and dashed lines are used to show the secondary paths.

Fluorinert, while the residual water resides in the aggregates (intra-aggregate pores). Some of the aggregates were isolated from water bridges and pools and were completely surrounded by Fluorinert. The water phase built bridges between aggregates and the solid grains. However, it is more efficient in interconnecting aggregates to each other and formed water pools. In this stage, the water saturation drops from 1.0 to 0.46.

In stage W1, water imbibed back into the pore network. In this process, the residual water in the aggregates played a vital role in the re-distribution of the water phase. Multiple flow paths were developed by interconnecting the water-saturated aggregates, while most of the inter-aggregate pores were still Fluorinert saturated. Three major flow paths existed at the top, center, and bottom of the model as displayed in Figure 6.4**,** plot W1. Due to the rapid interconnecting of water-saturated aggregates, the water saturation during stage W1 was increased from 0.46 to 0.59.

In stage F2, Fluorinert was injected for the second time and due to the large presence of Fluorinert inside the inter-aggregate pores the water connection inter-between the aggregates were broken off and breakthrough of the Fluorinert was achieved. The Fluorinert saturation was increased from 0.41 to 0.51, while this was lower than during stage F1 due to the rapid breakthrough due to the high presence of Fluorinert in the inter-aggregate pores.

In the last stage, W2, water was introduced again into the system. At the start of W2, there was more initial water present leading to paths being interconnected at a faster rate, subsequently earlier breakthrough of water which stopped the displacement at other parts of the micromodel. Due to this water flow paths were at the middle/top side of the micromodel during this stage(Figure 6.4, plot W2). During W2 the water saturation increased by 0.03, while the increase during the first cycle was 0.13. With respect to interface movement, only major interface movements were observed during F1. While, only minor saturation changes and no major movement of interfaces occurred.

Regions of interest – flow pathways. Figure 6.5 shows the fluid distributions for the regions of interest, A1 and A2. Region A1 is located at the center top of the micromodel. We describe particle transport by focusing on the aggregate located in the center of this region. During the primary drainage (F1), the Fluorinert phase invaded this region from the top and water resided within the aggregate as well within the inter-aggregate pore network connecting water to the surrounding aggregates to form a pool (Zhang et al., 2011). At stage W1 water imbibed the system and region A1 acted as a part of a main established flow path from the inlet towards the outlet (Figure 6.4), however only very minor changes were observed in the fluid distribution. At drainage step F2 the pool of

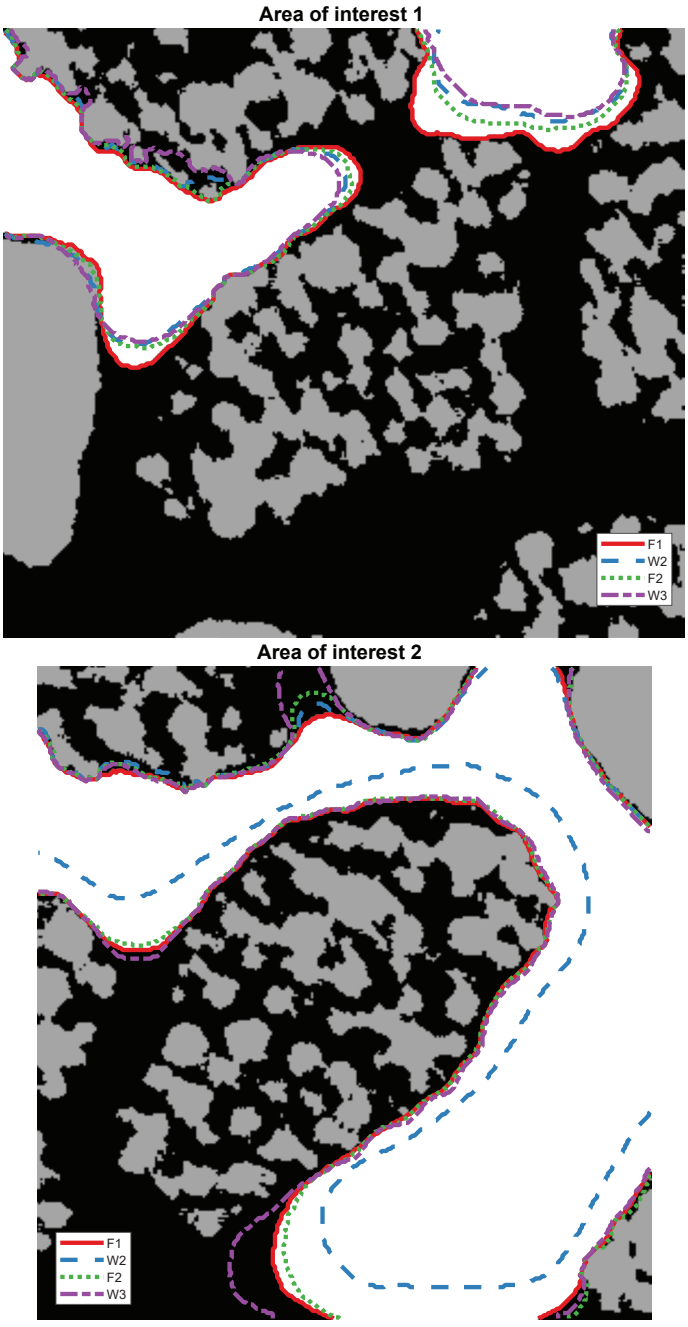

Figure 6.5. Immiscible Phase distributions. Distribution of water phases for sections A1 and A2 under displacement stages of F1, W1, F2, and W2. Black: water phase, white: Fluorinert phase, gray: solid phase. The Line indicates the Fluorinert phase distribution for the stages. The solid phase is not representative of the real pore space.

water became disconnected from the main flow path, which, upon the second imbibition step (W2) connected to the flow path again.

The region A2 was located at the bottom of the sample close to the lower boundary. Similar to region A1, the aggregate remained water saturated at stage F1, while mostly surrounded by Fluorinert. At stage W1 we observed a rather thick water film growing around the outer boundaries of the aggregate creating a connected path towards the next aggregate. Section A2 became part of one of the main flow paths from the inlet to the outlet (Figure 6.4). During the F2 stage, the water film thickness decreased again until the outer pores of the aggregate were drained. At stage W2, this pathway remained closed for the wetting phase, and, therefore, the aggregate was not contributing to the main flow path, i.e., the water phases remained stagnant and immobile from stage F2 onwards.

Regions of interest – colloid transport, region A1. Figure 6.6 shows colloid trajectories during different stages of the experiment in the region of interest A1. After stage SW1/SW2 6 colloids were retained within the aggregate pore space. As shown in Figure 6.5, colloid 1.1 was initially attached very close to colloid 1.2 and both were detached at the same time and moved to position F1, a minor change. At stage W1 colloids 1.1 and 1.2 were both remobilized. In this stage, colloid 1.1 was transported out of the aggregate and entered into the aggregate on the right side (i.e., downstream) and flowed out of the domain by the main flow trajectory indicated in Figure 6.4. However, in this stage, colloid 1.2 was attached again in the same aggregate. During stage F2, colloid 1.2 moved in a downward direction in response to the redistribution of the phases, and, during stage W2, this colloid is transported out of the aggregate and joined the main flow path to exit the sample. Colloid 1.3 remained attached during stage F1. This colloid was remobilized in stage W1 and re-attached again downstream of the flow inside the same aggregate. Similar to colloid 1.2, this colloid was moved downward during stage F2, and was finally remobilized during stage W2 and moved out of the domain. Colloid 1.5 remained attached until stage W2 during it was remobilized and transported out of the domain. Lastly, colloid 1.6 was not affected by the redistributions of the fluids and the established flow pathways during different stages and remained attached at the same location within the aggregate until the end of the experiment. Therefore, from a total of 6 attached colloids within this domain, only one colloid remained permanently attached. While 1 colloid was transported out of the domain during stage W1, other colloids were transported out of the domain only during the final cycle of drainage and imbibition.

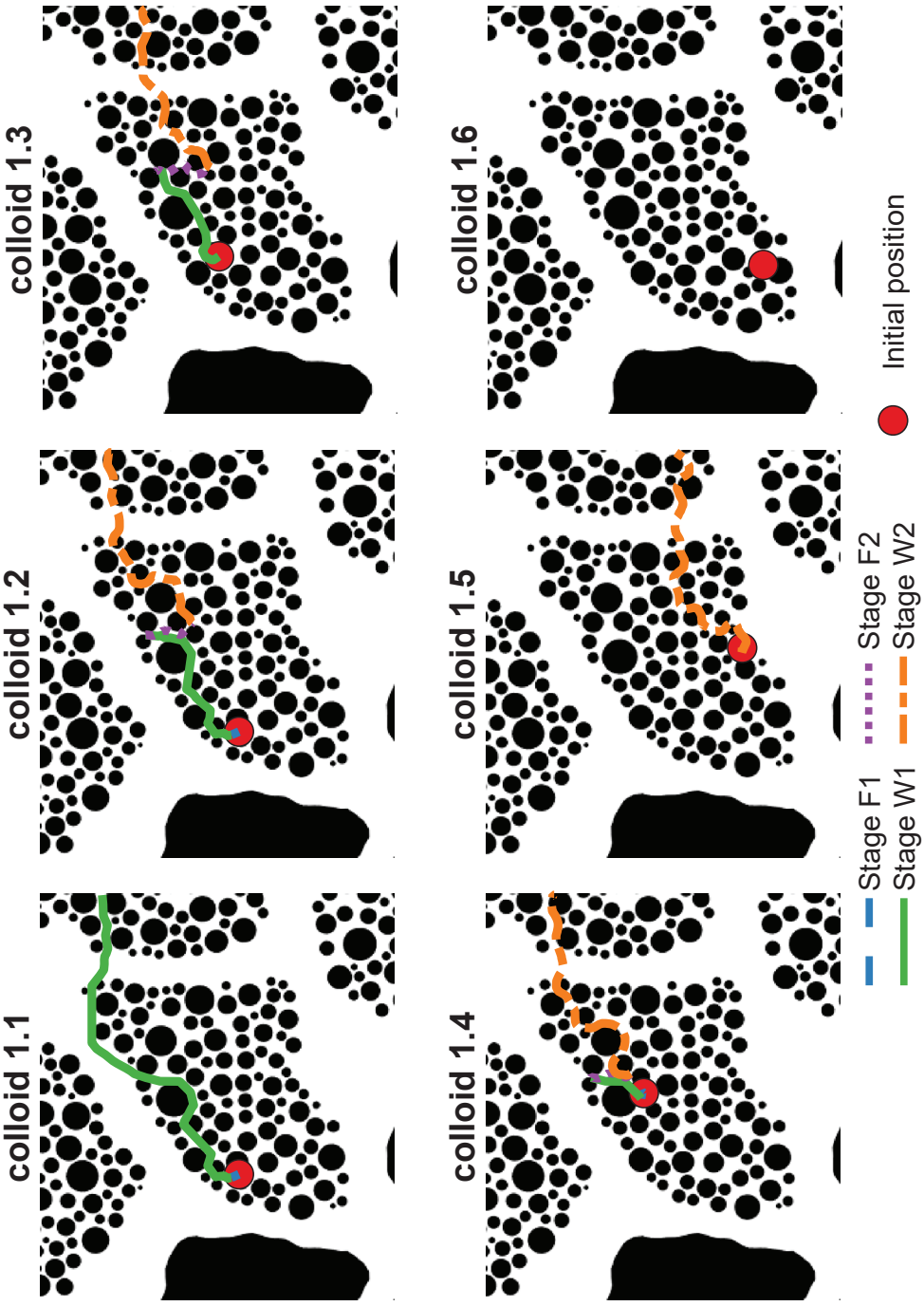

Figure 6.6. Colloid trajectories for the region of interest A1. The line indicates movement at a particular stage, the round symbol shows the initial position where the colloid is retained.

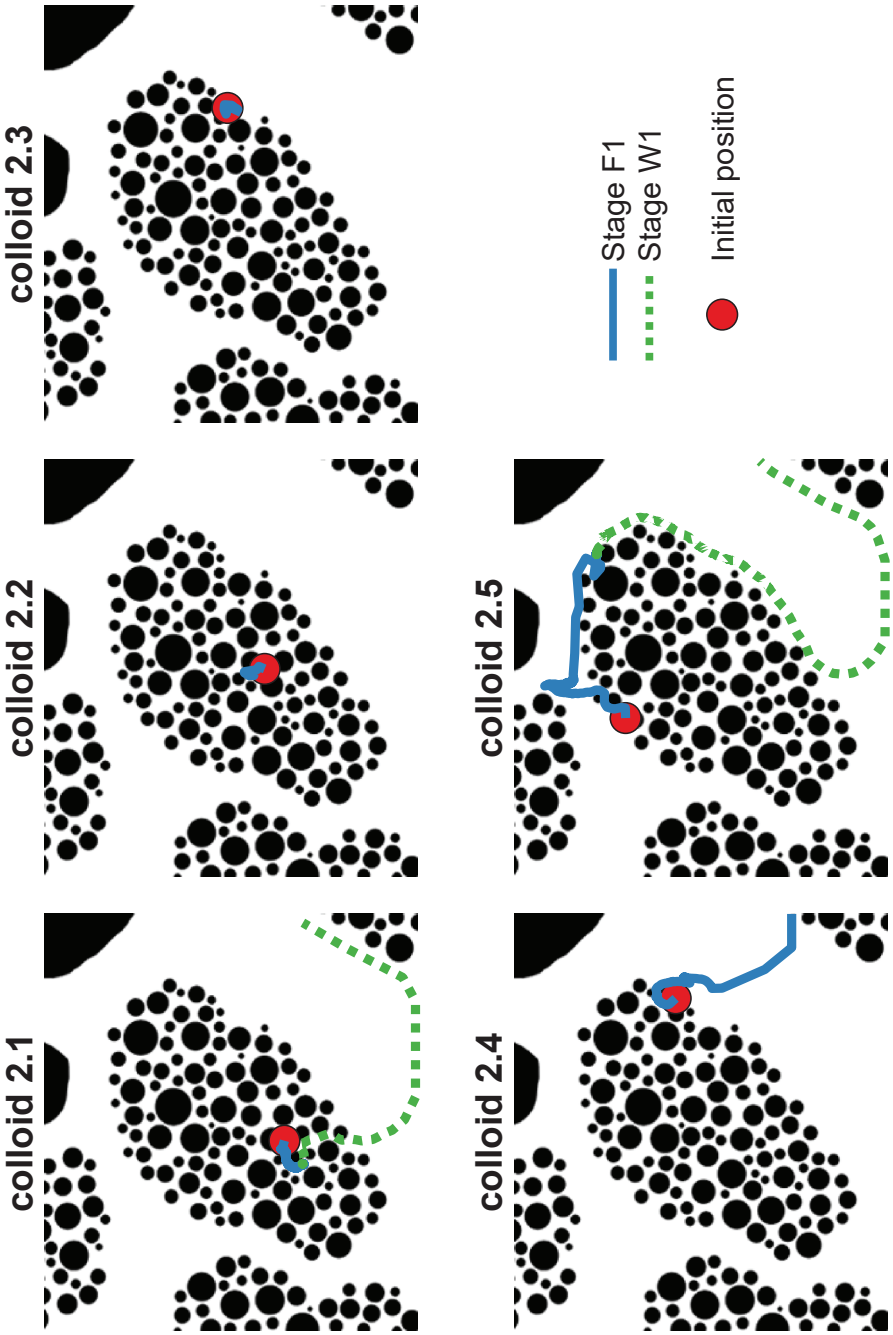

Figure 6.7. Colloid trajectories for the region of interest A2. The line indicates movement at a particular stage, the round symbol shows the initial position where the colloid is retained.

Regions of interest – colloid transport, region A2. Figure 6.7 shows region A2 where 5 colloids were attached after stage SW1/SW2. In contrast to the observed behavior in region A1, colloid movements were only observed during stages F1 and W1 as region A2 did not connect to any major flow path during the imbibition stage W2. Colloid 2.1 was remobilized and then re-deposited during stage F1 as the water phase was drained from the area around the aggregate. During stage W1 the aggregate joined the main flow path steaming from the inlet towards the outlet, colloid 2.1 was remobilized and transported out of the domain. Colloid 2.2 was transported and re-deposited during stage F1 where it remained attached during the rest of the cycles. Colloid 2.3 showed similar behavior to colloid 2.2. Colloid 2.4 was directly affected by the phase interfaces (i.e., by the moving water-Fluorinert interface) during stage F1. This colloid was taken by the interface and re-deposited downstream outside region A2. During stage F1, colloid 2.5 was transported out of the aggregate due to water displacement. Upon the arrival of the water-Fluorinert interface, this colloid was moved downstream and re-deposited at position F1. During stage W1 this colloid was transported out of the domain through the main water flow path.

As deionized water was used in our experiments, we expect that the role of the secondary energy minimum to be relatively small in colloid deposition (Figure 2.4) and local flow stagnation zones together with surface roughness contributed to colloids retention (Zhang et al., 2014; Argent et al., 2015; Bradford and Torkzaban, 2015; Bradford, Torkzaban, et al., 2015). Due to the rectangular cross-sectional pore shapes in microfluidics wedging is very unlikely to occur. When colloids can not freely move through pore throats pore straining may occur where colloid can be released by stabilizing reverse flow. In our sample, pore throat sizes are larger than 5 μm and pore straining could only occur for colloids which are transported in form of aggregates. The extend of straining is affected by the interplay between physical properties and chemistry of the solution as well as hydrodynamic forces (Bradford and Torkzaban, 2008). In our experiment, no straining was observed although some colloids were attached very close to each other (colloids 1.1 and 1.2). As flow velocity is lower within aggregates (due to the smaller pore sizes compared to the macropores), the hydrodynamic forces are relatively smaller in aggregate pore spaces and colloid attachment may occur. The cycles of drainage and imbibition cause a local increase in flow velocities which can re-mobilize colloids (Zhang et al., 2015). Our experiments have shown that colloid removal can occur by the direct effect of interfaces (such as removal of colloid 2.5 in the region A2) as well as using the bulk flow in response to the increased velocity caused by cycles of drainage and imbibition.

6.4. Conclusions

In this study, the transport of colloids and their trajectories were observed in a dual-porosity sample under cycles of drainage and imbibition. Micromodel with realistic pore structures, obtained from x-ray imaging, was used for experiments. A multi-camera setup was designed and used where fluid phase distributions were captured with one camera and the second camera was adjusted to record colloids and their movement over time. Using this setup, a dataset with over 20,000 images (with a total size of 200 GB) was collected and analyzed for colloid transport. Fluid distributions in the whole domain were measured to obtain phase saturation and two regions were chosen to explore transport and re-mobilization of colloids during several drainage and imbibition cycles. Our results have shown a major effect of aggregates on colloid transport. The majority of colloid attachment occurred within aggregates, where Fluorinert (i.e., the non-wetting phase) could not enter due to the small pore sizes in aggregates. While we observed remobilization of colloids by moving interfaces, the role of bulk fluid velocity and its flow paths was strongest in colloid remobilization.

Direct imaging of colloid transport in the whole domain, and with a resolution sufficient to observe colloid transport in individual micropores of aggregates, provides valuable details on colloid transport in complex pore structures that were not observed previously. This method provides opportunities for future analysis to explore the effects of solution chemistry and aggregate fraction on colloid transport and remobilization.

Chapter 7

Summary and Conclusion

The goal of this research was to explore transport of solutes and colloids over a large number of pores and for multiple scales using micromodel experiments and analysis. In addition, we provided detailed insight into the interactions of solute and colloids with pore space heterogeneities. This was achieved by systematically changing the fraction of aggregates to perform different micromodel experiments. On these samples, we began by performing saturated transport experiments and continued by investigating the effect of drainage and imbibition cycles on colloid remobilization in the dual-porosity samples. During this study, several customized experimental tools have been developed to enable investigation of flow and transport of non-adsorbing solutes and colloids at the pore scale. For the computational part, we have used pore network modeling to further investigate the interaction of non-adsorbing solutes between the inter-aggregate and intra-aggregate pores. We developed a pore network generator for dual-porosity models and studied the effect of aggregate porosity and aggregate permeability.

In Chapter 2, we have constructed a micromodel based on an x-ray tomography image to obtain the real complex porous structures in micromodels. The media type was a sandy porous media. To perform the experiment, we developed an efficient optic setup (i.e., an open microscope) that is able to track colloids in a domain size of 10×10 mm^2. This domain size provided a very large number of pores and grains to observe various transport mechanisms. Using this setup and sample, we captured the trajectories of over 1357 individual colloids. Having complete information for each trajectory through time and space, we have determined the system behavior. We have observed that 19 colloids were attached but subsequently remobilized, 29 were permanently attached, and the rest were fully mobile. In addition, we determined the tortuosity of the colloid trajectories, as well as their residence time, penetration depth, local velocities. We have also constructed the breakthrough curve in a novel way by assuming Dirac delta input of the colloid trajectories. We conclude that colloids were attached under unfavorable conditions mainly due to local flow velocities fluctuations and surface heterogeneities. By constructing the breakthrough curves, we could exclude or include colloids based on their behavior and study their influence on the average behavior - i.e., the shape of the breakthrough curve collected at the sample outlet.

In Chapter 3 we have employed the constructed micromodel in Chapter 2 and transformed fractions of the solid grains into aggregates. We have done this process systematically to obtain 4 dual-porosity micromodels with fractions of 0.25, 0.50, 0.75, and 1.0 for the aggregates. This provided several samples ranging from non-aggregate samples all the way to samples with 100% of grains being aggregates. This results in a dual-porosity system and bi-modal pore size distribution. We have built a fluorescence recovery after photobleaching

(FRAP) set-up, with this set-up we are able to record the concentration field of the 10×10 mm^2 domain and subsequently determine the front region area, front length, and the mean concentration gradient to provide insight into the pore-scale behavior in relation to dual-porosity domains. Furthermore, we constructed the breakthrough curves at the outlet of the domain and fitted them to the solution of macroscopic governing equations to obtain transport parameters. We performed the solute transport at 4 average velocities and found that an increased fraction of aggregates leads to a higher front bulk area, increased front length, and no significant change in concentration gradient was observed. While increased applied velocity led to no significant change in frontal area, although an increase in front length and gradient was observed. The pore-scale observations made it possible to observe changes in solute transport behavior while at the macroscopic scale no major influence was found.

In Chapter 4, we explored the effect of aggregate porosity and permeability on solute transport by pore network modeling. We constructed a macropore network of 100×20×20 mm^3 and super-imposed 1000 aggregates into this system. While the pore bodies and throats of the aggregates had a fixed position and connectivity, we have changed the aggregate porosity by altering the pore body size and changed the permeability by altering the throat diameter within the aggregates. We observed the solute breakthrough curve at three different locations along the pore network and fitted the results to the macroscopic Mobile-Immobile formulations to obtain the corresponding transport parameters. An increase in aggregate porosity was found to decrease mobile porosity (ϕ_m) and increase mass transfer (α), leading to considerable tailing in the BTCs. Changes in the aggregate pore throat size affected the relative flow velocity between the intra- and inter-aggregate domains. Higher flow velocities within the aggregates caused a change in the transport regime from diffusion dominated to more advection dominated. This change increased the exchange rate of solutes between the mobile and immobile domains, with a related increase in the value of the mass transfer coefficient and less tailing in the BTCs.

In Chapter 5, we used the dual-porosity micromodels developed in Chapter 3 and performed colloid experiments under a velocity of 12.0 m day^{-1} to investigate the effect of aggregate fraction on colloid transport. Furthermore, to investigate velocity effects, we performed several additional experiments on the micromodel with 50% of grains replaced by aggregates (i.e., sample S40/50) using 3 average velocities of 1.0, 5.0, and 20.0 m day^{-1}. As in Chapter 2, we captured colloid trajectories and observed the continuous transport of the colloids through the macro-and micropores. We observed only 11 retained colloids out of 1555 observed trajectories in the macro domain, while adding micropores to a macropore domain led to an increase of up to 43% of retained colloids (1226 trajectories

out of 2870 for sample S40/100). By introducing micropores, a considerable number of colloids were transported through the micropore domain which had lower velocities due to the small pores, as well as increased interactions with the surfaces of the grains (due to larger surface area), and higher retention of colloids was observed. Higher applied velocity led to a higher fraction of observed transport through the micropores, and we observed the highest attachment under a velocity of 1.0 m day^{-1}. This observation showed that the flow velocities, and associated hydrodynamic forces, within the micropores play a critical role in retention of colloids.

Finally, in Chapter 6, we examined two-phase flow and performed cycles of drainage and imbibition on sample S40/50. We first injected colloids under saturated conditions where a majority of the retained colloids we attached within the micropores. While transport of colloids by single-phase flow has stopped, we drained the sample with an immiscible Fluorinert solution and cycled between drainage and imbibition for another 2 periods. We obtained the fluid phase distribution of the whole domain and focused on analyzing colloid remobilization in two aggregates. The aggregates could not be drained by the Fluorinert phase due to their small pore sizes. We observed that the water-saturated aggregates play a vital role in the imbibition leading to connected pathways by the aggregates. This leads to remobilization of colloids due to the flow velocity changes within the aggregates as well as colloid remobilization by moving interfaces.

In conclusion, dual-porosity systems complicate the transport of solute and colloid transport under single-phase and multi-phase flow. We developed micromodels and pore networks to directly observe, at the underlying pore-scale, the transport behaviors by performing experiments and modeling. While we focused on aggregated soils, many other porous media with bimodal, or more, pore size distributions exist in both natural and industrial materials. The developed methods can be applied to these systems to provide more insight into observations made at larger scales by relating the pore-scale processes to the macroscopic behaviors.

Appendix A

Fluid Flow and Colloid Transport Experiment in Single-Porosity Samples

Tracking of Colloid Transport Behavior in a Saturated Micromodel

A.1. Sample properties

Figure A.1a provides the pore space of the generated sample where pores are labeled and shown using different colors. To break the continuous pore space into different pores we have used the location of pore throats as they insert maximum restriction to the flow between different pores. Figure A.1b provides the distribution of the generated pores. The pore body size is given as the equivalent diameter of the pore area and the throat as the mean diameter along the throat.

The micromodel was fabricated using soft lithography, SU8-2025 negative photoresist was used. It was spin-coated on a silicon wafer to obtain a thickness of 20 μm. Soft bake time of 2 min and hard back time of 6 minutes were applied. The photoresist was developed, and the silicon wafer was hard backed at 150 °C. The models are casted by pouring 40 grams of PDMS in a petri dish with the wafer. By corona discharge the casted model is bonded to a glass slide spin coated with a thin layer of PDMS. As well, holes were punched in the PDMS for the inlet and outlet.

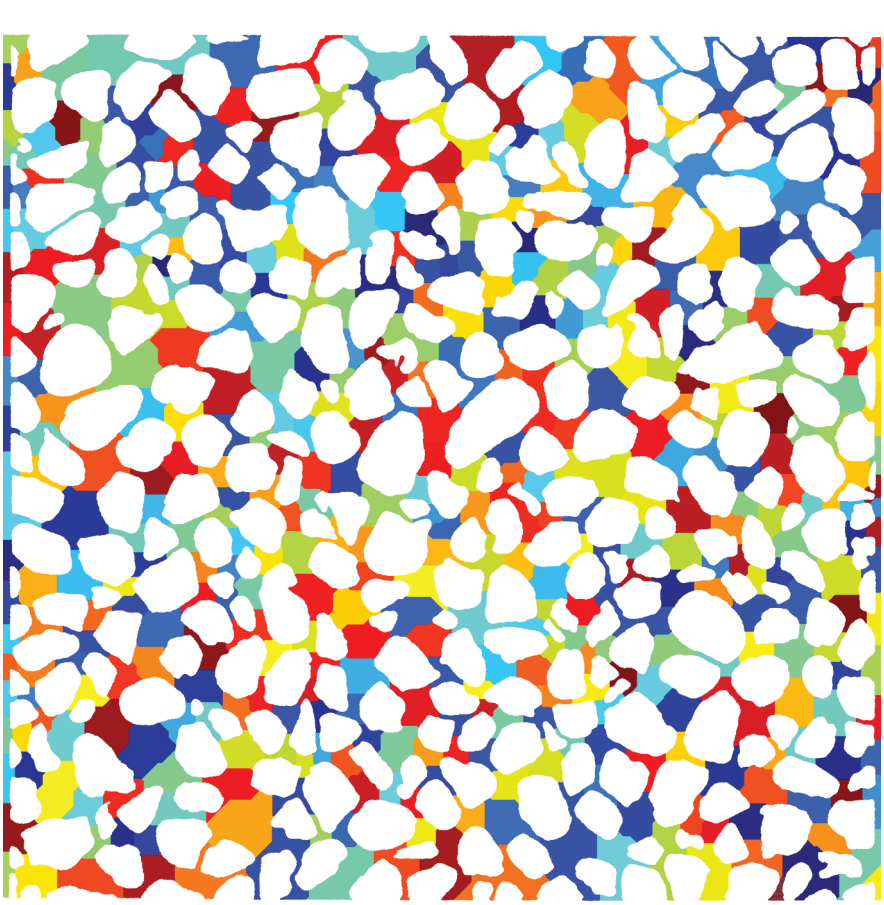

Figure A.1. a) The micromodel segregated into pores, colors indicate individual pores b) Pore size distribution of micromodel, equivalent body diameter and throat (boarders between pores) diameter.

A.2. Particle trajectory calculations

The following properties were calculated for each particle.

Tortuosity. For each particle trajectory, a tortuosity value was calculated using ,where Di is the displacement and d the Euclidean distance between the inlet and the particle location along the general flow direction.

Residence time. The residence time of a particle inside the domain is calculated using the time needed for each particle to completely pass through the domain (–i.e., from the inlet to the outlet). This information is used to look at individual behavior of colloids, as well as collective to construct the Breakthrough curves.

Penetration depth. The penetration depth is taken as the Euclidean distance from the inlet face to the location of attachment defined for the deposited colloids.

Attachment and remobilization events. Attachment and remobilization events were detected for each colloid trajectory. Between every two consecutive frames the displacement of a colloid was calculated, and when colloid displacement was very low (lower than a trenched values selected as 1.5 pixels for our experiment) particle was considered as immobile. Further, to minimize the error of such analysis, we required particles to remain immobile for at least 50 consecutive frames (corresponding to 5 seconds) to be considered as immobile.

1st and 2nd moments. Using trajectories, we have calculated the 1st and 2nd moment of the attached mass, which provided the mean deposition location from the inlet and the variance of the total attached mass, respectively. In these calculations, we only used the attached and remobilized particle categories. The two moments provide insight into the temporal evolution of the total attached mass.

A.3. DLVO interaction calculations

The DLVO interaction energies for colloid and collector were calculated by adding the Attractive van der Waals interaction (Φ_{VDW}) and the electric double layer interaction (Φ_{DL}). The Φ_{VDW} is calculated as follows (Gregory, 1981):

$$\Phi_{VDW}\left(h\right) = -\frac{AR_p}{6h}\left[1 - \frac{5.32h}{\lambda_0}\ln\left(1 + \frac{\lambda_0}{5.32h}\right)\right] \tag{A.1}$$

where A is the Hamaker constant taken as 3.9×10^{-21} J (Bradford and Torkzaban, 2008; Zhang et al., 2015), R_p is the radius of the colloid [m], h is the separation distance between

the colloid and the surface [m], λ_0 is the characteristic length taken as 100 nm.

The electric double layer interaction is given as (Zhang et al., 2015):

$$\Phi_{DL}\left(h\right)=64\pi\varepsilon_0\varepsilon_r R_p\left(\frac{k_bT}{ve}\right)\gamma_p\gamma_s exp\left(-\mathrm{K}h\right) \tag{A.2}$$

where ε_0 is the permittivity under vacuum (8.85 $\times 10^{-12}$ $CV^{-1}m^{-1}$) and ε_r the relative dielectric permittivity of water (78.54), k_b is the Boltzmann constant 1.38×10^{-12} JK^{-1}, and T the temperature (K), v the ion valence, γ_p, γ_s are the surface potential of the colloid and of the collector surface, respectively, which is given in eq. A.3, and K is the Debye-Huckel parameter (eq. A.4):

$$\gamma_i=\tanh\left(\frac{ve\xi_i}{4k_b\mathrm{T}}\right) \tag{A.3}$$

where ξ_i is the zeta potential of the colloid or of the collector.

$$\mathrm{K}=\sqrt{\frac{2000I_s e^2N_A}{\varepsilon_0\varepsilon_r k_bT}} \tag{A.4}$$

Where I_s is the ionic strength [mol L^{-1}] of the solution, and N_a is the avogadro constant (6.02×10^{23} mol^{-1}).

A.4. Error correction of trajectories obtained from Trackmate

In the particle/object and frame to frame linking detection the following error can occur: Particles can be at the same location but at different depth of the micromodel, this causes the LoG detector to detect the two particles as one particle for either one frame or several consecutive frames. This causes the tracks to merge and at a later time to split. This can mean that one of the tracks will be terminated inside the domain and will be initiated again as a new track in a later time step, or the tracks can be mixed up, i.e., one track will start following the other particle and vice versa. We found the mixing up of track does not influence our results and we did not make any effort to resolve this.

For resolving the issue of multiple particles being detected as one for a longer time we have made the following scheme in MATLAB. We first flag the tracks that were terminated and/or were initialized within the pore domain, we name these the daughter tracks. For the end node/particle of a daughter track that was terminated within in the domain we find if within the same time frame and within a certain radius there is another node of a track, we flag this as a mother track. We follow the same scheme for daughter tracks that were initialized within the domain and find mothers for those tracks as well. If we do not find any mother for the daughter track then these will be disregarded from any further analysis, except if this track was terminated at a location of an attached colloid. In the next step we will find for all the mother tracks their daughters. For each mother we check if the daughters are within a set time frame and radius. If we find a match combine the two daughters and the missing part between the daughters is copied from the mother track. We will follow this track for a set maximum time and see if we find within the same time frame and radius the start node/particle of the flagged tracks. We then link the two daughter tracks together by copying the missing part of the mother track and add it in between the daughters.

We have recorded several properties related to image intensity for each particle including the mean, median, minimum, maximum, total Intensity and the standard deviation. Furthermore, as particles may temporarily disappear in some of the frames, for each particle the frame number in which the particle was detected is calculated. The estimated particle diameter is also calculated, which is often larger than the actual radius of the particles depending on the amount of emitted light by the fluorescent particle, the camera exposure time and its gain coefficient. During that image analysis, the recorded signal to noise ratio was used to filter out undesired imaging spots.

We observed the movement of attached colloids due to the set-up as well as camera noise. We found that the mean is around 0.2 pixel/frame and a maximum of 1 pixel/frame.

0.2 pixel/frame, which adds up to +/-5.8×10^{-6} m s^{-1}. This is for a stationary colloid, for moving colloids this could be higher although with the frame rate and flow velocity we use the tracking seems quite accurate. Consequently, the error is relatively small.

A.5. Temporal evolution of adsorption using the 1st and the 2nd moments

The first and the second moments show the growth and propagation of the adsorbed mass into the domain over time, i.e., average distance from the inlet and the spreading of the attached mass (Figure A.2). In the calculations irreversible attached colloids and remobilized colloids were included. Remobilized colloids, due to their temporal attachment and release can cause the parameters to fluctuate over time more than irreversible attached colloids. Figure A.2 shows that colloid attachment begins close to the inlet with an increasing variance of the adsorbed mass. After 200 seconds colloid attachment become less dynamic, with colloids tending to attach at predefined distances (i.e., at similar distances of the previously attached mass). Once the system reached steady state (~600 seconds), after terminating colloid injection, these parameters converge towards their asymptotic values. The peaks and valleys in the 1st and 2nd moments show the time and location of considerable adsorption, and/or remobilization events.

A.6. Local colloid flow velocities

Probability density function for the local colloid velocities is given in Figure A.3.. The velocities were sampled at *dt* of 0.5 seconds and the trajectories were categorized as

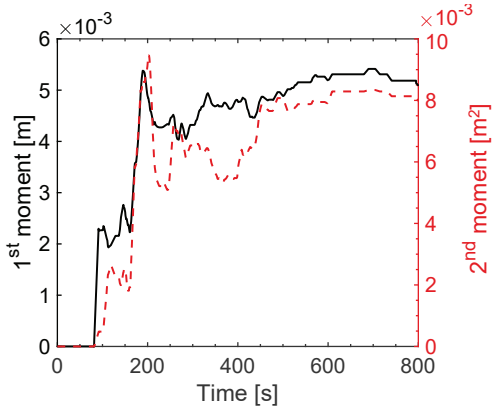

Figure A.2. a) The micromodel segregated into pores, colors indicate individual pores b) Pore size distribution of micromodel, equivalent body diameter and throat (boarders between pores) diameter.

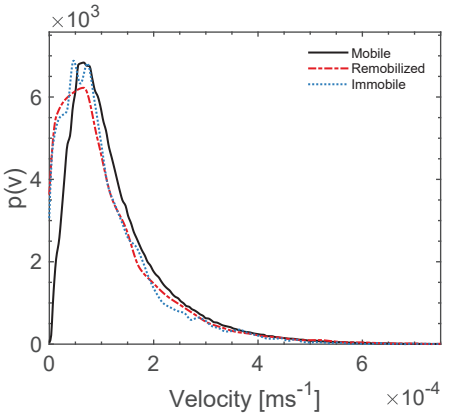

Figure A.3. The probability density function, p(v) for the local colloid velocity sampled at a *dt* of 0.5 seconds. The velocities were categorized based on the transport, mobile, remobilized or immobile.

mobile, remobilized or immobile. The velocities measurements of the fraction of the trajectory when a colloid was immobile (zero velocity) were excluded from the data. The probability of lower velocities was higher for colloids that were classified as remobilized or immobile. As well the observed lower velocities could indicate the rolling of colloids along the solid walls.

A.7. Probability density distributions on the transport parameters

The probability distributions for a) the residence time, b) tortuosity, c) distance to solid, and d) the average trajectory velocity are given in Figure A.4. The residence time for immobilized (retained) colloids are taken till the time of attachment, which is in general lower than the peak arrival time of mobile colloids. While remobilized colloids have in

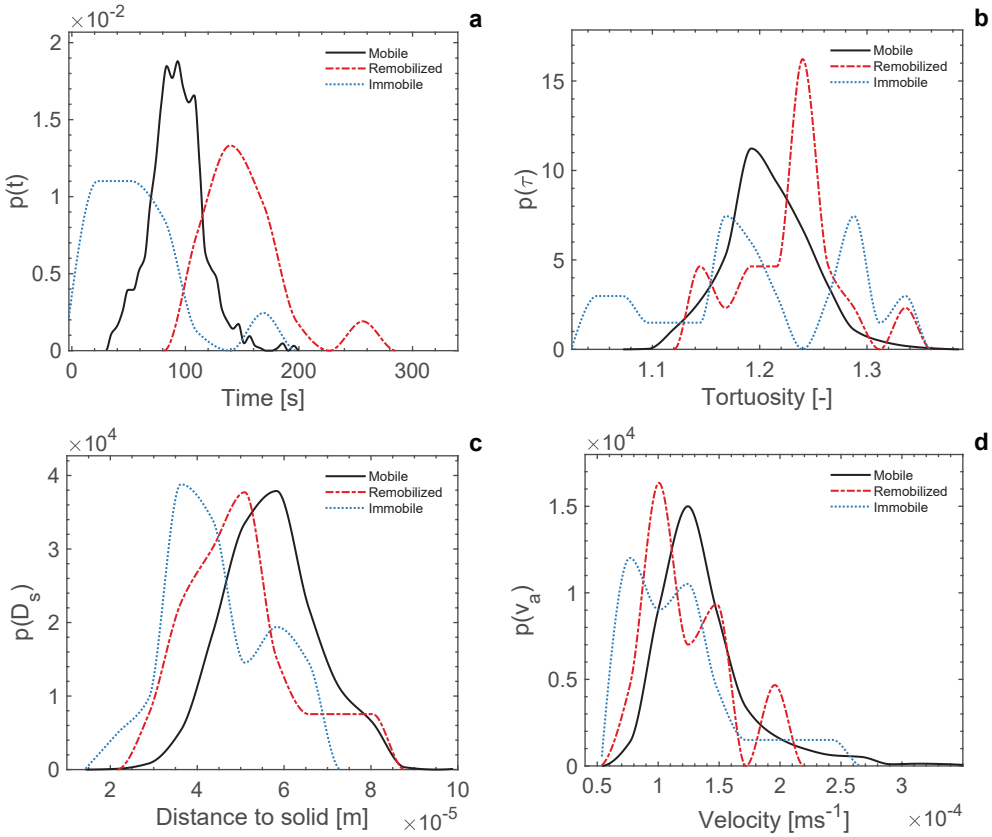

Figure A.4. a) The probability density function, p(t), for the transport time, b) p(τ) for the tortuosity, c) p(Dt) for the average distance to the solid for the colloid trajectory, d) p(va) for the average velocity of the colloid along its trajectory. The transport parameters were categorized based on the transport, mobile, remobilized or immobile.

general a later arrival time than mobile colloids due to the retention time. Tortuosity values for immobile colloids are fluctuating due to the low sampling rate as well due to the penetration depth, i.e., short travel distance can lead to lower tortuosity value as the colloid is only transported through few pores. For remobilized colloids we find a higher probability for higher tortuosity values due to the colloids being transported closer to the walls leading to more tortuous paths. This is observation was confirmed by the higher probabilities for lower average distance to solids for remobilized and immobile colloids. As shown by Figure S3 we observed higher probability for low average trajectory velocity for remobilized and immobile colloids than for mobile colloids.

A.8. Additional Breakthrough curves

Figure A.5 shows the Dirac delta input, i.e., all colloids released at t=0, breakthrough curves (BTCs) for trajectories of the mobile colloids, in like manner with all colloid trajectories included. It shows the progression of the BTCs in the domain and Figure A.6 shows the single fit results at the location of 9.8 mm (end of domain)

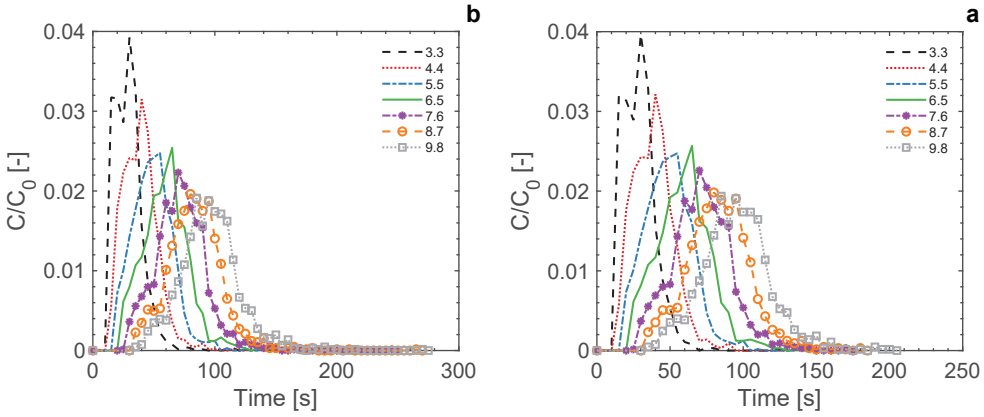

Figure A.5. Dirac delta input breakthrough curves. a) Colloids that were mobile during their transport through the pore domain, breakthrough at multiple locations (mm) through the domain. b) All Colloids that were transported through the pore domain, breakthrough at multiple locations (mm) through the domain.

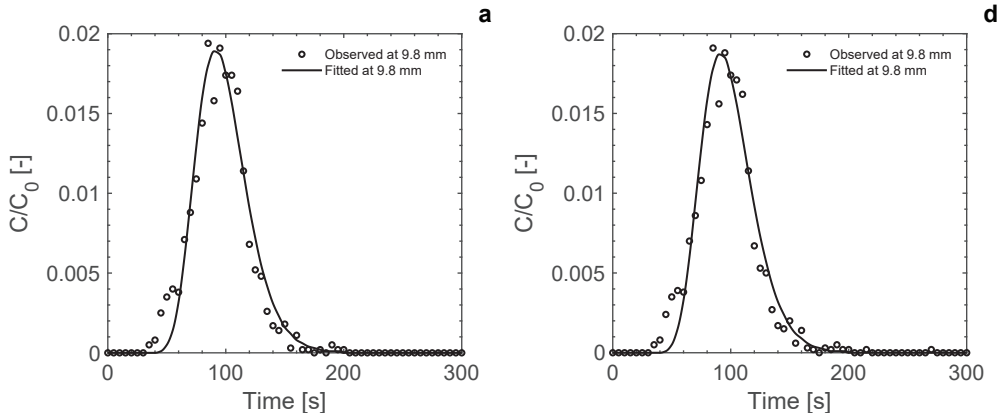

Figure A.6. Single fit results from StanMod. a) Mobile colloids only, b) All colloids.

Appendix B

Fluid Flow and Solute Transport Experiments in Dual-Porosity Samples

Direct Pore-Scale Observation in Saturated Micromodels

B.1. Concentration fields

The figures below show the concentration fields of samples S40/0, S40/25, S40/75, and S40/100 at an applied average flow velocity of 12 m day^{-1}. Figures for the other applied flow velocities (of 2.0, 5.0, and 20 m day^{-1}) are available upon request.

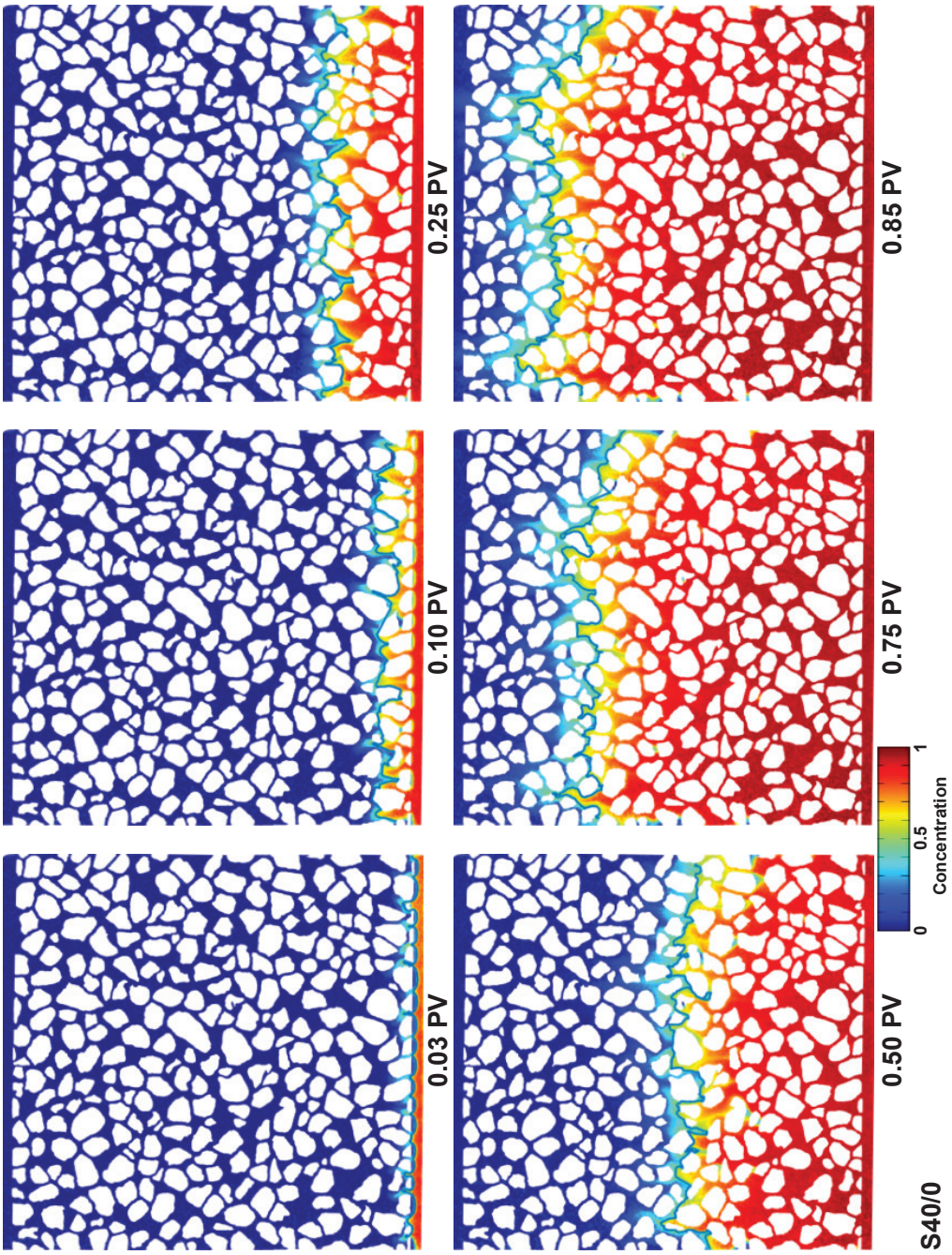

Figure B.1. Concentration fields showing the front development over time for sample S40/0 subjected to an average pore water velocity of 12.0 m day^{-1}. The plots belong to 0.03, 0.1, 0.25, 0.5, 0.75and 0.85 injected PV. The contour line shows the solute front at 0.5 concentration.

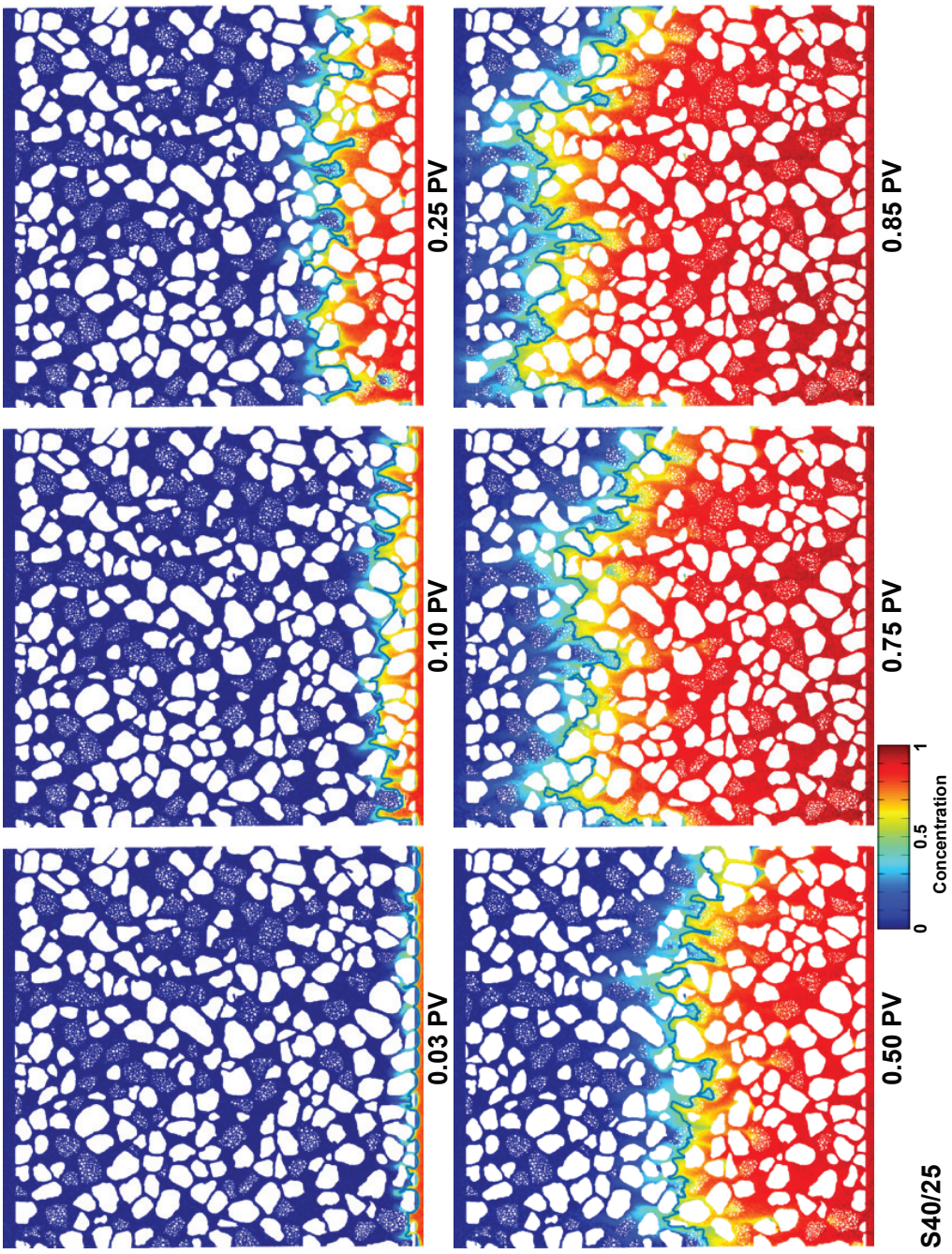

Figure B.2. Concentration fields showing the front development over time for sample S40/25 subjected to an average pore water velocity of 12.0 m day^{-1}. The plots belong to 0.03, 0.1, 0.25, 0.5, 0.75and 0.85 injected PV. The contour line shows the solute front at 0.5 concentration.

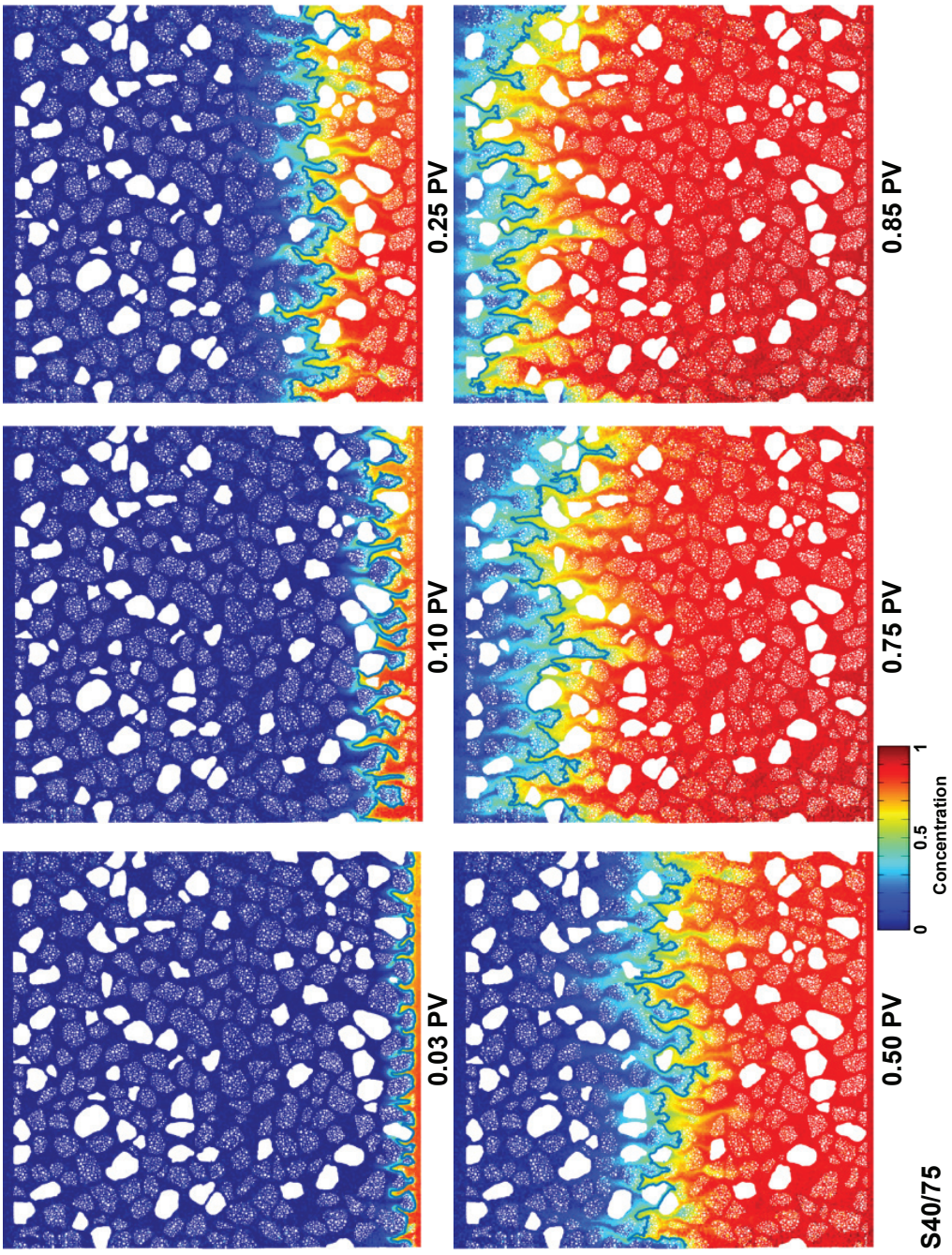

Figure B.3. Concentration fields showing the front development over time for sample S40/75 subjected to an average pore water velocity of 12.0 m day^{-1}. The plots belong to 0.03, 0.1, 0.25, 0.5, 0.75and 0.85 injected PV. The contour line shows the solute front at 0.5 concentration.

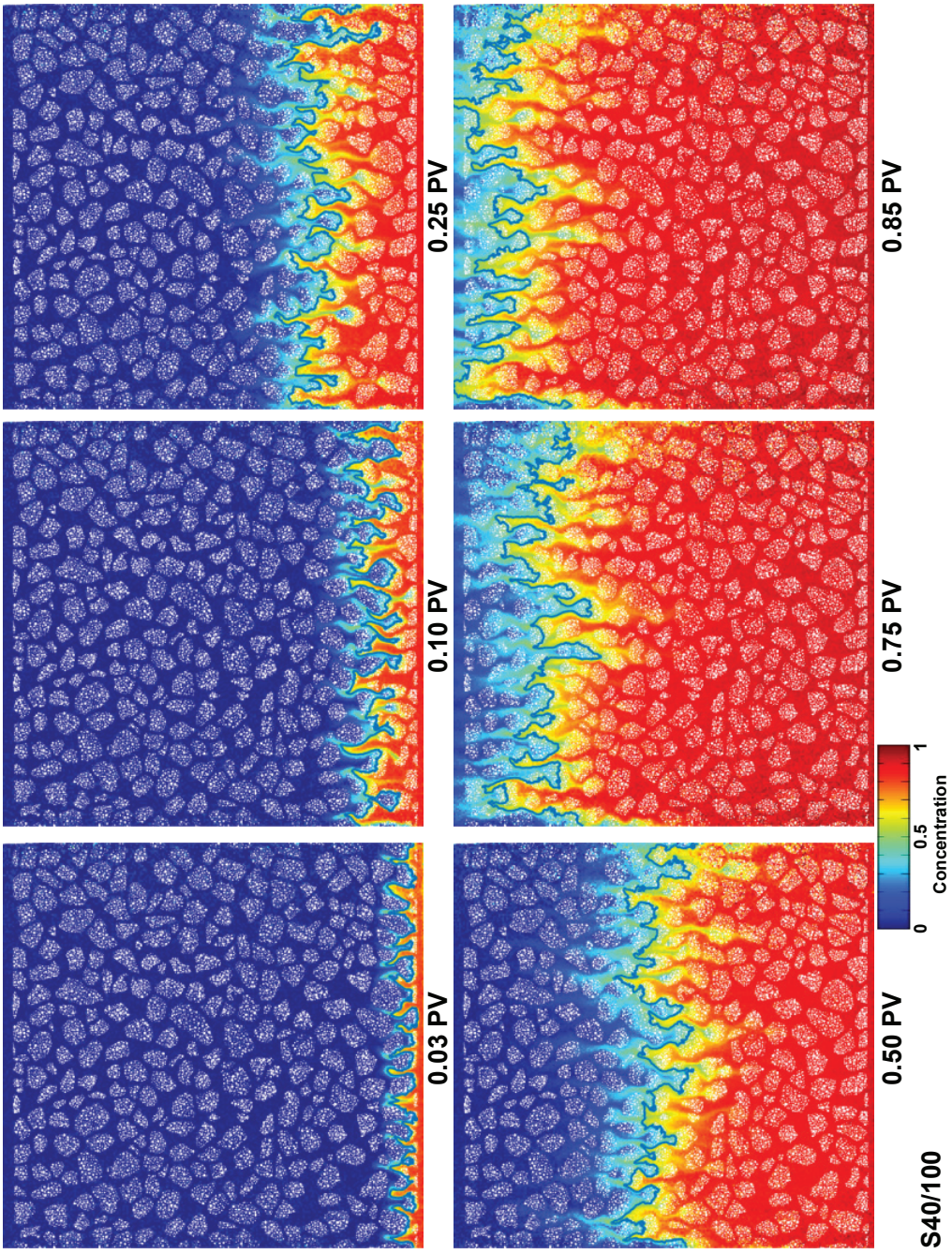

Figure B.4. Concentration fields showing the front development over time for sample S40/100 subjected to an average pore water velocity of 12.0 m day^{-1}. The plots belong to 0.03, 0.1, 0.25, 0.5, 0.75and 0.85 injected PV. The contour line shows the solute front at 0.5 concentration.

B.3. Velocity effect on Frontline length, gradient, front area, and BTC

For samples S40/0, S40/25, S40/75, and S40/100 the frontline length, gradient, front area, and the breakthough curve are given at 2, 5, 12, and 20 m day^{-1} to show the effect of applied velocity on the above-mentioned parameters. The data is subsampled due to the high amount of data available. The data acquisition of S40 and S40/25 at 2 m day^{-1} had failed.

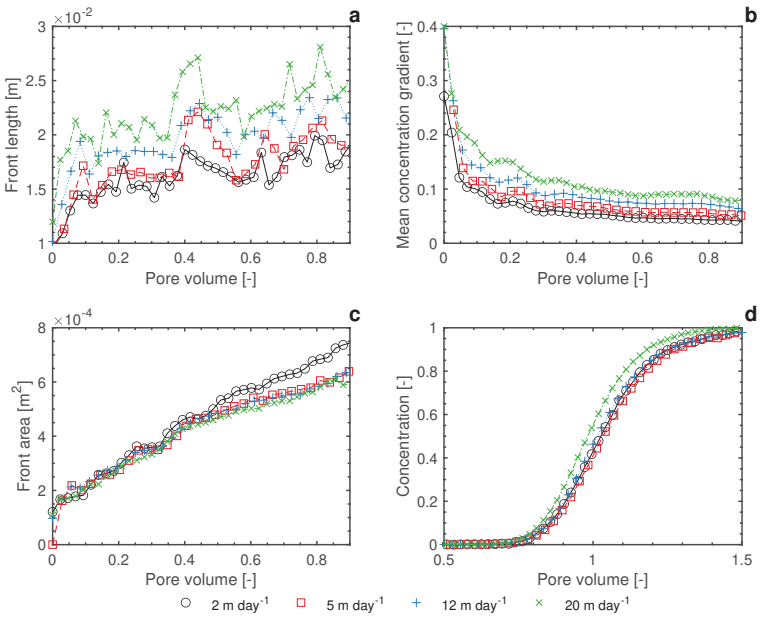

Figure B.5. a) front length over time, b) the mean concentration gradient of the concentration bulk area, c) concentration front area plotted against pore volume and d) breakthrough curve measured at the outlet of the porous media for S40/0. Experimental error in 2 m day^{-1}.

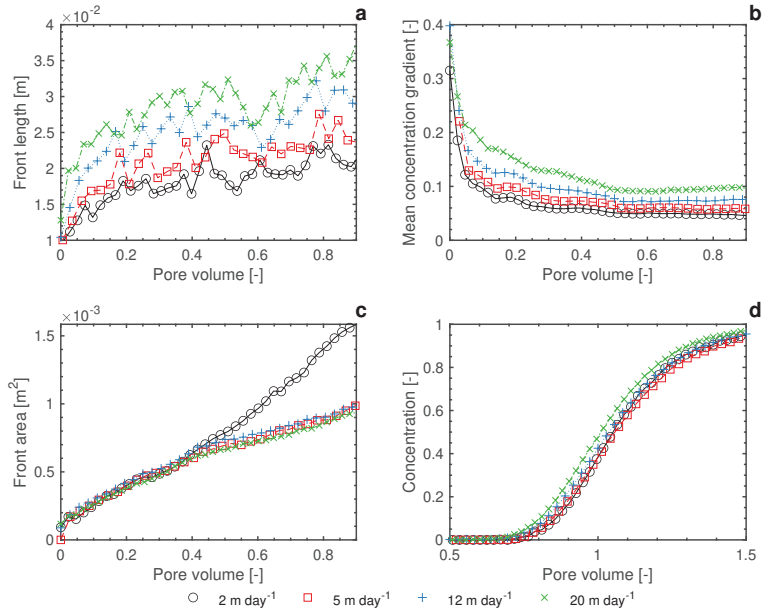

Figure B.6. a) front length over time, b) the mean concentration gradient of the concentration bulk area, c) concentration front area plotted against pore volume and d) breakthrough curve measured at the outlet of the porous media for S40/25. Experimental error in 2 m day^{-1}.

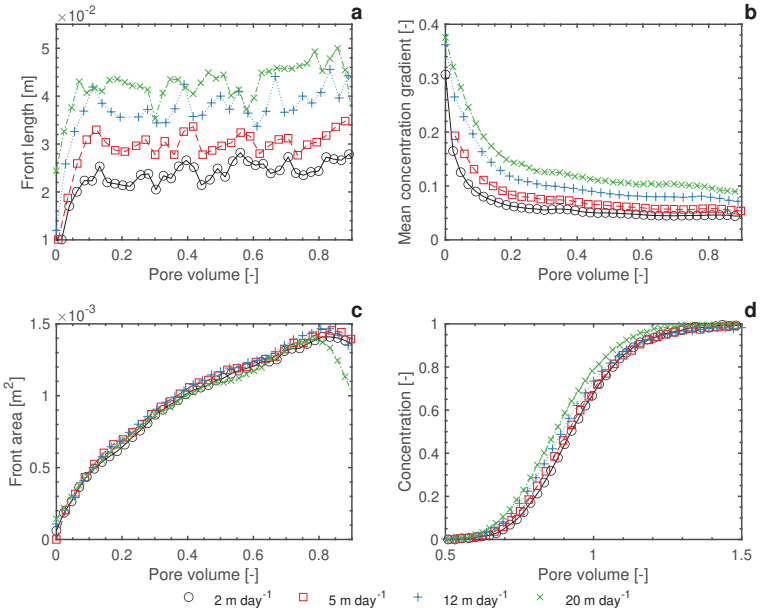

Figure B.7. a) front length over time, b) the mean concentration gradient of the concentration bulk area, c) concentration front area plotted against pore volume and d) breakthrough curve measured at the outlet of the porous media for S40/75.

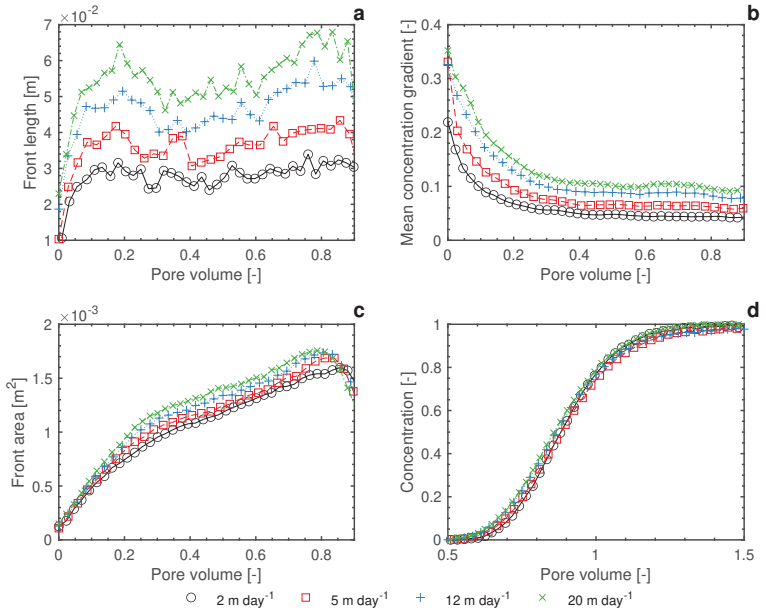

Figure B.8. a) front length over time, b) the mean concentration gradient of the concentration bulk area, c) concentration front area plotted against pore volume and d) breakthrough curve measured at the outlet of the porous media for S40/100.

B.2. Aggregate fraction effect on Frontline length, gradient, front area, and BTC

The data is plotted for all the samples at the flow rates of 2, 5, and 20 m day^{-1} to show the effect of the aggregate fraction on solute front length, gradient, area, and the breakthrough curve. The data acquisition of S40 and S40/25 at 2 m day^{-1} had failed. The shown markers are subsampled due to a large number of data points.

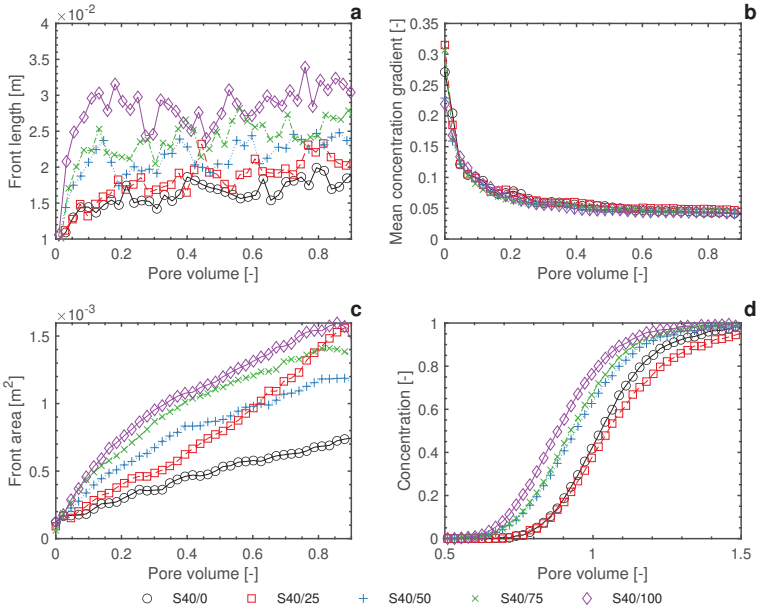

Figure B.9. a) front length over time, b) the mean gradient of the concentration of the bulk pore space, c) area of the front pore space against pore volume and d) breakthrough curve measured at the outlet of the porous media for a velocity of 2 m day^{-1}.

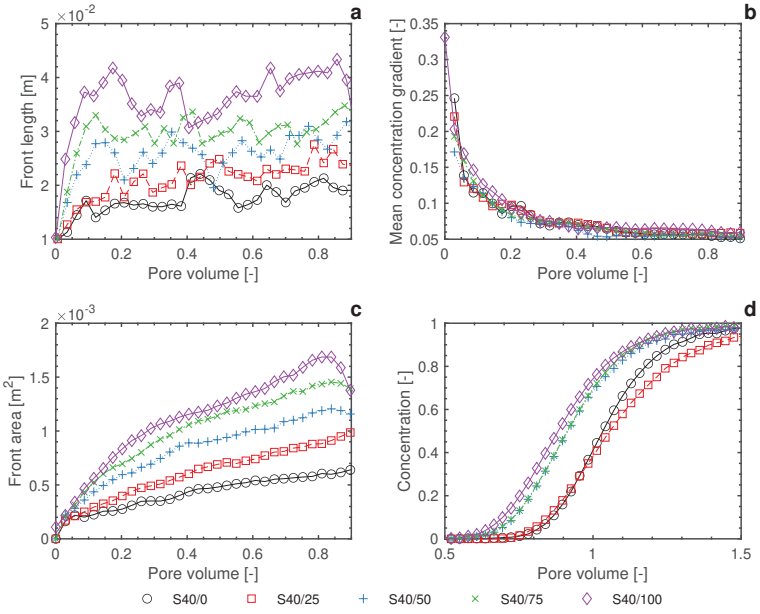

Figure B.10. a) front length over time, b) the mean gradient of the concentration of the bulk pore space, c) area of the front pore space against pore volume and d) breakthrough curve measured at the outlet of the porous media for a velocity of 5 m day^{-1}.

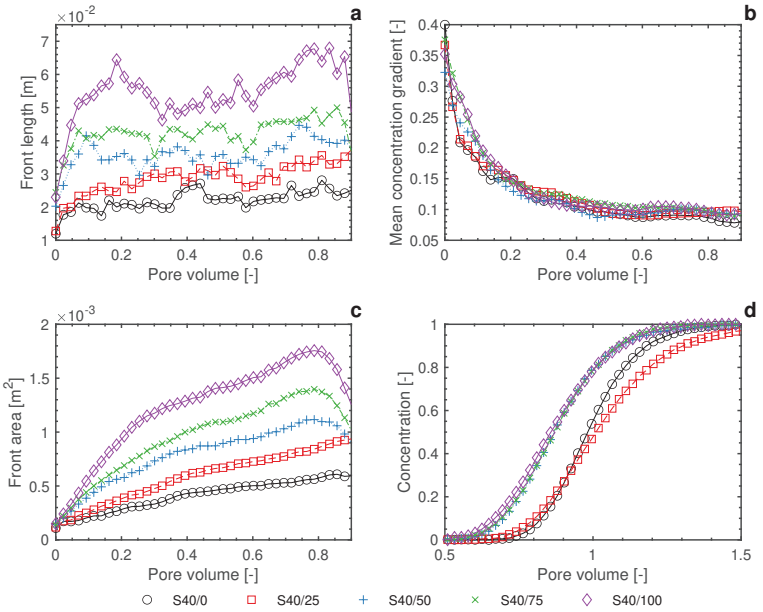

Figure B.11. a) front length over time, b) the mean gradient of the concentration of the bulk pore space, c) area of the front pore space against pore volume and d) breakthrough curve measured at the outlet of the porous media for a velocity of 20 m day^{-1}.

Appendix C

Multi-Scale Modeling of Flow and Transport in Dual-Porosity Porous Media

A Computational Pore-Scale Study for Flow and Solute Transport

C.1. Video's of simulation

The video's assosciated with this chapter can be online found as the supplementary materials of the published article of this chapter at https://dx.doi.org/10.1016/j.advwatres.2017.04.013.

C.2. Construction of multi-scale domain

In this study, the build-in pore network generator of PoreFlow (Raoof et al. 2013) is used in order to generate the macropore network. This provided a pore network with variable pore coordination numbers between 1 and 26. Next, a large number of aggregates are placed randomly within the generated macropore network. Aggregates are assumed to be spherical shaped and with random radii. A large number of micropores, with random locations, are placed within each aggregate and connected to each other based on the nearest neighbor method. A check is performed, and wherever the aggregates were placed on macropores, the corresponding macropores were removed from the network. At this stage, we have a macroporous multi-directional network and microporous network, and the next step is to connect the two pore systems (i.e., micro-and macropores) to create a single connected multi-scale network. To do so, we first identify the surface pores of aggregates using the convex hull method. Using the nearest neighbor method, we connect the surface micropores to their adjacent macropores. To illustrate the method, Figure C.1 shows a simple macropore network with one aggregate placed in it.

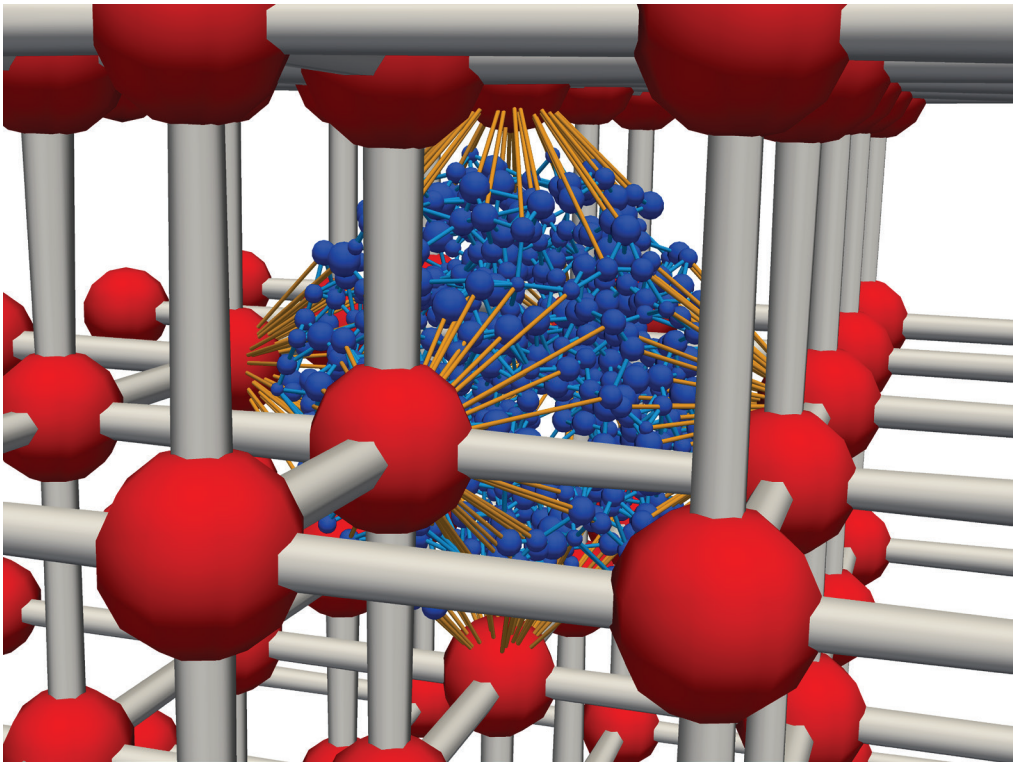

Figure C.1. An illustration of a single aggregate in a simple macro domain. The colors indicate macro pore bodies in red, macro pore throats in white, aggregate pore bodies in blue, micro pore throats in light blue, and aggregate connecting pores in orange.

C.3. Additional simulation results

The five figures below show the progress of solute advection and dispersion in the domains for Case I-1, I-3, and I-6 (representing the porosity effects) together with Cases II-1, II-2, and II-4 (representing the permeability effects).

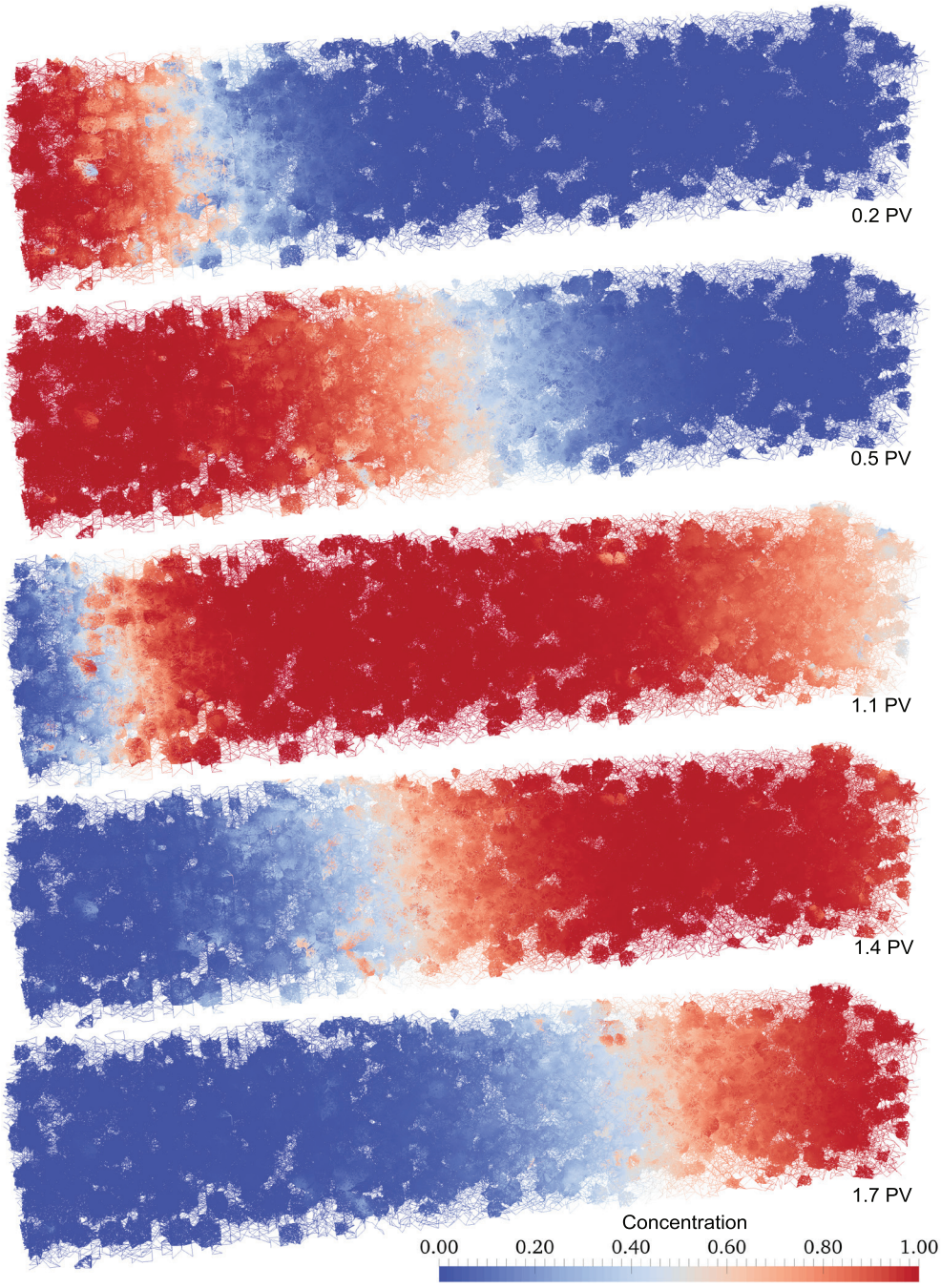

Figure C.2. Pore network simulation results for Case I-1 (ϕ=0.214). The corresponding pore volumes are provided below each plot. For plots at pore volumes larger than 1.0, after one pore volume the solute-free water is injected.

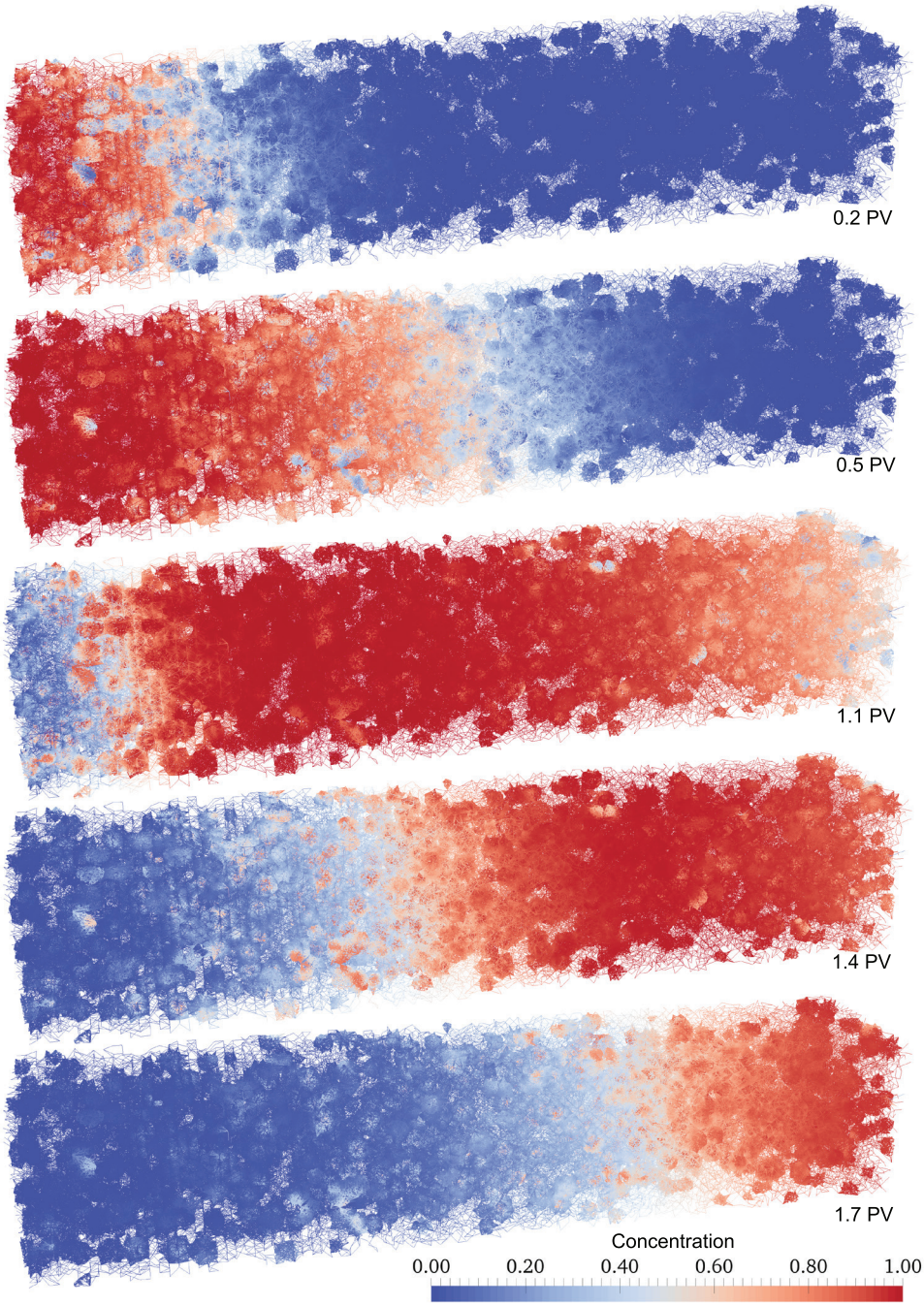

Figure C.3. Pore network simulation results for Case I-3 (ϕ=0.234), which is identical with Case II-2 (K=1.50×10^{-6}). The corresponding pore volumes are provided below each plot. For plots at pore volumes larger than 1.0, after one pore volume the solute-free water is injected.

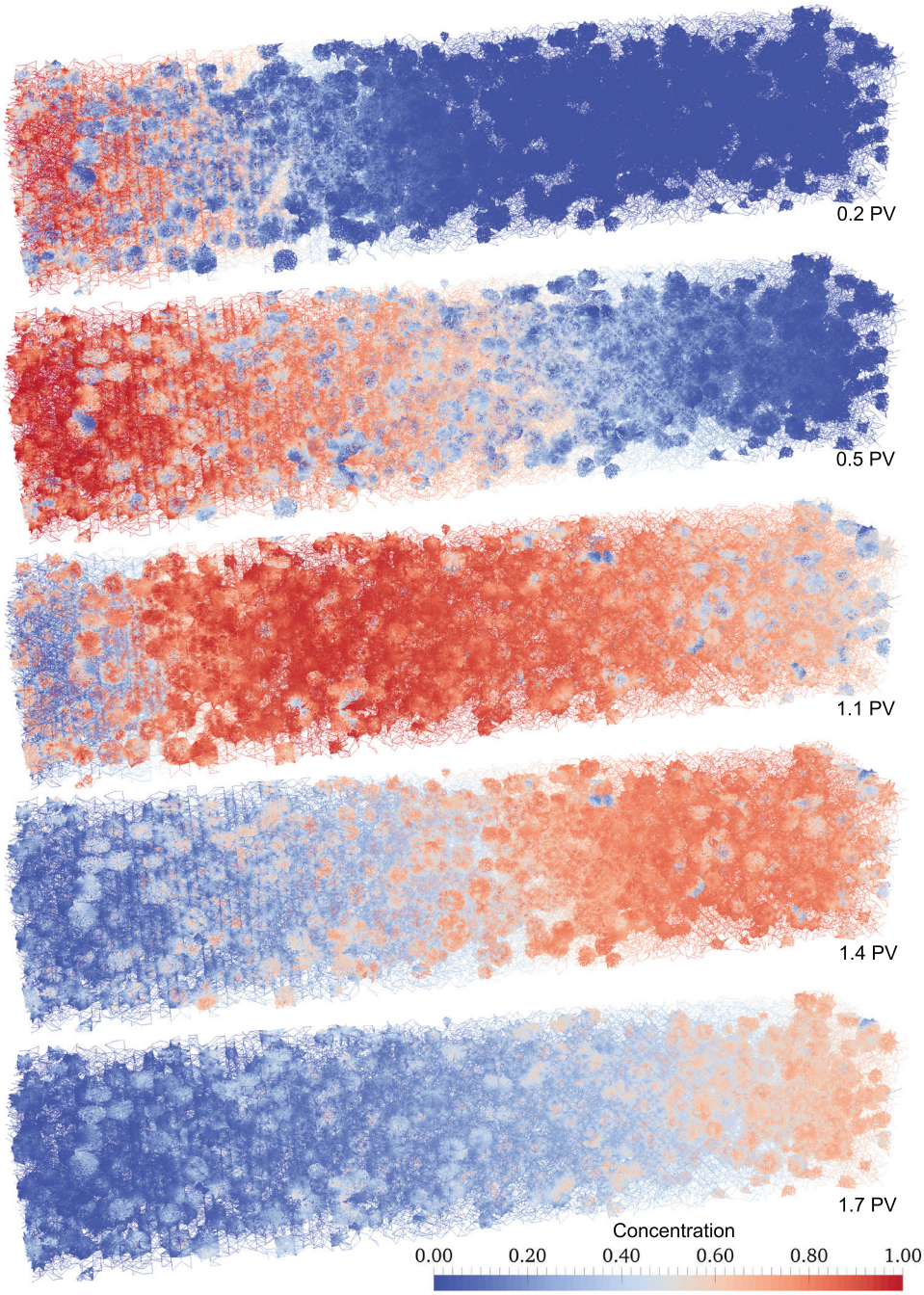

Figure C.4. Pore network simulation results for Case I-6 (ϕ=0.315). The corresponding pore volumes are provided below each plot. For plots at pore volumes larger than 1.0, after one pore volume the solute-free water is injected.

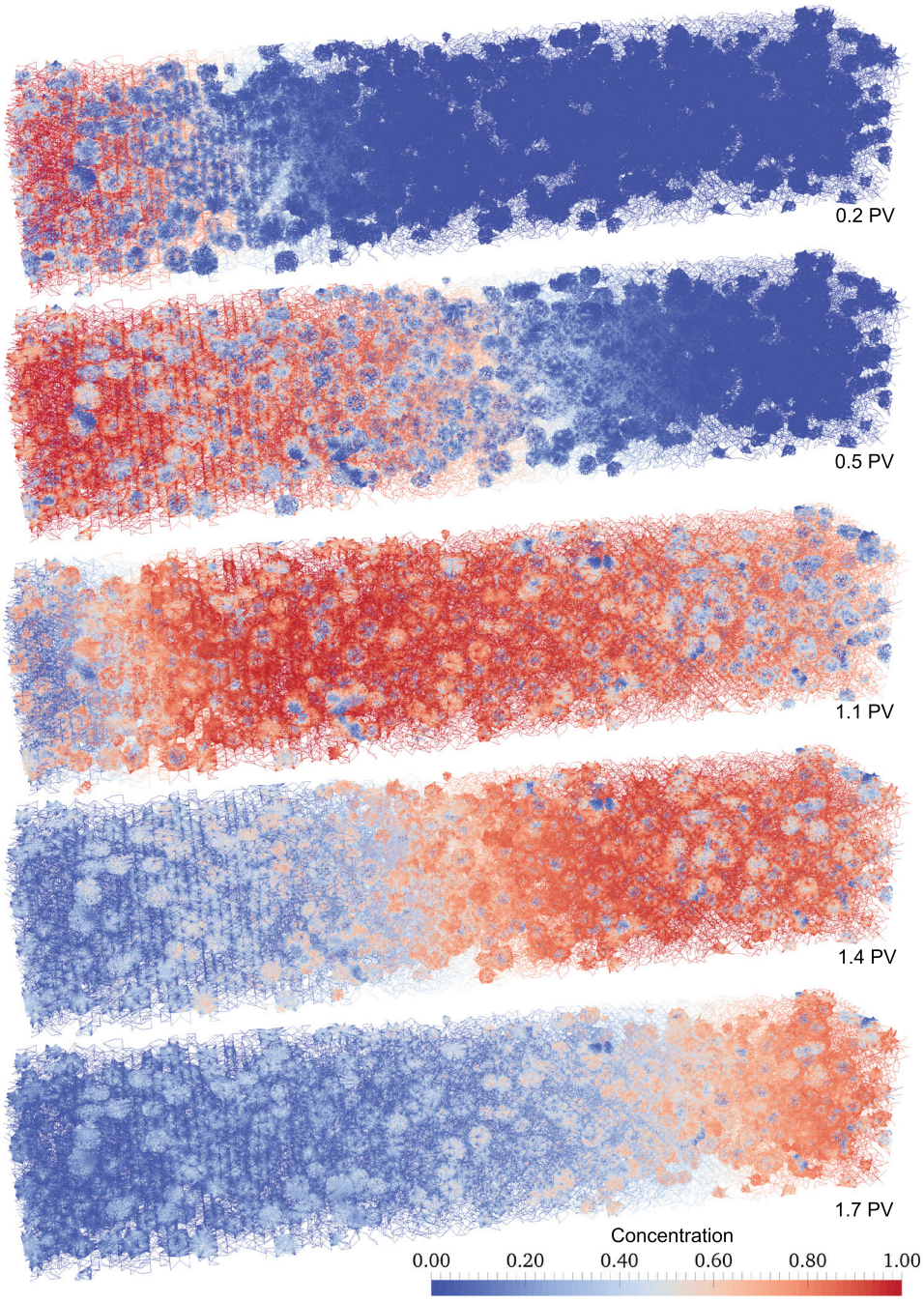

Figure C.5. Pore network simulation results for Case II-1 (K=1.62×10^{-8}). The corresponding pore volumes are provided below each plot. For plots at pore volumes larger than 1.0, after one pore volume the solute-free water is injected.

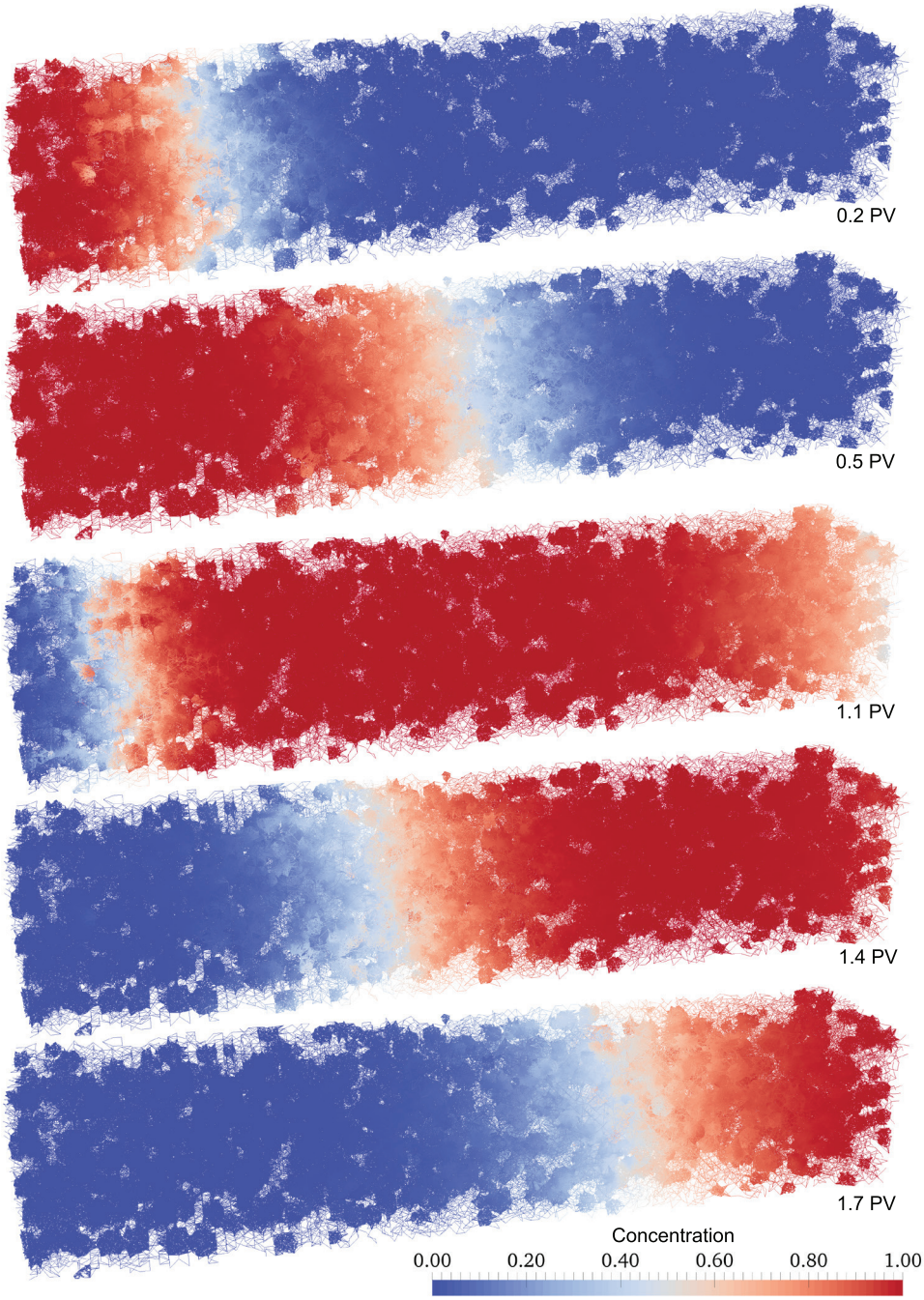

Figure C.6. Pore network simulation results for Case II-4 (K=1.27×10-4). The corresponding pore volumes are provided below each plot. For plots at pore volumes larger than 1.0, after one pore volume the solute-free water is injected.

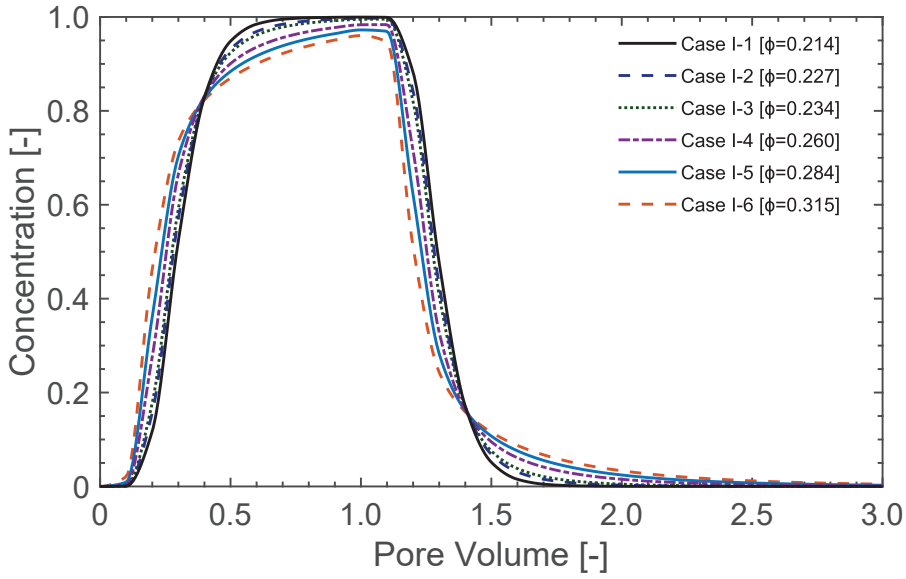

Figure C.7. BTCs of all six simulations belonging to the Case I, at 30 mm from the inlet.

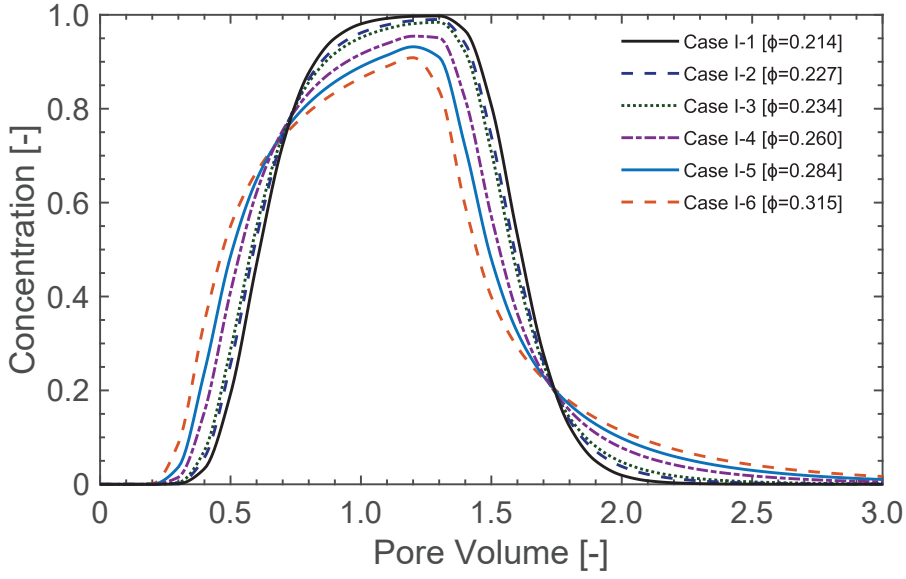

Figure C.8. BTCs of all six simulations belonging to the Case I, at 60 mm from the inlet.

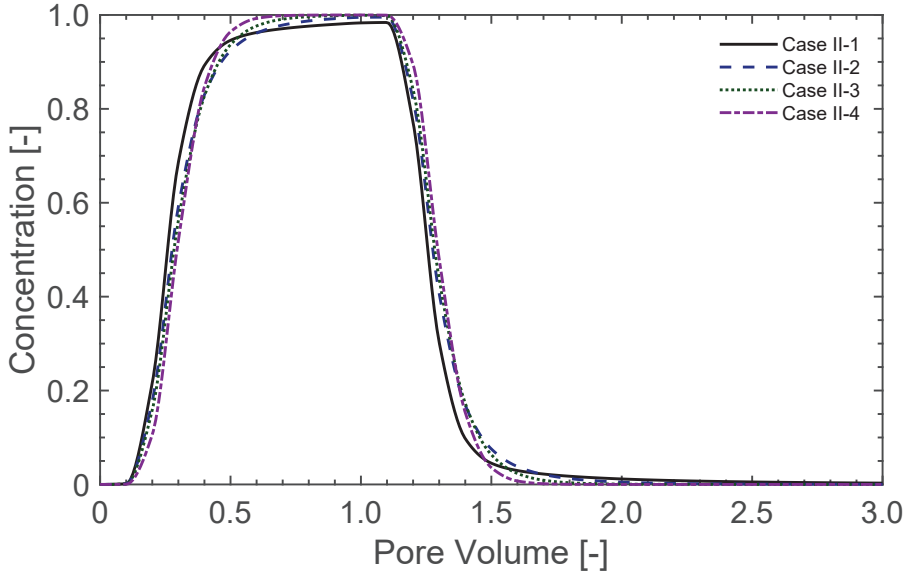

Figure C.9. BTCs of all six simulations belonging to the Case II, at 30 mm from the inlet.

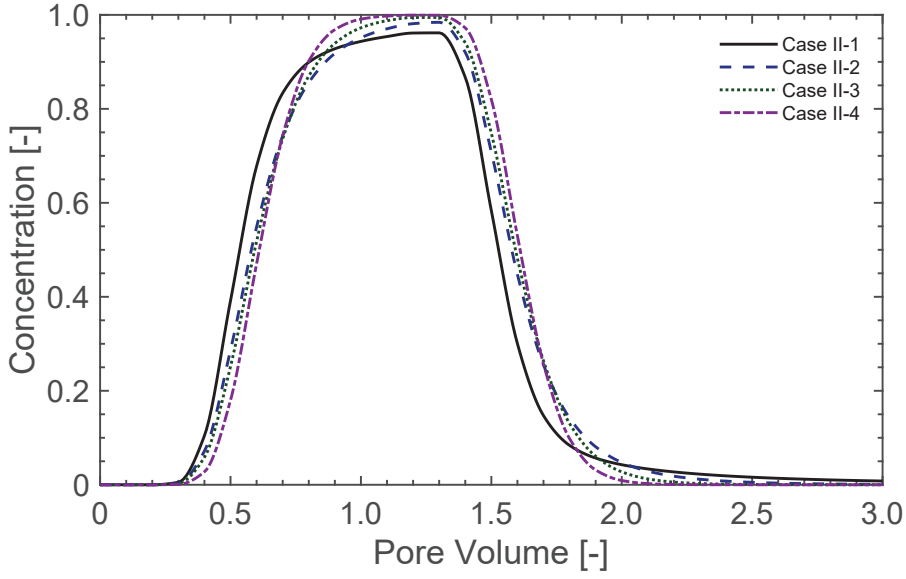

Figure C.10. BTCs of all six simulations belonging to the Case II, at 60 mm from the inlet.

Appendix D

Fluid Flow and Colloid Transport Experiments in Dual-Porosity Samples

Role of Micro-Porosity on the Transport Behavior of Colloids

D.1. Aggregate fraction effect

The pore domains and their colloid trajectories are given for samples S40/0, S40/25, S40/50, S40/75, and S40/100 at an average applied velocity of 12.0 m day^{-1}. The flow is from the left to the right. The trajectories are categorized based on their behavior: 1) Mobile in macropores, 2) Mobile in aggregates, 3) Remobilized, 4) Immobile (attached). Place of attachment and remobilization are indicated by red dots. Colors indicate: black; solid grains, gray; aggregates, white; pore network, various colored lines; colloid trajectories.

D.2. Flow velocity effect

The pore domains and their colloid trajectories are given for samples S40/50 at an average applied velocity of 1.0, 5.0, and 20.0 m day^{-1}. The trajectories are categorized based on their behavior: 1) Mobile in macropores, 2) Mobile in aggregates, 3) Remobilized, 4) Immobile (attached). Place of attachment and remobilization are indicated by red dots. Colors indicate: black; solid grains, gray; aggregates, white; pore network, various colored lines; colloid trajectories.

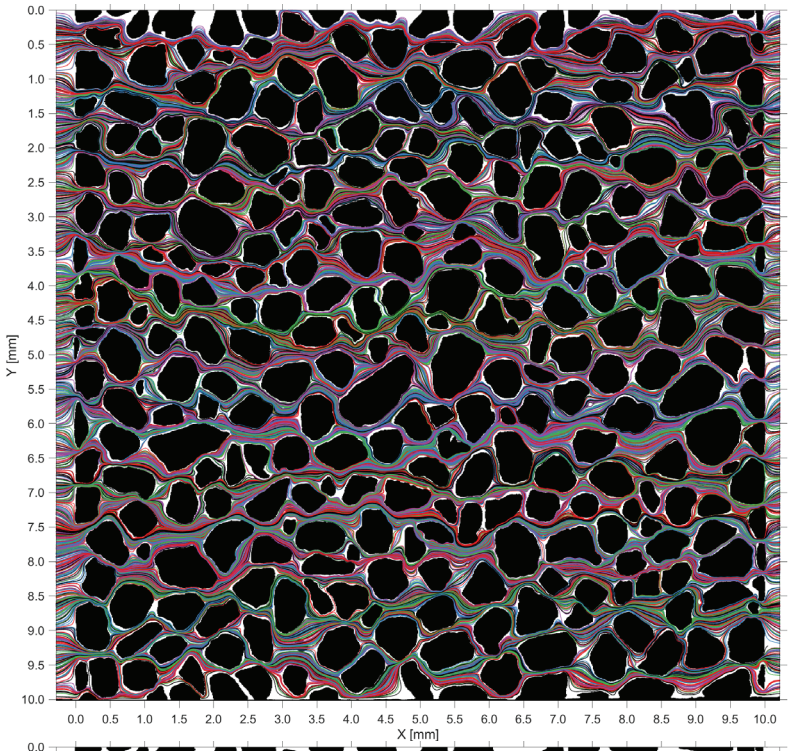

S40/0: Mobile in macropores

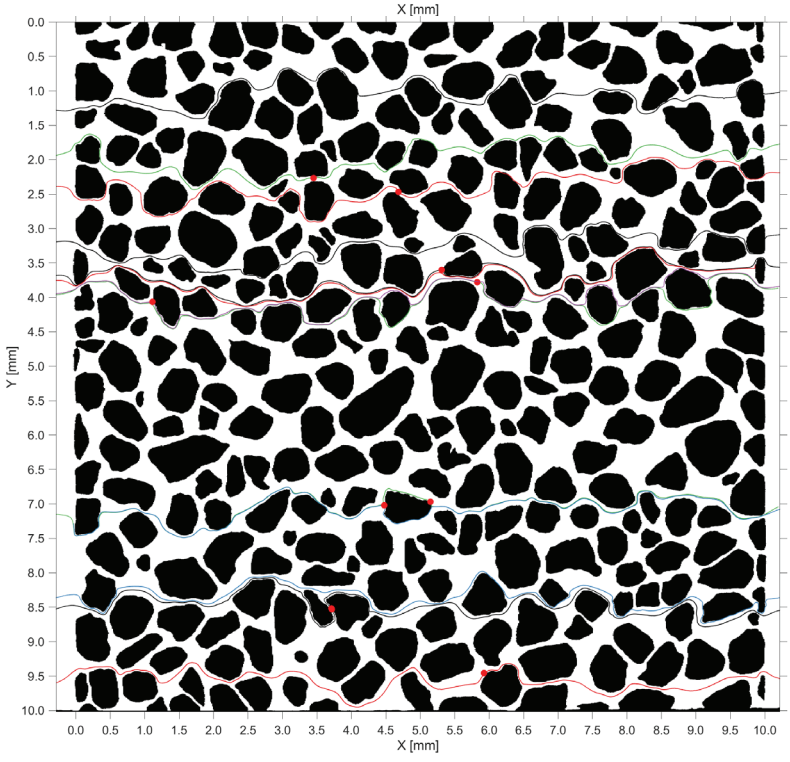

S40/0: Remobilized

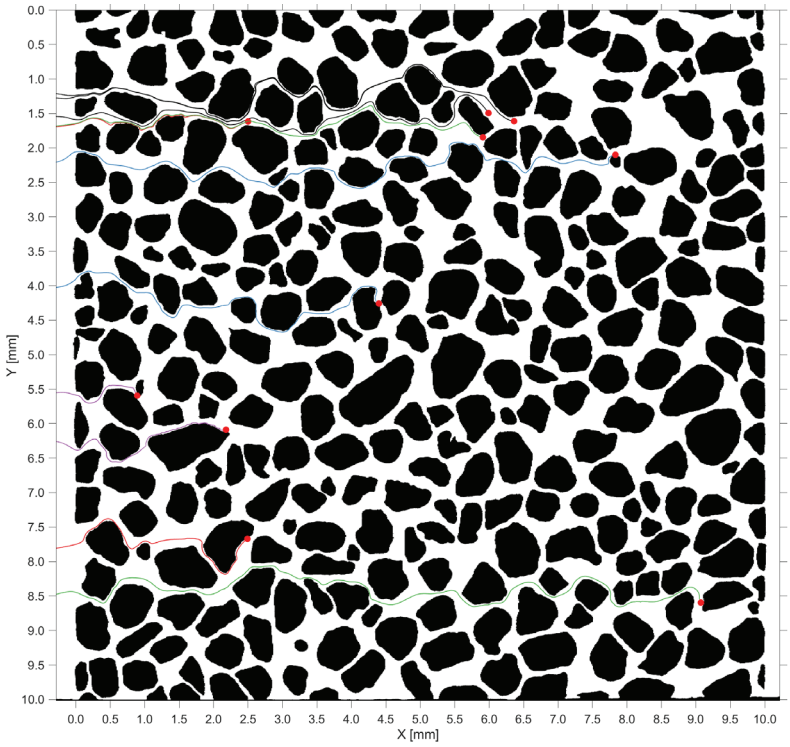

S40/0: Immobilized

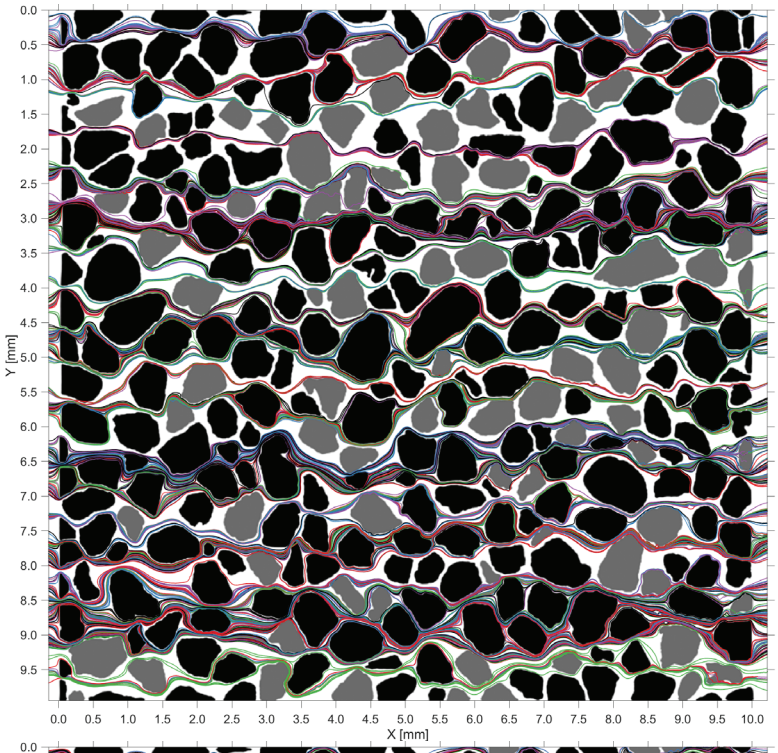

S40/25: Mobile in macropores

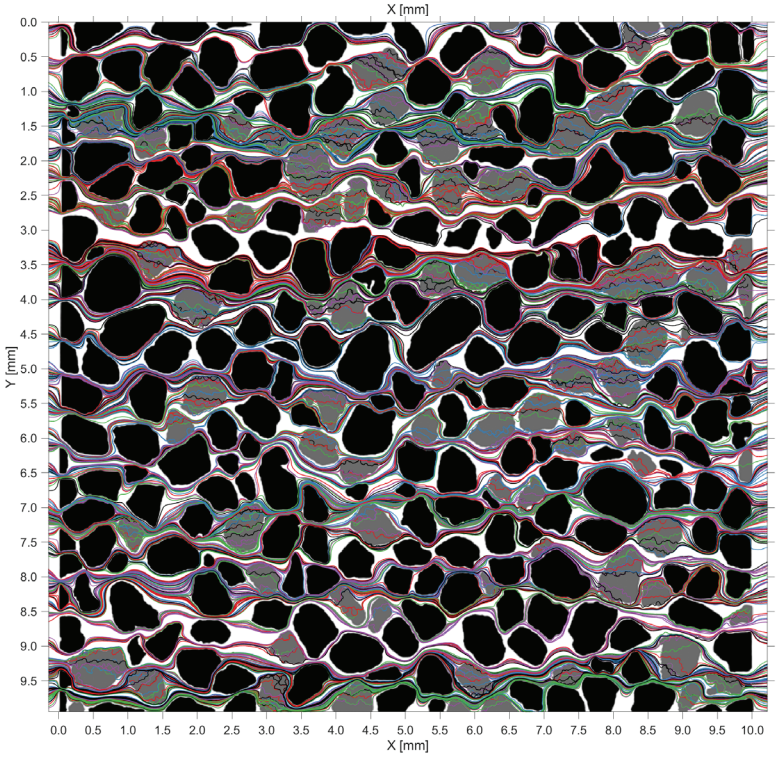

S40/25: Mobile in aggregates

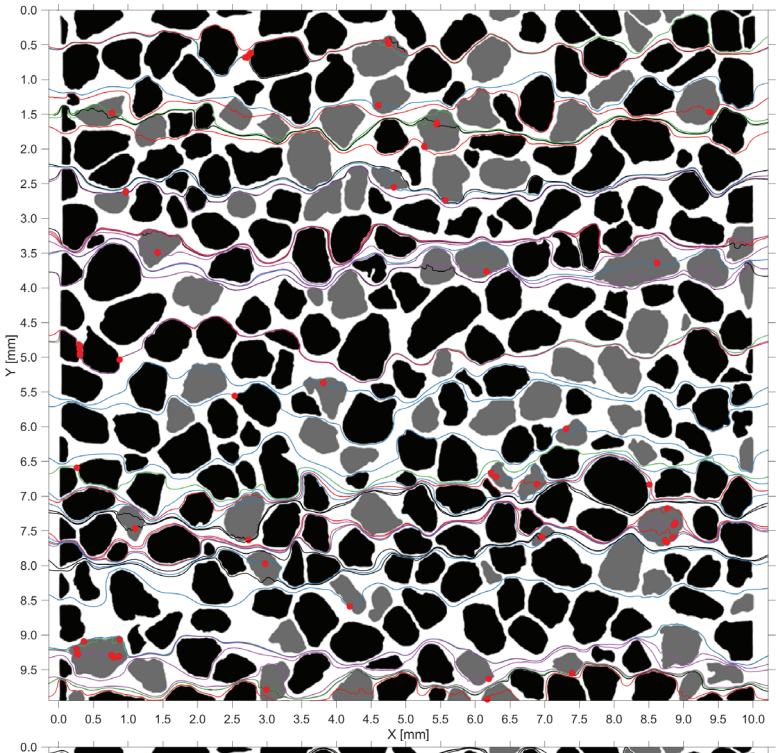

S40/25: Remobilized

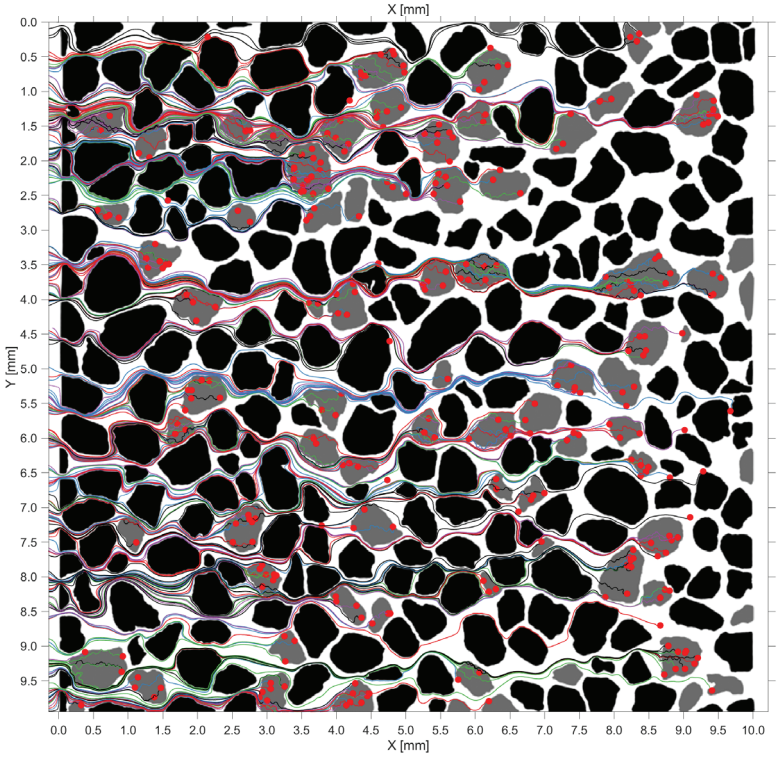

S40/25: Immobilized

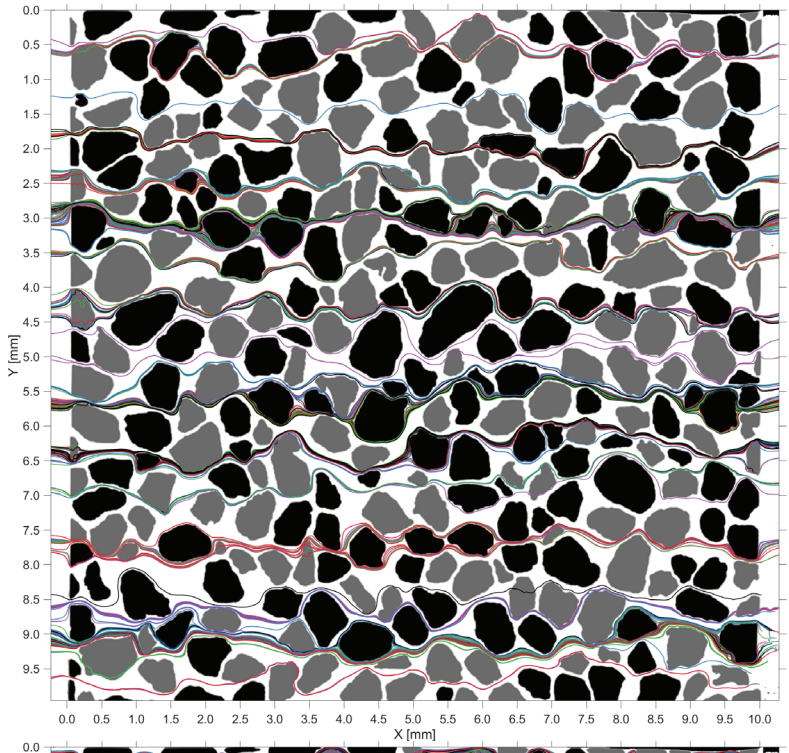

S40/50: Mobile in macropores

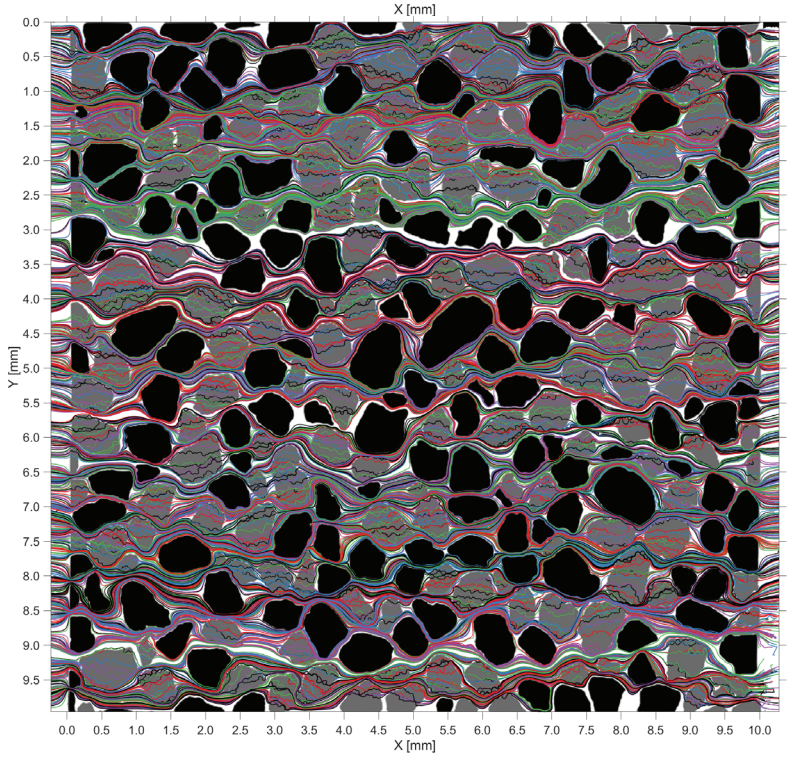

S40/50: Mobile in aggregates

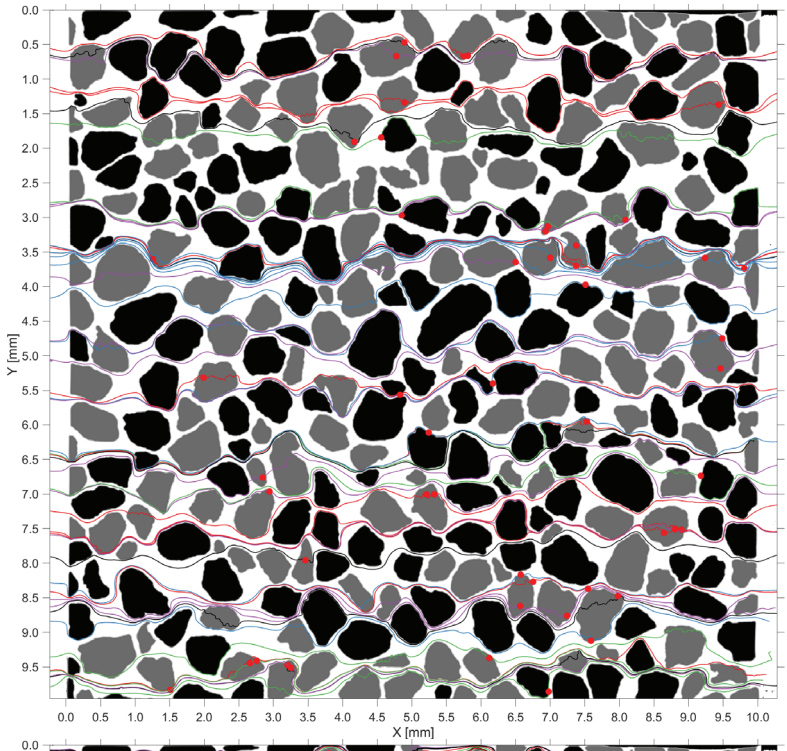

S40/50: Remobilized

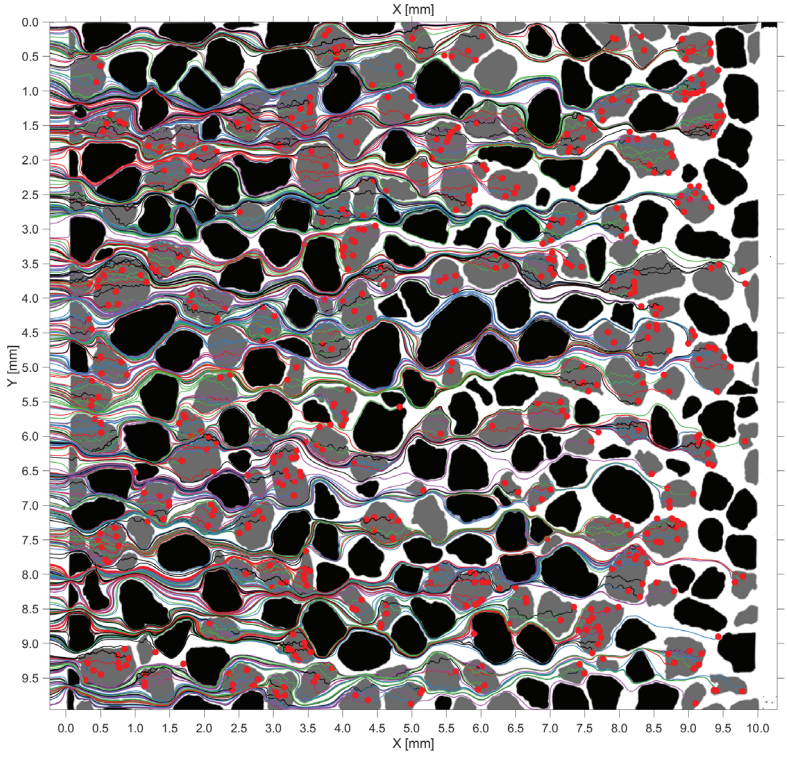

S40/50: Immobilized

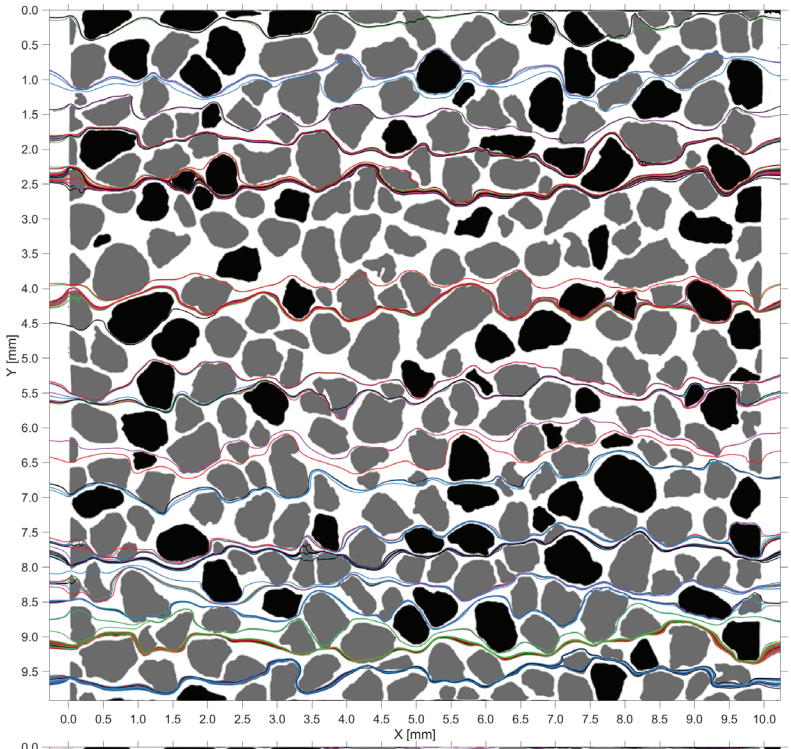

S40/75: Mobile in macropores

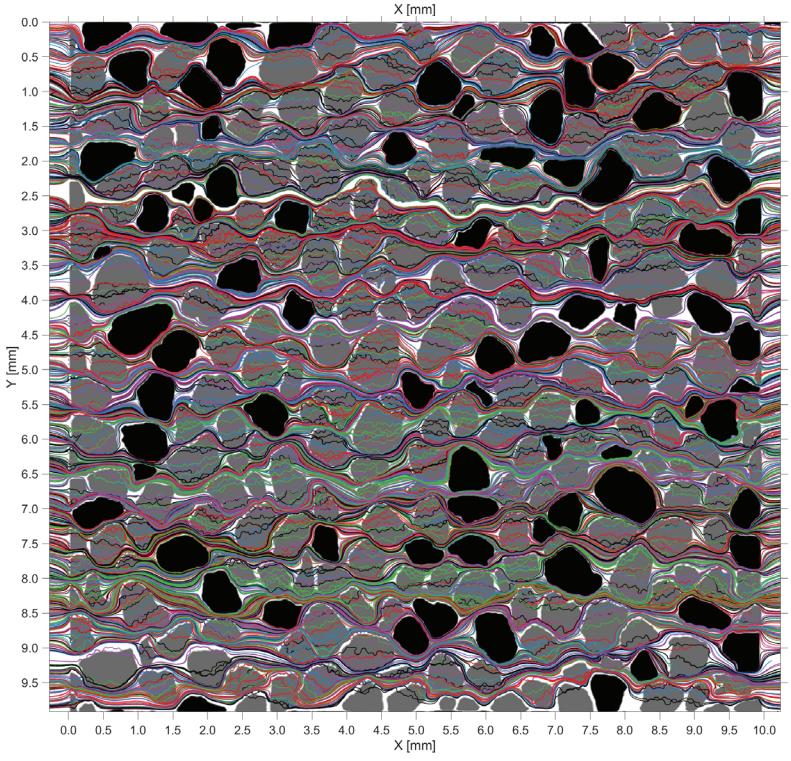

S40/75: Mobile in aggregates

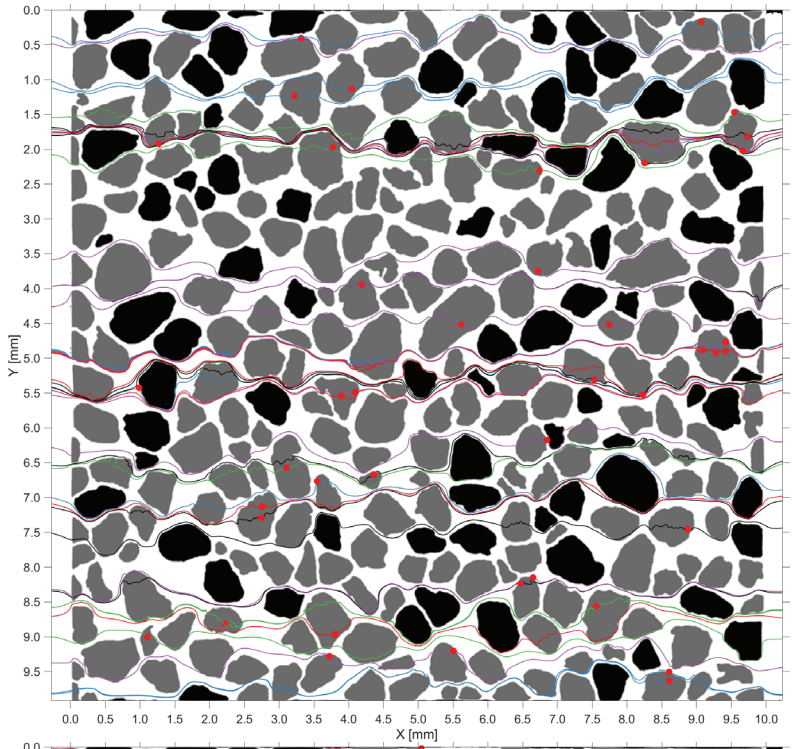

S40/75: Remobilized

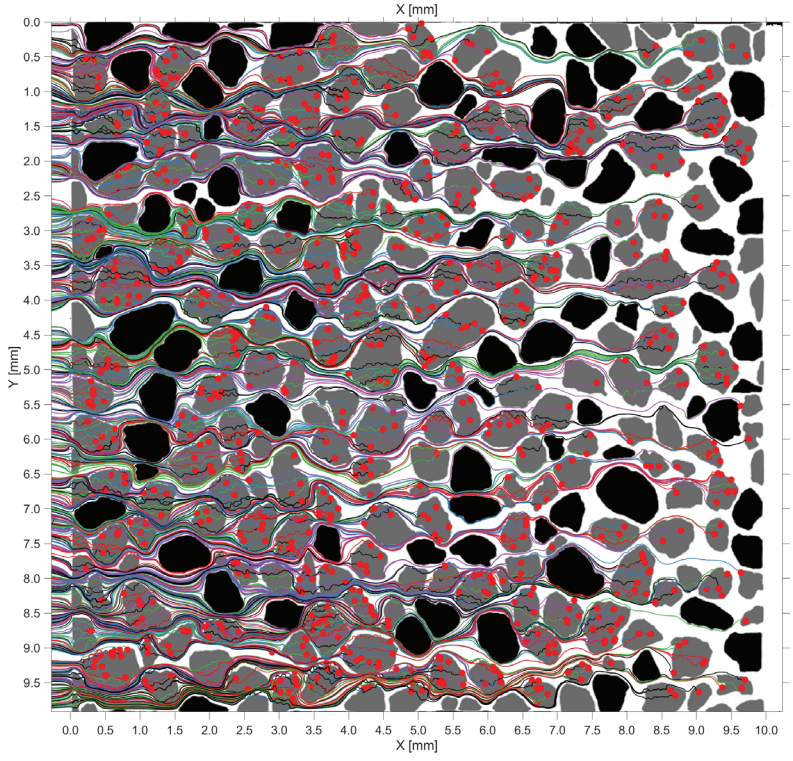

S40/75: Immobilized

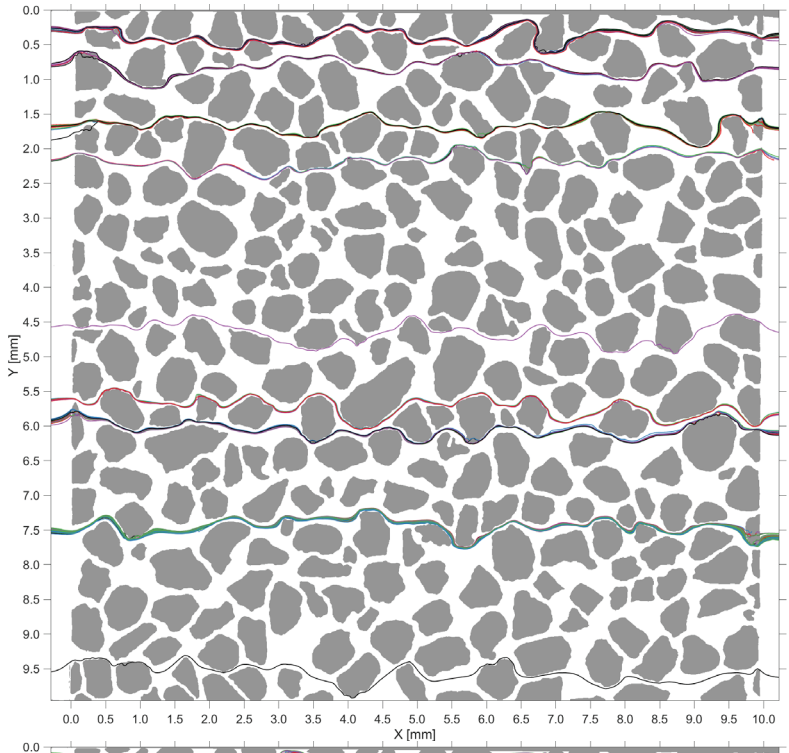

S40/100: Mobile in macropores

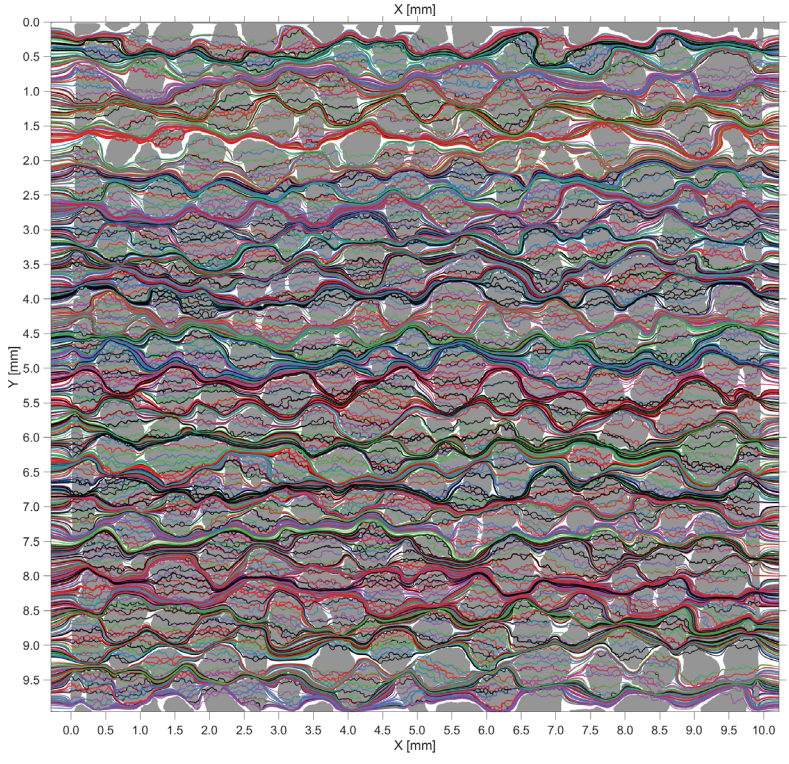

S40/100: Mobile in aggregates

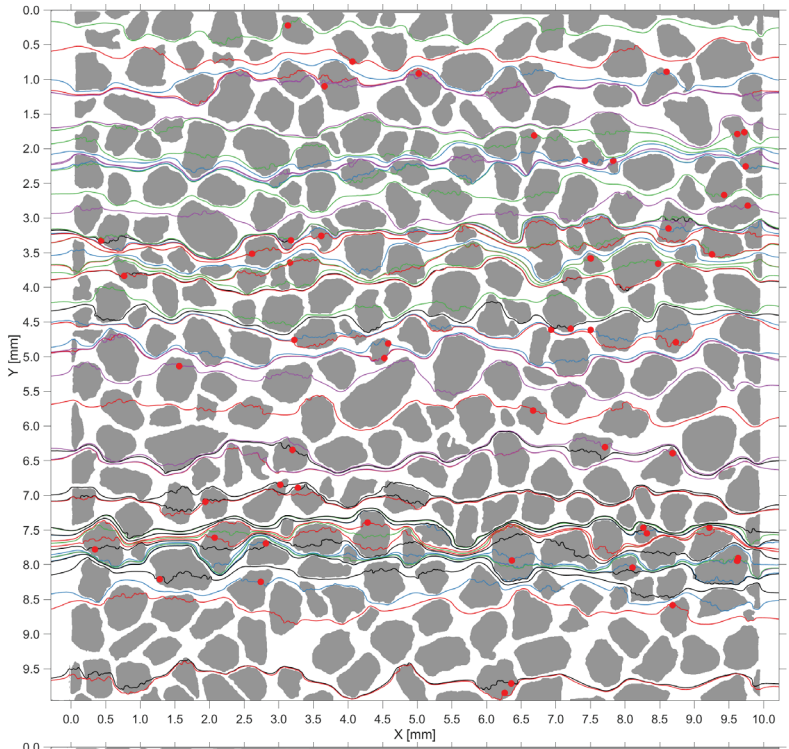

S40/100: Remobilized

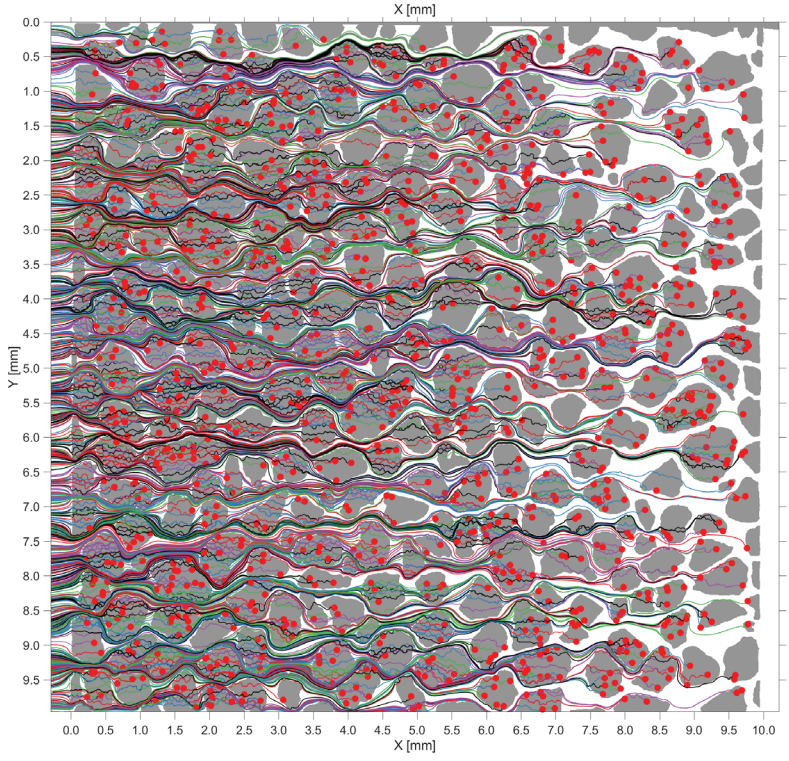

S40/100: Immobilized

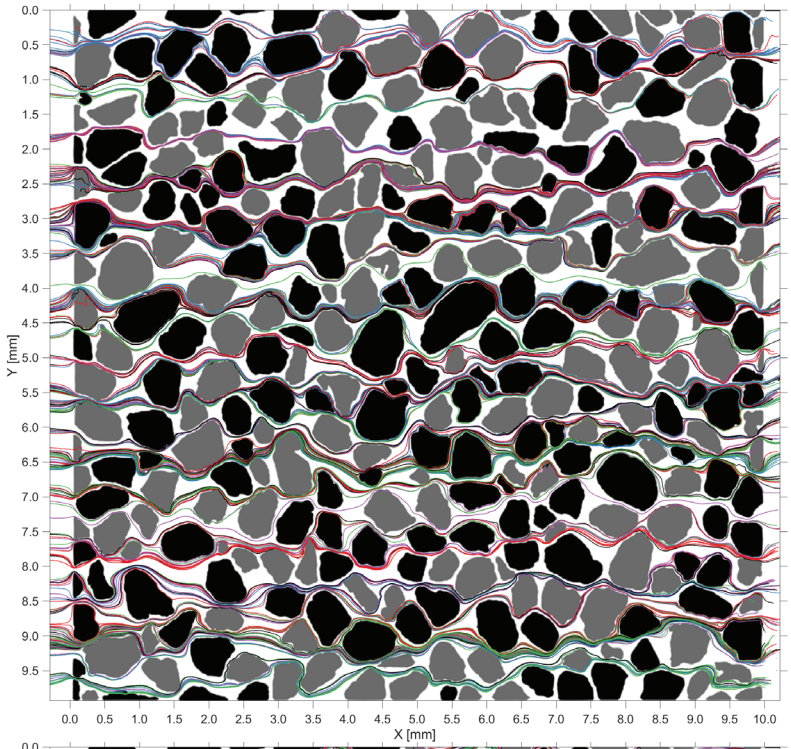

S40/50 - 1.0 m day^{-1}: Mobile in macropores

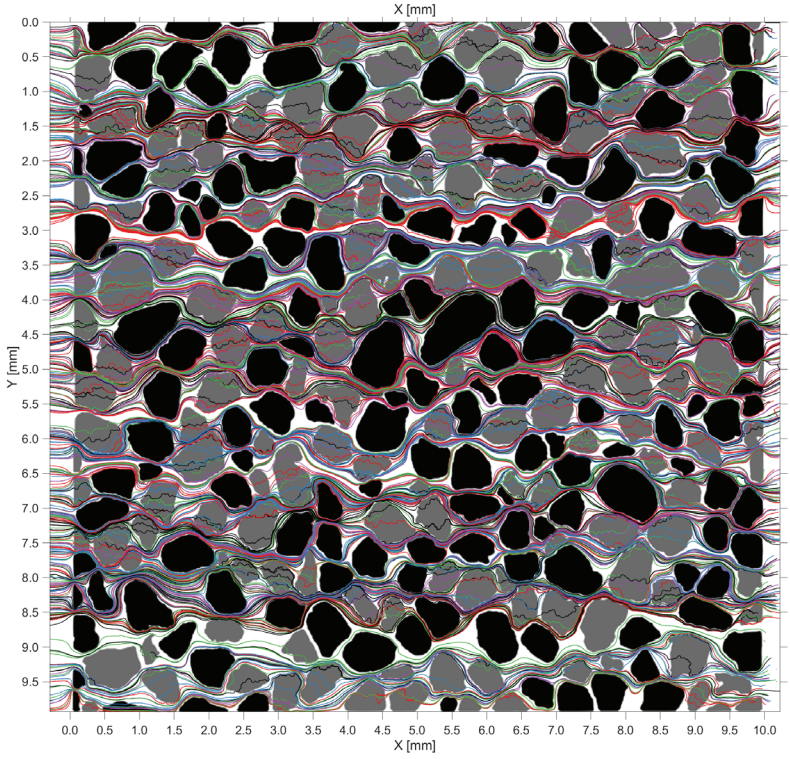

S40/50 - 1.0 m day^{-1}: Mobile in aggregates

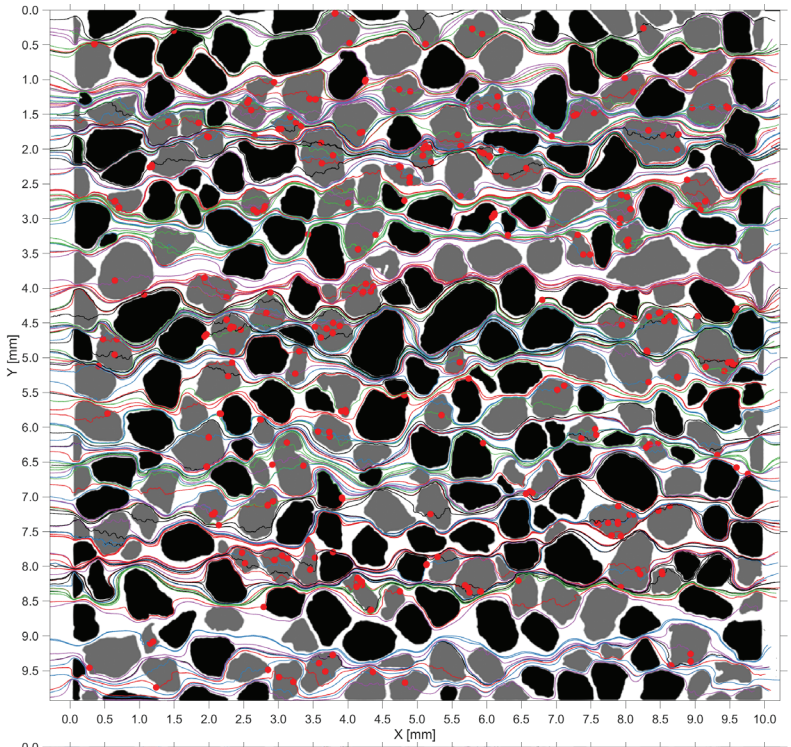

S40/50 - 1.0 m day^{-1}: Remobilized

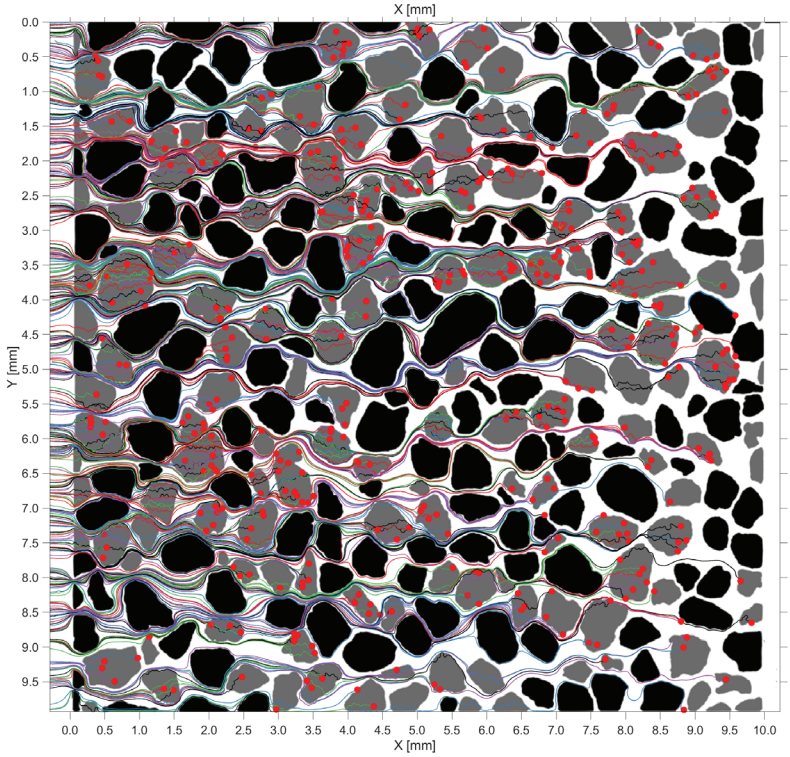

S40/50 - 1.0 m day^{-1}: Immobilized

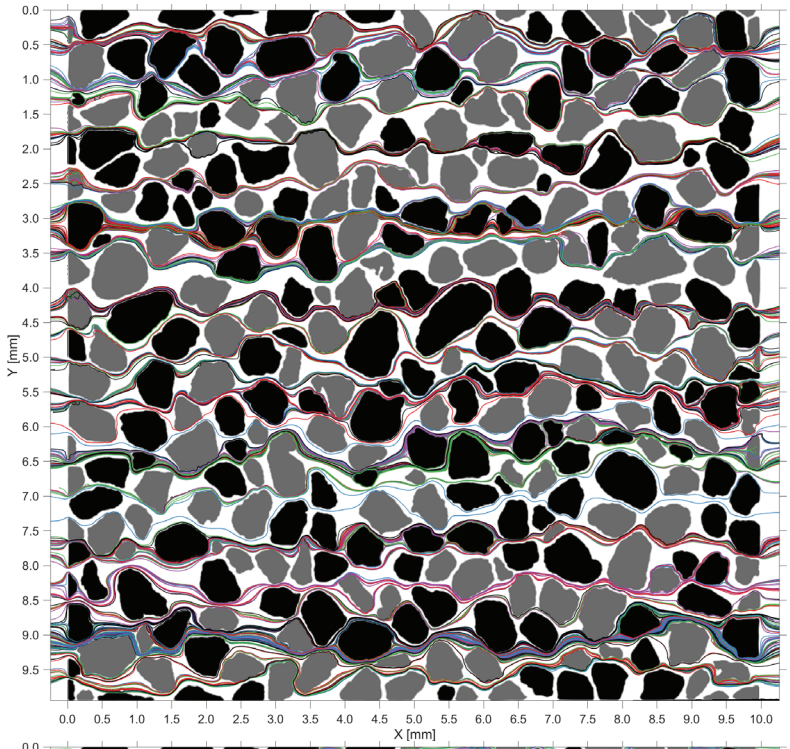

S40/50 - 5.0 m day^{-1}: Mobile in macropores

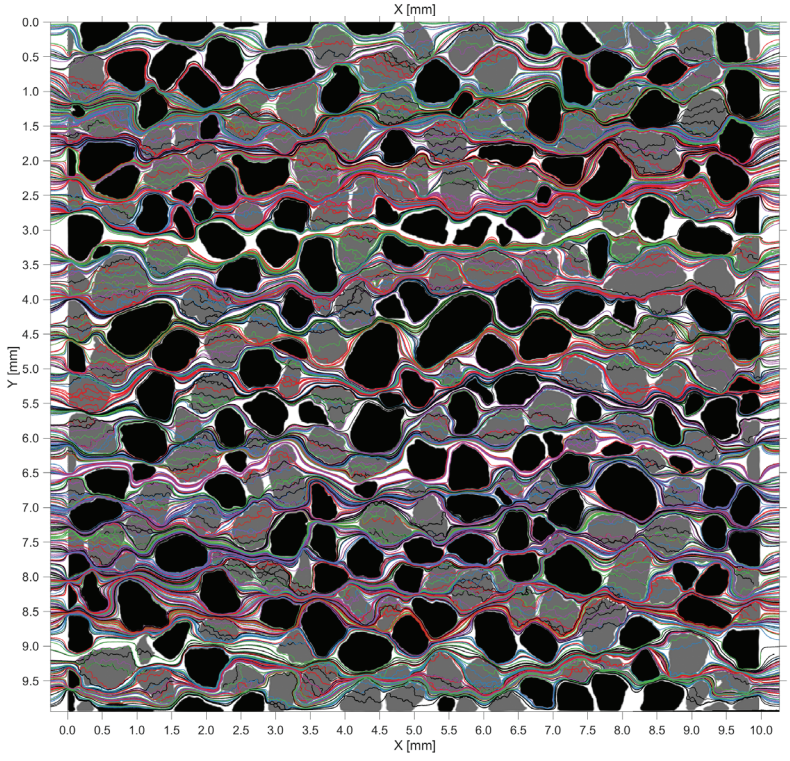

S40/50 - 5.0 m day^{-1}: Mobile in aggregates

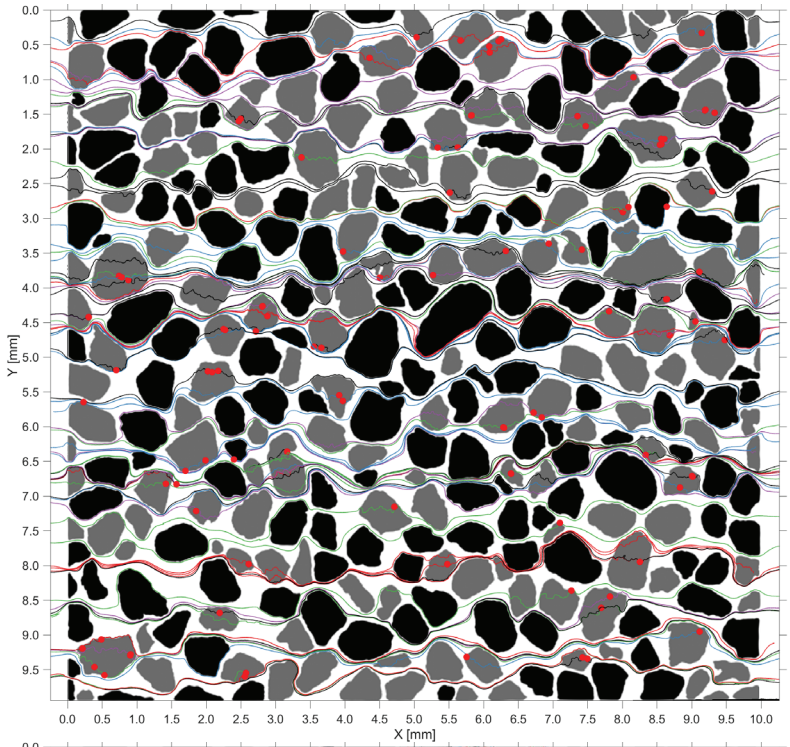

S40/50 - 5.0 m day^{-1}: Remobilized

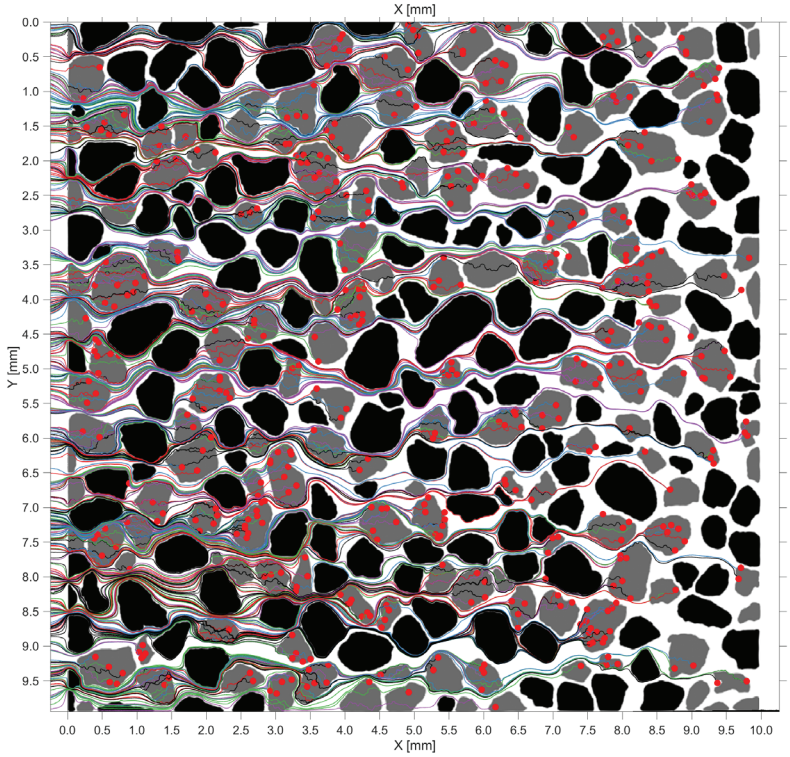

S40/50 - 5.0 m day^{-1}: Immobilized

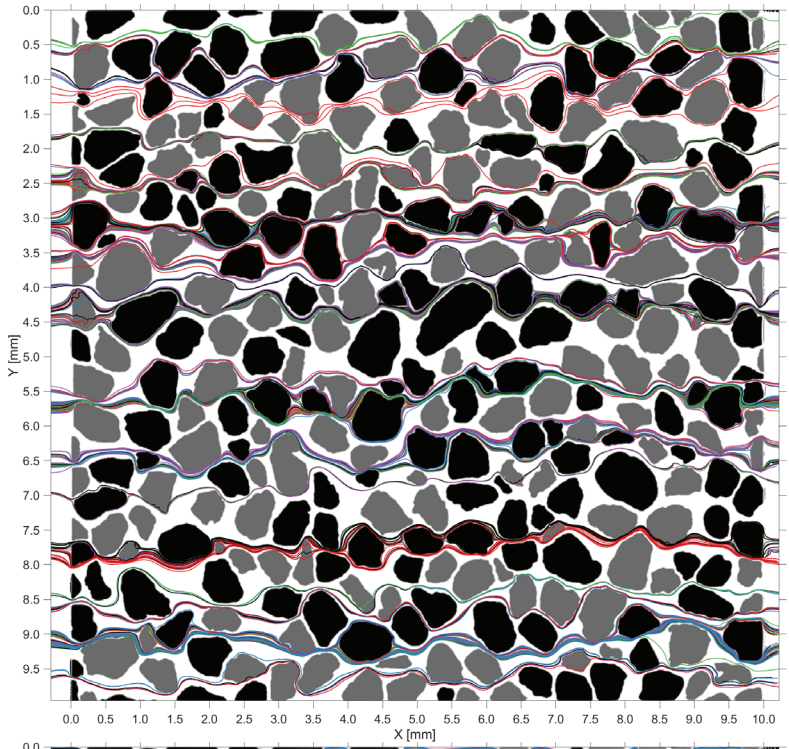

S40/50 - 12.0 m day^{-1}: Mobile in macropores

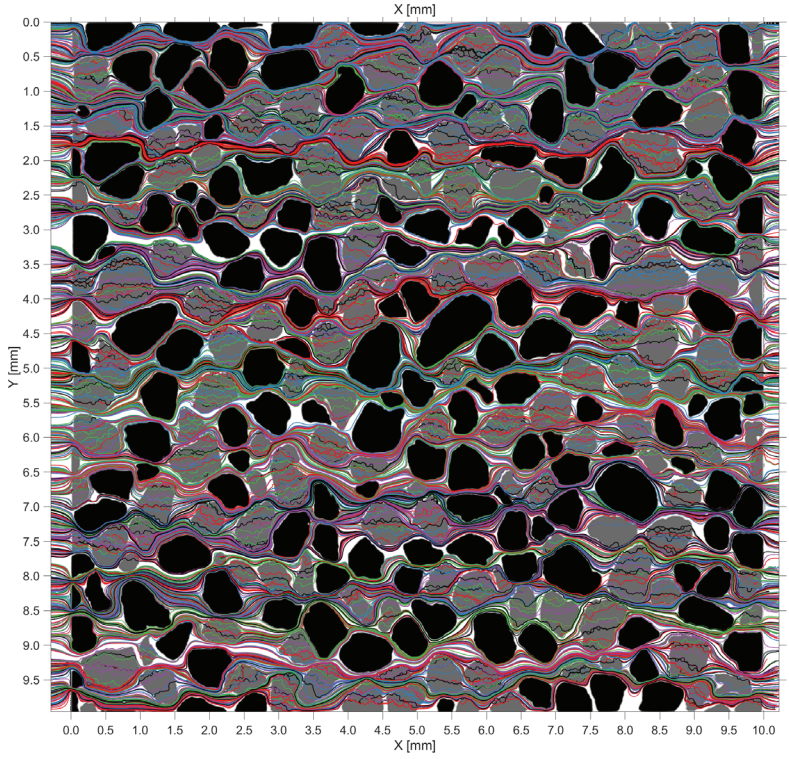

S40/50 - 12.0 m day^{-1}: Mobile in aggregates

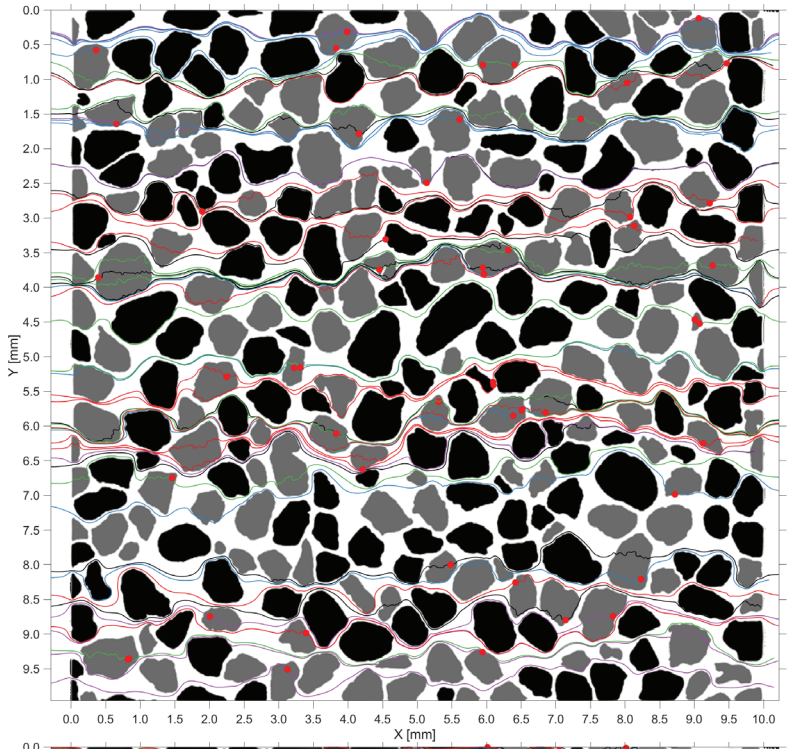

S40/50 - 12.0 m day^{-1}: Remobilized

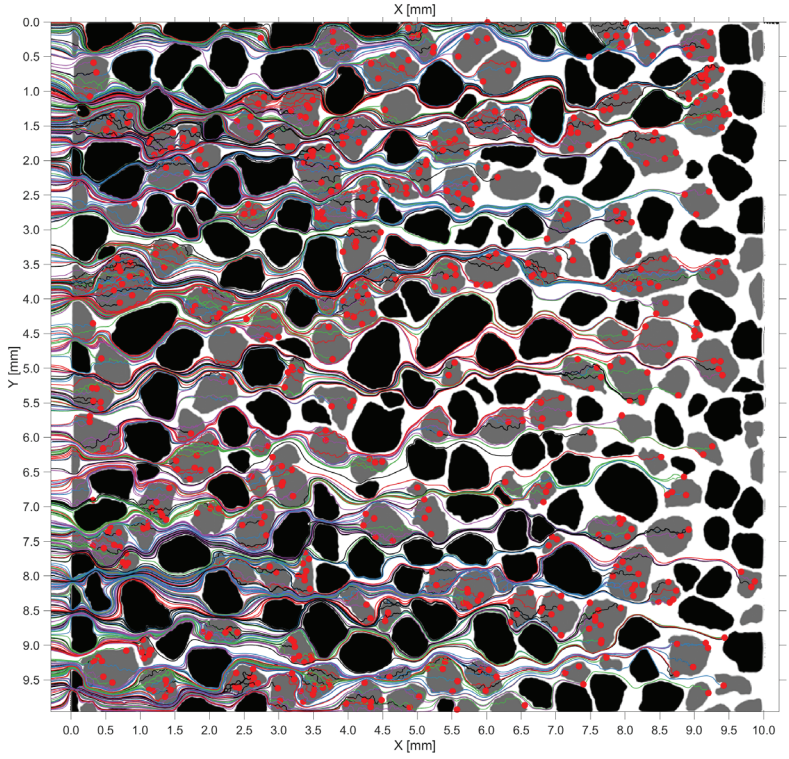

S40/50 - 12.0 m day^{-1}: Immobilized

References

Abbaspour, K. C., Kohler, A., Simunek, J., Fritsch, M., & Schulin, R. (2001a). Application of a two-dimensional model to simulate flow and transport in a macroporous agricultural soil with tile drains. *European Journal of Soil Science*, *52*(3), 433–447. doi:10.1046/j.1365-2389.2001.00389.x

Alim, K., Parsa, S., Weitz, D. A., & Brenner, M. P. (2017). Local Pore Size Correlations Determine Flow Distributions in Porous Media. *Physical Review Letters*, *119*(14), 144501. doi:10.1103/physrevlett.119.144501

Allaire, S. E., Roulier, S., & Cessna, A. J. (2009). Quantifying preferential flow in soils: A review of different techniques. *Journal of Hydrology*, *378*(1-2), 179–204. doi:10.1016/j.jhydrol.2009.08.013

Almutairi, Z., Ren, C. L., & Simon, L. (2012). Evaluation of polydimethylsiloxane (PDMS) surface modification approaches for microfluidic applications. *Colloids and Surfaces A: Physicochemical and Engineering Aspects*, *415*, 406–412. doi:10.1016/j.colsurfa.2012.10.008

Altman, S. J., Arnold, B. W., Barnard, R. W., Barr, G. E., Ho, C. K., McKenna, S. A., & Eaton, R. R. (1996). Flow calculations for Yucca Mountain groundwater travel time (GWTT-95) (No. SAND-96-0819). Sandia National Labs., Albuquerque, NM (United States).

Anna, P. de, Jimenez-Martinez, J., Tabuteau, H., Turuban, R., Borgne, T. L., Derrien, M., & Méheust, Y. (2013). Mixing and Reaction Kinetics in Porous Media: An Experimental Pore Scale Quantification. *Environmental Science & Technology*, *48*(1), 508–516. doi:10.1021/es403105b

Aramrak, S., Flury, M., & Harsh, J. B. (2011). Detachment of Deposited Colloids by Advancing and Receding Air–Water Interfaces. *Langmuir*, *27*(16), 9985–9993. doi:10.1021/la201840q

Aramrak, S., Flury, M., Harsh, J. B., Zollars, R. L., & Davis, H. P. (2013). Does Colloid Shape Affect Detachment of Colloids by a Moving Air–Water Interface? *Langmuir*, *29*(19), 5770–5780. doi:10.1021/la400252q

Argent, J., Torkzaban, S., Hubbard, S., Le, H., Amirianshoja, T., & Haghighi, M. (2015). Visualization of Micro-Particle Retention on a Heterogeneous Surface Using Micro-models: Influence of Nanoscale Surface Roughness. *Transp Porous Med*, *109*(2), 239–253. doi:10.1007/s11242-015-0511-z

Arias, M. E., González-Pérez, J. A., Gonzalez-Vila, F. J., & Ball, A. S. (2005). Soil health: A new challenge for microbiologists and chemists. *International microbiology*, *8*(1), 13–21.

Aslannejad, H., Hassanizadeh, S. M., & Celia, M. A. (2018). Characterization of the Interface Between Coating and Fibrous Layers of Paper. *Transport in Porous Media*, *127*(1), 143–155. doi:10.1007/s11242-018-1183-2

Auset, M., & Keller, A. A. (2006). Pore-scale visualization of colloid straining and filtration in saturated porous media using micromodels. *Water Resources Research*, *42*(12). doi:10.1029/2005wr004639

Baalousha, M., Lead, J. R., Kammer, F. von der, & Hofmann, T. (2009). Natural Colloids and Nanoparticles in Aquatic and Terrestrial Environments. *Environmental and human health impacts of nanotechnology*, 109–161. doi:10.1002/9781444307504.ch4

Bai, H., Cochet, N., Pauss, A., & Lamy, E. (2016). Bacteria cell properties and grain size impact on bacteria transport and deposition in porous media. *Colloids and Surfaces B: Biointerfaces*, *139*, 148–155. doi:10.1016/j.colsurfb.2015.12.016

Bai, H. J., Lassabatere, L., & Lamy, E. (2018). Colloid transport in aggregated porous media with intra-and interaggregate porosities. *Industrial & Engineering Chemistry Research*, *57*(18), 6553–6567. doi:10.1021/acs.iecr.8b00501

Bales, R. C., Gerba, C. P., Grondin, G. H., & Jensen, S. L. (1989). Bacteriophage transport in sandy soil and fractured tuff. *Applied and Environmental Microbiology*, *55*(8), 2061–2067.

Barker, J. A. (1985). Block-geometry functions characterizing transport in densely fissured media. *Journal of Hydrology*, *77*(1-4), 263–279. doi:10.1016/0022-1694(85)90211-2

Baumann, T., & Werth, C. J. (2004). Visualization and Modeling of Polystyrol Colloid Transport in a Silicon Micromodel. *Vadose Zone Journal*, *3*(2), 434–443. doi:10.2136/vzj2004.0434

Bijeljic, B., Mostaghimi, P., & Blunt, M. J. (2013). Insights into non-Fickian solute transport in carbonates. *Water Resources Research*, *49*(5), 2714–2728. doi:10.1002/wrcr.20238

Blois, G., Barros, J. M., & Christensen, K. T. (2015). A microscopic particle image velocimetry method for studying the dynamics of immiscible liquid–liquid interactions in a porous micromodel. *Microfluidics and Nanofluidics*, *18*(5-6), 1391–1406. doi:10.1007/s10404-014-1537-1

Bolt, G. H. (1979). Movement of Solutes in Soil: Principles of Adsorption/Exchange Chromatography. *Soil Chemistry: B. Physico-Chemical Models* (pp. 285–348). Elsevier. doi:10.1016/s0166-2481(08)70664-0

Bradford, S. A., Bettahar, M., Simunek, J., & Genuchten, M. T. van. (2004). Straining and Attachment of Colloids in Physically Heterogeneous Porous Media. *Vadose Zone Journal*, *3*(2), 384–394. doi:10.2113/3.2.384

Bradford, S. A., & Torkzaban, S. (2008). Colloid Transport and Retention in Unsaturated Porous Media: A Review of Interface-, Collector-, and Pore-Scale Processes and Models. *Vadose Zone Journal*, *7*(2), 667–681. doi:10.2136/vzj2007.0092

Bradford, S. A., Torkzaban, S., Leij, F., Šimnek, J., & Genuchten, M. T. van. (2009). Modeling the coupled effects of pore space geometry and velocity on colloid transport and retention. *Water Resources Research, 45*(2). doi:10.1029/2008wr007096

Bradford, S. A., & Torkzaban, S. (2015). Determining Parameters and Mechanisms of Colloid Retention and Release in Porous Media. *Langmuir*, *31*(44), 12096–12105. doi:10.1021/acs.langmuir.5b03080

Bradford, S. A., Torkzaban, S., Leij, F., & Simunek, J. (2015). Equilibrium and kinetic models for colloid release under transient solution chemistry conditions. *Journal of Contaminant Hydrology*, *181*(44), 141–152. doi:10.1016/j.jconhyd.2015.04.003

Bradford, S. A., Wang, Y., Torkzaban, S., & Šimrunek, J. (2015). Modeling the release ofE. coliD21g with transients in water content. *Water Resources Research*, *51*(5), 3303–3316. doi:10.1002/2014wr016566

Braun, A., Klumpp, E., Azzam, R., & Neukum, C. (2015). Transport and deposition of stabilized engineered silver nanoparticles in water saturated loamy sand and silty loam. *Science of The Total Environment*, *535*, 102–112. doi:10.1016/j.scitotenv.2014.12.023

Brusseau, M. L. (1993). The influence of solute size, pore water velocity, and intraparticle porosity on solute dispersion and transport in soil. *Water Resources Research*, *29*(4), 1071–1080. doi:10.1029/92wr02595

Bultreys, T., Boever, W. D., & Cnudde, V. (2016). Imaging and image-based fluid transport modeling at the pore scale in geological materials: A practical introduction to the current state-of-the-art. *Earth-Science Reviews*, *155*, 93–128. doi:10.1016/j.earscirev.2016.02.001

Bultreys, T., Hoorebeke, L. V., & Cnudde, V. (2015). Multi-scale, micro-computed tomography-based pore network models to simulate drainage in heterogeneous rocks. *Advances in Water Resources*, *78*, 36–49. doi:10.1016/j.advwatres.2015.02.003

Chatterjee, N., & Flury, M. (2013). Effect of Particle Shape on Capillary Forces Acting on Particles at the Air–Water Interface. *Langmuir*, *29*(25), 7903–7911. doi:10.1021/la4017504

Chindaprasirt, P., Hatanaka, S., Chareerat, T., Mishima, N., & Yuasa, Y. (2008). Cement paste characteristics and porous concrete properties. *Construction and Building Materials*, *22*(5), 894–901. doi:10.1016/j.conbuildmat.2006.12.007

Clothier, B. E., Kirkham, M. B., & McLean, J. E. (1992). In Situ Measurement of the Effective Transport Volume for Solute Moving Through Soil. *Soil Science Society of America Journal*, *56*(3), 733–736. doi:10.2136/sssaj1992.03615995005600030010x

Cnudde, V., & Boone, M. N. (2013). High-resolution X-ray computed tomography in geosciences: A review of the current technology and applications. *Earth-Science Reviews*, *123*, 1–17. doi:10.1016/j.earscirev.2013.04.003

Coats, K. H., & Smith, B. D. (1964). Dead-End Pore Volume and Dispersion in Porous Media. *Society of Petroleum Engineers Journal*, *4*(01), 73–84. doi:10.2118/647-pa

Corapcioglu, Y. M., Chowdhury, S., & Roosevelt, S. E. (1997). Micromodel visualization and quantification of solute transport in porous media. *Water Resources Research*, *33*(11), 2547–2558. doi:10.1029/97wr02115

Czachor, H., Charytanowicz, M., Gonet, S., Niewczas, J., Jozefaciuk, G., & Lichner, L. (2015). Impact of long-term mineral and organic fertilizer application on the water stability, wettability and porosity of aggregates obtained from two loamy soils. *European Journal of Soil Science*, *66*(3), 577–588. doi:10.1111/ejss.12242

Degens, B. P., Sparling, G. P., & Abbott, L. K. (1996). Increasing the length of hyphae in a sandy soil increases the amount of water-stable aggregates. *Applied Soil Ecology*, *3*(2), 149–159. doi:10.1016/0929-1393(95)00074-7

Engdahl, N. B. (2018). Simulating the mobility of micro-plastics and other fiber-like objects in saturated porous media using constrained random walks. *Advances in Water Resources*, *121*, 277–284. doi:10.1016/j.advwatres.2018.08.011

Fathi, H., Raoof, A., & Mansouri, S. H. (2017). Insights into the role of wettability in cathode catalyst layer of proton exchange membrane fuel cell; pore scale immiscible flow and transport processes. *Journal of Power Sources*, *349*, 57–67. doi:10.1016/j.jpowsour.2017.03.012

Fathi, H., Raoof, A., Mansouri, S. H., & Genuchten, M. T. van. (2017). Effects of Porosity and Water Saturation on the Effective Diffusivity of a Cathode Catalyst Layer. *Journal of The Electrochemical Society*, *164*(4), F298–F305. doi:10.1149/2.0871704jes

Ferro, N. D., Berti, A., Francioso, O., Ferrari, E., Matthews, G. P., & Morari, F. (2012). Investigating the effects of wettability and pore size distribution on aggregate stability: the role of soil organic matter and the humic fraction. *European Journal of Soil Science*, *63*(2), 152–164. doi:10.1111/j.1365-2389.2012.01427.x

Ferro, N. D., Charrier, P., & Morari, F. (2013). Dual-scale micro-CT assessment of soil structure in a long-term fertilization experiment. *Geoderma*, *204-205*, 84–93. doi:10.1016/j.geoderma.2013.04.012

Fetter, C. W., Boving, T., & Kreamer, D. (2017). Contaminant hydrogeology. *Waveland Press.*

Flury, M., & Aramrak, S. (2017). Role of air-water interfaces in colloid transport in porous media: A review. *Water Resources Research*, *53*(7), 5247–5275. doi:10.1002/2017wr020597

Flury, M., Flühler, H., Jury, W. a., & Leuenberger, J. (1994). Susceptibility of soils to preferential flow of water: A field study. *Water Resources Research*, *30*(7), 1945. doi:10.1029/94WR00871

Genuchten, M. T. van, & Parker, J. C. (1984). Boundary conditions for displacement experiments through short laboratory soil columns. Soil Science Society of America Journal, 48(4), 703-708.

Genuchten, M. T. van. (1985). General approach for modeling solute transport in structured soils. *Memoires Int. Assoc. Hydrogeol*, *17*(2), 473–480.

Genuchten, M. T. van, & Dalton, F. N. (1986). Models for simulating salt movement in aggregated field soils. *Geoderma*, *38*(1-4), 165–183. doi:10.1016/0016-7061(86)90013-3

Genuchten, M. T. van, Tang, D. H., & Guennelon, R. (1984). Some Exact Solutions for Solute Transport Through Soils Containing Large Cylindrical Macropores. *Water Resources Research*, *20*(3), 335–346. doi:10.1029/wr020i003p00335

Genuchten, M. T. van, & Wierenga, P. J. (1976). Mass Transfer Studies in Sorbing Porous Media I. Analytical Solutions. *Soil Science Society of America Journal*, *40*(4), 473–480. doi:10.2136/sssaj1976.03615995004000040011x

Gerke, H. H. (2006). Preferential flow descriptions for structured soils. *Journal of Plant Nutrition and Soil Science*, *169*(3), 382–400. doi:10.1002/jpln.200521955

Gerke, H. H., & Genuchten, M. T. van. (1993). A Dual-Porosity Model for Simulating the Preferential Movement of Water and Solutes in Structured Porous Media. *Water Resources Research*, *29*(2), 305–319.

Gerritse, R. G., & Singh, R. (1988). The relationship between pore water velocity and longitudinal dispersivity of Cl-, Br-, and D2O in soils. *Journal of Hydrology*, *104*(1-4), 173–180. doi:10.1016/0022-1694(88)90164-3

Godoy, W., Pontedeiro, E. M., Hoerlle, F., Raoof, A., Genuchten, M. T. van, Santiago, J., & Couto, P. (2019). Computational and experimental pore-scale studies of a carbonate rock sample. *Journal of Hydrology and Hydromechanics*, *67*(4), 372–383. doi:10.2478/johh-2019-0009

Goltz, M. N., & Roberts, P. V. (1987). Using the method of moments to analyze three-dimensional diffusion-limited solute transport from temporal and spatial perspectives. *Water Resources Research*, *23*(8), 1575–1585. doi:10.1029/wr023i008p01575

Gottschalk, F., & Nowack, B. (2011). The release of engineered nanomaterials to the environment. *Journal of Environmental Monitoring*, *13*(5), 1145. doi:10.1039/c0em00547a

Hantush, M. M., Govindaraju, R. S., Mariño, M. A., & Zhang, Z. (2002). Screening model for volatile pollutants in dual porosity soils. *Journal of Hydrology*, *260*(1-4), 58–74. doi:10.1016/s0022-1694(01)00597-2

Hantush, M. M., & Mariño, M. A. (1998). Interlayer Diffusive Transfer and Transport of Contaminants in Stratified Formation I: Theory. *Journal of Hydrologic Engineering*, *3*(4), 232–240. doi:10.1061/(asce)1084-0699(1998)3:4(232)

Hantush, M. M., Mariño, M. A., & Islam, M. R. (2000). Models for leaching of pesticides in soils and groundwater. *Journal of Hydrology*, *227*(1-4), 66–83. doi:10.1016/s0022-1694(99)00166-3

Helm, M. W. van der, Meer, A. D. van der, Eijkel, J. C. T., Berg, A. van den, & Segerink, L. I. (2016). Microfluidic organ-on-chip technology for blood-brain barrier research. *Tissue Barriers*, *4*(1). doi:10.1080/21688370.2016.1142493

Hemes, S., Desbois, G., Urai, J. L., Schröppel, B., & Schwarz, J.-O. (2015). Multi-scale characterization of porosity in Boom Clay (HADES-level, Mol, Belgium) using a combination of X-ray μ-CT, 2D BIB-SEM and FIB-SEM tomography. *Microporous and Mesoporous Materials*, *208*, 1–20. doi:10.1016/j.micromeso.2015.01.022

Hendrickx, J. M. H., & Flury, M. (2001). Uniform and preferential flow mechanisms in the vadose zone. *Conceptual models of flow and transport in the fractured vadose zone. Natl.Acad.Press, Washington, DC*, 149–187.

Hill, D. N., Popova, I. E., Hammel, J. E., & Morra, M. J. (2019). Transport of Potential Manure Hormone and Pharmaceutical Contaminants through Intact Soil Columns. *Journal of Environmental Quality*, *48*(1), 47–56. doi:10.2134/jeq2018.06.0233

Hillel, D. (2003). Introduction to environmental soil physics. *Elsevier*.

Jafari, S., Yamamoto, R., & Rahnama, M. (2011). Lattice-Boltzmann method combined with smoothed-profile method for particulate suspensions. *Physical Review E*, *83*(2), 026702. doi:10.1103/physreve.83.026702

Jaqaman, K., Loerke, D., Mettlen, M., Kuwata, H., Grinstein, S., Schmid, S. L., & Danuser, G. (2008). Robust single-particle tracking in live-cell time-lapse sequences. *Nature Methods*, *5*(8), 695–702. doi:10.1038/nmeth.1237

Jarvis, N. J. (2007). A review of non-equilibrium water flow and solute transport in soil macropores: principles, controlling factors and consequences for water quality. *European Journal of Soil Science*, *58*(3), 523–546. doi:10.1111/j.1365-2389.2007.00915.x

Jaynes, D., & Shao, M. (1999). Evaluation of a simple technique for estimating two-domain transport parameters. *Soil science*, *164*(2), 82–91.

Jenni, A., Gimmi, T., Alt-Epping, P., Mäder, U., & Cloet, V. (2017). Interaction of ordinary Portland cement and Opalinus Clay: Dual porosity modelling compared to experimental data. *Physics and Chemistry of the Earth, Parts A/B/C*, *99*, 22–37. doi:10.1016/j.pce.2017.01.004

Jiang, S., Pang, L., Buchan, G. D., Šimrunek, J., Noonan, M. J., & Close, M. E. (2010). Modeling water flow and bacterial transport in undisturbed lysimeters under irrigations of dairy shed effluent and water using HYDRUS-1D. *Water Research*, *44*(4), 1050–1061. doi:10.1016/j.watres.2009.08.039

Jiang, Z., Dijke, M. I. J. van, Sorbie, K. S., & Couples, G. D. (2013). Representation of multiscale heterogeneity via multiscale pore networks. *Water Resources Research*, *49*(9), 5437–5449. doi:10.1002/wrcr.20304

Jiménez-Martinez, J., Anna, P. de, Tabuteau, H., Turuban, R., Borgne, T. L., & Méheust, Y. (2015). Pore-scale mechanisms for the enhancement of mixing in unsaturated porous media and implications for chemical reactions. *Geophysical Research Letters*, *42*(13), 5316–5324. doi:10.1002/2015gl064513

Jiménez-Martinez, J., Borgne, T. L., Tabuteau, H., & Méheust, Y. (2017). Impact of saturation on dispersion and mixing in porous media: Photobleaching pulse injection experiments and shear-enhanced mixing model. *Water Resources Research*, *53*(2), 1457–1472. doi:10.1002/2016wr019849

Jiménez-Martinez, J., Porter, M. L., Hyman, J. D., Carey, J. W., & Viswanathan, H. S. (2016). Mixing in a three-phase system: Enhanced production of oil-wet reservoirs by CO2 injection. *Geophysical Research Letters*, *43*(1), 196–205. doi:10.1002/2015gl066787

Karadimitriou, N. K., Joekar-Niasar, V., Babaei, M., & Shore, C. A. (2016). Critical Role of the Immobile Zone in Non-Fickian Two-Phase Transport: A New Paradigm. *Environmental Science & Technology*, *50*(8), 4384–4392. doi:10.1021/acs.est.5b05947

Karadimitriou, N. K., Musterd, M., Kleingeld, P. J., Kreutzer, M. T., Hassanizadeh, S. M., & Joekar-Niasar, V. (2013). On the fabrication of PDMS micromodels by rapid prototyping, and their use in two-phase flow studies. *Water Resources Research*, *49*(4), 2056–2067. doi:10.1002/wrcr.20196

Kirby, B. J., & Hasselbrink, E. F. (2004). Zeta potential of microfluidic substrates: 2. Data for polymers. *Electrophoresis*, *25*(2), 203–213. doi:10.1002/elps.200305755

Kjeldsen, P., Barlaz, M. A., Rooker, A. P., Baun, A., Ledin, A., & Christensen, T. H. (2002). Present and Long-Term Composition of MSW Landfill Leachate: A Review. *Critical Reviews in Environmental Science and Technology*, *32*(4), 297–336. doi:10.1080/10643380290813462

Klotz, D., Seiler, K.-P., Moser, H., & Neumaier, F. (1980). Dispersivity and velocity relationship from laboratory and field experiments. *Journal of Hydrology*, *45*(3-4), 169–184. doi:10.1016/0022-1694(80)90018-9

Knappenberger, T., Flury, M., Mattson, E. D., & Harsh, J. B. (2014). Does Water Content or Flow Rate Control Colloid Transport in Unsaturated Porous Media? *Environmental Science & Technology*, *48*(7), 3791–3799. doi:10.1021/es404705d

Kohler-Milleret, R., Bayon, R.-C. L., Chenu, C., Gobat, J.-M., & Boivin, P. (2013). Impact of two root systems, earthworms and mycorrhizae on the physical properties of an unstable silt loam Luvisol and plant production. *Plant and Soil*, *370*(1-2), 251–265. doi:10.1007/s11104-013-1621-4

Köhne, J. M., Köhne, S., & Šimrunek, J. (2009). A review of model applications for structured soils: a) Water flow and tracer transport. *Journal of Contaminant Hydrology*, *104*(1-4), 4–35. doi:10.1016/j.jconhyd.2008.10.002

Kolpin, D. W., Furlong, E. T., Meyer, M. T., Thurman, E. M., Zaugg, S. D., Barber, L. B., & Buxton, H. T. (2002). Pharmaceuticals, Hormones, and Other Organic Wastewater Contaminants in U.S. Streams, 1999-2000: A National Reconnaissance. *Environmental Science & Technology*, *36*(6), 1202–1211. doi:10.1021/es011055j

Kretzschmar, R., Borkovec, M., Grolimund, D., & Elimelech, M. (1999). Mobile Subsurface Colloids and Their Role in Contaminant Transport. *Advances in Agronomy*, *66*, 121–193. doi:10.1016/s0065-2113(08)60427-7

Kretzschmar, R., & Schafer, T. (2005). Metal Retention and Transport on Colloidal Particles in the Environment. *Elements*, *1*(4), 205–210. doi:10.2113/gselements.1.4.205

Kumahor, S. K., Hron, P., Metreveli, G., Schaumann, G. E., & Vogel, H.-J. (2015). Transport of citrate-coated silver nanoparticles in unsaturated sand. *Science of The Total Environment*, *535*, 113–121. doi:10.1016/j.scitotenv.2015.03.023

Lazouskaya, V., Wang, L.-P., Gao, H., Shi, X., Czymmek, K., & Jin, Y. (2011). Pore-Scale Investigation of Colloid Retention and Mobilization in the Presence of a Moving Air–Water Interface. *Vadose Zone Journal*, *10*(4), 1250–1260. doi:10.2136/vzj2011.0003

Lazouskaya, V., Wang, L.-P., Or, D., Wang, G., Caplan, J. L., & Jin, Y. (2013). Colloid mobilization by fluid displacement fronts in channels. *Journal of Colloid and Interface Science*, *406*, 44–50. doi:10.1016/j.jcis.2013.05.078

Leij, F. J., & Bradford, S. A. (2013). Colloid transport in dual-permeability media. *Journal of Contaminant Hydrology*, *150*, 65–76. doi:10.1016/j.jconhyd.2013.03.010

Li, J., Song, Y., & Cai, Y. (2020). Focus topics on microplastics in soil: Analytical methods, occurrence, transport, and ecological risks. *Environmental Pollution*, *257*, 113570. doi:10.1016/j.envpol.2019.113570

Linares, N., Hartmann, S., Galarneau, A., & Barbaro, P. (2012). Continuous Partial Hydrogenation Reactions by Pd@unconventional Bimodal Porous Titania Monolith Catalysts. *ACS Catalysis*, *2*(10), 2194–2198. doi:10.1021/cs3005902

Lindeberg, T. (1998). Feature Detection with Automatic Scale Selection. *International Journal of Computer Vision*, *30*(2), 79–116. doi:10.1023/a:1008045108935

Liu, Q., Zhao, B., & Santamarina, J. C. (2019). Particle Migration and Clogging in Porous Media: A Convergent Flow Microfluidics Study. *Journal of Geophysical Research: Solid Earth*, *124*(9), 9495–9504. doi:10.1029/2019jb017813

Luque-Espinar, J. A., & Chica-Olmo, M. (2019). Impacts of Anthropogenic Activities on Groundwater Quality in a Detritic Aquifer in SE Spain. *Exposure and Health*, *12*(4), 681–698. doi:10.1007/s12403-019-00327-7

Ma, L., Liu, Y., Zhang, J., Yang, Q., Li, G., & Zhang, D. (2018). Impacts of irrigation water sources and geochemical conditions on vertical distribution of pharmaceutical and personal care products (PPCPs) in the vadose zone soils. *Science of The Total Environment*, *626*, 1148–1156. doi:10.1016/j.scitotenv.2018.01.168

Mahmoodlu, M. G., Hartog, N., Hassanizadeh, S. M., & Raoof, A. (2013). Oxidation of volatile organic vapours in air by solid potassium permanganate. *Chemosphere*, *91*(11), 1534–1538. doi:10.1016/j.chemosphere.2012.12.035

Mahmoodlu, M. G., Hassanizadeh, S. M., Hartog, N., & Raoof, A. (2014). Oxidation of trichloroethylene, toluene, and ethanol vapors by a partially saturated permeable reactive barrier. *Journal of Contaminant Hydrology*, *164*, 193–208. doi:10.1016/j.jconhyd.2014.05.013

Mahmoodlu, M. G., Raoof, A., Bultreys, T., Stappen, J. V., & Cnudde, V. (2020). Large-scale pore network and continuum simulations of solute longitudinal dispersivity of a saturated sand column. *Advances in Water Resources*, *144*, 103713. doi:10.1016/j.advwatres.2020.103713

Mangalassery, S., Sjögersten, S., Sparkes, D. L., Sturrock, C. J., & Mooney, S. J. (2013). The effect of soil aggregate size on pore structure and its consequence on emission of greenhouse gases. *Soil and Tillage Research*, *132*, 39–46. doi:10.1016/j.still.2013.05.003

Maraqa, M. A. (2001). Prediction of mass-transfer coefficient for solute transport in porous media. *Journal of Contaminant Hydrology*, *50*(1-2), 1–19. doi:10.1016/s0169-7722(01)00107-3

Martinez, F. S. J., Ortega, F. J. M., Monreal, F. J. C., Kravchenko, A. N., & Wang, W. (2015). Soil aggregate geometry: Measurements and morphology. *Geoderma*, *237-238*, 36–48. doi:10.1016/j.geoderma.2014.08.003

Massoudieh, A., & Ginn, T. R. (2010). Colloid-Facilitated Contaminant Transport in Unsaturated Porous Media. *ILM Publications*.

Mehmani, A., Mehmani, Y., Prodanovic, M., & Balhoff, M. (2015). A forward analysis on the applicability of tracer breakthrough profiles in revealing the pore structure of tight gas sandstone and carbonate rocks. *Water Resources Research*, *51*(6), 4751–4767. doi:10.1002/2015wr016948

Mehmani, A., & Prodanovic, M. (2014). The effect of microporosity on transport properties in porous media. *Advances in Water Resources*, *63*, 104–119. doi:10.1016/j.advwatres.2013.10.009

Miele, F., Anna, P. de, & Dentz, M. (2019). Stochastic model for filtration by porous materials. *Physical Review Fluids*, *4*(9). doi:10.1103/physrevfluids.4.094101

Miller, A. W., Rodriguez, D. R., & Honeyman, B. D. (2010). Upscaling Sorption/Desorption Processes in Reactive Transport Models To Describe Metal/Radionuclide Transport: A Critical Review. *Environmental Science & Technology*, *44*(21), 7996–8007. doi:10.1021/es101822v

Mitropoulou, P. N., Syngouna, V. I., & Chrysikopoulos, C. V. (2013). Transport of colloids in unsaturated packed columns: Role of ionic strength and sand grain size. *Chemical Engineering Journal*, *232*, 237–248. doi:10.1016/j.cej.2013.07.093

Mohanty, S. K., Saiers, J. E., & Ryan, J. N. (2015). Colloid Mobilization in a Fractured Soil during Dry–Wet Cycles: Role of Drying Duration and Flow Path Permeability. *Environmental Science & Technology*, *49*(15), 9100–9106. doi:10.1021/acs.est.5b00889

Mohanty, S. K., Saiers, J. E., & Ryan, J. N. (2016). Colloid Mobilization in a Fractured Soil: Effect of Pore-Water Exchange between Preferential Flow Paths and Soil Matrix. *Environmental Science & Technology*, *50*(5), 2310–2317. doi:10.1021/acs.est.5b04767

Molnar, I. L., Gerhard, J. I., Willson, C. S., & O'Carroll, D. M. (2015). The impact of immobile zones on the transport and retention of nanoparticles in porous media. *Water Resources Research*, *51*(11), 8973–8994. doi:10.1002/2015wr017167

Molnar, I. L., Johnson, W. P., Gerhard, J. I., Willson, C. S., & O'Carroll, D. M. (2015). Predicting colloid transport through saturated porous media: A critical review. Water Resources Research, 51(9), 6804–6845. doi:10.1002/2015wr017318

Neukum, C., Braun, A., & Azzam, R. (2014). Transport of stabilized engineered silver (Ag) nanoparticles through porous sandstones. *Journal of Contaminant Hydrology*, *158*, 1–13. doi:10.1016/j.jconhyd.2013.12.002

Nguyen, H. T., Reichhardt, C., & Reichhardt, C. J. O. (2017). Clogging and jamming transitions in periodic obstacle arrays. *Physical Review E, 95*(3), 030902. doi:10.1103/physreve.95.030902

NRC. (2001). Conceptual models of flow and transport in the fractured vadose zone. *National Research Council, National Academies Press*.

O'Donnell, A. G., Young, I. M., Rushton, S. P., Shirley, M. D., & Crawford, J. W. (2007). Visualization, modelling and prediction in soil microbiology. *Nature Reviews Microbiology*, *5*(9), 689–699. doi:10.1038/nrmicro1714

Pang, L., McLeod, M., Aislabie, J., Šimrunek, J., Close, M., & Hector, R. (2008). Modeling Transport of Microbes in Ten Undisturbed Soils under Effluent Irrigation. *Vadose Zone Journal*, *7*(1), 97–111. doi:10.2136/vzj2007.0108

Parker, J. C., & Valocchi, A. J. (1986). Constraints on the Validity of Equilibrium and First-Order Kinetic Transport Models in Structured Soils. *Water Resources Research*, *22*(3), 399–407. doi:10.1029/wr022i003p00399

Parvan, A., Jafari, S., Rahnama, M., Norouzi-Apourvari, S., & Raoof, A. (2021). Insight into particle detachment in clogging of porous media; a pore scale study using lattice Boltzmann method. *Advances in Water Resources, 151*, 103888. doi:10.1016/j.advwatres.2021.103888

Pekdeger, A., & Matthess, G. (1983). Factors of bacteria and virus transport in groundwater. Environmental Geology, 5(2), 49–52. doi:10.1007/bf02381095

Peng, Z., Doroodchi, E., & Evans, G. (2010). DEM simulation of aggregation of suspended nanoparticles. *Powder Technology*, *204*(1), 91–102. doi:10.1016/j.powtec.2010.07.023

Péter, H., Libál, A., Reichhardt, C., & Reichhardt, C. J. (2018). Crossover from jamming to clogging behaviours in heterogeneous environments. Scientific reports, 8(1), 1–9. doi:10.1038/s41598-018-28256-6

Peth, S., Horn, R., Beckmann, F., Donath, T., Fischer, J., & Smucker, A. J. M. (2008). Three-Dimensional Quantification of Intra-Aggregate Pore-Space Features using Synchrotron-Radiation-Based Microtomography. *Soil Science Society of America Journal*, *72*(4), 897–907. doi:10.2136/sssaj2007.0130

Petrášek, Z., & Schwille, P. (2008). Precise measurement of diffusion coefficients using scanning fluorescence correlation spectroscopy. *Biophysical journal*, *94*(4), 1437–1448. doi:10.1529/biophysj.107.108811

Pontedeiro, E. M., Genuchten, M. T. van, Cotta, R. M., & Simunek, J. (2010). The effects of preferential flow and soil texture on risk assessments of a NORM waste disposal site. *Journal of Hazardous Materials*, *174*(1-3), 648–655. doi:10.1016/j.jhazmat.2009.09.100

Prodanovic, M., Mehmani, A., & Sheppard, A. P. (2014). Imaged-based multiscale network modelling of microporosity in carbonates. *Geological Society, London, Special Publications*, *406*(1), 95–113. doi:10.1144/sp406.9

Qin, C.-Z., & Hassanizadeh, S. M. (2015). Pore-Network Modeling of Solute Transport and Biofilm Growth in Porous Media. *Transport in Porous Media*, *110*(3), 345–367. doi:10.1007/s11242-015-0546-1

Raoof, A., & Hassanizadeh, S. M. (2009). A New Method for Generating Pore-Network Models of Porous Media. *Transport in Porous Media*, *81*(3), 391–407. doi:10.1007/s11242-009-9412-3

Raoof, A., & Hassanizadeh, S. M. (2012). A new formulation for pore-network modeling of two-phase flow. *Water Resources Research*, *48*(1). doi:10.1029/2010wr010180

Raoof, A., & Hassanizadeh, S. M. (2013). Saturation-dependent solute dispersivity in porous media: Pore-scale processes. *Water Resources Research*, *49*(4), 1943–1951. doi:10.1002/wrcr.20152

Raoof, A., Hassanizadeh, S. M., & Leijnse, A. (2010). Upscaling Transport of Adsorbing Solutes in Porous Media: Pore-Network Modeling. *Vadose Zone Journal*, *9*(3), 624–636. doi:10.2136/vzj2010.0026

Raoof, A., Nick, H. M., Hassanizadeh, S. M., & Spiers, C. J. (2013). PoreFlow: A complex pore-network model for simulation of reactive transport in variably saturated porous media. *Computers and Geosciences*, *61*, 160–174. doi:10.1016/j.cageo.2013.08.005

Rasmuson, A., & Neretnieks, I. (1980). Exact solution of a model for diffusion in particles and longitudinal dispersion in packed beds. *AIChE Journal*, *26*(4), 686–690. doi:10.1002/aic.690260425

Reichhardt, C., & Reichhardt, C. hspace0. 167emJ. hspace0. 167emO. (2018). Controlled Fluidization, Mobility, and Clogging in Obstacle Arrays Using Periodic Perturbations. Physical Review Letters, 121(6), 068001. doi:10.1103/physrevlett.121.068001

Reichhardt, C., & Reichhardt, C. J. O. (2017). Negative differential mobility and trapping in active matter systems. Journal of Physics: Condensed Matter, 30(1), 015404. doi:10.1088/1361-648x/aa9c5f

Reichhardt, C., & Reichhardt, C. J. O. (2021). Directional clogging and phase separation for disk flow through periodic and diluted obstacle arrays. Soft Matter, 17(6), 1548–1557. doi:10.1039/d0sm01714k

Rillig, M.C., Muller, L.A., & Lehmann, A., 2017. Soil aggregates as massively concurrent evolutionary incubators. The ISME journal, 11(9), 1943–1948. doi :10.1038/ismej.2017.56

Rodrigues, S. M., Trindade, T., Duarte, A. C., Pereira, E., Koopmans, G. F., & Römkens, P. F. A. M. (2016). A framework to measure the availability of engineered nanoparticles in soils: Trends in soil tests and analytical tools. *Trends in Analytical Chemistry*, *75*, 129–140. doi:10.1016/j.trac.2015.07.003

Rousseau, M., Pietro, L. D., Angulo-Jaramillo, R., Tessier, D., & Cabibel, B. (2004). Preferential Transport of Soil Colloidal Particles: Physicochemical Effects on Particle Mobilization. *Vadose Zone Journal*, *3*(1), 247–261. doi:10.2113/3.1.247

Roy, S. B., & Dzombak, D. A. (1997). Chemical Factors Influencing Colloid-Facilitated Transport of Contaminants in Porous Media. *Environmental Science & Technology*, *31*(3), 656–664. doi:10.1021/es9600643

Ryan, J. N., & Elimelech, menachem. (1996). Colloid mobilization and transport in groundwater. *Colloids and Surfaces A: Physicochemical and Engineering Aspects*, *107*, 1–56. doi:10.1016/0927-7757(95)03384-x

Sahimi, M. (2011). Flow and transport in porous media and fractured rock: from classical methods to modern approaches. *John Wiley & Sons*. doi:10.1002/9783527636693

Samari-Kermani, M., Jafari, S., Rahnama, M., & Raoof, A. (2021). Ionic strength and zeta potential effects on colloid transport and retention processes. Colloid and Interface Science Communications, 42, 100389. doi:10.1016/j.colcom.2021.100389

Sang, W., Morales, V. L., Zhang, W., Stoof, C. R., Gao, B., Schatz, A. L., Zhang, Y., et al. (2013). Quantification of Colloid Retention and Release by Straining and Energy Minima in Variably Saturated Porous Media. *Environmental Science & Technology*, *47*, 8256–8264. doi:10.1021/es400288c

Schelde, K., Moldrup, O. H. P. Jacobsen, Jonge, L. W. de H. de Jonge, & Komatsu, T. (2002). Diffusion-Limited Mobilization and Transport of Natural and Colloids in Macroporous and Soil. *Vadose Zone Journal*, *1*, 125–136. doi:doi:10.2136/vzj2002.1250

Schijven, J. F., & Hassanizadeh, S. M. (2000). Removal of viruses by soil passage: Overview of modeling, processes, and parameters. Critical reviews in environmental science and technology, 30(1), 49–127. doi:10.1080/10643380091184174

Schijven, J. F., & Šimrunek, J. (2002). Kinetic modeling of virus transport at the field scale. Journal of Contaminant Hydrology, 55(1-2), 113–135. doi:10.1016/s0169-7722(01)00188-7

Sharma, P., Flury, M., & Zhou, J. (2008). Detachment of colloids from a solid surface by a moving air–water interface. *Journal of Colloid and Interface Science*, *326*(1), 143–150. doi:10.1016/j.jcis.2008.07.030

Shulkla, M. K. (2013). *Soil physics: an introduction.* CRC Press.

Šimůnek, J., Van Genuchten, M. T., Šejna, M., Toride, N., & Leij, F. J. (1999). The STANMOD computer software for evaluating solute transport in porous media using analytical solutions of convection–dispersion equation. International Ground Water Modeling Center.

Šimrunek, J., & Genuchten, M. T. van. (2008). Modeling Nonequilibrium Flow and Transport Processes Using HYDRUS. *Vadose Zone Journal*, *7*(2), 782–797. doi:10.2136/vzj2007.0074

Šimůnek, J., Jarvis, N. J., Genuchten, M. T. van, & Gärdenäs, A. (2003). Review and comparison of models for describing non-equilibrium and preferential flow and transport in the vadose zone. *Journal of Hydrology*, *272*(1–4), 14–35. doi:10.1016/s0022-1694(02)00252-4

Šimůnek, J., Van Genuchten, M. T., Šejna, M., Toride, N., & Leij, F. J. (1999). The STANMOD computer software for evaluating solute transport in porous media using analytical solutions of convection–dispersion equation. *International Ground Water Modeling Center*.

Sirivithayapakorn, S., & Keller, A. (2003). Transport of colloids in saturated porous media: A pore-scale observation of the size exclusion effect and colloid acceleration. *Water Resources Research*, *39*(4). doi:10.1029/2002wr001583

Sudicky, E. A., & Frind, E. O. (1982). Contaminant transport in fractured porous media: Analytical solutions for a system of parallel fractures. *Water Resources Research*, *18*(6), 1634–1642. doi:10.1029/wr018i006p01634

Sun, J., Tandogan, N., Gu, A. Z., Müftü, S., Goluch, E. D., & Wan, K.-T. (2018). Quantification of colloidal filtration of polystyrene micro-particles on glass substrate using a microfluidic device. *Colloids and Surfaces B: Biointerfaces*, *165*, 381–387. doi:10.1016/j.colsurfb.2018.02.044

Syngouna, V. I., & Chrysikopoulos, C. V. (2015). Experimental investigation of virus and clay particles cotransport in partially saturated columns packed with glass beads. *Journal of Colloid and Interface Science*, *440*, 140–150. doi:10.1016/j.jcis.2014.10.066

Sze, A., Erickson, D., Ren, L., & Li, D. (2003). Zeta-potential measurement using the Smoluchowski equation and the slope of the current–time relationship in electroosmotic flow. *Journal of Colloid and Interface Science*, *261*(2), 402–410. doi:10.1016/s0021-9797(03)00142-5

Tang, D. H., Frind, E. O., & Sudicky, E. A. (1981). Contaminant transport in fractured porous media: Analytical solution for a single fracture. *Water Resources Research*, *17*(3), 555–564. doi:10.1029/wr017i003p00555

Tinevez, J.-Y., Perry, N., Schindelin, J., Hoopes, G. M., Reynolds, G. D., Laplantine, E., Bednarek, S. Y., et al. (2017). TrackMate: An open and extensible platform for single-particle tracking. *Methods*, *115*, 80–90. doi:10.1016/j.ymeth.2016.09.016

Tisdall, J. M., & Oades, J. M. (1982). Organic matter and water-stable aggregates in soils. *Journal of soil science*, *33*, 141–163. doi:10.1111/j.1365-2389.1982.tb01755.x

Toride, N., Leij, F. J., & Van Genuchten, M. T. (1995). The CXTFIT code for estimating transport parameters from laboratory or field tracer experiments. *Riverside: US Salinity Laboratory*.

Troester, M., Brauch, H.-J., & Hofmann, T. (2016). Vulnerability of drinking water supplies to engineered nanoparticles. *Water Research*, *96*, 255–279. doi:10.1016/j.watres.2016.03.038

Tufenkji, N., & Elimelech, M. (2004). Deviation from the Classical Colloid Filtration Theory in the Presence of Repulsive DLVO Interactions. *Langmuir*, *20*(25), 10818–10828. doi:10.1021/la0486638

Vasilyev, L., Raoof, A., & Nordbotten, J. M. (2012). Effect of Mean Network Coordination Number on Dispersivity Characteristics. *Transport in Porous Media*, *95*(2), 447–463. doi:10.1007/s11242-012-0054-5

Vitousek, P. M., Aber, J. D., Howarth, R. W., Likens, G. E., Matson, P. A., Schindler, D. W., Schlesinger, W. H., et al. (1997). Human alteration of the global nitrogen cycle: Sources and consequences. *Ecological Applications*, *7*(3), 737–750. doi:10.1890/1051-0761(1997)007[0737:haotgn]2.0.co;2

Vogel, T., Sanda, M., Dusek, J., Dohnal, M., & Votrubova, J. (2010). Using Oxygen-18 to Study the Role of Preferential Flow in the Formation of Hillslope Runoff. *Vadose Zone Journal*, *9*(2), 252–259. doi:10.2136/vzj2009.0066

Vorosmarty, C. J. (2000). Global Water Resources: Vulnerability from Climate Change and Population Growth. *Science*, *289*(5477), 284–288. doi:10.1126/science.289.5477.284

Vries, E. T. de, Raoof, A., & Genuchten, M. T. van. (2017). Multiscale modelling of dual-porosity porous media; a computational pore-scale study for flow and solute transport. *Advances in Water Resources*, *105*, 82–95. doi:10.1016/j.advwatres.2017.04.013

Wang, C., Bobba, A. D., Attinti, R., Shen, C., Lazouskaya, V., Wang, L.-P., & Jin, Y. (2012). Retention and Transport of Silica Nanoparticles in Saturated Porous Media: Effect of Concentration and Particle Size. *Environmental Science & Technology*, *46*(13), 7151–7158. doi:10.1021/es300314n

Wang, M., Gao, B., & Tang, D. (2016). Review of key factors controlling engineered nanoparticle transport in porous media. *Journal of Hazardous Materials*, *318*, 233–246. doi:10.1016/j.jhazmat.2016.06.065

Wang, Q., Lee, J.-H., Jeong, S.-W., Jang, A., Lee, S., & Choi, H. (2011). Mobilization and deposition of iron nano and sub-micrometer particles in porous media: A glass micromodel study. *Journal of Hazardous Materials*, *192*(3), 1466–1475. doi:10.1016/j.jhazmat.2011.06.066

Wang, Y., Bradford, S. A., & Šimrunek, J. (2013). Transport and fate of microorganisms in soils with preferential flow under different solution chemistry conditions. *Water Resources Research*, *49*(5), 2424–2436. doi:10.1002/wrcr.20174

Wildenschild, D., & Sheppard, A. P. (2013). X-ray imaging and analysis techniques for quantifying pore-scale structure and processes in subsurface porous medium systems. *Advances in Water Resources*, *51*, 217–246. doi:10.1016/j.advwatres.2012.07.018

Willingham, T. W., Werth, C. J., & Valocchi, A. J. (2008). Evaluation of the Effects of Porous Media Structure on Mixing-Controlled Reactions Using Pore-Scale Modeling and Micromodel Experiments. *Environmental Science & Technology*, *42*(9), 3185–3193. doi:10.1021/es7022835

Wu, M., Xiao, F., Johnson-Paben, R. M., Retterer, S. T., Yin, X., & Neeves, K. B. (2012). Single- and two-phase flow in microfluidic porous media analogs based on Voronoi tessellation. *Lab on a Chip*, *12*(2), 253–261. doi:10.1039/C1LC20838A

Xu, B., Liu, F., Cryder, Z., Huang, D., Lu, Z., He, Y., Wang, H., et al. (2019). Microplastics in the soil environment: Occurrence, risks, interactions and fate – A review. *Critical Reviews in Environmental Science and Technology*, *50*(21), 2175–2222. doi:10.1080/10643389.2019.1694822

Yao, K.-M., Habibian, M. T., & O'Melia, C. R. (1971). Water and waste water filtration. Concepts and applications. *Environmental Science & Technology*, *5*(11), 1105–1112. doi:10.1021/es60058a005

Yin, X., Aslannejad, H., Vries, E. T. de, Raoof, A., & Hassanizadeh, S. M. (2018). Droplet Imbibition into Paper Coating Layer: Pore-Network Modeling Simulation. *Transport in Porous Media*, *125*(2), 239–258. doi:10.1007/s11242-018-1116-0

Zarikos, I. M., Hassanizadeh, S. M., Oosterhout, L. M. van, & Oordt, W. van. (2018). Manufacturing a Micro-model with Integrated Fibre Optic Pressure Sensors. *Transport in Porous Media*, *122*(1), 221–234. doi:10.1007/s11242-018-1000-y

Zarikos, I., Terzis, A., Hassanizadeh, S. M., & Weigand, B. (2018). Velocity distributions in trapped and mobilized non-wetting phase ganglia in porous media. *Scientific Reports*, *8*(1). doi:10.1038/s41598-018-31639-4

Zhang, C., Oostrom, M., Wietsma, T. W., Grate, J. W., & Warner, M. G. (2011). Influence of Viscous and Capillary Forces on Immiscible Fluid Displacement: Pore-Scale Experimental Study in a Water-Wet Micromodel Demonstrating Viscous and Capillary Fingering. *Energy & Fuels*, *25*(8), 3493–3505. doi:10.1021/ef101732k

Zhang, Q., Hassanizadeh, S. M., Karadimitriou, N. K., Raoof, A., Liu, B., Kleingeld, P. J., & Imhof, A. (2013). Retention and remobilization of colloids during steady-state and transient two-phase flow. *Water Resources Research*, *49*(12), 8005–8016. doi:10.1002/2013WR014345

Zhang, Q., Hassanizadeh, S. M., Liu, B., Schijven, J. F., & Karadimitriou, N. K. (2014). Effect of hydrophobicity on colloid transport during two-phase flow in a micromodel. *Water Resources Research*, *50*(10), 7677–7691. doi:10.1002/2013wr015198

Zhang, Q., Hassanizadeh, S. M., Raoof, A., Genuchten, M. T. van, & Roels, S. M. (2012). Modeling Virus Transport and Remobilization during Transient Partially Saturated Flow. *Vadose Zone Journal*, *11*(2). doi:10.2136/vzj2011.0090

Zhang, Q., Raoof, A., & Hassanizadeh, S. M. (2015). Pore-Scale Study of Flow Rate on Colloid Attachment and Remobilization in a Saturated Micromodel. *Journal of Environment Quality*, *44*(5), 1376. doi:10.2134/jeq2015.01.0058

Zhou, B. B., Li, Y., Wang, Q. J., Jiang, Y. L., & Li, S. (2014). Simulation of chloride transport in an aggregated soil using three conceptual models. *Arabian Journal of Geosciences*, *7*(7), 2539–2546. doi:10.1007/s12517-013-0970-x

Zhou, H., Peng, X., Perfect, E., Xiao, T., & Peng, G. (2013). Effects of organic and inorganic fertilization on soil aggregation in an Ultisol as characterized by synchrotron based X-ray micro-computed tomography. *Geoderma*, *195-196*, 23–30. doi:10.1016/j.geoderma.2012.11.003

Zhou, J., Liu, D., Zhang, W., Chen, X., Huan, Y., & Yu, X. (2017). Colloid characterization and in situ release in shallow groundwater under different hydrogeology conditions. *Environmental Science and Pollution Research*, *24*(16), 14445–14454. doi:10.1007/s11356-017-8856-1

Zvikelsky, O., & Weisbrod, N. (2006). Impact of particle size on colloid transport in discrete fractures. *Water Resources Research*, *42*(12). doi:10.1029/2006wr004873

Samenvatting

Het doel van deze dissertatie was om stromingsexperimenten uit te voeren met de focus op het transport van opgeloste stoffen en colloïden. We onderzoeken het transport hiervan over meerdere schalen en over een groot aantal poriën om zo meer inzicht te vergaren in de interactie van de opgeloste deeltjes en colloïden met de microporositeit. Daarvoor maakten wij gebruik van micro-modellen waar we een samenvoeging van kleine korrels (aggregaat) aan toevoegen om een duaal-porositeit model te creëren. Deze modellen werden gebruikt om verzadigde experimenten uit te voeren, evenals het effect van drainage en imbibitie (doordrenking) cycli op de remobilisatie van colloïden in een duaal-porositeit model te onderzoeken. Voor deze experimenten hebben wij meerdere opstellingen ontwikkeld om de opgeloste stoffen en colloïden te kunnen volgen op de poriënschaal. Voor het rekenkundige deel is gebruik gemaakt van een porie netwerkmodel om verder onderzoek te doen naar de interactie tussen inter-aggregaat en intra-aggregaat poriën. Hiervoor is een poriën netwerk generator ontwikkeld en is onderzoek verricht naar het effect van de aggregaat porositeit en aggregaat permeabiliteit (doorlaatbaarheid).

In hoofdstuk 2 hebben we een micromodel ontwikkeld die gebaseerd is op röntgen tomografie beelden van een zand monster om zo de porie complexiteit te integreren in het micromodel. Met dit micromodel is een colloïden experiment uitgevoerd met een in-huis ontwikkelde opstelling waarbij het mogelijk is om de colloïden te volgen in een 10×10 mm^2 domein. Deze domeingrootte zorgde voor een groot aantal poriën en korrels om zo de verschillende transportmechanismen te observeren. We hebben in totaal van 1357 colloïden de stromingsbaan geregistreerd. Voor elke colloïde zijn de gedragingen bepaald in het poreuze domein, 29 colloïden waren geïmmobiliseerd, 19 werden geïmmobiliseerd en weer geremobiliseerd en de rest was mobiel. Alsook is de bochtigheidscoëfficiënt, verblijftijd, penetratiediepte en de lokale stroomsnelheidsverschillen bepaald. Verder hebben wij de doorbraakcurve op een nieuwe manier geconstrueerd waarbij we Dirac delta input aannemen van de colloïden stromingsbanen. Colloïden werden voornamelijk geïmmobiliseerd door lokale stroomsnelheid verschillen en de heterogeniteit van het micro-model oppervlak. Door de doorbraakcurve op een nieuwe manier te construeren kunnen we bepaald gedrag uitsluiten waardoor we beter het effect van de poriën schaal op de veldschaal kunnen onderzoeken.

In het derde hoofdstuk hebben we het ontwikkelde micromodel van hoofdstuk 2 getransformeerd naar meerdere duaal-porositeit modellen. Hiervoor zijn de vaste korrels getransformeerd naar aggregaten, dit is voor vier verschillende fracties gedaan: 0.25, 0.50, 0.75 en 1.0 fractie van de vaste korrels. Dit resulteerde in één niet geaggregeerd domein en vier micromodellen met bimodale poriegrootteverdelingen. Om de opgeloste deeltjes te kunnen volgen in het micro-model hebben wij een "fluorescence recovery after photobleaching (FRAP)" opstelling gebouwd. Dit geeft ons de mogelijkheid om de concentratie van de opgeloste stof te volgen in een 10×10 mm^2 domein en kunnen we van het front van het concentratieveld de oppervlakte, lengte en gemiddelde concentratiegradiënt bepalen. Deze parameters geven ons meer inzicht in het effect van duaal-porositeit op het transport van opgeloste deeltjes. Eveneens werd de doorbraakcurve geconstrueerd en de transport parameters bepaald. De experimenten zijn voor vier gemiddelde stroomsnelheden uitgevoerd op de vijf micromodellen. Een grotere fractie van aggregaten leidde tot een grotere oppervlakte en lengte van het front van het concentratieveld, maar er werden geen significante verschillen in de concentratiegradiënten waargenomen. Een verhoogde gemiddelde stroomsnelheid leidde tot geen significant verschil in de oppervlakte, terwijl er een toename van de lengte en gradiënt van het front van het concentratieveld werd waargenomen. De waarnemingen op poriënschaal maakten het mogelijk om de veranderingen in het transportgedrag van opgeloste stoffen waar te nemen onder de invloed van duaal-porositeit. Al werden in de doorbraakcurve weinig veranderingen werden waargenomen.

In het derde hoofdstuk hebben we opgeloste stof transport experimenten uitgevoerd op micromodellen en hebben het effect van aggregatie fractie onderzocht. In het vierde hoofdstuk onderzochten we het effect van aggregaat porositeit en permeabiliteit door middel van het gebruik van porienetwerk modelering. Een porienetwerk bestaat uit bolvormige lichamen, ook wel porielichamen genoemd, deze lichamen zijn verbonden door één of meerder connecties, porienekken genoemd. We hebben een macroschaal porienetwerk gegenereerd van $100\times20\times20$ mm^3 en daarin zijn 1000 aggregaten geplaatst. De porie elementen hebben een vaste locatie en connectiviteit, de porositeit van de aggregaten is veranderd door de grootte van de porielichamen te veranderen en de doorlaatbaarheid van de aggregaten is aangepast door de grootte van de porienekken aan te passen. We hebben de concentratie van de opgeloste stof op 3 locaties in het porienetwerk gemeten en aan de hand van deze metingen de doorbraakcurves bepaald. We hebben de transport parameters bepaald door de doorbraakcurves te fitten aan de macroscopische Mobiele-Immobiele formuleringen. Bij het verhogen van de aggregaat porositeit vonden we een verlaging van het mobiele water (ϕ_m), een verhoging van de

massaoverdracht (α) en we observeerden staartvorming in de doorbraakcurve. Grotere porienekken leidde tot veranderingen in de relatieve stroomsnelheden tussen de intra-aggregaat en inter-aggregaat poriën. Hogere stroomsnelheden in de aggregaten leidde tot een verandering van het transport regime, van diffusie gedomineerd naar advectie gedomineerd. Het gevolg hiervan was dat de massa overdracht tussen de mobiele en immobiele domeinen werd verhoogd en minder staartvorming werd geobserveerd in de doorbraakcurve.

In hoofdstuk 5 gebruikten we de in hoofdstuk 3 ontwikkelde micro-modellen voor het uitvoeren van colloïden transport experimenten. We onderzochten het effect van verschillende fracties duaal-porositeit en het effect van de gemiddelde stroomsnelheid op het transport van de colloïden. We hebben dezelfde procedure gebruikt die in hoofdstuk 2 was ontwikkeld om de colloïden te volgen en te analyseren. We volgden de colloïden door de macro- en microporiën. In het micromodel zonder microporiën vonden we 11 colloïden die waren geïmmobiliseerd van de in totaal 1555 geobserveerde stroombanen, terwijl het toevoegen van microporiën leidde tot een toename van maximaal 43% in geïmmobiliseerde colloïden (1226 van de 2870 in monster S40/100). Door de introductie van de microporiën werd een aanzienlijk deel van de colloïden door de microporiën getransporteerd. De lagere snelheden evenals verhoogde interactie met de korrel oppervlakken leidden tot de hoger waargenomen retentie van colloïden. Het verhogen van de stroomsnelheid leidde tot meer waargenomen colloïden die door de aggregaten werden getransporteerd, alhoewel we de hoogste retentie observeerden met de laagst toegepaste gemiddelde stroomsnelheid van 1.0 m dag^{-1}. Deze observaties laten zien dat de stroomsnelheden en de daar bijhorende hydrodynamische krachten een cruciale rol spelen bij de retentie van de colloïden.

Ten slotte hebben wij in hoofdstuk 6 twee fasen stroming cycli van imbibitie en drainage uitgevoerd op monster S40/50. Ten eerste injecteren we colloïden in water verzadigde condities, zoals uitgevoerd in hoofdstuk 5. We draineren het monster met Fluorinert en volgden de colloïden gedurende twee cycli van imbibitie en drainage. We verkregen de faseverdeling over het hele domein en we observeerden de colloïde remobilisatie in detail in twee aggregaten. We hebben geobserveerd dat de aggregaten een vitale rol spelen in faseverdeling, doordat deze water gesatureerd blijven door de kleine poriën. Gedurende imbibtie worden er paden gevormd door water gesatureerde aggregaten en de stroomsnelheidsverandering leidde tot remobilisatie van de colloïden die geïmmobiliseerd waren in de aggregaten, ook hebben we remobilisatie van colloïden geobserveerd door bewegende vloeistofgrensvlakken.

Concluderend, systemen met dubbele porositeit bemoeilijken het transport van opgeloste stoffen en colloiden in enkel en meerfase stroming. We ontwikkelden micromodellen en porienetwerken om direct op de poriënschaal het transportgedrag te observeren door experimenten en computermodellen uit te voeren. Alhoewel wij onze focus op geaggregeerde poreuze media hebben gericht bestaan er veel andere poreuze media met bimodale poriegrootteverdelingen in zowel natuurlijke als industriële materialen. De ontwikkelde methoden kunnen op deze systemen worden toegepast om meer inzicht te geven in de waarnemingen op grotere schaal door de processen op poriënschaal aan deze te relateren.

Curriculum Vitae

Enno Tijmen de Vries was born on 2nd of June 1992 in Wijk bij Duurstede, The Netherlands. He grew up in Veenendaal and attended Rembrandt College. In 2011, he started his Earth Sciences Bachelor at Utrecht University. He finished his bachelor's in 2014, the title of his bachelor thesis was "Modeling Maize yield for variable rainfall conditions in the West Usambara Mountains, Tanzania". Next, he proceeded with his master's degree in Earth Surface and Water, following the hydrology track. He obtained his degree in 2016 which is conferred cum laude. During his masters he worked on flow and transport modeling, he developed dual-porosity pore networks and researched the effect of multi-scale porous media on the transport parameters. During his guided research, he focused on the drainage of dual-porosity samples using pore network modeling. In 2016, he continued his work on multi-scale porous media during his Ph.D. project. He developed multiple set-ups for micromodel solute and colloid experiments together with Amir Raoof, Sanli Faez, and Qianjing Tang and established, together with Ioannis Zarikos, the cleanroom for soft lithography production in the Multi-scale porous media lab at Utrecht University. During his Ph.D. he assisted multiple courses of the Earth sciences bachelor and masters and supervised 5 master thesis' and 2 guided research projects.

List of Publications

Chapter 2: accepted for publication in Advances in Water Resources; Vries, E. T. de, Tang, Q., Faez, S., & Raoof, A. Fluid Flow and Colloid Transport Experiment in Single-Porosity Samples; Tracking of Colloid Transport Behavior in a Saturated Micromodel

Chapter 3: prepared for submission; Fluid Flow and Solute Transport Experiments in Dual-Porosity Samples; Direct Pore-Scale Observation in Saturated Micromodels

Chapter 4: Published as; Vries, E. T. de, Raoof, A., & Genuchten, M. T. van. (2017). Multiscale modelling of dual-porosity porous media; a computational pore-scale study for flow and solute transport. Advances in Water Resources, 105, 82–95. doi:10.1016/j.advwatres.2017.04.013

Chapter 5: prepared for submission; Fluid Flow and Colloid Transport Experiments in Dual-Porosity Samples; Role of Micro-Porosity on the Transport Behavior of Colloids

Chapter 6: prepared for submission; Two-phase Flow Drainage and Imbibition Cycles in Dual-Porosity Samples; Role of Micro-Porosity and moving Interfaces on Retention and Remobilization of Colloids

Other: Yin, X., Aslannejad, H., Vries, E. T. de, Raoof, A., & Hassanizadeh, S. M. (2018). Droplet imbibition into paper coating layer: pore-Network modeling simulation. *Transport in porous media, 125*, 239-258. doi: 10.1007/s11242-018-1116-0

Yin X., Vries E.T. de, Raoof A., Hassanizadeh S.M. (2019) Dynamic Pore-Network Models Development. In: *Singh V., Gao D., Fischer A. (eds) Advances in Mathematical Methods and High Performance Computing. Advances in Mechanics and Mathematics, vol 41. Springer, Cham.* doi:10.1007/978-3-030-02487-1_21